





# Optical Isolators in Silicon Based Photonic Integrated Circuits

Optische isolatoren in fotonische geïntegreerde schakelingen  
op basis van silicium

Samir Ghosh

Promotoren: prof. dr. ir. R. Baets, prof. dr. ir. G. Roelkens  
Proefschrift ingediend tot het behalen van de graad van  
Doctor in de Ingenieurswetenschappen: Fotonica

Vakgroep Informatietechnologie  
Voorzitter: prof. dr. ir. D. De Zutter  
Faculteit Ingenieurswetenschappen en Architectuur  
Academiejaar 2012 - 2013



ISBN 978-90-8578-618-4  
NUR 959  
Wettelijk depot: D/2013/10.500/51



Universiteit Gent  
Faculteit Ingenieurswetenschappen en Architectuur  
Vakgroep Informatietechnologie

## Optical Isolators in Silicon Based Photonic Integrated Circuits

optische isolatoren in fotonische geïntegreerde schakelingen op basis van silicium

---

Samir Ghosh



Proefschrift tot het bekomen van de graad van  
Doctor in de Ingenieurswetenschappen:  
Fotonica  
Academiejaar 2012-2013





Universiteit Gent  
Faculteit Ingenieurswetenschappen en Architectuur  
Vakgroep Informatietechnologie

Promotor:

Prof. Dr. Ir. Roel Baets  
Prof. Dr. Ir. Gunther Roelkens

Examencommissie:

Prof. Dr. Ir. Rik Van de Walle (voorzitter)	Universiteit Gent, MMLab
Prof. Dr. Ir. Roel Baets (promotor)	Universiteit Gent, INTEC
Prof. Dr. Ir. Gunther Roelkens (promotor)	Universiteit Gent, INTEC
Prof. Dr. Ir. Dries Van Thourhout (secretaris)	Universiteit Gent, INTEC
Prof. Dr. Ir. Jeroen Beeckman	Universiteit Gent, ELIS
Dr. Ir. Wim Van Roy	IMEC
Dr. Ir. Mathias Vanwolleghem	CNRS, IEMN

Universiteit Gent  
Faculteit Ingenieurswetenschappen en Architectuur

Vakgroep Informatietechnologie  
Sint-Pietersnieuwstraat 41, B-9000 Gent, België

Tel.: +32-9-264.33.16

Fax.: +32-9-331.35.93



# Acknowledgments

This is the most important as well as the most difficult part of my thesis. It is important because this thesis would not have been successful without helps from various people, and it is difficult because the number is really uncountable. However, one good thing about this section is that it will not be proofread, corrected etc. I want to clarify that the order of names appeared here is not linked with the order of importance.

The first person to be thanked is Prof. Roel Baets. He gave me an excellent opportunity to pursue highest academic degree in one of the top ranked universities. He not only provides me countless advices towards research work but other aspects of life. I want to express my deepest gratitude for all his kind help. The second person to be thanked is Prof. Gunther Roelkens. Initially he was not involved with my PhD work but after almost 2 years Roel proposed his name as my co-promotor. For that also I am indebted to Roel. Without Gunther's guidance I could hardly imagine my thesis. His ever welcoming nature makes me confident and eases working environment. Once again, thank you very much for your friendly endless efforts. I am also thankful to honourable jury members for their assessments and suggestions which helped me to improve my thesis.

I would like to acknowledge kind co-operations from Prof. Tetsuya Mizumoto's lab in Tokyo Institute of Technology, Japan. He used to supply us magnetic materials which were indispensable for my work. I would like to thank Ryohei Takei who has visited our lab during the early times of my PhD. He taught me various aspects of isolators.

My cordial thanks also goes to Wim Van Roy from imec, Belgium and Prof. Beth Stadler from University of Minnesota, USA for their excellent collaborations. A plenty of thanks to Celso, Mauricio and Kristof for their assistance and company in imec.

I would like to thank my Iranian colleague and friend Shahram especially for his help related to bonding in the clean room. Liesbet, Steven, Kasia... thanks a lot for your help. Without their sincere efforts my PhD could not have been successful. Martin and his girlfriend deserve a special thanks for translating

(and proofreading) my English summary into Dutch and various other helps related to my thesis. Thanks to Ananth also for correcting my thesis upto some extent.

I am grateful to Emmanuel, who was my office mate few years ago. If I have learned some mask designing, then that is solely because of his endeavor. Thanks to all of my great current and former group colleagues..nothing for particular but for everything in general. Particularly I am under debt of Kristien, Ilse, Mike, Eddy, Ann, Luc and Peter Gun for their endless supports.

All my compatriots made Belgium as my second home. Thanks to Sukumar, Rajesh, Ananth, Adil, Aditya, Pijush, Sarvagya, Shibnath. A huge round of applause for my cricket mates: Abhisek, Asoke, Ark(a.k.a Liverock), Amit, Ananth, Aditya, Sukumar, Karthik, Sandeep, Shailesh, Manan, Unmesh, Kamal, Pravin...your presence elated me. Thanks to Debasish (Talu), Kapil (Heichhh Sir), Joyjit (Kaka), Sayan (Fastu), Kuntal (Balu), Diotima (Kakima), Suwendu (Hangpo), Rajib, Ananda, Suwendu Guin, Rams, Amit (Baby)...for your support and best wishes from abroad.

I am indebted to my family for their support in each and every moment. My deepest gratitude to my mother, mother-in-law and father-in-law. I am thankful to Bishnu (my brother-in-law) for taking care of everything in my absence. Finally one person is missing..my beautiful wife sweet-heart Seuli...I do not want to thank you because a thank is not sufficient for all which you have done for me. You are truly my soul-mate, my life...thanks to Almighty.

*Gent, August 2013  
Samir Ghosh*

# Table of Contents

<b>Acknowledgments</b>	<b>i</b>
<b>Nederlandse Samenvatting</b>	<b>xxv</b>
<b>English summary</b>	<b>xxxiii</b>
<b>1 Introduction</b>	<b>1</b>
1.1 Objective of this work . . . . .	1
1.2 Waveguide based isolator . . . . .	3
1.2.1 Free space bulk isolator . . . . .	3
1.2.2 Magneto-optic materials . . . . .	5
1.2.3 Faraday rotator based waveguide isolator . . . . .	6
1.2.4 Nonreciprocal phase shift (NRPS) based isolators . . . . .	7
1.2.5 Nonreciprocal loss (NRL) based isolators . . . . .	10
1.2.6 Non-magnetic approaches to optical isolators . . . . .	11
1.3 Rationale and outline of this thesis . . . . .	12
1.4 Publications . . . . .	14
1.4.1 International Journals . . . . .	14
1.4.2 Conference Proceedings . . . . .	14
References . . . . .	15
<b>2 Theoretical study of Non-reciprocity in Magneto-optics</b>	<b>23</b>
2.1 Magneto-optics . . . . .	23
2.1.1 Historical introduction . . . . .	23
2.1.2 Constitutive relations . . . . .	25
2.1.3 EM wave propagating through a gyrotropic medium . . . . .	27
2.1.4 Reflection-type magneto-optical effects . . . . .	31
2.2 Waveguide with magneto-optic cladding . . . . .	33
2.3 Perturbation method . . . . .	34
2.4 Numerical calculation of the NRPS . . . . .	36
2.4.1 Slab waveguide geometry . . . . .	36
2.4.2 Strip waveguide geometry . . . . .	38

---

2.5	Influence of Ce:YIG layer . . . . .	39
2.6	Conclusion . . . . .	40
	References . . . . .	40
<b>3</b>	<b>Push-Pull Mach Zehnder interferometer optical isolator</b>	<b>43</b>
3.1	Mach Zehnder interferometer (MZI) . . . . .	43
3.2	Nonreciprocal MZI based optical isolator . . . . .	46
3.2.1	Design schemes . . . . .	46
3.2.2	Analytical calculations of NRPS . . . . .	48
3.3	Adhesively Bonded Garnet on SOI MZI . . . . .	49
3.3.1	Waveguide design parameters and tolerance study . . . . .	51
3.4	Fabrication Procedure . . . . .	55
3.5	Measurement Details . . . . .	57
3.5.1	Isolation measurement . . . . .	57
3.5.2	Hysteresis analysis . . . . .	59
3.6	Loss analysis . . . . .	60
3.7	Conclusion . . . . .	64
	References . . . . .	64
<b>4</b>	<b>Asymmetric Arm Width Mach-Zehnder Interferometer Isolator</b>	<b>69</b>
4.1	Isolator design . . . . .	70
4.2	Analytical calculations . . . . .	70
4.3	Nonreciprocal phase shifter design . . . . .	73
4.4	MMI design details . . . . .	76
4.5	Fabrication and Measurements . . . . .	78
4.6	Analysis of as-fabricated device . . . . .	80
4.7	Conclusion . . . . .	84
	References . . . . .	84
<b>5</b>	<b>Isolator For Transverse Electric Polarized Light</b>	<b>87</b>
5.1	Introduction . . . . .	88
5.2	Designs and operation principle . . . . .	88
5.2.1	Design of Nonreciprocal Phase shifter . . . . .	91
5.2.2	Design of polarization rotator . . . . .	94
5.2.3	Design of MMI . . . . .	98
5.2.4	Design of spot-size converter . . . . .	99
5.3	Fabrication procedure . . . . .	99
5.4	Analysis of fabricated polarization rotator . . . . .	101
5.5	Measurement results . . . . .	103
5.6	Conclusion . . . . .	110
	References . . . . .	111

---

<b>6</b>	<b>Optical Circulator on Silicon-on-Insulator(SOI)</b>	<b>113</b>
6.1	Basics of an optical circulator . . . . .	113
6.2	Integrated circulator . . . . .	114
6.3	Principle of operation . . . . .	115
6.4	Narrowband device . . . . .	117
6.5	Design of directional coupler . . . . .	118
6.5.1	MMI as a replacement for directional coupler . . . . .	121
6.6	Measurements . . . . .	122
6.7	Conclusion . . . . .	129
	References . . . . .	129
<b>7</b>	<b>Nonreciprocal Nested Ring Mach-Zehnder Interferometer</b>	<b>133</b>
7.1	Nested ring resonator MZI . . . . .	133
7.2	Isolator design concepts . . . . .	137
7.2.1	Asymmetric directional coupler . . . . .	137
7.2.2	Symmetric directional coupler . . . . .	140
7.3	Device fabrication and measurements . . . . .	140
7.4	Conclusion . . . . .	143
	References . . . . .	144
<b>8</b>	<b>Sputtering Deposition Approach of Garnet for Integrated Nonreciprocal Optical devices on SOI</b>	<b>145</b>
8.1	Introduction . . . . .	145
8.2	Garnet deposition by magnetron sputtering . . . . .	147
8.2.1	Process flow . . . . .	147
8.2.2	YIG deposition . . . . .	148
8.2.3	Ce:YIG deposition . . . . .	149
8.3	Isolator design . . . . .	151
8.4	Loss measurements . . . . .	152
8.5	Conclusion . . . . .	153
	References . . . . .	154
<b>9</b>	<b>Conclusions and Outlook</b>	<b>157</b>
9.1	Conclusions . . . . .	157
9.2	Outlook . . . . .	159



# List of Figures

1	(a) Schematische doorsnede van een met granaat gebonde golfgeleider (b) NRPS in functie van de siliciumgolfgeleider dikte (c) Schematische weergave van een push-pull MZI-type isolator (d) Gemeten spectrum voor voor-en achterwaartse propagatie. . . . .	xxviii
2	(a) Schematische weergave van een met granaat gebonde MZI met verschillende armbreedtes (b) NRPS in functie van de siliciumgolfgeleider breedte voor een siliciumdikte van 220 nm (c) Gemeten MZI transmissie. . . . .	xxix
3	Schematische weergave van een TE isolator. . . . .	xxix
4	SEM afbeeldingen van de symmetrische en asymmetrische golfgeleidersecties voor de gefabriceerde polarizator (a) zicht van bovenaf (b) zicht vanuit een hoek. . . . .	xxx
5	Schema van een met granaat gebonde NRMZI. . . . .	xxx
1	(a) Schematic diagram of a garnet bonded waveguide cross-section (b) NRPS vs. silicon waveguide thickness (c) Schematic drawing of a push-pull MZI type isolator (d) Measured spectra for forward and backward propagations. . . . .	xxxv
2	(a) Schematic diagram of the garnet bonded MZI with dissimilar arm widths (b) NRPS vs. silicon waveguide width for 220 nm Si thickness (c) Measured MZI transmission. . . . .	xxxvi
3	Schematic diagram of TE isolator. . . . .	xxxvi
4	SEM images of symmetric and asymmetric waveguide sections of the fabricated polarization rotator (a) top-view (b) view from and angle. . . . .	xxxvii
5	Schematic of a NRMZI with bonded garnet. . . . .	xxxviii
1.1	Schematic diagram of bulk free space isolator. . . . .	4
1.2	(a) Schematic diagram of a push-pull type NRPS based MZI isolator. . . . .	8
1.3	Schematic diagram of a (a) push-pull type NRPS based SOI-MZI isolator [55] (b) nonreciprocal ring resonator [57]. . . . .	9

1.4	(a) Schematic diagram of a NRL isolator in an SOA [20] working for TE polarization. . . . .	11
1.5	(a) Schematic diagram of a NRL isolator in an SOA [21] working for TM polarization. M is the direction of magnetization. . . . .	11
2.1	(a) Set-up to demonstrate Zeeman effect (b) observed perpendicular to the magnetic field (c) observed along the magnetic field. . . . .	24
2.2	Magnetic hysteresis loop between M and H. . . . .	26
2.3	Vector representation of the wave propagation. . . . .	28
2.4	Magneto-optical Kerr effects (a) Polar Kerr effect, (b) longitudinal Kerr effect and (c) transverse Kerr effect. . . . .	32
2.5	Optical waveguide with magneto-optic cladding. Light propagating along z-axis with an external magnetic field applied along y-axis. . . . .	34
2.6	Slab waveguide geometry with a garnet stack bonded by BCB. . . . .	37
2.7	Simulation of NRPS as a function of silicon waveguide thickness and BCB bonding layer thickness . . . . .	37
2.8	Variation of confinement factor of TM mode in Ce:YIG layer as a function of silicon waveguide thickness for various BCB thickness. . . . .	38
2.9	(a) Cross-section of a strip waveguide with a garnet die bonded on top by BCB and (b) simulation of the NRPS as a function of waveguide width (W) considering a silicon thickness and Ce:YIG thickness of 220 nm and 260 nm respectively. . . . .	39
2.10	Confinement factor of TM mode in the Ce:YIG layer as a function of Ce:YIG thickness for various BCB thicknesses. . . . .	39
2.11	Variation of NRPS with Ce:YIG thickness for slab waveguide structure. . . . .	40
3.1	Schematic diagram of a Mach-Zehnder interferometer. . . . .	44
3.2	Illustration of transmission spectra of an unbalanced ( $\Delta L = 80 \mu\text{m}$ ) Mach Zehnder interferometer with different NRPS. . . . .	45
3.3	Schemes of isolator designs for (a) anti-parallel, (b) unidirectional magnetic field. $\mathbf{H}$ is the external magnetic field and $\mathbf{k}$ is the wave/light propagation vector. The arrows indicating the direction of the corresponding vectors. RPS is the reciprocal phase shifter . . . . .	46
3.4	Illustration of transmission spectra of a broadband Mach Zehnder interferometer with NRPS = $\pi$ considering lossless waveguides. . . . .	48
3.5	(a) Schematic top-view diagram of adhesively garnet bonded push-pull MZI for optical isolator, (b) schematic cross-section view of bonded waveguide stack and (c) optical micrograph of garnet bonded MZI. . . . .	49

3.6	Efficiency of the designed MMIs as a function of $L_{MMI}$ for $W_{MMI} = 4.0\mu\text{m}$ and output waveguide offset of $1.1\mu\text{m}$ at $1550\text{ nm}$ wavelength. . . . .	50
3.7	Variation of effective refractive index as a function of waveguide width for an air clad Si waveguide of thickness $220\text{ nm}$ at $1550\text{ nm}$ wavelength. . . . .	50
3.8	Variation of effective refractive index as a function of waveguide width for different BCB layer thickness at $1550\text{ nm}$ wavelength with $260\text{ nm}$ thick Ce:YIG layer. . . . .	52
3.9	Intensity plot of (a) the fundamental guided TM in a BCB bonded garnet clad silicon waveguide of width $900\text{ nm}$ and thickness $220\text{ nm}$ and (b) leaky mode in the Ce:YIG layer. In this case a $260\text{ nm}$ thick Ce:YIG layer bonded by $100\text{ nm}$ BCB is assumed. . . . .	52
3.10	Variation of effective refractive index as a function of the silicon waveguide thickness for different BCB thicknesses at $1550\text{ nm}$ wavelength with $260\text{ nm}$ thick Ce:YIG layer and waveguide of width $900\text{ nm}$ . . . . .	53
3.11	Variation of effective refractive index as a function of the Ce:YIG thickness for different BCB thicknesses at $1550\text{ nm}$ wavelength for a silicon waveguide of width $900\text{ nm}$ and thickness $220\text{ nm}$ . . . . .	53
3.12	Spectral dependence of effective refractive index for various BCB thickness with waveguide of width $900\text{ nm}$ and thickness $220\text{ nm}$ , $260\text{ nm}$ thick Ce:YIG. . . . .	54
3.13	Bonding steps. . . . .	55
3.14	FIB cross-section of the inverted garnet bonded waveguide stack. . . . .	56
3.15	Artistic impression of the measurement set-up and the magnet stack. . . . .	57
3.16	Sample-I: (a) Normalized MZI transmission spectra for the forward and backward propagation and (b) Picture of the garnet bonded SOI. . . . .	58
3.17	Sample-II: MZI transmission spectra for the forward and backward propagation (a) $L = 400\mu\text{m}$ (b) $L = 920\mu\text{m}$ (not normalized). . . . .	58
3.18	Normalized transmission spectra of the MZI (sample-I) for different angular orientations of the magnetic field with respect to the light propagation direction: (a) $90^\circ$ , (b) $0^\circ$ , (c) $270^\circ$ and (d) $180^\circ$ . . . . .	60
3.19	(a) Nonreciprocal wavelength shift as a function of the $(h^2 + l^2)^{-3/2}$ , where $h$ is the distance between the magnet and the Ce:YIG layer and $2l$ is the distance between the two poles of the magnet stack. Negative values for $(h^2 + l^2)^{-3/2}$ indicate that the magnet was rotated $180^\circ$ , (b) magnetization curve of the Ce:YIG layer after subtracting contribution from paramagnetic SGGG substrate. . . . .	61

3.20	Contour plots of the $E_x$ field of the $TM_{00}$ mode for 900 nm wide and 220 nm silicon waveguides with (a) 50 nm BCB as top cladding and (b) 50 nm BCB plus garnet stack as top cladding. . . . .	61
3.21	(a) Schematic diagram for measuring transmission loss and (b) Measured optical transmission for only BCB covered and BCB plus garnet covered straight TM waveguide. . . . .	62
3.22	(a) Simulated insertion loss and reflection at the interface between a plain SOI waveguide and a Ce: YIG on SOI waveguide as a function of BCB bonding layer thickness and (b) field plot of light propagating from a plain BCB covered silicon waveguide to a BCB plus garnet covered silicon waveguide. . . . .	62
3.23	(a) Contour plot of the $E_x$ field of the quasi-TM polarized mode and (b) field enhancement in the BCB bonding layer due to a vertical slot waveguide effect. . . . .	63
3.24	Estimation of insertion loss from a $\pi$ nonreciprocal phase shifter for various BCB thickness at 1550 nm wavelength. In this simulation width of 220 nm thick silicon waveguide is 900 nm with a 260 nm thick Ce:YIG layer bonded by BCB. Material loss of Ce:YIG is taken as 60 dB/cm [30]. . . . .	63
4.1	Layout of the proposed isolator using a Mach-Zehnder interferometer design. . . . .	70
4.2	Schematic cross-sectional view of the MZI arms with a garnet stack bonded on top of it. . . . .	71
4.3	Illustration of simulated intensity profile of the designed MZI. . . . .	72
4.4	(a) Cross-section view of the garnet bonded trapezoidal silicon waveguide (b) NRPS vs. $W_t$ for 210 nm thick silicon at 1500 nm wavelength. . . . .	74
4.5	NRPS vs. $W_t$ for (a) 220 nm (b) 230 nm thick silicon waveguide at 1500 nm wavelength. . . . .	74
4.6	$\Delta$ NRPS between waveguides of width ( $W_t = 350$ nm, $W_b = 430$ nm) and ( $W_t = 850$ nm, $W_b = 930$ nm) as a function of $t_{BCB}$ for various silicon thicknesses at 1500 nm. . . . .	75
4.7	Influence of waveguide cross-section on NRPS as function of $W_b$ for (a) 210 nm (b) 220 nm thick silicon waveguide at 1500 nm wavelength with 80 nm thick BCB between Si waveguide and 260 nm thick Ce:YIG layer. In this case $W_t$ is varied as $W_t = (W_b - 2 \times 40)$ nm. . . . .	75
4.8	Analytical calculation of transmission of the MZI with dissimilar arm widths for three different splitting ratios considering lossless waveguides. . . . .	76

---

4.9	Normalized MMI power coupling/splitting efficiency vs. $L_{MMI}$ for various BCB thicknesses at 1500 nm wavelength. Power coupling/splitting efficiency of a MMI arm is defined as the power on that arm divided by total power. In this case total power is equal to unity. . . . .	77
4.10	(a) Spectral dependence of normalized splitting efficiency of the MMI for 50 nm BCB and $t_{Si} = 220$ nm (b) MMI splitting efficiency vs. $t_{Si}$ for 100 nm BCB. $L_{MMI} = 12.5 \mu\text{m}$ for both the cases. . . . .	77
4.11	Schematic diagram of MZIs of varying lengths bonded by same garnet chip operating at unidirectional transverse magnetic field. . . . .	78
4.12	Measured transmission spectra for different MZI under the external magnetic field. . . . .	79
4.13	Plot of $\Delta\lambda/\text{FSR}$ vs. $L$ . . . . .	79
4.14	SEM cross-section view of the garnet stack bonded on the SOI. . . . .	80
4.15	Schematic cross-section of fabricated MZI arms with the garnet bonded on top of it. . . . .	80
4.16	Coupling efficiency of the MMI to the wider and narrower arm as function of (a) BCB thickness at 1500 nm wavelength (b) Wavelength for 80 nm BCB thickness. . . . .	81
4.17	Spectra of the MZIs (a) Simulated (b) Measured. . . . .	81
4.18	(a) Comparison between the measured and simulated FSR (b) Spectral dependence of $\Delta n_g$ for the 210 nm thick silicon waveguide with 80 nm of BCB. . . . .	82
4.19	(a) Analytically calculated MZI spectrums considering $\alpha_w = 3.45/\text{cm}$ (equivalently 15 dB/cm), $\alpha_n = 5.76/\text{cm}$ (equivalently 25 dB/cm) (b) Fitting of measured extinction ratios (ER) for different MZIs between 1494-1510 nm wavelength. . . . .	83
4.20	(a) Simulated $\Delta\Gamma$ as a function of $t_{BCB}$ at 1500 nm wavelength for the fabricated waveguide stack. . . . .	83
5.1	TE mode isolator: advanced passive waveguide/nonreciprocal phase shifter in one arm while the other arm is designed purely for TE mode. . . . .	89
5.2	Push-pull type TE mode isolator: with one section of advanced passive waveguide on each arm of the MZI. . . . .	89
5.3	Push-pull type TE mode isolator: with two sections of advanced passive waveguide on each arm of the MZI. . . . .	90

5.4	Enlarged sketch of an advanced passive (ADP) waveguide containing two spot-size converters, two polarization rotators and a nonreciprocal phase shifter. SEM pictures: inset (I) shows the taper tip of the spot-size converter; inset (II) shows the transition section between symmetrical and asymmetrical sections of polarization rotator (PR). (a) Type-I, where the nonreciprocal phase shifter is tapered to narrower symmetrical waveguide section of the PR (b) Type-II, widths of symmetrical section of the PR and the nonreciprocal phase shifter section are identical without any tapering. Spot-size converters and polarization rotators are defined by etching 160 nm thick poly-Si overlay situated on top of 220 nm thick c-Si.	91
5.5	(a) Schematic cross-section of the garnet bonded waveguide at the nonreciprocal phase shifter of the ADP (b) Variation of NRPS per unit length as a function of BCB thickness ( $t_{BCB}$ ) at 1540 nm wavelength. . . . .	92
5.6	Variation of effective refractive index $n_{eff}$ as a function of (a) $W_{poly}$ for $r_w = 60$ nm, 50 nm BCB at 1540 nm wavelength (b) $r_w$ for $W_{poly} = 0.6 \mu\text{m}$ , 50 nm BCB at 1540 nm wavelength. . . . .	92
5.7	Variation of effective refractive index $n_{eff}$ as a function of (a) $r_w$ for $W_{poly} = 0.28 \mu\text{m}$ , 50 nm BCB at 1540 nm wavelength (b) $t_{BCB}$ for $W_{poly} = 0.28 \mu\text{m}$ , $r_w = 60$ nm at 1540 nm wavelength. . . . .	93
5.8	Schematic drawing of implemented polarization rotator (a) air clad top-view. Views of the garnet bonded waveguide stack at (b) symmetrical and (c) asymmetrical waveguide cross-section of the designed polarization rotator . . . . .	94
5.9	Contour plots of the electric fields ( $E_x, E_y$ ) for the hybrid modes at the asymmetrical waveguide cross-section of the polarization rotator. . . . .	95
5.10	SEM image of the fabricated polarization rotator with air cladding.	96
5.11	(a) Determination of cross-sections for the symmetrical and asymmetrical waveguides of the polarization rotator by varying the FF for 100 nm BCB, $r_w = 60$ nm at 1540 nm wavelength (b) Normalized power transfer efficiency between TE and TM modes of the polarization rotator as a function of $L_{PR}$ for 100 nm BCB thickness, $r_w = 60$ nm at 1540 nm wavelength. . . . .	96
5.12	Normalized efficiency as a function of (a) FF at $1.54 \mu\text{m}$ wavelength, $L_{PR} = 15 \mu\text{m}$ , $r_w = 60$ nm, 100 nm BCB thickness, $W = 280$ nm; (b) $r_w$ for 100 nm BCB thickness, FF = 0.8, $L_{PR} = 15 \mu\text{m}$ , $W = 280$ nm, at $1.54 \mu\text{m}$ wavelength. . . . .	97

5.13	Normalized efficiency vs. (a) BCB thickness at 1.54 $\mu\text{m}$ wavelength, $L_{PR} = 15 \mu\text{m}$ , $\text{FF} = 0.8$ , $W = 280 \text{ nm}$ (d) wavelength for $L_{PR} = 15 \mu\text{m}$ , BCB thickness = 50 nm, $W = 280 \text{ nm}$ , $\text{FF} = 0.8$ . . . . .	97
5.14	Simulated field views of a 97 % efficient polarization rotator for the various cases: (a) $E_x$ for the $\text{TM}_{00}$ as the input (b) $E_y$ for the $\text{TM}_{00}$ as the input (c) $E_y$ for the $\text{TE}_{00}$ as the input (d) $E_x$ for the $\text{TE}_{00}$ as the input. The input is on the L.H.S and the output is on the R.H.S for every figure. . . . .	98
5.15	Spectral behaviour of the designed MMI with a top cladding consisting of (50 + 160) nm thick BCB together with the garnet stack. .	99
5.16	(a) Schematic of spot-size converter between 380 nm thick Si and 220 nm thick Si (b) Intensity profile of the spot-size converter when viewed from the side (c) Intensity at different cross-sections of the spot-size converter. . . . .	100
5.17	SEM image of the fabricated polarization rotator with air cladding (a) symmetric waveguide section (b) asymmetric waveguide section.	101
5.18	Schematic diagram of the waveguide cross-sections at the (a) symmetrical and (b) asymmetrical portions of the polarization rotator with garnet stack bonded by BCB. Note that the BCB is not flat on top of the waveguide trench. A wedge shape is assumed in which $p_1, p_2, p_3, p_4, p_5, p_6, p_7$ and $p_8$ are any arbitrary points considered to approximate the BCB shape. $p_1, p_2$ and $p_3$ are identically situated for both the cross-sections whereas the co-ordinates of the points on the R.H.S are different for both the cases. . . . .	102
5.19	(a) Estimation of polarization rotation efficiency of the fabricated polarization rotator as a function of FF for $W_t = 180 \text{ nm}$ with planarized BCB plus garnet stack and (b) Comparison of spectral responses of the fabricated polarization rotator with planarized BCB to the wedge shaped BCB on top of the waveguide for $W_t = 180 \text{ nm}$ and $\text{FF} = 0.8$ . Both the simulations are performed at 1540 nm wavelength. . . . .	103
5.20	Normalized MZI transmission spectra for forward and backward propagation for (a) MZI-1 (b) MZI-2. . . . .	104
5.21	Normalized MZI transmission spectra for forward and backward propagation for (a) MZI-3 (b) MZI-4. . . . .	105
5.22	Normalized MZI transmission spectra for forward and backward propagation for (a) MZI-5 (b) MZI-6. . . . .	105
5.23	Normalized MZI transmission spectra for forward and backward propagation for (a) MZI-7 (b) MZI-8. . . . .	106
5.24	Normalized MZI transmission spectra for forward and backward propagation for (a) MZI-9 (b) MZI-11. . . . .	106

5.25	Normalized MZI transmission spectra for forward and backward propagation for (a) MZI-12 (b) MZI-14. . . . .	107
5.26	Normalized MZI transmission spectra for forward and backward propagation for (a) MZI-7 (b) MZI-8. . . . .	107
5.27	Normalized MZI transmission spectra for forward and backward propagation for (a) MZI-9 (b) MZI-10. . . . .	108
5.28	Normalized MZI transmission spectra for forward and backward propagation for (a) MZI-11 (b) MZI-12. . . . .	108
5.29	Normalized MZI transmission spectra for forward and backward propagation for (a) MZI-13 (b) MZI-14. . . . .	109
5.30	(a) Normalized MZI transmission spectra for forward and backward propagation of MZI-8 when the wave propagation vector ( $k$ ) and the external magnetic field ( $H$ ) are in parallel orientation (b) Simulation of the confinement factor ( $\Gamma$ ) of the TM mode into poly-Si overlay and Ce:YIG layer at 1540 nm wavelength. . . . .	109
5.31	Plots of $\Delta\lambda/FSR$ vs. $L_{NRPS}$ considering MZI-2, 8 and 14 for (a) sample-I and (b) sample-II, where $\Delta\lambda$ is the spectral shift between forward and backward light propagations as measured under the unidirectional transverse magnetic field. . . . .	110
6.1	Symbolic representation of a 3-port circulator operating in (a) CW (b) CCW directions. . . . .	114
6.2	Schematic diagram of a 3-port broadband circulator . . . . .	115
6.3	Schematic diagram of a 3-port narrow-band circulator. . . . .	118
6.4	Variation of $\Delta n_g$ as a function of the vacuum wavelength for waveguides of width 900 nm and height 220 nm with 100 nm BCB and 300 nm thick Ce:YIG layer. . . . .	119
6.5	Artistic impression of directional coupler (a) Cross-section view of coupling section, (b) Top-view of directional coupler. . . . .	119
6.6	Coupling efficiency as a function of coupling length ( $L_c$ ) for a 250 nm gap (g) between two identical rectangular shaped silicon waveguides of width 900 nm and thickness 220 nm with a trench filled with $SiO_2$ and 100 nm thick BCB as top cladding. . . . .	120
6.7	(a) Coupling efficiency as a function of wavelength ( $\lambda_0$ ) for different $L_c$ , (b) Phase difference between the bar and the cross port as a function of wavelength ( $\lambda_0$ ). The width and height of the identical waveguides are 900 nm and 220 nm respectively with 100 nm BCB. . . . .	120

6.8	(a) Coupling efficiency as a function of silicon waveguide thickness for $L_c = 15 \mu\text{m}$ , 100 nm thick BCB at 1577 nm wavelength (b) Phase difference between the bar and the cross port as a function of wavelength ( $\lambda_0$ ). The width and thickness of the identical waveguides are 900 nm and 220 nm respectively with 100 nm BCB. . . . .	121
6.9	(a) Schematic diagram of a $2 \times 2$ MMI (b) simulation of the length of the multimode section ( $L_{MMI}$ ) of the MMI for 100 nm BCB at 1550 nm wavelength. . . . .	122
6.10	(a) Power splitting efficiencies of the MMI at the bar and cross ports of a $2 \times 2$ MMI when the wavelength is varied (b) Phase difference between the bar and cross ports as a function of wavelength. The BCB thickness is 100 nm. . . . .	122
6.11	(a) Power splitting efficiencies to the bar and cross ports of a $2 \times 2$ MMI as a function (a) silicon waveguide thickness and (b) BCB thickness. . . . .	123
6.12	Sample-I: Measured optical transmission spectra at different ports of the circulator under a constant magnetic field (a) CCW (b) CW. . . . .	124
6.13	Sample-II: Measured optical transmission spectra at different ports of the circulator under a constant magnetic field (a) CCW (b) CW. . . . .	125
6.14	Sample-III: Measured optical transmission spectra at different ports of the circulator under a constant magnetic field (a) CCW (b) CW. . . . .	126
6.15	Sample-I: Measured optical transmission spectra at bar and cross ports of different reference directional couplers. . . . .	127
6.16	Sample-II: Measured optical transmission spectra at bar and cross ports of different reference directional couplers. . . . .	128
6.17	Sample-III: Measured optical transmission spectra at bar and cross ports of the reference directional coupler. . . . .	128
7.1	Micro-ring resonator configurations (a) all-pass (b) add-drop. . . . .	134
7.2	Schematic diagram of a nested ring MZI (NRMZI). . . . .	134
7.3	Analytically calculated transmission spectra for forward and backward light propagation for NRPS = 1 rad and $k = 0.2$ . . . . .	136
7.4	(a) Dependence of extinction ratio of the NRMZI on NRPS for $k = 0.2$ (b) transmission as a function of NRPS at 1532.57 nm wavelength for $k = 0.2$ . . . . .	137
7.5	Schematic diagram of a nested ring MZI with asymmetric directional couplers. Waveguide cross-section at coupling section (inset). . . . .	138
7.6	Effective index variation as a function of waveguide width for 260 nm thick Ce:YIG layer at 1550 nm wavelength. . . . .	138

7.7	Efficiency of the asymmetric directional coupler (a) as a function of coupling length ( $L_c$ ) at 1550 nm wavelength (b) when wavelength tuned for various $L_c$ . Width of the bus and ring waveguide are 900 nm and 336 nm respectively for $g = 230$ nm and 100 nm of BCB. . . . .	139
7.8	Efficiency of the asymmetric directional coupler as a function of (a) ring waveguide width for 900 nm wide bus waveguide and 100 nm BCB at 1560 nm wavelength (b) BCB thickness for 336 nm wide ring waveguide and 900 nm wide bus waveguide at 1560 nm wavelength. . . . .	139
7.9	(a) Schematic diagram of a nested ring MZI with symmetric directional couplers. Waveguide cross-sections at MZI section shown in inset (b) Artistic impression of the bonded stack. . . . .	141
7.10	Differential NRPS ( $\Delta NRPS$ ) as a function of $Si_3N_4$ thickness for various BCB thicknesses at 1550 nm wavelength. . . . .	142
7.11	Measured transmitted power spectra for the forward and backward directions through NRMZI containing asymmetrical directional couplers corresponding to (a) $L_c = 187 \mu m$ (b) $L_c = 157 \mu m$ . . . . .	142
7.12	SEM image of the asymmetric directional coupler (a) top-view (b) cross-sectional view. . . . .	143
8.1	RF magnetron sputtering system. . . . .	147
8.2	Process steps for selective garnet deposition by sputtering. . . . .	148
8.3	(a) X-ray diffraction (XRD) patterns of the as-deposited/not-annealed and annealed films (b) Hysteresis curves of the as-deposited and the annealed films detected by an alternating gradient force magnetometer (AGFM). . . . .	149
8.4	(a) Dark-field microscopic image (b) Atomic force microscopic (AFM) image of the annealed YIG on Si substrate. . . . .	150
8.5	(a) XRD patterns for Ce:YIG with and without seed layer (b) in-plane and out-of-plane Magnetization of the Ce:YIG film measured by VSM. . . . .	150
8.6	(a) MZI based isolator design (b) Garnet deposited on MZI arm. . . . .	151
8.7	Simulation of nonreciprocal phase shift (NRPS) when the Faraday rotation coefficient is 1500 deg/cm. . . . .	152
8.8	(a) Measured transmission spectra for the MZIs of varying lengths (b) plot of MZI transmission at constructive interference points vs. length of the garnet covered MZI arm lengths ( $L$ ). . . . .	153
8.9	Waveguide cross-sections (a) Ce:YIG on non-planarized SOI waveguide (b) Ce:YIG on top of planarized SOI waveguide. . . . .	153

## List of Tables

1.1	Typical performance specifications of a commercially available free-space optical isolator. . . . .	5
1.2	SOI based magneto-optical isolators. . . . .	9
3.1	Total phases at the final ports. . . . .	47
5.1	MZI details . . . . .	104
6.1	Total phases at final ports without loop path . . . . .	116
6.2	Total phases at final ports with loop path . . . . .	117
6.3	Sample-I: Measured transmissions(T) at 1568 nm . . . . .	124
6.4	Sample-II: Measured transmissions(T) at 1573 nm . . . . .	126
6.5	Sample-III: Measured transmissions(T) at 1580 nm . . . . .	127



# List of Acronyms

## A

ADP	Advanced Passive
AGFM	Alternating Gradient Force Magnetometer

## B

BCB	Benzocyclobutene
BIG	Bismuth Iron Garnet
BOX	Buried Oxide

## C

CAMFR	CAvity Modelling FRamework
CCW	Counter Clockwise
Ce:YIG	Cerium substituted Yttrium Iron Garnet
CMOS	Complementary Metal Oxide Semiconductor
CMP	Chemical Mechanical Polishing
CW	Clockwise
CVD	Chemical Vapor Deposition

## D

DNRPS Differential Nonreciprocal Phase Shift  
DUV Deep Ultra Violet

## **E**

EM Electromagnetic  
ER Extinction Ratio

## **F**

FSR Free Spectral Range  
FOM Figure Of Merit  
FEM Finite Element Method  
FDM Finite Difference Method  
FIB Focused Ion Beam

## **I**

IPA Isopropylalcohol  
IL Insertion Loss

## **L**

LD Laser Diode  
LCP Left Circularly Polarized

## **M**

MZI Mach Zehnder Interferometer  
MO Magneto-optic

MOKE	Magneto-Optical Kerr Effect
MMI	Multimode Interference
MPW	Multi Project Wafer
MRR	Micro Ring Resonator

## **N**

NRPS	Nonreciprocal Phase Shift
NRMZI	Nested Ring Mach Zehnder Interferometer
NRL	Nonreciprocal Loss

## **O**

OCT	Optical Coherence Tomography
-----	------------------------------

## **P**

PDL	Polarization Dependent Loss
PR	Polarization Rotator
PMD	Polarization Mode Dispersion
PLC	Photonic Lightwave Circuits
PCF	Photonic Crystal Fibre
PVD	Physical Vapor Deposition

## **R**

RCP	Right Circularly Polarized
RPS	Reciprocal Phase Shifter
RTA	Rapid Thermal Annealing

## **S**

SEM	Scanning Electron Microscope
SGGG	Substituted Gadolinium Gallium Garnet
SMF	Single Mode Fiber
SOI	Silicon-On-Insulator
SOA	Semiconductor Optical Amplifier
STP	Standard Temperature and Pressure

**T**

TE	Transverse Electric
TM	Transverse Magnetic
TGG	Terbium Gallium Garnet

**U**

UV	Ultra Violet
----	--------------

**V**

VHF	Very High Frequency
VSM	Vibrating Sample Magnetometer

**W**

WDM	Wavelength Division Multiplexing
-----	----------------------------------

**X**

XRD	X-Ray Diffraction
-----	-------------------

**Y**

YIG                      Yttrium Iron Garnet



# Nederlandse Samenvatting

Tegenwoordig kan ons leven moeilijk worden ingebeeld zonder een telefoon of het Internet. Telecommunicatie is een belangrijk aspect geworden van ons dagelijks leven. Om dit waar te maken is enorm veel onderzoek en ontwikkeling gebeurd om communicatiesystemen te verbeteren, waardoor veel nieuwe toestellen en applicaties ontstaan zijn. Om aan onze dagelijkse behoeften tegemoet te komen, verwachten we dat een toestel zowel compact is als veel functionaliteit bevat. Naast compactheid, is ook snelheid een belangrijk aspect. De huidige elektronische chips botsen op fundamentele limieten van informatieoverdracht, en daarom wordt fotonica steeds belangrijker. Om de miniaturisatie van fotonische toestellen verder te zetten zonder in te boeten aan prestatie, hebben we on-chip kost-effectieve platformen nodig. Een van deze platformen is het siliciumfotonica platform (Silicon photonics). Silicium is een uitstekend optisch materiaal en kan licht binnen een golfgeleider concentreren op een zeer kleine oppervlakte dankzij het hoge indexcontrast.

Een optisch communicatiesysteem bevat drie hoofdonderdelen: een lichtbron, een signaalverwerkingseenheid en een lichtdetector. Op het siliciumfotonica platform speelt de halfgeleider laser diode de rol van een lichtbron. Dit licht komt binnen in een optisch circuit, dat verschillende overzettingen naar verschillende golfgeleiders en/of connectoren bevat. Deze omzettingen kunnen ongewenste reflecties veroorzaken, die een negatieve invloed hebben op de prestatie van een laserdiode. Dit komt omdat het gereflecteerde licht terug in de laser caviteit komt. Om dit te voorkomen hebben we een optische isolator nodig. Een optische isolator is een toestel dat toelaat om de propagatie van het licht in een bepaalde richting door te laten, terwijl het licht in de tegengestelde richting geblokkeerd wordt.

Een commercieel beschikbare isolator bestaat uit verschillende bulk optische componenten, waaronder twee polariseerders, een stuk magneto-optisch materiaal (een Faraday rotator), waarvan het werkingspunt is verplaatst met behulp van externe magnetische velden, en enkele gecollimeerde lenzen. Een groot probleem met deze opstelling is dat deze zeer groot is, en incompatibel is met geïntegreerde, golfgeleidergebaseerde platformen, zoals het siliciumfotonica platform. Deze platformen zijn gebaseerd op halfgeleiders, die over

het algemeen niet magneto-optisch actieve materialen zijn. Daarom zijn extra magneto-optische materialen nodig die geïntegreerd worden op het platform. Historisch gezien zijn meerdere pogingen ondernomen om hetzelfde principe van optische isolatie te miniaturiseren naar een geïntegreerd platform, maar al snel werden de beperkingen van dit principe duidelijk, en werden verschillende onderzoeksroutes bekeken, gebaseerd op andere fysische principes. Golfgeleider-gebaseerde magneto-optische isolatoren werken ofwel met behulp van het niet-reciproke verlies, ofwel met een niet-reciproke fase verandering (nonreciprocal phase shift, NRPS). NRPS gebaseerde golfgeleiderisolatoren zijn het onderwerp van deze thesis.

Een conventionele optische isolator is gebaseerd op het principe van niet-reciprociteit, geïntroduceerd door een ferromagnetisch / ferrimagnetisch granaat, onder invloed van een extern magnetisch veld. Ferrimagnetische granaten zijn unieke materialen met sterk magneto-optische eigenschappen (gekarakteriseerd door de Faraday rotatie coëfficiënt), en lage verliezen voor golflengtes die belangrijk zijn voor telecommunicatie. Ondanks deze goede optische eigenschappen, is de grootste uitdaging om deze materialen op een goede manier te integreren op het halfgeleider platform. Verschillende onderzoeksgroepen hebben reeds meerdere pogingen ondernomen, met verschillende strategieën. Deze strategieën kunnen onderverdeeld worden in twee klassen: binden van het materiaal op het substraat, of depositie op het substraat. Beide methodes hebben hun voor- en nadelen. Een depositie wordt uitgevoerd op het niveau van de volledige wafer, maar heeft als gevolg dat de kwaliteit van het gedeponeerde materiaal niet even zuiver is als die van de zuiver kristallijne vorm. Bij het binden kan men vertrekken van een uitstekend epitaxiaal gegroeide magneto-optische chip (*die*), maar dit is intrinsiek een proces waarbij de chip op de wafer (*die to wafer*), of de chip op een andere chip (*die to die*) gebonden wordt. Hierdoor is het moeilijker om de chips in massa te produceren. Het binden kan op twee manieren gebeuren: ofwel met behulp van oppervlakte-geactiveerde directe moleculaire binding, ofwel met adhesieve binding. In deze thesis is de nadruk op adhesieve binding met behulp van benzocyclobuteen (BCB), omdat deze meerdere voordelen heeft ten opzichte van directe moleculaire binding.

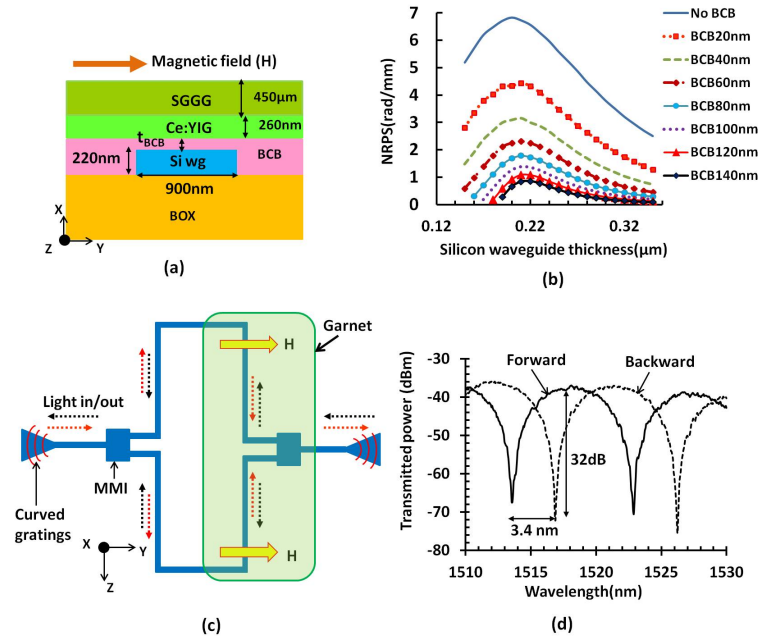
BCB, met een brekingsindex van 1.535 bij een golflengte van 1550 nm, is een bekend en veelgebruikt polymeer, en wordt in dit werk gebruikt als tussenmateriaal om te binden (*bonding agent*), om het granaatmateriaal op een Silicium op Isolator (*Silicon-on-insulator*, SOI) substraat te binden. De granaat chip bevat een dunne laag Cerium gedopeerd Yttrium Ijzer Granaat (Ce:YIG) bovenop een (Ca, Mg, Zr) gedopeerd Gadolinium Gallium granaat (SGGG) substraat. De Faraday rotatie coëfficiënt ( $\Phi_F$ ) van het epitaxiaal gegroeide Ce:YIG is ongeveer 4500 deg/cm bij een golflengte van 1550 nm. Indien licht wordt geleid door een golfgeleider met een top laag van Ce:YIG, interageren de elektrische velden

van de geleide modi met het elkaar, waarbij een extra niet-reciproke (dus tegengesteld in voorwaarts/achterwaartse richting) fase gegenereerd wordt. Het teken van de niet-reciproke fase hangt af van de relatieve orientatie tussen de golfpropagatievector ( $\mathbf{k}$ ) en het externe magnetische veld ( $\mathbf{H}$ ). Om een NRPS te bekomen met het granaat als toplaag, moeten  $\mathbf{k}$  en  $\mathbf{H}$  loodrecht op elkaar staan. Dit staat bekend als de Voigt configuratie.

Een elektromagnetische golf in een eendimensionale golfgeleider (een opeenstapeling van verschillende lagen waarbij de kernlaag de hoogste brekingsindex heeft) kan ofwel transversaal elektrisch (TE), ofwel transversaal magnetisch (TM) gepolariseerd zijn. De TE en TM modi worden aangeduid met de elektrische veldcomponenten ( $H_x, E_y, H_z$ ), respectievelijk ( $E_x, H_y, E_z$ ). Hierbij is het belangrijk te vermelden dat de modi in een rechthoekige golfgeleider niet zuiver TE of TM gepolariseerd zijn. In dit geval spreekt men van quasi-TE en quasi-TM. Voor de eenvoud spreken we in het vervolg eenvoudigweg van de TE en TM polarizatie van een mode. De typische lagenstructuur van een met Ce:YIG gebonde golfgeleider wordt weergegeven in Figuur 1(a). Het  $E_x$  veld van de TM mode heeft een discontinuïteit aan de overgang tussen twee lagen in de x-richting, terwijl het  $E_y$  veld van de TE mode een discontinuïteit heeft langsheen de y-richting. Indien een elektrisch magnetisch veld wordt aangelegd langsheen de y-richting, dan zorgt interactie tussen het  $E_x$  en  $E_z$  voor het opwekken van de NRPS. In dit geval wordt de NRPS bepaald door gebruik te maken van volgende perturbatieformule:

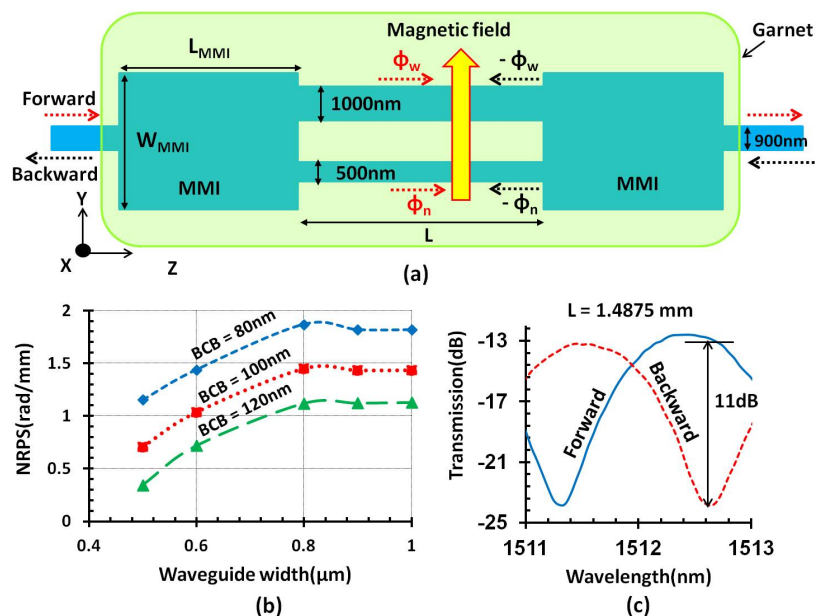
$$NRPS \propto \frac{g_{xz} \iint_{\text{Ce:YIG}} E_x \cdot E_z dx dy}{\iint [E_x \cdot H_y - H_x \cdot E_y] dx dy} \quad (1)$$

In deze formule is  $g_{xz}$  de gyrotropische constante van het magneto-optische materiaal. De waarde van de NRPS hangt af van de dikte van de BCB laag ( $t_{BCB}$ ), zoals getoond in Figuur 1(b). Om de NRPS te modelleren vertrekken we van een benaderend eendimensionaal golfgeleidermodel. Het is belangrijk te vermelden dat dit de eerste poging is om een optische isolator op SOI te maken met behulp van de bondingtechniek. Om dit succesvol te demonstreren, moet bewezen worden dat de met granaat gebonden SOI golfgeleider een voldoende grote NRPS heeft. Om een kleine NRPS te meten kan een interferometrisch toestel gebouwd worden met een kleine vrije spectraalbereik (*free spectral range*, FSR). In deze thesis wordt een ongebalanceerde Mach-Zehnder interferometer (MZI) gebruikt. Het schema van deze MZI, die dan uiteindelijk zal dienen als de optische isolator, wordt weergegeven in Figuur 1(c). De NRPS in de ene arm van de MZI is hierbij tegengesteld aan de NRPS in de andere arm van de MZI. Hierdoor werkt het toestel in een *push-pull* configuratie, terwijl het magnetisch veld ( $\mathbf{H}$ ) unidirectioneel is, transversaal op de propagatie van het licht. Voor het hele

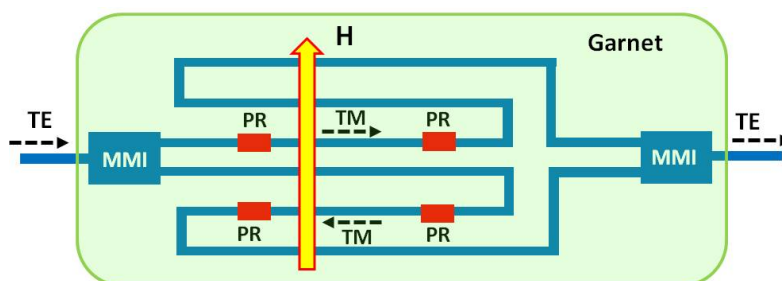


**Figuur 1:** (a) Schematische doorsnede van een met granaat gebonde golfgeleider (b) NRPS in functie van de siliciumgolfgeleider dikte (c) Schematische weergave van een push-pull MZI-type isolator (d) Gemeten spectrum voor voor- en achterwaartse propagatie.

circuit werd gewerkt met een golfgeleider met een breedte van 900 nm. Hierbij werd een isolatie van 32 decibel (dB) bereikt. Het granaat bedekt hierbij ongeveer 0.96 mm in lengte van de onderliggende golfgeleider. Uit de experimenteel gemeten NRPS kunnen we de BCB dikte terugrekenen uit Figuur 1(b). Deze is ongeveer 50 nm. In een tweede experiment hebben we een MZI gebouwd waarvan de lengte in beide armen even groot is, maar de breedte van de golfgeleiders zijn verschillend. Dit kan leiden tot een veel compacter toestel. Door het verschil in breedte van de armen van de MZI, wordt een differentiële NRPS opgewekt wanneer het unidirectionele magnetische veld transversaal op de lichtpropagatie wordt aangelegd. Het schema en de breedte-afhankelijkheid van de NRPS wordt in Figuur 2(a) en Figuur 2(b) weergegeven, respectievelijk. De MZI golfgeleiders zijn 1000 nm lang, 500 nm breed en 220 nm hoog. De verhouding van het gesplitste vermogen in de asymmetrische multimode interferentie (MMI) bepaalt de uitdovingscoëfficiënt van de MZI. Op deze manier hebben we, voor een lengte van 1.49 mm, een isolatie gemeten van 11 dB. We hebben dus gedemonstreerd dat we een optische isolator kunnen bouwen die werkt met

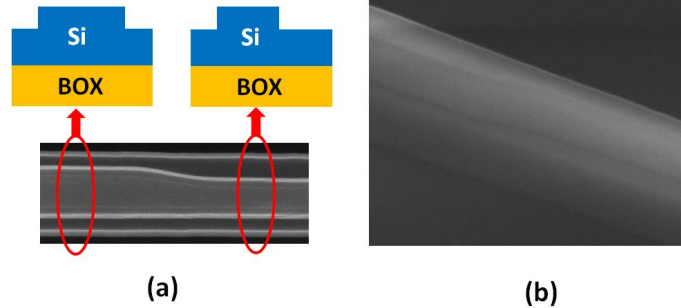


**Figuur 2:** (a) Schematische weergave van een met granaat gebonde MZI met verschillende armbreedtes (b) NRPS in functie van de siliciumgolfsleider breedte voor een siliciumdikte van 220 nm (c) Gemeten MZI transmissie.



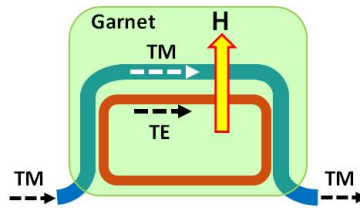
**Figuur 3:** Schematische weergave van een TE isolator.

TM gepolariseerd licht. Echter, de meeste halfgeleider laserdiodes sturen TE gepolariseerd licht uit, dus is het belangrijk om een optische isolator te kunnen bouwen die werkt met TE gepolariseerd licht. Met de huidige bindingsstrategie is het onmogelijk om een isolator te maken die werkt voor de TE modi van een golfsleider. Om dit probleem op te lossen hebben we een MZI gebouwd, waarbij in beide armen een polarisatiedraaiend element (*polarization rotator*, PR) is geplaatst om de TE polarisatie om te zetten in een TM polarisatie in het begin,



**Figuur 4:** SEM afbeeldingen van de symmetrische en asymmetrische golfgeleidersecties voor de gefabriceerde polarizatirotator (a) zicht van bovenaf (b) zicht vanuit een hoek.

en omgekeerd aan het eind van de armen. Dit is weergegeven in Figuur 3. De PR werken in dit geval op basis van de verticale symmetriebreking van het  $E_x$  veld. De PR hebben een golfgeleiderbreedte van 380 nm, waarbij de assymetrie wordt verwezelijkt door een deel van het Silicium weg te etsen, zoals weergegeven in Figuur 4. Wanneer een TE gepolariseerde mode in de PR terecht komt, roteert de PR de mode tot het een TM gepolariseerde mode is. De TM gepolariseerde mode heeft vervolgens een NRPS, waarna de mode terug wordt geroteerd tot een TE gepolariseerde mode. Het plaatsen van de niet-reciproce faseverschuivers is zo gedaan dat het toestel in een *push-pull* configuratie werkt (bij aanwezigheid van een unidirectioneel H-veld), waarbij het granaat beide armen bedekt. De grootte van het toestel (*footprint*) is een van de belangrijkste aspecten



**Figuur 5:** Schema van een met granaat gebonde NRMZI.

voor een fotonisch geïntegreerd circuit (*Photonic Integrated Circuit, PIC*). Het is daarom interessant om te kijken naar microringresonatoren (MRR) om een isolator te bouwen. Het grote probleem bij MRR is echter de bandbreedte, die heel klein is. In het geval dat het toestel slechts moet werken op enkele geïsoleerde posities (vb bij meerdere-golflengtelasers), kunnen MRR-gebaseerde isolatoren interessant zijn. Hierbij zijn meerdere configuraties mogelijk. In dit werk heb-

ben we een geneste ring-MZI gebouwd (nested ring-MZI, NRMZI), zoals weergegeven in Figuur 5. De koppelsecties zijn zo ontwikkeld dat de fundamentele TE mode van de smalle ringgolfsgeleider in fase overeenkomt (*phase matched*) met de fundamentele TM mode van de bredere bus golfsgeleider, met een top-laag van granaat. De isolator werkt op basis van de NRPS die de TM mode voelt in de MZI arm van de bus golfsgeleider, wanneer een extern transversaal magnetisch veld wordt aangelegd. De NRPS van de MZI arm verandert hierbij de resonantievoorwaarde van de NRMZI. Een ideaal toestel voor optische isolatie zou dan werken doordat het licht dat voorwaarts propageert in de ring kritisch gekoppeld is, terwijl het toestel is ondergekoppeld voor het achterwaarts propagerende licht.

In een PIC zijn drie-of multipoort niet-reciproke toestellen nodig voor vele applicaties. Hierbij is een belangrijke klasse de optische circulator. Een deel van de thesis gaat dan ook over het bouwen van een 3-poort circulator, met behulp van een MZI-type toestel, gelijkaardig als diegene die we net besproken hebben. Het toestel dat we tonen is ontwikkeld voor een smalbandige operatie met 22 dB isolatie. De prestatie kan hierbij nog worden geoptimaliseerd om betere isolatie te bekomen en om te werken over een breder golflengtebereik.

Samengevat hebben we verschillende type optische isolatoren gedemonstreerd op het SOI platform, met behulp van adhesieve BCB bonding met een granaat bovenop een SOI golfsgeleider. Met dezelfde techniek hebben we ook een optische circulator gedemonstreerd. De nadruk lag op deze thesis op het demonstreren van de mogelijkheid tot optische isolatie on-chip, maar er is nog veel ruimte voor prestatieverbeteringen. De belangrijkste bijdrage van dit werk is dat het de weg effent om laser diodes en niet-reciproke toestellen te integreren op het siliciumfotonica platform.



## English summary

**I**N the modern era communication is indispensable. Life can hardly be imagined without telephone or Internet. Tremendous developments have been pursued to improve communication systems. Based on these progresses numerous new devices and applications have been realized as alternatives to existing technologies. To feed our requirements in daily life it is expected that one device should provide a lot of functionalities within a compact size. Besides compactness speed is also an important aspect of such devices. Therefore photonics came into the picture and now plays a crucial role in communication technology to make devices faster, more compact and less expensive. To meet the goal of miniaturization without compromising performance on-chip cost effective platforms are required.

One such platform is the Silicon photonics platform. Silicon is an excellent optical material and provides tight confinement of an optical guided mode inside the core of a high index contrast waveguide. An optical communication system consists of three major parts like a source of light, a signal processing unit and a photodetector. Semiconductor laser diodes serve the role of light source. An optical circuit may contain several joints or connectors. Various types of spurious reflections can occur from such junctions. The performance of a laser diode is very much disturbed by back-reflected light into the laser cavity. An optical isolator is a device which allows propagation of light in a particular direction while it suppresses propagation in the opposite direction. Therefore an isolator is generally used to block back-reflection into the laser cavity. A commercially available isolator is built by assembling several bulk optical components like two polarizers, a piece of magneto-optic material known as Faraday rotator biased with the aid of an external magnetic field and some collimating lenses. However the free-space configuration of an isolator is totally incompatible with the integrated waveguide based platforms due to various unavoidable issues. Generally semiconductors are not magneto-optically active materials. Therefore an integration of magneto-optic materials with semiconductor waveguides is required. Historically different attempts were made to convert the bulk form of an isolator to integrated waveguide platforms. But soon the

limitations of these efforts were clear and hence research on integrated isolators took several new routes based on different physical principles. Waveguide based magneto-optical isolators rely on either nonreciprocal loss difference or nonreciprocal phase shift (NRPS). NRPS based waveguide isolators form the subject of this thesis.

A conventional optical isolator is based on the principle of nonreciprocity induced by a ferromagnetic / ferrimagnetic garnet under the influence of an external magnetic field. Ferrimagnetic garnets are unique materials with strong magneto-optical properties (or Faraday rotation coefficient) and low optical absorption at telecom wavelengths. In spite of possessing very good material properties for magneto-optical applications the main hurdle is the difficulty of incorporating garnet materials on a semiconductor platform. Numerous trials have already been carried out by several research groups around the globe adopting different strategies. These are classified into two broad categories: bonding and deposition. Both approaches have merits and weaknesses. A deposition is a wafer scale process but it suffers from degraded material properties as compared to its single crystalline form. On the other hand bonding envisages an opportunity to incorporate excellent epitaxially grown magneto-optic material on the waveguide but it is intrinsically a die-to-wafer or die-to-die scale technique which limits its mass production possibility. Bonding can be performed in two ways: by means of surface activated direct molecular bonding or by means of adhesive bonding. This work mainly emphasizes on the adhesive BCB bonding approach because of several advantages over direct molecular bonding.

Benzocyclobutene or BCB (refractive index:1.535 at 1550 nm) is a well-known polymer which is used in this work as a bonding agent to incorporate a garnet die on a Silicon-on-insulator (SOI) based waveguide circuit. The garnet die contains a thin layer of Cerium substituted Yttrium Iron Garnet (Ce:YIG) on (Ca, Mg, Zr) substituted Gadolinium Gallium Garnet (SGGG) substrate. The Faraday rotation coefficient ( $\theta_F$ ) of epitaxially grown Ce:YIG is about  $4500^\circ/\text{cm}$  at 1550 nm wavelength. When light passes through a waveguide with a magnetized Ce:YIG layer as top cladding the electric field components of the guided mode interact with each other and as a result an extra phase shift is generated. This is known as the nonreciprocal phase. The sign of the nonreciprocal phase explicitly depends on the relative orientation between the wave propagation vector ( $\mathbf{k}$ ) and the external magnetic field ( $\mathbf{H}$ ). To achieve NRPS from a garnet clad waveguide  $\mathbf{k}$  and  $\mathbf{H}$  should be in perpendicular orientation. This is known as the Voigt configuration.

An electromagnetic guided wave in a rectangular waveguide can be either transverse electric (TE) or transverse magnetic (TM) polarized. TE and TM modes are designated by  $(H_x, E_y, H_z)$  and  $(E_x, H_y, E_z)$  field components respectively. It is noteworthy to mention that optical modes in rectangular

waveguides are not purely TE or TM. Rather they are quasi-TE or quasi-TM in a rectangular waveguide. For the sake of simplicity the term quasi is dropped for the rest of the discussions. A typical garnet bonded waveguide stack is depicted in Fig.1(a). The  $E_x$  field for the TM mode has discontinuities at the interfaces between two different layers along the x-axis whereas the  $E_y$  field of the TE mode has the same scenario along the y-axis. Interaction between  $E_x$  and  $E_z$  is responsible for the NRPS when an external magnetic field is applied along y-axis. In this case (magnetic field along y-axis) the NRPS is calculated by using the perturbation formula

$$NRPS \propto \frac{g_{xz} \iint_{Ce:YIG} E_x \cdot E_z dx dy}{\iint [E_x \cdot H_y - H_x \cdot E_y] dx dy} \quad (2)$$

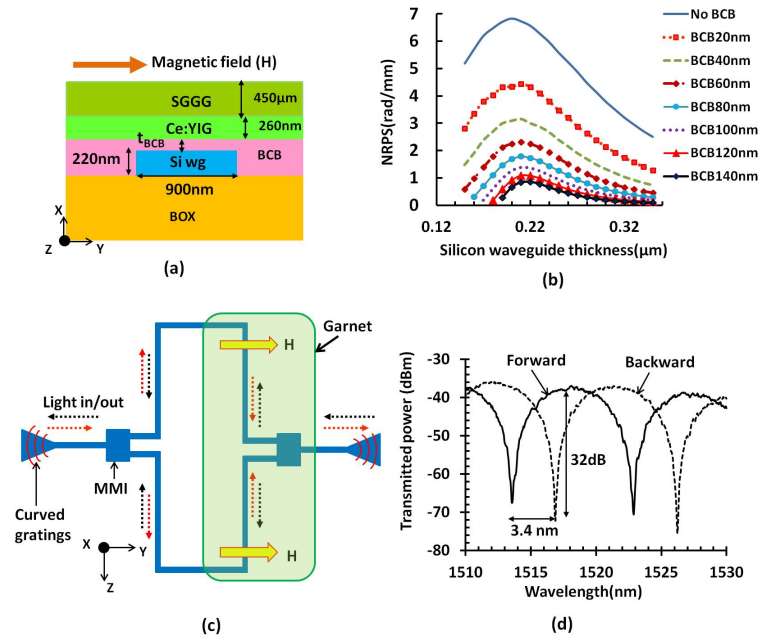


**Figure 1:** (a) Schematic diagram of a garnet bonded waveguide cross-section (b) NRPS vs. silicon waveguide thickness (c) Schematic drawing of a push-pull MZI type isolator (d) Measured spectra for forward and backward propagations.

$g_{xz}$  is known as the gyrotropic constant of the magneto-optic material. The value of the NRPS depends on the thickness of the BCB layer ( $t_{BCB}$ ) as shown in Fig.1(b). To simulate the NRPS a slab waveguide model is considered. It is

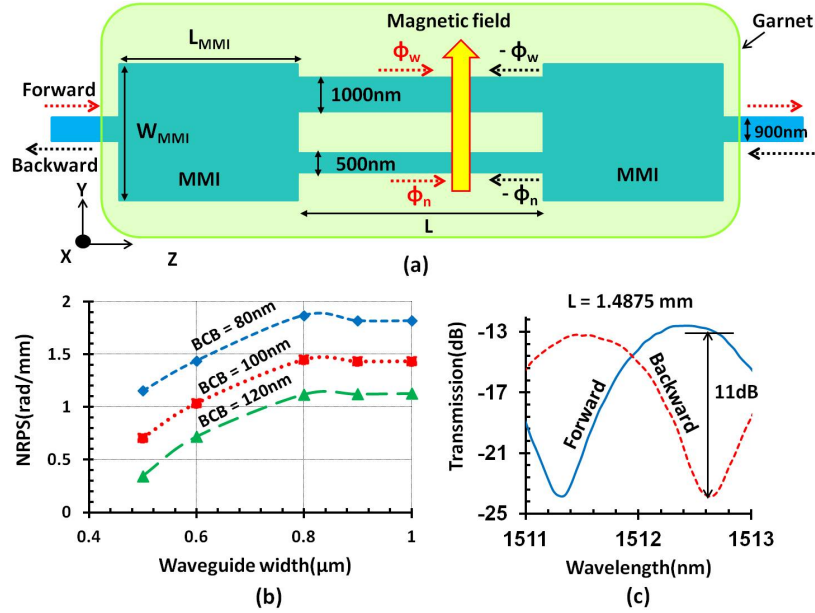


**Figure 2:** (a) Schematic diagram of the garnet bonded MZI with dissimilar arm widths (b) NRPS vs. silicon waveguide width for 220 nm Si thickness (c) Measured MZI transmission.

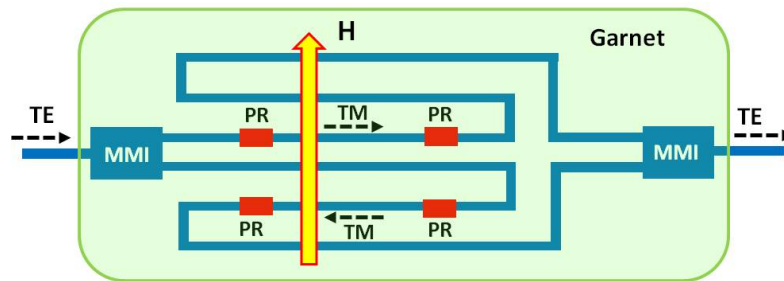


**Figure 3:** Schematic diagram of TE isolator.

important to mention that this is the first attempt to realize an optical isolator on SOI using BCB bonding technique. That means we need a confirmation of achievable NRPS from a garnet bonded SOI waveguide. To observe a small NRPS an interferometric design with small free spectral range (FSR) can be used. In this work an unbalanced Mach-Zehnder interferometer (MZI) is adopted. The schematic diagram of the isolator design using a MZI structure is shown in Fig.1(c). The NRPS experienced by light in one arm is opposite to that

of the other arm. Hence the device works in push-pull manner with a unidirectional constant magnetic field ( $H$ ) transverse to the light propagation. The width of the waveguide is designed to be 900 nm for the whole circuit. An isolation of 32 dB is achieved for a MZI of garnet covered length of approximately 0.96 mm as shown in Fig.1(d). After mapping the experimentally obtained NRPS from this device to Fig.1(b) reveals that the BCB thickness is around 50 nm. One next

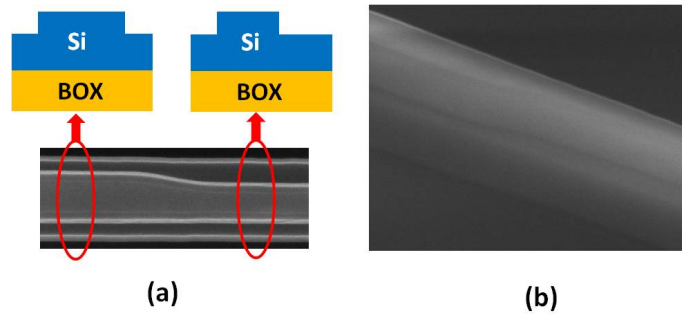


**Figure 4:** SEM images of symmetric and asymmetric waveguide sections of the fabricated polarization rotator (a) top-view (b) view from and angle.

attempt has been made to build a MZI in which the length of both arms is the same but their width is different. This leads to a much smaller foot-print for the isolator. The arms of the MZI are designed with dissimilar widths and as a result a differential NRPS is obtained when an unidirectional magnetic field is applied transverse to the light propagation direction. The scheme and the width dependence of the NRPS are depicted in Fig.2(a) and Fig.2(b) respectively. The MZI waveguides are 1000 nm and 500 nm wide with 220 nm thickness. The power splitting ratio of the asymmetrical multimode interference (MMI) determines the extinction ratio of the MZI. An isolation of 11 dB is measured for a MZI with an arm length about 1.49 mm as presented in Fig.2(c).

So we have demonstrated optical isolators based on interferometric designs working for TM polarized light. But most semiconductor laser diodes emit TE polarized light, so an isolator working for TE polarization is also highly desirable. By using the current bonding strategy an isolator working for TE mode is not feasible. To circumvent this problem a MZI type design has been realized in which polarization rotators (PR) are implemented on the MZI arms to rotate TE polarization to TM and vice-versa as shown in Fig.3. Polarization rotators (PR) in this case work on the basis of vertical symmetry breaking of the  $E_x$  field. Polarization rotators are designed in a 380 nm thick Silicon waveguide in which the asymmetry is created by etching part of the silicon waveguide as shown in Fig.5.8. When a TE polarized light is injected at a PR it rotates the po-

larization into TM and then the TM mode experiences a NRPS while traveling through the same waveguide. Afterwards this phase shifted TM mode passes through another PR where it is rotated back into the TE mode. Placement of the nonreciprocal phase shifters on the MZI arms is made in such a way that the device works in a push-pull manner under a unidirectional magnetic field with the garnet die covering both arms.

The device footprint is one of the important aspects in photonic integrated circuits (PIC). So a microring resonator (MRR) based isolator design is an obvious choice in this context. But the main problem with a MRR is its bandwidth. The bandwidth of a MRR is extremely narrow. For the case of multi-wavelength lasers where isolation is required only for some particular wavelengths, MRR based isolators could be interesting. There can be various possible configurations based on MRRs. In our work we have adopted a nested ring-MZI (NRMZI) as shown in Fig.5. The coupling sections are designed in such a way that the fundamental TE mode in the narrow ring waveguide is phase matched with the fundamental TM mode of a wider bus waveguide with garnet as top cladding. The device works on the basis of the NRPS experienced by the TM mode in the

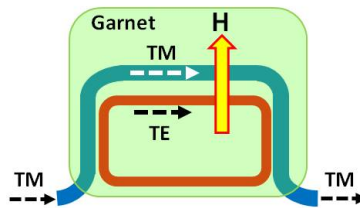


**Figure 5:** Schematic of a NRMZI with bonded garnet.

MZI arm (bus waveguide) when a unidirectional transverse magnetic field is applied externally. The NRPS from the MZI arm could change the resonance condition of the NRMZI. An ideal device for isolation can be designed in such a way that for forward light propagation the NRMZI is in critically coupled condition whereas it is under-coupled for the backward propagation in the presence of a unidirectional magnetic field.

In PICs three or multi-ports nonreciprocal devices are required for various applications. This type of devices is generally called circulators, which are nothing but an extension of the two port optical isolator. Optical circulators are one of the important and demanding devices on an integrated platform with a myriad of potential applications in different branches of optics and photonics. As a part of this thesis a 3-port circulator is demonstrated by using a MZI type device similar to the push-pull isolator. The device presented here is designed for narrowband operation which shows a maximum of 22 dB isolation. The per-

formance of the device can be tuned to achieve better isolation and broadband operation.

To summarize, different types of optical isolators have been demonstrated on the SOI platform by means of adhesive BCB bonding of garnet on SOI waveguide circuits. An optical circulator has also been demonstrated by utilizing the same bonding approach. Although the devices presented in this thesis are designed as a the proof-of-principle, there is still a large scope for improvement. Most importantly this work paves the way for the co-integration of laser diodes and nonreciprocal devices such as optical isolators or circulators on a silicon photonics platform.



# 1

## Introduction

**T**HE objective of this research is to demonstrate nonreciprocal optical devices like isolators and circulators on a planar waveguide-based platform. The key idea behind this work is to exploit the nonreciprocal behavior of a magnetized magnetic material. To start with, the necessity of an optical isolator in an optical communication system is discussed. As magnetic material is used in this work to bring nonreciprocity via magneto-optical interaction, a brief introduction to magnetic materials will be given. A thorough survey of literature review is presented to determine our position in this field. Finally the chapter concludes by discussing the rationale and outline of the thesis.

### **1.1 Objective of this work**

An optical isolator is a device which allows light to propagate in one particular direction whereas it suppresses propagation opposite to that direction. It plays a crucial role in fiber-optic communication systems. The most important application of an optical isolator is related to the protection of a laser system from any kind of unwanted reflection. Any stray reflection could jeopardize the operation of a laser in various ways. In the past decade this has become an important subject with the advent of coherent communication systems and high line-rate communication links. The sources of reflections in an optical system are numerous, including reflections at connectors, fiber end facets and inter-

faces between bulk optical components. Furthermore Rayleigh backscattering from fiber may also contribute to substantial back reflection.

Physically there are numerous effects that can occur when light is fed back into a semiconductor laser cavity. In 1980 Lang and Kobayashi showed the effect of optical feedback into the laser cavity both theoretically and experimentally [1]. Line-width broadening is one of the common phenomena related to optical feedback into the cavity [2, 3]. This broadening of the line-width is called a coherence collapse state and it is one form of chaos in a laser cavity. The behavior of the laser diode depends on the feedback levels. Five regimes are possible in the long cavity limit as demonstrated in this article [4]. Back reflection also causes nonlinearities in the laser response, which manifests as kinks in the signal and should be avoided for most analog and for some digital applications [5].

Due to the boom of the internet technology throughout the world the market pressure on the selling price of optical telecommunication accessories is very high and results in the reduction of the average unit price of telecommunication lasers and transceivers [6].

The cost reduction of a semiconductor laser diode (LD) module depends on several factors. One of the major factors is the packaging cost rather than individual costs of the element in a laser module. As an example the cost of a laser diode is about 5\$ while the total price of a high speed transceiver is around several thousands of dollars. This jump in cost can be explained as follows. The use of semiconductor laser diodes allows mass production through wafer-scale processing. A high speed laser module consists of at-least four discrete elements such as a laser diode, a monitoring photodiode, an optical isolator and an output optical fiber. All these components require perfect optical alignment with respect to each other, which make the packaging very complicated. On top of that an external modulator and wavelength tuning etalon are sometimes required to circumvent issues related to dispersion and wavelength tunability. An extra component means an additional large aperture lens and a time consuming active alignment approach. An isolator itself requires two polarizers. In summary we can say that assembling all these delicate, sensitive components is challenging for the manufacturer and increases the total cost. We can identify several distinct paths towards minimizing the manufacturing cost of a LD module.

- **Tailoring laser module:** This can be achieved by modifying the laser diode in such manner that it can be operated without temperature controller [7], without isolator [8], or modulated directly [9]. The scope for cost reduction is clear in this case because the number of components are reduced and the alignment becomes more straight forward. However it should be noted that there are limitations regarding the extent of simplifications that can be made

imposed by specific applications of laser modules.

- **Co-integration of subcomponents:** Combining the subcomponents all together either in a hybrid or a monolithic manner allows cost reduction. If passive and active components are attached rigidly to each other or if two dissimilar materials are combined together on the same platform to get the same functionality as produced by the individual elements then it is called hybrid integration. On the other hand if the different subcomponents (active and passives) are grown on the same host substrate this is called monolithic integration. One of the obvious advantages of integration is that it paves the way for smaller foot-print. Additionally integration eliminates thermal and mechanical instability. Here it is appropriate to mention that the advancement of photonic lightwave circuits (PLC) incorporating several active and passive components onto a single chip is of paramount importance. To reach that goal waveguide based modulators, isolators / circulators are very much needed.

In both routes cost reduction is readily observable although both approaches have their advantages and disadvantages. The most ubiquitous problem lies in the integration technique. Not all the materials used are integration friendly. Keeping the performance as a priority, the integration approach should be taken rather than tailoring laser module. In this case waveguide-based isolators are indispensable for the laser. The isolator is one of the most wanted nonreciprocal device which is not available in integrated form [10]. The search for an integrated optical isolator started when the field of integrated optics started itself [11]. In few sections we will discuss chronological development of isolators and outline the context of our work. To conclude this section we argue that isolators not only protect the source but also reduce interferometric effects from two interfaces in a fiber optic transmission line (at least if the isolator is positioned in between the two interfaces). Multiple reflections within a transmission system can result in the interferometric conversion of laser phase noise to intensity noise. In a system containing an optical amplifier reflections can lead to noise enhancements and sometimes can cause lasing, which restrict the level of amplifier gain. So it is fair to say that isolators improve the performance of a fiber optic transmission system by controlling reflections throughout the circuit.

## 1.2 Waveguide based isolator

### 1.2.1 Free space bulk isolator

A bulk free space optical isolator is based on the Faraday effect. The arrangement of a bulk isolator using two polarizers and a  $45^\circ$  Faraday rotator is depicted in Fig.1.1. Vertically polarized light passes through the front polarizer

and then rotated by an angle of  $45^\circ$  while traveling through the Faraday rotator. The Faraday rotator is usually a piece of rare earth garnet material in which a longitudinal magnetic field ( $H$ ) is present. For the materials other than ferromagnetic or ferrimagnetic the Faraday rotation is linearly proportional to the applied magnetic field ( $H$ ) and length of the magnetic material ( $L$ ), the resulting angle can be written as  $\theta_F = V.L.H$ , where  $V$  is known as Verdet constant which is a characteristic feature of the material.  $V$  depends on the wavelength of light propagating through the medium and also on the temperature of the medium. The back polarizer is kept at  $45^\circ$  with respect to front polarizer which allows light to pass through. So the incoming forward propagating light will face no obstacle. In a similar manner when this  $45^\circ$  rotated light reflects back, it again rotated by  $45^\circ$  while passing through the Faraday rotator. The sense of rotation is independent of light propagation. So the plane of polarization of the back-

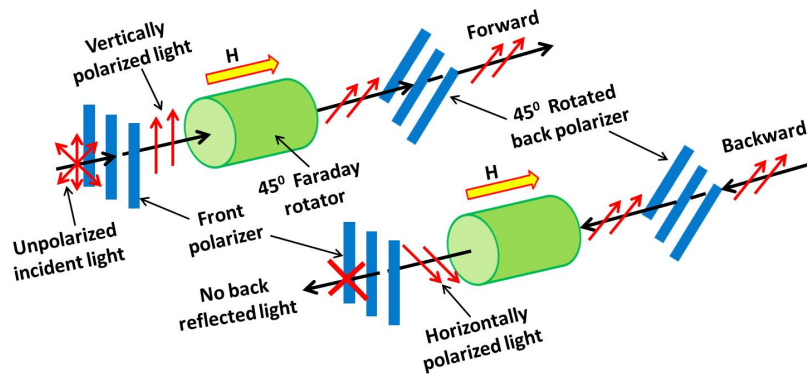


**Figure 1.1:** Schematic diagram of bulk free space isolator.

ward propagating light is finally rotated by an angle of  $90^\circ$  and hence the light is blocked by the front polarizer. Therefore this arrangement acts as an optical isolator. It is worth to mention that this type of isolator is obviously polarization dependent. Polarization independent schemes are also available and can be found in [12–14] using a Faraday rotator. The most common materials used as a Faraday rotator are Yttrium iron garnet (YIG) or Bismuth iron garnet (BIG) which are known to provide a very high Verdet constant in the telecommunication wavelength window with almost zero optical transmission loss. In the 700–1100 nm wavelength range the most common material used for a Faraday rotator is Terbium gallium garnet (TGG). A typical commercial optical isolator working in the telecom window gives an isolation between 30–40 dB with 0.5 dB of insertion loss. The bandwidth of such an isolator is about 20 nm with a working temperature range between  $-20$  to  $70^\circ\text{C}$ . Other losses like polariza-

Central wavelength (nm)	1310, 1480, 1550 or 1585
Bandwidth (nm)	20
Peak isolation	40 dB
Minimum isolation (at $\pm 20$ nm)	30 dB
Insertion loss	0.5 dB
PDL	0.1 dB
PMD	0.2 dB
Operating temperature ( $^{\circ}$ C)	-20 to +70

**Table 1.1:** Typical performance specifications of a commercially available free-space optical isolator.

tion dependent loss (PDL) and polarization mode dispersion (PMD) are negligibly small. A typical performance specifications of a commercially available free space optical isolator is summarized in Table 1.1.

### 1.2.2 Magneto-optic materials

The basic requirement for a magneto-optic material to build an optical isolator is a high Verdet constant with a low optical absorption at telecom wavelengths. In the context of magneto-optical applications two types of materials are considered such as ferrimagnetic garnets and ferromagnetic transition metals (and their alloys). Garnet materials are generally expressed as  $X_3\text{Fe}_5\text{O}_{12}$  in which X represents elements like Yttrium, Bismuth etc. A unique combination of high Faraday rotation (or Verdet constant) and low optical absorption at telecom wavelengths make the garnets a very popular choice among the magneto-optic materials. A detailed study on magneto-optic garnet materials can be found in literature [15]. It has been demonstrated that substituting a small fraction of the X by Cerium (Ce) enhances the magneto-optical properties. That is why nowadays Ce:YIG is a leading magneto-optical material with a Faraday rotation of  $4500^{\circ}/\text{cm}$  at 1550 nm wavelength. In spite of excellent magneto-optical properties the most critical challenge with this material is related to its integration on a waveguide platform. There are two routes for integrating garnet on waveguide circuits: sputtering and bonding. The main hurdle behind the sputtering approach is the mismatch in lattice parameters between the garnet and the host platform. The growth of garnet by sputtering on a semiconductor waveguide platform can be found in several articles [16–18]. Recently an excellent improvement was demonstrated in Ce:YIG sputtering deposition on SOI [19], in which a Ce:YIG film was deposited on top of a YIG seed layer using a two step deposition method.

Transition metals and their alloys are also relevant materials for magneto-optic applications. The main problem with these materials is the high optical absorption at telecom wavelengths. Magneto-optic recording transition metals and their alloys based on iron (Fe), cobalt (Co) and nickel (Ni) have had a lot of attention in the research community [15] due to their relatively strong magneto-optic effect and the fact that they can be deposited easily on any substrate [20–23]. The properties of these alloys depend on the composition of the constituent elements. Mn based compounds like MnAs and MnSb have been studied in the recent past as these can be grown epitaxially or sputtered on III-V semiconductor [24–28].

Recently magneto-optic (MO) polymers have been developed [29–31]. The highest MO figure of merit ( $FOM = 2\theta_F^s / \alpha$ , where  $2\theta_F^s$  and  $\alpha$  are stand for Faraday rotation at saturation magnetic field and optical absorption loss respectively) of one of such polymers was measured as  $2.1^\circ$  at 60 mT and 980 nm wavelength [30]. The FOM for the case of crystalline YIG measured at same wavelength is  $4.2^\circ$  at 160 mT. The major advantage of using polymers is that these materials can be spin coated on waveguide circuits. A further extensive research is still required to establish these polymers as suitable candidates for low cost MO devices.

### 1.2.3 Faraday rotator based waveguide isolator

The idea of miniaturizing a bulk optical isolator on a waveguide platform was first theoretically and experimentally demonstrated by Wang [32]. After that several concepts have been proposed. In this section we are going to concentrate only on waveguide-based concepts. It was a very obvious and pragmatic step to copy the bulk approach of optical isolators. But several challenges need to be overcome to make this happen. First, the planar waveguide geometry breaks the symmetry of bulk optical devices. This brings structurally induced birefringence with two possible linearly polarized eigenstates: transverse electric (TE) and transverse magnetic (TM). This means that the propagation constants are different for TE and TM modes and therefore they are not phase matched. From coupled mode theory it can be proved that complete power transfer between these modes is not possible when they are not phase matched. So this leads to incomplete power transfer between the TE and TM modes. To solve this problem a perfect phase matching is required. A comprehensive overview of various attempts to solve this issue can be found in this reference [33]. Another elegant approach to solve this problem is by quasi-phase matching as demonstrated in [18].

Secondly, the bulk Faraday rotator requires two polarizers set at  $45^\circ$  to perform as an optical isolator. The same approach can be followed in the case of

a waveguide isolator based on Faraday rotator. In the past numerous attempts have been taken to integrate a reciprocal  $45^\circ$  polarization rotator together with a nonreciprocal Faraday rotator. A birefringent material like  $\text{LiNbO}_3$  can be used as a top cladding for magneto-optic garnet in which the optic axis lies in the plane of the film and rotated with respect to the TE-direction. In this way by choosing the offset angle in a proper way a mode conversion in forward direction can be canceled, whereas mode conversion is still present in the backward direction. Historically this is considered to be the first attempt to achieve an integrated optical isolator [34, 35]. Mizumoto took the same approach and demonstrated the idea in 2001 [36] and then in 2007 [37]. Ando utilized the Cotton-Mouton effect [15] to introduce a reciprocal polarization rotator [38].

While the major research efforts to implement a Faraday rotator in a waveguide configuration gave reasonable isolation, the extra arrangements required to replicate the free space Faraday rotator on a waveguide version make the device complicated. Therefore other physical processes were investigated to realize integrated isolators without using a Faraday rotator.

#### 1.2.4 Nonreciprocal phase shift (NRPS) based isolators

As we have already discussed the difficulties to realize a Faraday rotator on a waveguide platform, another magneto-optical effect, called nonreciprocal phase shift (NRPS), can be used to implement an optical isolator. Unlike the Faraday geometry where the magnetic field and the light propagation are parallel, in this case they are oriented perpendicularly. This is known as the Voigt geometry. When light passes through a transversely magnetized waveguide the effective index for the forward light propagation will be different from the effective index for the backward light propagation. A detailed theoretical discussion is presented in the next chapter. The devices presented in this work are based on NRPS. This method was already proposed by Auracher in 1975 [39] but it only gained importance when the limitations of waveguide Faraday rotators were identified. Most importantly this effect does not require any TE-TM phase matching. How optical isolation can be achieved from a MZI type design can be understood from Fig.1.2. A piece of Ce:YIG is bonded on top of the MZI arms. Each arm acts as a nonreciprocal phase shifter under the influence of a transverse magnetic field by an anti-parallel magnet. The lengths of the garnet covered parts on the arms are designed in such a manner that for one direction the NRPS between the arms is  $\pm\pi/2$ , the sign depends on the relative orientation between magnetic field and light propagation. Apart from the nonreciprocal phase shifter one arm is designed slightly longer with respect to the other arm so that a  $\pi/2$  reciprocal phase shift can be obtained. The working principle of this type of isolator is discussed in chapter 3. NRPS

based optical isolators working for TE-mode [40, 41] and TM-mode [42, 43] have been reported for rib waveguide systems. In 2000 Fujita demonstrated a garnet waveguide based MZI isolator working for TM mode with an optical isolation of 19 dB for the first time [44]. Due to the long interferometer arm length (8 mm) several other device designs were proposed and studied theoretically since the first demonstration of Fujita. These include polarization independent isolators [45, 46], nonreciprocal multimode imaging devices [47, 48] and ring resonator type devices [49]. Recently Ruiyi published the idea of asymmetric multimode interference (MMI) isolators based on NRPS [50].

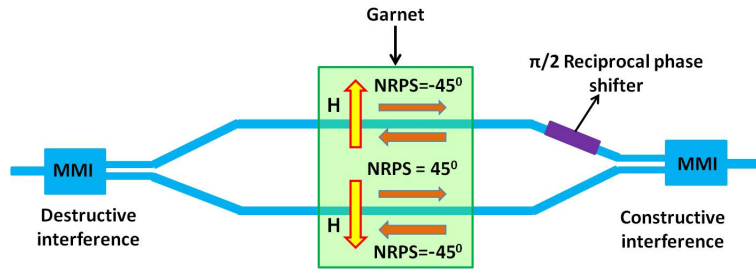


**Figure 1.2:** (a) Schematic diagram of a push-pull type NRPS based MZI isolator.

After the garnet waveguide interferometer the research community started to focus on the integration of the garnet on a semiconductor platform. Yokoi proposed the idea of wafer bonding a garnet die onto a waveguide circuit [51]. After a few years he demonstrated the idea experimentally. This is considered to be the first NRPS type optical isolator realized by bonding of a garnet die onto a waveguide platform [52]. A Ce:YIG die was bonded on top of a InP-InGaAsP MZI for that work. The isolation was limited to 4.9 dB for the several millimeter long device. Different attempts were made to improve the performance of the isolator [53]. Co-integration of the isolator with a laser is also demonstrated by Kazumasa [54]. However the wafer bonding process was not suitable for the active devices because of a high temperature annealing step which is essential to achieve a strong bonding. Therefore new approaches like surface activated direct molecular were required in which the high temperature annealing step is not required. Also the integration on a silicon waveguide platform was started. The extra advantage of a using high index contrast SOI waveguide ( $n_{Si} = 3.45$ ,  $n_{SiO_2} = 1.45$  at 1550 nm) is that the device size can be reduced to a large extent. In the recent past optical isolators based on MZI [55, 56] and ring resonator [57] configurations were demonstrated by adopting direct molecular bonding approach. Some of the recent results based on NRPS is presented in Table 1.2. Here IL stands for insertion loss of the device at the maximum iso-

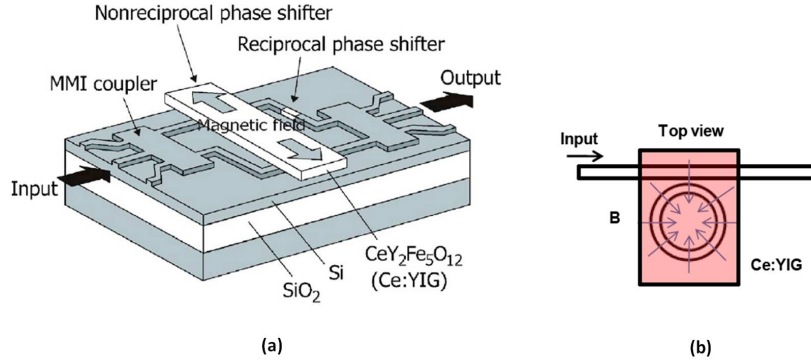


**Figure 1.3:** Schematic diagram of a (a) push-pull type NRPS based SOI-MZI isolator [55] (b) nonreciprocal ring resonator [57].

Research Group(Year)	Device type	Fabrication Technique	Isolation	IL	Bandwidth
Ghent University(2013)	MZI	BCB bonding	32 dB	22 dB	Narrow
Ghent University(2012)	MZI	BCB bonding	25 dB	14 dB	Narrow
Ghent University(2012)	MZI	BCB bonding	11 dB	14 dB	Narrow
Tokyo Inst. of Tech.(2012)	MZI	Direct bonding	18 dB	6 dB	Narrow
UCSB(2011)	Ring	Direct bonding	9 dB	-	Narrow
MIT(2011)	Ring	PLD	19.5 dB	20 dB	Narrow
Tokyo Inst. of Tech.(2008)	MZI	Direct bonding	21 dB	8 dB	Narrow

**Table 1.2:** SOI based magneto-optical isolators.

lation point. Although NRPS based devices are free from the phase matching requirement there are other challenges. The obtainable bandwidth is governed by the wavelength dependence of Faraday rotation of magneto-optical materials as well as device design. For the moment we could neglect the wavelength sensitivity of Faraday rotation. Then design plays a vital role to determine the operational bandwidth. For instance ring resonator based isolators are inherently narrowband. For the case of a MZI-based design a  $\pi/2$  reciprocal phase shifter is wavelength sensitive which limits its operational bandwidth. Shoji has

demonstrated an idea to achieve a wide-band design by adjusting the length of the reciprocal phase shifter [58].

### 1.2.5 Nonreciprocal loss (NRL) based isolators

The effective refractive index for an absorbing waveguide medium is generally expressed as  $n_{eff} = n_r + jn_k$ , where  $n_r$  determines the phase velocity of an electromagnetic wave and  $n_k$  is related to the absorption loss. We have seen from the previous section that NRPS arises when there is a nonreciprocal change in  $n_r$  due to an external magnetic field. However it is possible to change  $n_k$  in a nonreciprocal way using the same trick. So another type of isolator idea has originated based on this physical phenomenon. This kind of nonreciprocal device works on the basis of the magneto-optical Kerr effect (MOKE) at the interface between a magneto-optic layer and a waveguide under an external magnetic field which basically brings a nonreciprocal change in  $n_k$ . The backward propagating light penetrates more into the absorbing magneto-optic layer as compared to the forward propagating light due to MOKE. Hence an optical isolator can be achieved by incorporating an absorptive magnetic metal in the vicinity of an optical gain medium such as a semiconductor optical amplifier (SOA). Optical loss in the forward direction can be compensated by gain of the SOA whereas the loss in the backward direction is still high enough to attenuate the reflected optical signal. The first theoretical idea was presented in 1999 by Wadim [22]. Fig.1.4 shows a NRL-SOA based isolator in which a iron (Fe) layer is deposited on one side wall of the SOA and a magnetic field is applied along the vertical direction. This configuration works for TE polarization. An isolation of 14.7 dB/mm was reported [20]. TM polarized light can also be isolated using the same phenomenon using a different orientation of the magnetic field as shown in Fig.1.5. Studies on SOA-based active optical isolators working for TM polarization were already done by Mathias Vanwolleghem and then Wouter Van Parys at Ghent University, the results of which can be found in [21, 23, 59–62].

There are several advantages to this configuration. First it does not require a MZI configuration as needed for the case of NRPS based isolators. Another important merit is that the maximum isolation only depends on the device length and hence a very high isolation can be achieved. Despite its simplicity in design and its potential for high optical isolation, there is a fundamental disadvantage. A high insertion loss is unavoidable as the optical mode penetrates into the magneto-optic absorbing layer. It is important to mention that isolation depends on device length as well as confinement of optical mode in the magneto-optic layer. Therefore a SOA is required to compensate for the insertion loss in the forward direction. In this context a passive isolator would be preferable because it would not consume any power.

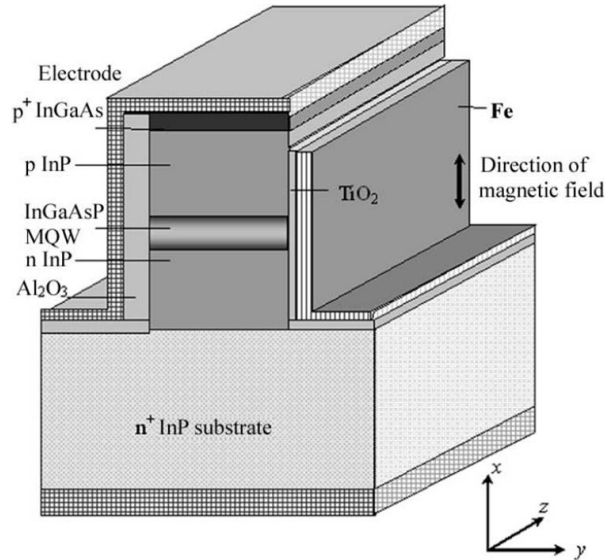


**Figure 1.4:** (a) Schematic diagram of a NRL isolator in an SOA [20] working for TE polarization.

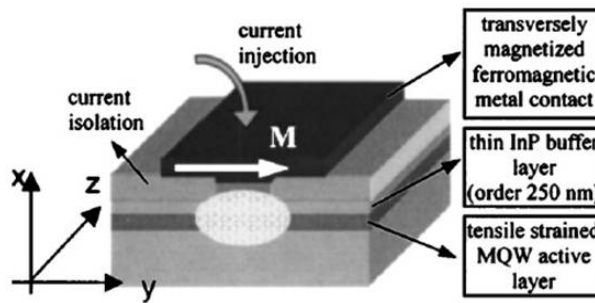


**Figure 1.5:** (a) Schematic diagram of a NRL isolator in an SOA [21] working for TM polarization. M is the direction of magnetization.

### 1.2.6 Non-magnetic approaches to optical isolators

Apart from conventional magneto-optical approaches several non-magnetic approaches were also proposed recently. Non-magnetic approaches are only possible in either non-linear optical devices or time-dependent optical devices. The idea of using opto-mechanical force to realize an optical isolator was introduced by Manipatrani [63] in which a Fabry-Perot cavity formed by two mirrors is used. Out of two mirrors one of them is fixed whereas the other one is movable. This device shows nonreciprocal optical transmission when a differential

radiation pressure imparts on the movable mirror for forward and backward incident light. It is worth to mention that this is a power dependent phenomena. The nonreciprocal devices based on material nonlinearity can be found in [64, 65].

The scheme of controlling or modulating an optical signal by an acoustic wave is very interesting for many applications because of wider tuning range and faster switching capability. A strong opto-acoustic interaction can be achieved by confining both the waves in a very small volume. Recently optical isolation and unidirectional amplification was demonstrated in photonic crystal fibre (PCF) based on opto-acoustic interaction. In this case the acoustic wave was generated by electrostriction by the polarization beating of two orthogonally polarized frequency shifted beams propagating in the same direction [66]. This acoustic wave satisfies the phase matching condition with the optical mode only in forward direction. Hence the optical mode in the forward direction is attenuated after coupling with an acoustic mode or phonon. The backward propagating optical mode remained unaffected from the phonon. On-chip realization of this idea has already been proposed on chalcogenide rib waveguides [67].

The concept of non-magnetic optical isolators based on photonic transitions induced by dynamical modulation of the refractive index of silicon waveguide has been studied. In short the idea is the following: light of frequency  $\omega_1$  in forward direction is converted to a higher frequency  $\omega_2$  by modulation whereas in the reverse direction none of these frequencies are affected by modulation. The theoretical idea of interband transition in photonic crystal was published in 1999 [68] and was recently experimentally demonstrated in [69, 70], though with very poor performance. Yu and Fan have shown that with appropriately designed band structure and by choosing a proper spatial-temporal refractive index modulation a linear broadband isolator can be accomplished [71, 72].

In these non-magnetic structures optical isolation occurs either only in range of incident power or with either modulation sidebands or substantial intrinsic loss. To conclude, although all these non-magnetic approaches are very interesting from a physical point of view, they are very far from being implemented in practical applications.

### 1.3 Rationale and outline of this thesis

The goal of this work is to demonstrate passive optical isolators and then circulators on an SOI platform working at telecom wavelengths. Different types of designs are demonstrated. In all the demonstrations a piece of garnet containing a thin layer of ferrimagnetic Ce:YIG on SGGG substrate is adhesively bonded

on top of the SOI waveguide circuits by means of BCB. The same bonding could be performed by a surface activated direct molecular bonding. But the main issue related to the direct bonding is that it demands an atomically smooth surface. In a process flow of integration of a laser diode with an optical isolator on the same platform, the surface is no longer atomically smooth after the laser fabrication. Hence an adhesive bonding like BCB bonding has advantage over the direct molecular bonding because it is free from stringent surface requirements. A route of sputtering deposition of garnet material on top of SOI waveguide is also taken because it has several advantages over the bonding method.

The outline of this PhD thesis is as follows: Chapter 2 is devoted to the basic theoretical introduction of magneto-optical effects. Afterwards more specific details about the NRPS in a garnet clad SOI waveguide under an external magnetic field are discussed considering both a slab waveguide model and a strip waveguide. The NRPS is simulated for variations of various parameters such as waveguide width, waveguide thickness, Ce:YIG thickness etc.

In Chapter 3 a push-pull MZI type configuration for an optical isolator is studied in detail. In the first part various aspects like a calculation method of the NRPS, the mode profile of garnet clad waveguide etc. are discussed. Later on fabrication details and measurement results are presented. This has led to the first time demonstration of an optical isolator using an adhesive BCB bonding technique.

Push-pull type MZIs with a unidirectional magnetic field demand a critical alignment of garnet die on the MZI. Therefore a new MZI design is proposed in chapter 4 in which the arms are of equal length but of dissimilar widths. Due to the dependence of the NRPS on the waveguide width a differential NRPS could be achieved between forward and backward light propagation under a unidirectional magnetic field applied externally. In the first part of this chapter a calculation method for the NRPS, the simulation of NRPS as a function of waveguide width and the design of MZIs are presented. Afterwards in the second part the measurements are discussed.

Chapter 5 is focused on studying an optical isolator for TE polarization. In this case the device works on the basis of the NRPS experienced by TM polarization but the design includes polarization rotators for TE-TM conversions.

Chapter 6 is devoted to discuss an optical circulator on the SOI platform. A three port optical circulator is realized using an MZI. The underlying working principle of the device is the same as the push-pull type TM isolator. This was also a first time demonstration of an optical circulator on the SOI platform.

Ring resonator based devices are inherently narrowband but the device footprint could be extremely small as compared to a MZI. For a multi-wavelength laser lasing at some particular wavelengths broadband isolators are not required. This is the subject of Chapter 7.

In chapter 8 sputtering deposition is discussed briefly. Initially the deposition of YIG on SOI waveguides was started at IMEC, Belgium but later on we had to stop this because a new bi-layer deposition technique of Ce:YIG on SOI developed by MIT was not available at IMEC. So a close collaboration was started with University of Minnesota, USA where bi-layer deposition was achievable. This is nowadays an active field of research because it provides a path towards the realization of optical isolators by means of a wafer-scale technology.

Finally in the last chapter the conclusions of this work are drawn with scopes for future improvements and perspectives.

## 1.4 Publications

The scientific output stemming from this work has been published in a number of international peer-reviewed journals and also presented at several national and international conferences. The list is presented below.

### 1.4.1 International Journals

1. S. Ghosh, S. Keyvaninia, Y. Shirato, T. Mizumoto, G. Roelkens, and R. Baets. "Optical isolator for TE polarized light realized by adhesive bonding of Ce:YIG on Silicon-on-Insulator waveguide circuits," IEEE Photonics Journal, accepted for publication, 2013.
2. S. Ghosh, S. Keyvaninia, W. Van Roy, T. Mizumoto, G. Roelkens, and R. Baets. "Adhesively bonded Ce:YIG/SOI integrated optical circulator," Optics Letters, 38(6), p.965-967 (2013).
3. S. Ghosh, S. Keyvaninia, Y. Shoji, W. Van Roy, T. Mizumoto, G. Roelkens, and R. Baets. "Compact Mach-Zehnder Interferometer Ce:YIG/SOI Optical Isolator," Photonics Technology Letters, 24(18), p.1653-1656 (2012).
4. S. Ghosh, S. Keyvaninia, W. Van Roy, T. Mizumoto, G. Roelkens, and R. Baets. "A Ce:YIG/Silicon-on-Insulator waveguide optical isolator realized by adhesive bonding," Optics Express, 20(2), p.1839-1848 (2012).

### 1.4.2 Conference Proceedings

1. S. Ghosh, S. Keyvaninia, W. Van Roy, T. Mizumoto, G. Roelkens, and R. Baets. "Demonstration of a Ce:YIG/SOI isolator by BCB bonding," 16th Annual Symposium of the IEEE Photonics Benelux Chapter, Belgium, p.33-36 (2011).

2. S. Ghosh, S. Keyvaninia, W. Van Roy, T. Mizumoto, G. Roelkens, and R. Baets. "Ce:YIG/SOI optical isolator realized by BCB bonding," 8th International Conference in Group IV Photonics 2011, United Kingdom, p.196-198 (ThC3) (2011).
3. S. Ghosh, W. Van Roy, B.J.H. Stadler, and R. Baets. "Optical isolator in silicon photonics using sputtered deposited YIG," 10e Ugent-Firw Doctoraatssymposium, Belgium, (2009).

## References

- [1] Roy Lang and Kohroh Kobayashi. *External optical feedback effects on semiconductor injection laser properties*. IEEE Journal of Quantum Electronics, 16(3):347–355, 1980.
- [2] Daan Lenstra, B Verbeek, and A Den Boef. *Coherence collapse in single-mode semiconductor lasers due to optical feedback*. IEEE Journal of Quantum Electronics, 21(6):674–679, 1985.
- [3] Lew Goldberg, Henry F Taylor, Anthony Dandridge, Joseph F Weller, and Ronald O Miles. *Spectral characteristics of semiconductor lasers with optical feedback*. IEEE Transactions on Microwave Theory and Techniques, 30(4):401–410, 1982.
- [4] R Tkach and AR Chraplyvy. *Regimes of feedback effects in 1.5- $\mu\text{m}$  distributed feedback lasers*. Journal of Lightwave Technology, 4(11):1655–1661, 1986.
- [5] C Henry and R Kazarinov. *Instability of semiconductor lasers due to optical feedback from distant reflectors*. IEEE Journal of Quantum Electronics, 22(2):294–301, 1986.
- [6] R. V. Steele. *Review and forecast of the laser markets: Part II: Diode lasers*. Laser Focus World, February 2004.
- [7] Kiyohide Sakai, Hiroshi Aruga, Shin-Ichi Takagi, Minoru Kawano, Masato Negishi, Yousuke Kondoh, and Shin-Ichi Kaneko. *1.3- $\mu\text{m}$  Uncooled DFB Laser-Diode Module With a Coupled Differential Feed for 10-Gb/s Ethernet Applications*. Journal of lightwave technology, 22(2):574, 2004.
- [8] *Eblana Photonics ships single wavelength laser diodes for applications requiring ultra-narrow line-width and low phase noise*. Press release on <http://www.eblanaphotonics.com>, September 2007.

- [9] K Sato, S Kuwahara, Y Miyamoto, and N Shimizu. *40 Gbit/s direct modulation of distributed feedback laser for very-short-reach optical links*. Electronics Letters, 38(15):816–817, 2002.
- [10] L. Eldada. *Integrated optics need magnets*. www.EETimes.com, September 2001.
- [11] PK Tien. *Integrated optics and new wave phenomena in optical waveguides*. Reviews of Modern Physics, 49(2):361, 1977.
- [12] Kok Wai Chang and WW Sorin. *Polarization independent isolator using spatial walkoff polarizers*. IEEE Photonics Technology Letters, 1(3):68–70, 1989.
- [13] K Nakajima, Y Numajiri, and Y Nomi. *New design of a polarization-independent optical isolator with high performance*. IEEE Transactions on Magnetics, 27(6):5399–5401, 1991.
- [14] Kok Wai Chang and Wayne V Sorin. *High-performance single-mode fiber polarization-independent isolators*. Optics letters, 15(8):449–451, 1990.
- [15] A.K. Zvezdin and V.A. Kotov. *Modern Magneto-optics and Magneto-optical Materials*. Condensed Matter Physics. Taylor & Francis, 2010.
- [16] Sang-Yeob Sung, Xiaoyuan Qi, and Bethanie JH Stadler. *Integrating yttrium iron garnet onto nongarnet substrates with faster deposition rates and high reliability*. Applied Physics Letters, 87(12):121111–121111, 2005.
- [17] Samir K Mondal and Bethanie JH Stadler. *Novel designs for integrating YIG/air photonic crystal slab polarizers with waveguide Faraday rotators*. IEEE Photonics Technology Letters, 17(1):127–129, 2005.
- [18] BM Holmes and DC Hutchings. *Demonstration of quasi-phase-matched nonreciprocal polarization rotation in III-V semiconductor waveguides incorporating magneto-optic upper claddings*. Applied physics letters, 88(6):061116–061116, 2006.
- [19] Lei Bi, Juejun Hu, Peng Jiang, Dong Hun Kim, Gerald F Dionne, Lionel C Kimerling, and CA Ross. *On-chip optical isolation in monolithically integrated non-reciprocal optical resonators*. Nature Photonics, 5(12):758–762, 2011.
- [20] Hiromasa Shimizu and Yoshiaki Nakano. *Fabrication and characterization of an InGaAsP/InP active waveguide optical isolator with 14.7 dB/mm TE mode nonreciprocal attenuation*. Journal of Lightwave Technology, 24(1):38–43, 2006.

- [21] Mathias Vanwolleghem, Wouter Van Parys, Dries Van Thourhout, Roel Baets, François Lelarge, Olivier Gauthier-Lafaye, Bruno Thedrez, Roel Wirix-Speetjens, and Liesbet Lagae. *Experimental demonstration of non-reciprocal amplified spontaneous emission in a CoFe clad semiconductor optical amplifier for use as an integrated optical isolator*. Applied physics letters, 85:3980, 2004.
- [22] Wadim Zaets and Koji Ando. *Optical waveguide isolator based on nonreciprocal loss/gain of amplifier covered by ferromagnetic layer*. IEEE Photonics Technology Letters, 11(8):1012–1014, 1999.
- [23] Wouter Van Parys, Bart Moeyersoon, Dries Van Thourhout, Roel Baets, Mathias Vanwolleghem, Beatrice Dagens, Jean Decobert, Odile Le Gouezigou, Dalila Make, Reinier Vanheertum, et al. *Transverse magnetic mode nonreciprocal propagation in an amplifying AlGaInAs/ InP optical waveguide isolator*. Applied physics letters, 88:071115, 2006.
- [24] Tomohiro Amemiya, Hiromasa Shimizu, Yoshiaki Nakano, PN Hai, Masafumi Yokoyama, and Masaaki Tanaka. *Semiconductor waveguide optical isolator based on nonreciprocal loss induced by ferromagnetic MnAs*. Applied physics letters, 89(2):021104–021104, 2006.
- [25] Tomohiro Amemiya, Hiromasa Shimizu, Pham Nam Hai, Masafumi Yokoyama, Masaaki Tanaka, and Yoshiaki Nakano. *Waveguide-Based 1.5  $\mu\text{m}$  Optical Isolator Based on Magneto-Optic Effect in Ferromagnetic MnAs*. Japanese journal of applied physics, 46:205, 2007.
- [26] Tomohiro Amemiya, Yusuke Ogawa, Hiromasa Shimizu, Masaaki Tanaka, Hiro Munekata, and Yoshiaki Nakano. *Semiconductor waveguide optical isolators incorporating ferromagnetic epitaxial MnX (X= As or Sb)*. In Conference on Lasers and Electro-Optics. Optical Society of America, 2008.
- [27] Tomohiro Amemiya, Hiromasa Shimizu, PN Hai, Masaaki Tanaka, and Yoshiaki Nakano. *Nonreciprocal propagation of light without external magnetic fields in a semiconductor waveguide isolator with a MnAs layer*. Journal of Magnetism and Magnetic Materials, 310(2):2161–2163, 2007.
- [28] Tomohiro Amemiya, Yusuke Ogawa, Hiromasa Shimizu, Hiro Munekata, and Yoshiaki Nakano. *Semiconductor waveguide optical isolator incorporating ferromagnetic epitaxial MnSb for high temperature operation*. Applied physics express, 1(2):2002, 2008.
- [29] Palash Gangopadhyay, Ramakrishna Voorakaranam, Alejandra Lopez-Santiago, Stijn Foerier, Jayan Thomas, Robert A Norwood, Andre Persoons, and Nasser Peyghambarian. *Faraday Rotation Measurements on Thin*

- Films of Regioregular Alkyl-Substituted Polythiophene Derivatives*. The Journal of Physical Chemistry C, 112(21):8032–8037, 2008.
- [30] A Lopez-Santiago, P Gangopadhyay, J Thomas, RA Norwood, A Persoons, and N Peyghambarian. *Faraday rotation in magnetite-polymethylmethacrylate core-shell nanocomposites with high optical quality*. Applied Physics Letters, 95:143302, 2009.
- [31] Palash Gangopadhyay, Alejandra Lopez-Santiago, Ramakrishna Voorakaranam, Roland Himmelhuber, Charles Greenlee, Jayan Thomas, André Persoons, Robert A Norwood, T Verbieat, Hitoshi Yamada, et al. *Magnetite-polymethylmethacrylate core-shell nanocomposites: applications in all optical magnetometers*. Nonlinear Optics and Quantum Optics 41, pages 87–104, 2010.
- [32] Shyh Wang, Manhar Shah, and John D Crow. *Studies of the Use of Gyrotropic and Anisotropic Materials for Mode Conversion in Thin-Film Optical-Waveguide Applications*. Journal of Applied Physics, 43(4):1861–1875, 1972.
- [33] Horst Dötsch, Norbert Bahlmann, Oleksandr Zhuromskyy, Manfred Hammer, Ludger Wilkens, Reinald Gerhardt, Peter Hertel, and Anatoly F Popkov. *Applications of magneto-optical waveguides in integrated optics: review*. JOSA B, 22(1):240–253, 2005.
- [34] John Warner. *Nonreciprocal magneto-optic waveguides*. IEEE Transactions on Microwave Theory and Techniques, 23(1):70–78, 1975.
- [35] S Yamamoto, Y Okamura, and T Makimoto. *Analysis and design of semileaky-type thin-film optical waveguide isolator*. IEEE Journal of Quantum Electronics, 12(12):764–770, 1976.
- [36] T Mizumoto, H Yokoi, M Shimizu, and S Narikawa. *Semi-leaky optical isolator fabricated by wafer bonding of magneto-optic garnet and LiNbO<sub>3</sub>*. In Lasers and Electro-Optics Society, 2001. LEOS 2001. The 14th Annual Meeting of the IEEE, volume 2, pages 580–581. IEEE, 2001.
- [37] Tetsuya Mizumoto and Hideki Saito. *Semi-leaky waveguide optical isolator*. In Optical Fiber Communication Conference. Optical Society of America, 2007.
- [38] Koji Ando, Tokio Okoshi, and Naoki Koshizuka. *Waveguide magneto-optic isolator fabricated by laser annealing*. Applied physics letters, 53(1):4–6, 1988.

- 
- [39] F Auracher and HH Witte. *A new design for an integrated optical isolator*. Optics Communications, 13(4):435–438, 1975.
- [40] AF Popkov, M Fehndrich, M Lohmeyer, and H Dotsch. *Nonreciprocal TE-mode phase shift by domain walls in magneto-optic rib waveguides*. Applied Physics Letters, 72(20):2508–2510, 1998.
- [41] N Bahlmann, M Lohmeyer, H Dotsch, and P Hertel. *Integrated magneto-optic Mach-Zehnder interferometer isolator for TE modes*. Electronics Letters, 34(22):2122–2123, 1998.
- [42] M Shamonin and Paul Hertel. *Analysis of nonreciprocal mode propagation in magneto-optic rib-waveguide structures with the spectral-index method*. Applied optics, 33(27):6415–6421, 1994.
- [43] J Fujita, M Levy, RU Ahmad, RM Osgood, M Randles, C Gutierrez, and R Villareal. *Observation of optical isolation based on nonreciprocal phase shift in a Mach-Zehnder interferometer*. Applied physics letters, 75(7):998–1000, 1999.
- [44] J Fujita, M Levy, RM Osgood, L Wilkens, and H Dotsch. *Waveguide optical isolator based on Mach-Zehnder interferometer*. Applied Physics Letters, 76(16):2158–2160, 2000.
- [45] Oleksandr Zhuromskyy, Manfred Lohmeyer, Norbert Bahlmann, Peter Hertel, AF Popkov, et al. *Analysis of polarization independent Mach-Zehnder-type integrated optical isolator*. Journal of lightwave technology, 17(7):1200, 1999.
- [46] J Fujita, M Levy, RM Osgood Jr, L Wilkens, and H Dotsch. *Polarization-independent waveguide optical isolator based on nonreciprocal phase shift*. IEEE Photonics Technology Letters, 12(11):1510–1512, 2000.
- [47] O Zhuromskyy, M Lohmeyer, N Bahlmann, P Hertel, H Dötsch, and AF Popkov. *Analysis of nonreciprocal light propagation in multimode imaging devices*. Optical and quantum electronics, 32(6-8):885–897, 2000.
- [48] M Lohmeyer, L Wilkens, O Zhuromskyy, H Dötsch, and P Hertel. *Integrated magneto-optic cross strip isolator*. Optics Communications, 189(4):251–259, 2001.
- [49] Naoya Kono, Kuniaki Kakiyama, Kunimasa Saitoh, and Masanori Koshihara. *Nonreciprocal microresonators for the miniaturization of optical waveguide isolators*. Optics Express, 15(12):7737–7751, 2007.

- [50] Ruiyi Chen, Dongjie Tao, Haifeng Zhou, Yinlei Hao, Jianyi Yang, Minghua Wang, and Xiaoqing Jiang. *Asymmetric multimode interference isolator based on nonreciprocal phase shift*. Optics Communications, 282(5):862–866, 2009.
- [51] Hideki Yokoi and Tetsuya Mizumoto. *Proposed configuration of integrated optical isolator employing wafer-direct bonding technique*. Electronics Letters, 33(21):1787–1788, 1997.
- [52] Hideki Yokoi, Tetsuya Mizumoto, Nobuhiro Shinjo, Naoki Futakuchi, and Yoshiaki Nakano. *Demonstration of an optical isolator with a semiconductor guiding layer that was obtained by use of a nonreciprocal phase shift*. Applied optics, 39(33):6158–6164, 2000.
- [53] Yuya Shoji, Hideki Yokoi, and Tetsuya Mizumoto. *Enhancement of magneto optic effect in optical isolator with GaInAsP guiding layer by selective oxidation of AlInAs*. Japanese journal of applied physics, 43(2):590–593, 2004.
- [54] Kazumasa Sakurai, Hideki Yokoi, Tetsuya Mizumoto, Daisuke Miyashita, and Yoshiaki Nakano. *Fabrication of semiconductor laser for integration with optical isolator*. Japanese journal of applied physics, 43:1388, 2004.
- [55] Yuya Shoji, Tetsuya Mizumoto, Hideki Yokoi, I-Wei Hsieh, and Richard M Osgood. *Magneto-optical isolator with silicon waveguides fabricated by direct bonding*. Applied Physics Letters, 92(7):071117–071117, 2008.
- [56] Yuya Shoji, Masatoshi Ito, Yuya Shirato, and Tetsuya Mizumoto. *MZI optical isolator with Si-wire waveguides by surface-activated direct bonding*. Optics express, 20(16):18440–8, July 2012.
- [57] Ming-Chun Tien, Tetsuya Mizumoto, Paolo Pintus, Herbert Kromer, and John E. Bowers. *Silicon ring isolators with bonded nonreciprocal magneto-optic garnets*. Opt. Express, 19(12):11740–11745, Jun 2011.
- [58] Yuya Shoji and Tetsuya Mizumoto. *Wideband operation of Mach-Zehnder interferometric magneto-optical isolator using phase adjustment*. Optics express, 15(20):13446–13450, 2007.
- [59] Kamil Postava, Mathias Vanwolleghem, Dries Van Thourhout, Roel Baets, S Visnovský, Pierre Beauvillain, and J Pistora. *Modeling of a novel InP-based monolithically integrated magneto-optical waveguide isolator*. JOSA B, 22(1):261–273, 2005.
- [60] Mathias Vanwolleghem, Philippe Gogol, Pierre Beauvillain, Wouter Van Parys, and Roel Baets. *Design and optimization of a monolithically integratable InP-based optical waveguide isolator*. JOSA B, 24(1):94–105, 2007.

- [61] Mathias Vanwolleghem. *An integrated InP-based Optical Waveguide Isolator Using Ferromagnetic CoFe Contacts*. PhD thesis, Universiteit Gent, 2005.
- [62] Wouter Van Parys. *Optimization of an Integrated Optical Isolator Based on a Semiconductor Amplifier with a Ferromagnetic Metal Contact*. PhD thesis, Universiteit Gent, 2009.
- [63] Sasikanth Manipatruni, Jacob T Robinson, and Michal Lipson. *Optical nonreciprocity in optomechanical structures*. Physical review letters, 102(21):213903, 2009.
- [64] Marin Soljačić, Chiyan Luo, JD Joannopoulos, and Shanhui Fan. *Nonlinear photonic crystal microdevices for optical integration*. Optics letters, 28(8):637–639, 2003.
- [65] Katia Gallo, Gaetano Assanto, Krishnan R Parameswaran, and Martin M Fejer. *All-optical diode in a periodically poled lithium niobate waveguide*. Applied Physics Letters, 79(3):314–316, 2001.
- [66] MS Kang, A Butsch, and P St J Russell. *Reconfigurable light-driven opto-acoustic isolators in photonic crystal fibre*. Nature Photonics, 5(9):549–553, 2011.
- [67] Christopher G Poulton, Ravi Pant, Adam Byrnes, Shanhui Fan, MJ Steel, Benjamin J Eggleton, et al. *Design for broadband on-chip isolator using stimulated Brillouin scattering in dispersion-engineered chalcogenide waveguides*. Optics Express, 20(19):21235–21246, 2012.
- [68] Joshua N Winn, Shanhui Fan, John D Joannopoulos, and Erich P Ippen. *Interband transitions in photonic crystals*. Physical Review B, 59(3):1551, 1999.
- [69] Po Dong, Stefan F Preble, Jacob T Robinson, Sasikanth Manipatruni, and Michal Lipson. *Inducing photonic transitions between discrete modes in a silicon optical microcavity*. Physical review letters, 100(3):033904, 2008.
- [70] Hugo Lira, Zongfu Yu, Shanhui Fan, and Michal Lipson. *Electrically driven nonreciprocity induced by interband photonic transition on a silicon chip*. Physical Review Letters, 109(3):033901, 2012.
- [71] Zongfu Yu and Shanhui Fan. *Complete optical isolation created by indirect interband photonic transitions*. Nature photonics, 3(2):91–94, 2009.
- [72] Zongfu Yu and Shanhui Fan. *Optical isolation based on nonreciprocal phase shift induced by interband photonic transitions*. Applied Physics Letters, 94(17):171116–171116, 2009.



# 2

## Theoretical study of Non-reciprocity in Magneto-optics

**T**HE interaction of an electromagnetic (EM) wave with a material in which an external magnetic field present is the subject of magneto-optics. In this chapter we will introduce the concept of magneto-optics with a brief historical introduction. We start with the concept of bulk magneto-optics and then we move towards a magneto-optical waveguide. To calculate the nonreciprocal phase shift (NRPS) from a garnet-clad SOI waveguide we will introduce a perturbation method. We will reveal the dependence of NRPS on various parameters of the waveguide such as waveguide thickness, waveguide width with varying adhesive bonding layer thickness. Finally the influence of the Ce:YIG layer thickness on the obtainable NRPS is discussed.

### **2.1 Magneto-optics**

#### **2.1.1 Historical introduction**

Magneto-optics is a subject which deals with physical phenomena arising as a consequence of the interaction between light and matter in which an external magnetic field is present. The very first magneto-optical effect was observed in the year 1845 by Michael Faraday and is known as Faraday effect. It involves

a rotation of the plane of polarization of linearly polarized light in a material under the influence of an external magnetic field. A similar effect was also observed by Kerr in 1876 and is known as magneto-optical Kerr effect (MOKE). It is important to mention that Faraday effect is the transmission type effect whereas MOKE is the reflection type effect. The effect of a magnetic field on the emission spectra of atoms was discovered by the Dutch physicist Pieter Zeeman in 1896 and then was immediately explained by Lorentz's classical electron theory. Zeeman observed that in the presence of an external magnetic field certain spectral lines emitted from an atom split into two circularly polarized components when viewed longitudinally to the magnetic field, the frequencies of these components being shifted to either side of the line in the absence of the magnetic field. The connection between the Zeeman effect and the Faraday effect was established immediately. The shift between the emission frequencies also means

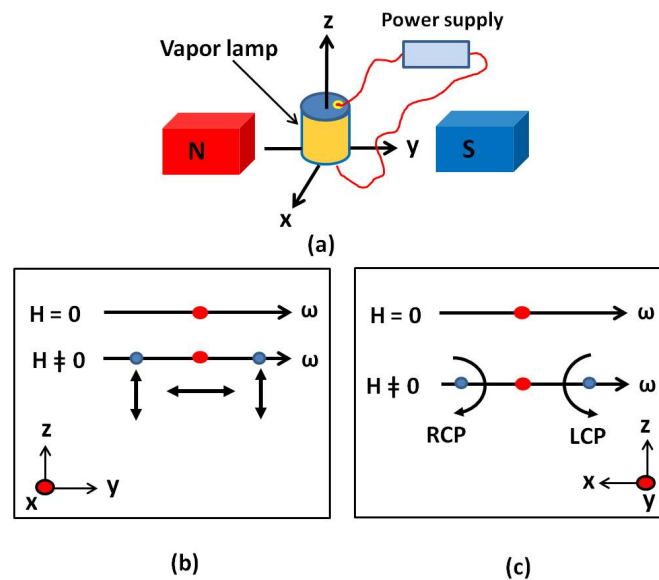


**Figure 2.1:** (a) Set-up to demonstrate Zeeman effect (b) observed perpendicular to the magnetic field (c) observed along the magnetic field.

a shift in the frequencies where the molecule absorbs. Now the optical absorption and the refractive index of the medium are interrelated as established by the dispersion theory of Maxwell and Sellmeier. Hence the spectral lines are exhibiting circular birefringence due to the Zeeman effect. As the absorption is also dependent on the state of polarization of the lines it is also called circular dichroism (two colours), which simply means that the absorption of the right circularly polarized light (RCP) is different from the left circularly polarized light

(LCP). A sketch of the Zeeman effect is depicted in Fig.2.1 in which a magnetic field ( $\mathbf{H}$ ) is applied along the  $y$ -axis. When the emitted spectrum is observed in the direction perpendicular to  $\mathbf{H}$ , it is found that the spectral line of frequency  $\omega$  is split into three components. One component remains unchanged with the electric field vector ( $\mathbf{E}$ ) linearly polarized along the direction of  $\mathbf{H}$  whereas the other two components are displaced equally on either side of the central line with the linearly polarized  $\mathbf{E}$  perpendicular to the magnetic field. On the other hand when the emission spectrum is measured along the direction of  $\mathbf{H}$  two circularly polarized lines are observed in which one is RCP and the other one is LCP. The spectral shift is the same as in the first case. In 1902 Voigt discovered that, double refraction occurs when light is passing through a vapor with a strong magnetic field applied transverse to the light propagation. This is known as the Voigt effect or magnetic double refraction. Further detailed theoretical overviews on magneto-optics can be found in [1–3].

Thus the relative orientation between the wave propagation vector ( $\mathbf{k}$ ) and the magnetic field ( $\mathbf{H}$ ) is a determining factor for magneto-optical effects to occur. Depending on the orientation, magneto-optical phenomena can be classified into two fundamental categories given below:

- Faraday geometry:  $\mathbf{k}$  and  $\mathbf{H}$  are parallel, related to the longitudinal Zeeman effect
- Voigt geometry:  $\mathbf{k}$  and  $\mathbf{H}$  are perpendicular, related to the transverse Zeeman effect

### 2.1.2 Constitutive relations

As the magneto-optical effects are intimately linked to the magnetic properties of a material, we start by summarizing the magnetic properties of materials. It could be surprising that all the materials that exist on earth are magnetic, even though they are weakly magnetic. All materials can be classified into five different categories: diamagnetic, paramagnetic, ferromagnetic, ferrimagnetic and antiferromagnetic. A detailed discussion on magnetic materials can be found in [4]. When a material is placed in an external magnetic field ( $\mathbf{H}$ ), its internal magnetization ( $\mathbf{M}$ ) and magnetic induction ( $\mathbf{B}$ ) are related by the relation given by Eq. 2.1,

$$\mathbf{B}(\omega) = \mu_0(\mathbf{H}(\omega) + \mathbf{M}(\omega)) = \boldsymbol{\mu}(\omega) \cdot \mathbf{H}(\omega) \quad (2.1)$$

where

$$\mathbf{M}(\omega) = \boldsymbol{\chi}_m \cdot \mathbf{H}(\omega) \quad (2.2)$$

and the magnetic permeability is defined as

$$\boldsymbol{\mu} = \mu_0(1 + \boldsymbol{\chi}_m) \quad (2.3)$$

which is generally a tensor.  $\boldsymbol{\chi}_m$  is known as the magnetic susceptibility tensor.

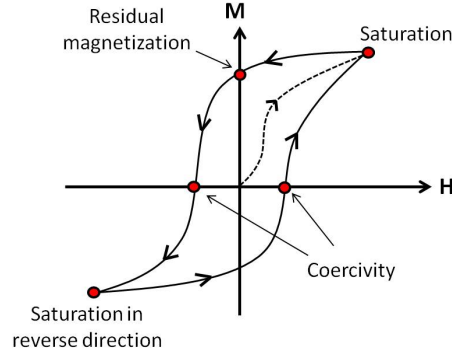


**Figure 2.2:** Magnetic hysteresis loop between M and H.

The variation of M with respect to H for a ferromagnetic / ferrimagnetic material is depicted in Fig.2.2. From Fig.2.2 we can see that at saturation points M does not follow H. As the electric and magnetic components in an electromagnetic wave are mutually coupled, optically induced magnetization can not be separated from optically induced electric polarization. At optical frequencies  $\chi_m \cong 0$  and consequently  $\mu = \mu_0$ , so in this case the response of the material in the presence of an external magnetic field solely depends on the electric permittivity tensor  $\epsilon(\omega)$ . In the presence of an external static magnetic field ( $\mathbf{H}_0$ ) the displacement vector ( $\mathbf{D}$ ) can be written as

$$\mathbf{D}(\omega, \mathbf{H}_0) = \epsilon(\omega) \cdot \mathbf{E}(\omega) + \Delta\epsilon(\omega, \mathbf{H}_0) \cdot \mathbf{E}(\omega) \quad (2.4)$$

where the first term in the R.H.S of Eq.2.4 indicates the intrinsic properties of the medium in the absence of a magnetic field and the last term is due to the perturbation by the magnetic field. It is worth to mention that the perturbation term is very small as compared to the first term. At optical frequencies the properties of a magnetically ordered materials like ferromagnetic and ferrimagnetic materials are dependent on the static magnetization  $\mathbf{M}_0$ . Then the Eq.2.4 can be rewritten as

$$\mathbf{D}(\omega, \mathbf{M}_0) = \epsilon(\omega) \cdot \mathbf{E}(\omega) + \Delta\epsilon(\omega, \mathbf{M}_0) \cdot \mathbf{E}(\omega) \quad (2.5)$$

Therefore the magneto-optical effects are unambiguously characterized by  $\epsilon(\omega, \mathbf{H}_0)$  or  $\epsilon(\omega, \mathbf{M}_0)$  with or without external static magnetic field respectively. It seems that the magneto-optic effects are analogous to the electro-optic effects (with a permittivity tensor  $\epsilon(\omega, \mathbf{E}_0)$ , where  $\mathbf{E}_0$  is the static external electric field). However, there are fundamental differences between them regarding the rules of transformation under space and time reversal which will be discussed later.

### 2.1.3 EM wave propagating through a gyrotropic medium

In the previous subsection we have discussed the material responses in the response of a magnetic field. Here we will explore theoretically what happens to an EM wave propagating through a gyrotropic medium under the influence of an external magnetic field. A medium is said to be gyrotropic if the permittivity of the medium depends on the external magnetic field. The optical properties of the material are described by Maxwell's equations and the constitutive relations. Maxwell equations for a plane wave can be expressed as

$$\nabla \times \mathbf{E} = -\frac{\delta \mathbf{B}}{\delta t} \quad (2.6)$$

$$\nabla \times \mathbf{H} = \mathbf{J} + \frac{\delta \mathbf{D}}{\delta t} \quad (2.7)$$

For the sake of simplicity we are considering a source free medium in which surface current density  $\mathbf{J} = 0$ . For a gyrotropic medium the electric displacement vector  $\mathbf{D}$  and the magnetic induction vector  $\mathbf{B}$  can be expressed respectively as

$$\mathbf{D} = \boldsymbol{\epsilon} \cdot \mathbf{E} \quad (2.8)$$

$$\mathbf{B} = \mu \mathbf{H} \quad (2.9)$$

where  $\boldsymbol{\epsilon} = \epsilon_0 \boldsymbol{\epsilon}_r$ .  $\epsilon_0$  is the vacuum or free space permittivity and  $\boldsymbol{\epsilon}_r$  is the relative permittivity or dielectric constant of the medium. Similarly  $\mu = \mu_0 \mu_r$ , where  $\mu_0$  is the permeability of free space and  $\mu_r$  is the relative permeability of the medium. It is important to mention that both relative permittivity and relative permeability are the tensorial quantities and depends on the external applied magnetic or electric fields. At optical frequencies  $\mu_r$  is equal to unity. So the Eq.2.6 and Eq.2.7 can be rewritten respectively as

$$\nabla \times \mathbf{E} = -\mu_0 \frac{\delta \mathbf{H}}{\delta t} \quad (2.10)$$

$$\nabla \times \mathbf{H} = \epsilon_0 \boldsymbol{\epsilon}_r \cdot \frac{\delta \mathbf{E}}{\delta t} \quad (2.11)$$

Let us consider a plane EM wave that is propagating through a medium, in which the E-field and H-field are represented by

$$\mathbf{E} = \mathbf{E}_0 e^{j(\omega t - \mathbf{k} \cdot \mathbf{r})}, \mathbf{H} = \mathbf{H}_0 e^{j(\omega t - \mathbf{k} \cdot \mathbf{r})} \quad (2.12)$$

We can see that both  $\mathbf{E}$  and  $\mathbf{H}$  field have the same spatial dependence  $e^{-j\mathbf{k} \cdot \mathbf{r}}$ , so the Maxwell's equations can be rewritten simply by using  $\nabla e^{-j\mathbf{k} \cdot \mathbf{r}} \rightarrow -j\mathbf{k} e^{-j\mathbf{k} \cdot \mathbf{r}}$ . Hence the modified forms of Eq.2.10 and Eq.2.11 can be written respectively as

$$\mathbf{k} \times \mathbf{E} = \mu_0 \omega \mathbf{H} \quad (2.13)$$

$$\mathbf{k} \times \mathbf{H} = -\epsilon_0 \omega \epsilon_r \cdot \mathbf{E} \quad (2.14)$$

Using Eq.2.13 and Eq.2.14 we obtained

$$\mathbf{k} \times (\mathbf{k} \times \mathbf{E}) = \mu_0 \omega \mathbf{k} \times \mathbf{H} = -\frac{\omega^2}{c^2} \epsilon_r \cdot \mathbf{E} \quad (2.15)$$

where  $\mathbf{k} = \hat{x}k_x + \hat{z}k_z = \hat{x}k \sin \alpha + \hat{z}k \cos \alpha$  is the wave propagation vector as pictorially represented in Fig.2.3 and the velocity of light in free space is  $c = \frac{1}{\sqrt{\mu_0 \epsilon_0}}$ .

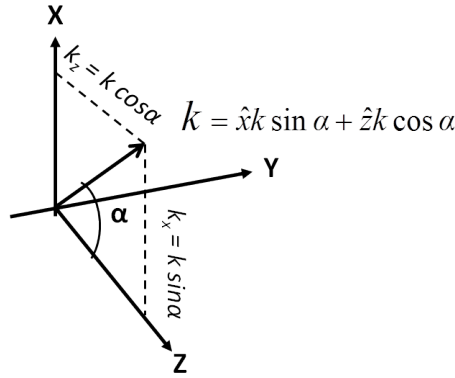


**Figure 2.3:** Vector representation of the wave propagation.

Let us consider a cubic crystal under the influence of a static magnetic field applied along the z-axis, then the relative permittivity takes the form as expressed by a  $3 \times 3$  matrix given below [5, 6]

$$\epsilon_r = \begin{pmatrix} \epsilon_1 & j\epsilon_g & 0 \\ -j\epsilon_g & \epsilon_1 & 0 \\ 0 & 0 & \epsilon_2 \end{pmatrix} \quad (2.16)$$

where  $\epsilon_g$  is known as the gyrotropic constant of the magnetic material which depends on the magnetization of the magnetic material. Rewriting Eq.2.15 in a matrix format we can get

$$\begin{pmatrix} 0 & -k_z & 0 \\ k_z & 0 & -k_x \\ 0 & k_x & 0 \end{pmatrix}^2 \begin{pmatrix} E_x \\ E_y \\ E_z \end{pmatrix} = -\frac{\omega^2}{c^2} \begin{pmatrix} \epsilon_1 & j\epsilon_g & 0 \\ -j\epsilon_g & \epsilon_1 & 0 \\ 0 & 0 & \epsilon_2 \end{pmatrix} \begin{pmatrix} E_x \\ E_y \\ E_z \end{pmatrix} \quad (2.17)$$

Rearranging Eq.2.17 we get

$$\begin{pmatrix} -k_z^2 + \frac{\omega^2}{c^2} \epsilon_1 & j\frac{\omega^2}{c^2} \epsilon_g & k_x k_z \\ -j\frac{\omega^2}{c^2} \epsilon_g & -(k_x^2 + k_z^2) + \frac{\omega^2}{c^2} \epsilon_1 & 0 \\ k_x k_z & 0 & -k_x^2 + \frac{\omega^2}{c^2} \epsilon_2 \end{pmatrix} \begin{pmatrix} E_x \\ E_y \\ E_z \end{pmatrix} = 0 \quad (2.18)$$

To find a nonzero solution for the electric field vector ( $\mathbf{E}$ ), the determinant of the  $3 \times 3$  matrix should vanish and by doing so we arrive at the algebraic equation given below

$$\left(k_x^2 + k_z^2 - \frac{\omega^2}{c^2}\epsilon_1\right)\left(\frac{\omega^4}{c^4}\epsilon_1\epsilon_2 - \frac{\omega^2}{c^2}\epsilon_1k_x^2 - \frac{\omega^2}{c^2}\epsilon_2k_z^2\right) - \frac{\omega^4}{c^4}\epsilon_g^2\left(-\frac{\omega^2}{c^2}\epsilon_2 + k_x^2\right) = 0 \quad (2.19)$$

By substituting the values of  $k_x$  and  $k_z$  as indicated in Fig.2.3 onto Eq.2.19 we can write

$$\begin{aligned} k^4\left(\frac{\omega^2}{c^2}\epsilon_1\sin^2\alpha + \frac{\omega^2}{c^2}\epsilon_2\cos^2\alpha\right) \\ - k^2\left[\left(\frac{\omega^4}{c^4}\epsilon_1^2 + \frac{\omega^4}{c^4}\epsilon_g^2\right)\sin^2\alpha + \frac{\omega^4}{c^4}\epsilon_1\epsilon_2\cos^2\alpha + \frac{\omega^4}{c^4}\epsilon_1\epsilon_2\right] \\ - \frac{\omega^6}{c^6}\epsilon_2(\epsilon_1^2 - \epsilon_g^2) = 0 \end{aligned} \quad (2.20)$$

This is a quadratic equation in  $k^2$  of the form

$$ak^4 + bk^2 + c = 0 \quad (2.21)$$

with two solutions given by

$$k^2 = \frac{-b \pm \sqrt{b^2 - 4ac}}{2a} \quad (2.22)$$

In Eq.2.20 a, b, and c can be written as

$$a = \frac{\omega^2}{c^2}\epsilon_1\sin^2\alpha + \frac{\omega^2}{c^2}\epsilon_2\cos^2\alpha \quad (2.23)$$

$$b = -\left[\left(\frac{\omega^4}{c^4}\epsilon_1^2 + \frac{\omega^4}{c^4}\epsilon_g^2\right)\sin^2\alpha + \frac{\omega^4}{c^4}\epsilon_1\epsilon_2\cos^2\alpha + \frac{\omega^4}{c^4}\epsilon_1\epsilon_2\right] \quad (2.24)$$

$$c = -\frac{\omega^6}{c^6}\epsilon_2(\epsilon_1^2 - \epsilon_g^2) \quad (2.25)$$

Using the values of  $k_x$  and  $k_z$ , Eq.2.18 can be rewritten as

$$\begin{pmatrix} k^2\cos^2\alpha - \frac{\omega^2}{c^2}\epsilon_1 & -j\frac{\omega^2}{c^2}\epsilon_g & -k^2\sin\alpha\cos\alpha \\ j\frac{\omega^2}{c^2}\epsilon_g & k^2 - \frac{\omega^2}{c^2}\epsilon_1 & 0 \\ -k^2\sin\alpha\cos\alpha & 0 & k^2\sin^2\alpha - \frac{\omega^2}{c^2}\epsilon_2 \end{pmatrix} \begin{pmatrix} E_x \\ E_y \\ E_z \end{pmatrix} = 0 \quad (2.26)$$

where  $k^2$  is determined by the roots of Eq.2.20. As the determinant of the above matrix is zero we have three linearly dependent algebraic equations such as

$$\left(k^2\cos^2\alpha - \frac{\omega^2}{c^2}\epsilon_1\right)E_x - j\frac{\omega^2}{c^2}\epsilon_g E_y - k^2 E_z \sin\alpha\cos\alpha = 0 \quad (2.27)$$

$$jE_x \frac{\omega^2}{c^2} \epsilon_g + \left( k^2 - \frac{\omega^2}{c^2} \epsilon_1 \right) E_y = 0 \quad (2.28)$$

$$-k^2 E_x \sin \alpha \cos \alpha + \left( k^2 \sin^2 \alpha - \frac{\omega^2}{c^2} \epsilon_2 \right) E_z = 0 \quad (2.29)$$

From Eq.2.28 and Eq.2.29 we can get

$$\frac{E_x}{E_y} = \frac{\frac{\omega^2}{c^2} \epsilon_1 - k^2}{j \epsilon_g \frac{\omega^2}{c^2}} \quad (2.30)$$

$$\frac{E_x}{E_z} = \frac{k^2 \sin^2 \alpha - \frac{\omega^2}{c^2} \epsilon_2}{k^2 \sin \alpha \cos \alpha} \quad (2.31)$$

respectively. Now we are interested in two special cases as discussed below.

**Case-I:**  $\alpha = 0$  and the wave is propagating along the direction parallel to the magnetic field. Eq.2.26 can be written as

$$\begin{pmatrix} k^2 - \frac{\omega^2}{c^2} \epsilon_1 & -j \frac{\omega^2}{c^2} \epsilon_g & 0 \\ j \frac{\omega^2}{c^2} \epsilon_g & k^2 - \frac{\omega^2}{c^2} \epsilon_1 & 0 \\ 0 & 0 & -\frac{\omega^2}{c^2} \epsilon_2 \end{pmatrix} \begin{pmatrix} E_x \\ E_y \\ E_z \end{pmatrix} = 0 \quad (2.32)$$

For a non-trivial solution of the determinant of the matrix in Eq.2.32 should be zero. Therefore we get

$$k^4 - 2k^2 \frac{\omega^2}{c^2} \epsilon_1 + \left( \frac{\omega^4}{c^4} \epsilon_1^2 - \frac{\omega^4}{c^4} \epsilon_g^2 \right) = 0 \quad (2.33)$$

and  $E_z = 0$ , as  $\frac{\omega^2}{c^2} \epsilon_2 \neq 0$ .

The roots of  $k^2$  are given as

$$k^2 = \frac{\omega^2}{c^2} (\epsilon_1 \pm \epsilon_g) \quad (2.34)$$

After substituting the value of  $k^2$  in Eq.2.32 we find

$$\frac{E_y}{E_x} = \mp j \quad (2.35)$$

For a wave propagating along the z-direction we have two possibilities:

$$\frac{E_y}{E_x} = -j, k^2 = \frac{\omega^2}{c^2} (\epsilon_1 + \epsilon_g) \quad (2.36)$$

$$\frac{E_y}{E_x} = +j, k^2 = \frac{\omega^2}{c^2} (\epsilon_1 - \epsilon_g) \quad (2.37)$$

Eq.2.36 and Eq.2.37 are representing LCP and RCP waves respectively. Eq.2.36 and Eq.2.37 indicate that LCP and RCP have different indices of refraction when

a magnetic field is applied along the light propagation direction. This is known as the Faraday effect.

**Case-II:**  $\alpha = \pi/2$  and the wave is propagating perpendicular to the magnetic field. Eq.2.26 can be written as

$$\begin{pmatrix} -\frac{\omega^2}{c^2}\epsilon_1 & -j\frac{\omega^2}{c^2}\epsilon_g & 0 \\ j\frac{\omega^2}{c^2}\epsilon_g & k^2 - \frac{\omega^2}{c^2}\epsilon_1 & 0 \\ 0 & 0 & k^2 - \frac{\omega^2}{c^2}\epsilon_2 \end{pmatrix} \begin{pmatrix} E_x \\ E_y \\ E_z \end{pmatrix} = 0 \quad (2.38)$$

The existence of a nontrivial solution demands again that the determinant of the matrix should be zero and hence we can write

$$\left( k^2 - \frac{\omega^2}{c^2}\epsilon_2 \right) \left[ \left( k^2 - \frac{\omega^2}{c^2}\epsilon_1 \right) \epsilon_1 + \frac{\omega^2}{c^2}\epsilon_g^2 \right] = 0 \quad (2.39)$$

$$\frac{\omega^2}{c^2}\epsilon_1 E_x + j\frac{\omega^2}{c^2}\epsilon_g E_y = 0 \quad (2.40)$$

$$j\frac{\omega^2}{c^2}\epsilon_g E_x + \left( k^2 - \frac{\omega^2}{c^2}\epsilon_1 \right) E_y = 0 \quad (2.41)$$

$$\left( k^2 - \frac{\omega^2}{c^2}\epsilon_2 \right) E_z = 0 \quad (2.42)$$

Now from Eq.2.39 we could have two situations:

(1)  $k^2 = \frac{\omega^2}{c^2}\epsilon_2$  and this leads to  $E_z \neq 0$  according to Eq.2.42. In this case both  $E_x = 0$  and  $E_y = 0$ . Hence we obtain linearly polarized light along the z-direction with a propagation constant  $k = \frac{\omega}{c}\sqrt{\epsilon_2}$ .

(2)  $k^2 = \frac{\omega^2}{c^2}\left(\epsilon_1 - \frac{\epsilon_g^2}{\epsilon_1}\right)$  which means  $E_z = 0$  and  $E_x = -j\frac{\epsilon_g}{\epsilon_1}E_y$ . So the wave is elliptically polarized in the x-y plane and has a wave propagation constant  $k = \sqrt{\frac{\omega^2}{c^2}\left(\epsilon_1 - \frac{\epsilon_g^2}{\epsilon_1}\right)}$ .

This is known as Voigt effect or Cotton-Mouton effect.

## 2.1.4 Reflection-type magneto-optical effects

Apart from transmission type magneto-optical effects such as the Faraday effect or the Voigt effect also reflection-type effects exist. In this subsection we will discuss briefly this reflection-type magneto-optic effects. When an EM wave is reflected from the surface of a magnetized medium or a medium subjected to an external magnetic field, its state of polarization could differ from the incident wave or the reflectivity could change depending on the orientation of the external magnetic field or magnetization. This phenomenon is popularly known as the magneto-optic Kerr effect (MOKE). The physical origin of the Faraday effect and MOKE is the same and both are first order magneto-optic effects. The distinction between the two is that Faraday effect is a transmission type effect

whereas MOKE is a reflection phenomenon. Depending on the direction of the external magnetic field or internal magnetization with respect to the incident light MOKE is classified into three categories such as

- Polar Kerr effect: Magnetization is normal to the reflecting surface of the medium
- Longitudinal (meridional) Kerr effect: Magnetization is parallel to the reflecting surface of the medium but lies in the plane of incident wave
- Transverse (equatorial) Kerr effect: Magnetization is parallel to the reflecting surface of the medium but lies perpendicular to incident plane of the wave.

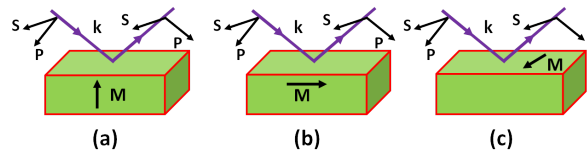


**Figure 2.4:** Magneto-optical Kerr effects (a) Polar Kerr effect, (b) longitudinal Kerr effect and (c) transverse Kerr effect.

All the situations are depicted in Fig.2.4. The physical understanding will be clear if we consider two polarizations of light namely p-polarized (E-vector is parallel to the incident plane) or transverse magnetic (TM) mode and s-polarized (E-vector is perpendicular to the incident plane) or transverse electric (TE) mode. In the case of reflection from an interface between two non-magnetic media s and p polarizations are the normal modes of propagation for incident and reflected waves. However they do not remain normal modes when there is a magnetic field present. Upon reflection at such a surface the TE mode can couple to the TM mode and vice versa. We know that the only component of the electric field perpendicular to the magnetic field (or internal magnetization) interacts with the magnetization and results in birefringence. For polar and longitudinal Kerr effects both TE and TM mode interact with the magnetization as clearly depicted in Fig.2.4(a) and Fig.2.4(b). In both the cases there is rotation of the plane of polarization and the reflected light is elliptically polarized. This scenario is different from the case of the transverse Kerr effect because here only the TM mode is at a right angle with the magnetization direction. Hence the TM mode solely experiences a rotation of the plane of polarization and also change in intensity. The polar Kerr effect especially has an important application in magneto-optic recoding. In the context of optical isolators only the transverse configuration of the Kerr effect is relevant.

## 2.2 Waveguide with magneto-optic cladding

We have already seen that the Faraday effect is utilized to build a bulk optical isolator. But several limitations to realizing a bulk isolator geometry on a waveguide platform forced researchers to adopt different physical principles for an integrated on-chip isolator. These integrated isolators are either nonreciprocal loss difference based [7] or nonreciprocal phase shift [8] based. As the central idea of this thesis is to explore NRPS based optical isolators we will restrict our discussions only to NRPS. Now let us clarify the concepts of reciprocity and nonreciprocity. To understand this idea we have to see how the electric and magnetic fields transform under time reversal ( $t \rightarrow -t$ ). In a  $(x, y, z, t)$  coordinate system, Maxwell's equations can be written as

$$\nabla \times \mathbf{E} = -\frac{\delta \mathbf{B}}{\delta t} \quad (2.43)$$

$$\nabla \times \mathbf{H} = \mathbf{J} + \frac{\delta \mathbf{D}}{\delta t} \quad (2.44)$$

$$\nabla \cdot \mathbf{D} = \rho \quad (2.45)$$

$$\nabla \cdot \mathbf{B} = 0 \quad (2.46)$$

and the Lorentz's force law can be expressed as

$$\mathbf{F} = q(\mathbf{E} + \mathbf{v} \times \mathbf{B}) \quad (2.47)$$

where  $q$  is the charge of a particle moving with a velocity of  $\mathbf{v}$ . The fact that classical electrodynamics is invariant under time reversal transformation. Now it is obvious that  $\mathbf{j}$  and  $\mathbf{v}$  flip their signs under time reversal while  $\rho$  is invariant. Therefore the invariance of above mentioned equations inferred that  $\mathbf{E}$  is invariant while  $\mathbf{H}$  flips sign under time reversal. So, we can write

$$\mathbf{E}(x, y, z, t) \rightarrow \mathbf{E}(x, y, z, -t) \quad (2.48)$$

$$\mathbf{H}(x, y, z, t) \rightarrow -\mathbf{H}(x, y, z, -t) \quad (2.49)$$

A reciprocal medium follows this time reversal transformation. In a simplified world an optical signal can run in the backward direction without changing the physics. This scenario will be different if the medium through which the optical signal is propagating is nonreciprocal. In a nonreciprocal medium there is no symmetry when interchanging between source and detector. The dielectric permittivity tensor of a homogeneous isotropic material without an external magnetic field can be expressed as

$$\epsilon = \epsilon_0 \begin{pmatrix} n^2 & 0 & 0 \\ 0 & n^2 & 0 \\ 0 & 0 & n^2 \end{pmatrix} \quad (2.50)$$

But when there is a magnetic field along the y-direction the permittivity tensor takes the form as [5, 6]

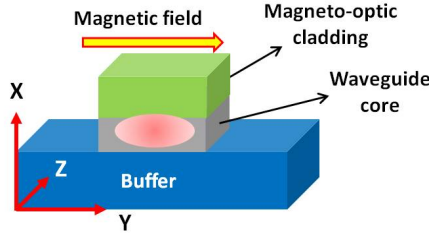


**Figure 2.5:** Optical waveguide with magneto-optic cladding. Light propagating along z-axis with an external magnetic field applied along y-axis.

$$\epsilon = \epsilon_0 \begin{pmatrix} n^2 & 0 & -j\epsilon_{xz} \\ 0 & n^2 & 0 \\ j\epsilon_{xz} & 0 & n^2 \end{pmatrix} \quad (2.51)$$

Similarly if the magnetic field is applied along the x-direction then the matrix will change to

$$\epsilon = \epsilon_0 \begin{pmatrix} n^2 & 0 & 0 \\ 0 & n^2 & j\epsilon_{yz} \\ 0 & -j\epsilon_{yz} & n^2 \end{pmatrix} \quad (2.52)$$

The off-diagonal terms  $\epsilon_{xz}$  or  $\epsilon_{yz}$  (same as  $\epsilon_g$  on Eq.2.16) are called the gyrotropic constant of the magneto-optic material and are related to the Faraday rotation coefficient  $\theta_F$  and refractive index ( $n$ ) of that medium by  $\epsilon_{xz}$  or  $\epsilon_{yz} = n\theta_F\lambda/\pi$ , in which  $\lambda$  is the wavelength of the light propagating through the waveguide. The off-diagonal terms of the dielectric permittivity tensor couple one of the transverse (x or y) field components with the longitudinal (z) field component and result in a difference in propagation constants between forward and backward directions. In the next section we will see how the gyrotropic constant is related to the NRPS of a waveguide.

### 2.3 Perturbation method

A perturbation method is an approximate mathematical approach to find a solution of a physical problem when an exact solution is not possible. The elements of the gyrotropic part  $\epsilon_{xz}$  of the permittivity tensor are small compared to  $n^2$  and therefore perturbation theory can be used [9]. An EM wave in a rectangular waveguide is either transverse electric (TE) or transverse magnetic (TM)

(more precisely quasi-TE or quasi-TM). The nonreciprocal phase shift experienced by a TM mode was first introduced by Yamamoto [10]. Popkov predicted the same effect for the TE mode using a rib waveguide parallel to a stripe domain [11]. Bahlmann calculated the TE mode NRPS for the rib waveguide using a finite element method (FEM) [12]. The derivation of the perturbation formula for lossy magneto-optic waveguides has been done by Mathias Vanwolleghe [13]. The same formula is used throughout this work without going into the detailed mathematical derivation.

The unperturbed field components of an EM wave for TE and TM modes propagating along the z-axis through a rectangular waveguide can be expressed as

TE mode:

$$\mathbf{E}(x, y, z, t) = [0, E_y^0, 0] \exp(j\omega t - j\beta^{TE} z) \quad (2.53)$$

$$\mathbf{H}(x, y, z, t) = [H_x^0, 0, H_z^0] \exp(j\omega t - j\beta^{TE} z) \quad (2.54)$$

TM mode:

$$\mathbf{E}(x, y, z, t) = [E_x^0, 0, E_z^0] \exp(j\omega t - j\beta^{TM} z) \quad (2.55)$$

$$\mathbf{H}(x, y, z, t) = [0, H_y^0, 0] \exp(j\omega t - j\beta^{TM} z) \quad (2.56)$$

in which  $\beta^{TE} = 2\pi n^{TE} / \lambda$ ,  $\beta^{TM} = 2\pi n^{TM} / \lambda$  and  $\omega$  is the angular frequency of the EM wave. The first order approximation of the perturbation formula for the TM mode NRPS (in case the material is magnetized along the y-direction) can be written as

$$\Delta\beta^{TM} = -j\omega\epsilon_0 \frac{\iint \epsilon_{xz} E_x^0 E_z^0 dx dy}{2 \iint [E_x^0 H_y^0 - E_y^0 H_x^0] dx dy} \quad (2.57)$$

Similarly the first order approximation of the perturbation formula for the TE mode NRPS with magnetization along the y-direction can be expressed as

$$\Delta\beta^{TE} = -j\omega\epsilon_0 \frac{\iint \epsilon_{xz} E_x^0 E_z^0 dx dy}{2 \iint [E_x^0 H_y^0 - E_y^0 H_x^0] dx dy} \quad (2.58)$$

In Eq.2.57 and Eq.2.58,  $E_x^0, E_y^0, E_z^0, H_x^0, H_y^0$  and  $H_z^0$  are denoted as the amplitudes of the unperturbed field components. The integral in the numerator is carried over the magneto-optic region of the waveguide and the integral in the denominator is evaluated over the whole waveguide cross-section. From Eq.2.57 several important conclusions can be drawn:

- A plane wave propagating in a bulk magneto-optic (MO) medium perpendicular to the magnetic field direction does not experience a NRPS (due to either  $E_z^0 = 0$  or  $E_x^0 = 0$ ).
- The effect is intimately related to the asymmetry in the waveguide cross-section. The TM mode propagating perpendicular to the in-plane magnetic field in a vertically symmetric MO waveguide will not experience a net NRPS

due to the fact that the overall integral in the numerator is zero.

- The TE mode propagating perpendicular to the in-plane magnetization does not experience a net NRPS because  $E_z^0 = 0$ .

Hence NRPS based isolators are polarization dependent. To obtain a polarization independent isolator using NRPS, the magnetic field needs to be applied along the x- and y- directions simultaneously. The corresponding demonstration can be found in [14]. The main problem with this polarization independent approach is that it requires in-plane and out-of-plane magnetization simultaneously which is not favorable for a magnetic material. The length required to achieve a NRPS of  $\theta_{NRPS}$  between the forward and backward propagation directions for the TM mode can be calculated as:

$$L_{NRPS} = \frac{\theta_{NRPS}}{|Re[\Delta\beta^{TM}]|} \quad (2.59)$$

## 2.4 Numerical calculation of the NRPS

### 2.4.1 Slab waveguide geometry

In this subsection we will discuss the NRPS of a slab magneto-optic waveguide. A slab structure as shown in Fig.2.6 guides purely TE or TM modes. For a slab waveguide  $E_z^0$  of a TM mode can be expressed as

$$E_z^0 = \frac{-j}{k_0 n_{eff}} \frac{dE_x}{dx} \quad (2.60)$$

Hence the integral in the numerator of Eq.2.57 reduces to

$$\begin{aligned} \iint E_x^0 E_z^0 dx dy &= \frac{-j}{2k_0 n_{eff}} \iint \frac{d(E_x^2)}{dx} dx \\ &= \frac{-j}{2k_0 n_{eff}} [(E_x)_i^2 - (E_x)_e^2] \end{aligned} \quad (2.61)$$

where 'i' and 'e' denote the x-coordinate of the two extremities of the magneto-optic layer. Therefore by calculating the  $E_x$  field distribution the NRPS of the slab waveguide can be determined. In the context of adhesively bonded isolators the influence of the adhesive inter-layer between the waveguide core and the magneto-optic layer is a crucial parameter to the NRPS. Therefore it is of paramount importance to find out the variation of NRPS as a function of adhesive layer thickness. The slab waveguide model used for this calculation is shown in Fig.2.6. The waveguide stack consists of a garnet die adhesively bonded by Benzocyclobutene (BCB) on a silicon waveguide. The garnet die in this case is an epitaxially grown Ce:YIG on substituted Gadolinium Gallium Garnet (SGGG) substrate. The CAvity Modelling FRamework (CAMFR) [15, 16]

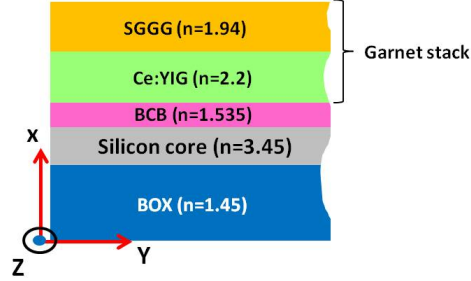


**Figure 2.6:** Slab waveguide geometry with a garnet stack bonded by BCB.

tool has been used to simulate the NRPS as a function of waveguide thickness for different adhesive bonding layer thicknesses. Since this is 2D full-vectorial model, the NRPS obtained is approximately equal to that for a 900 nm wide waveguide which is discussed in chapter 3. The resulting NRPS for the fundamental TM mode at 1550 nm as function of silicon waveguide thickness for various BCB thicknesses is presented in Fig.2.7. The Faraday rotation coeffi-

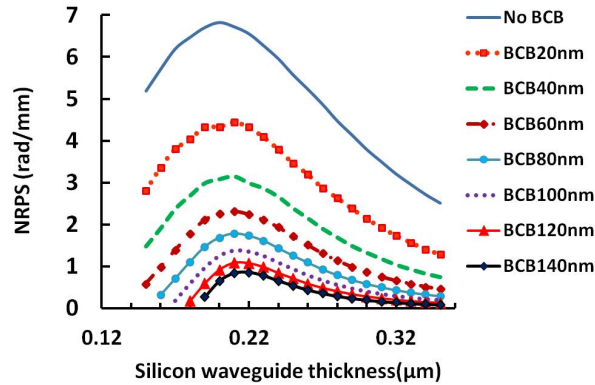


**Figure 2.7:** Simulation of NRPS as a function of silicon waveguide thickness and BCB bonding layer thickness

cient of the Ce:YIG is taken as  $-4500^\circ/\text{cm}$  at 1550 nm wavelength. The thickness of the Ce:YIG layer is about 260 nm on a  $450\ \mu\text{m}$  SGGG substrate. It can be seen from the simulation that the NRPS is maximum at 220 nm thickness of silicon core which is equal to the silicon waveguide thickness of commercially available Silicon-on-insulator (SOI) wafer. NRPS decreases when core thickness increases as the TM mode is confined more to the core. On the other hand for thinner silicon cores the TM mode is extending into the Ce:YIG. The confine-

ment factor [17] of the TM mode in the Ce:YIG layer for different silicon core thicknesses is depicted in Fig.2.8 for various BCB thicknesses. Mathematically

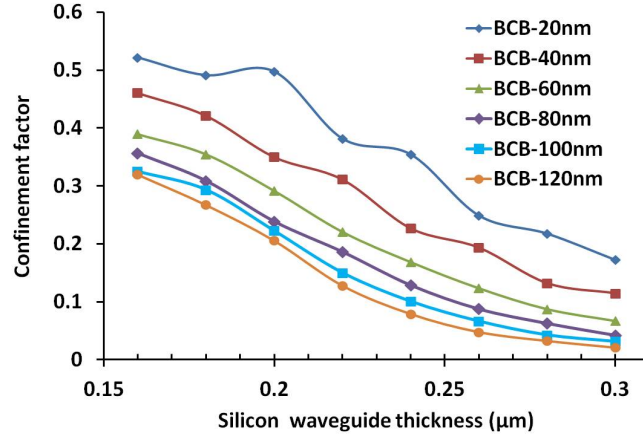


**Figure 2.8:** Variation of confinement factor of TM mode in Ce:YIG layer as a function of silicon waveguide thickness for various BCB thickness.

confinement factor ( $\Gamma$ ) of TM mode in Ce:YIG layer is defined as [18]:

$$\Gamma = \frac{\int_{-\infty}^{\infty} H_y^2 dx}{\int_{-\infty}^{\infty} H_y^2 dx} \quad (2.62)$$

### 2.4.2 Strip waveguide geometry

In a strip waveguide the EM wave is bound in both x and y directions. For the strip waveguide the slab approximation for  $E_z$  (see Eq.2.60) will not hold anymore and all the field components mentioned in Eq.2.57 need to be calculate separately to evaluate NRPS. In this section we will unfold the effect of finite waveguide width on NRPS. The waveguide cross-section for this study is shown in Fig.2.9(a). For the sake of simplicity only rectangular waveguide cross-sections are assumed. The NRPS for trapezoidal waveguide cross-sections is discussed in chapter 4. A finite difference method (FDM) implemented in FIMMWAVE software is used to evaluate all the field components required for NRPS calculation [19]. The resolution of the simulation window along the x-axis is taken as 4 nm whereas the resolution along the y-axis is 20 nm. The wavelength for all cases is taken as 1500 nm and the Faraday rotation coefficient is  $4500^\circ/\text{cm}$ . It can be seen in Fig.2.9(b) that the NRPS saturates at a waveguide width of around 800 nm to a value that corresponds with the slab calculation.

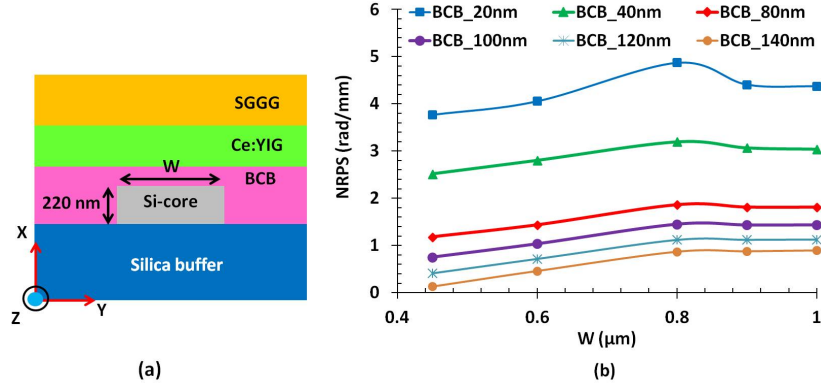


**Figure 2.9:** (a) Cross-section of a strip waveguide with a garnet die bonded on top by BCB and (b) simulation of the NRPS as a function of waveguide width ( $W$ ) considering a silicon thickness and Ce:YIG thickness of 220 nm and 260 nm respectively.

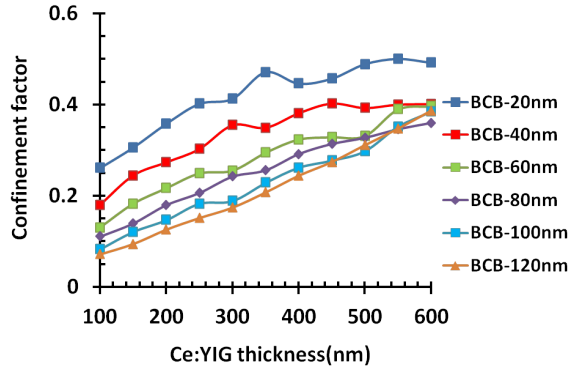


**Figure 2.10:** Confinement factor of TM mode in the Ce:YIG layer as a function of Ce:YIG thickness for various BCB thicknesses.

## 2.5 Influence of Ce:YIG layer

In this section we will discuss how the thickness of the Ce:YIG layer controls the value of the NRPS. From Fig.2.10 we can see that the confinement of the TM mode in the Ce:YIG layer increases with the increase of Ce:YIG thickness for any BCB thickness. Here the confinement factor is calculated for a silicon waveguide width of 900 nm and a thickness of 220 nm. It is also straight forward to understand that as the BCB thickness increases the confinement into Ce:YIG layer decreases for a particular Ce:YIG thickness. The thickness of the

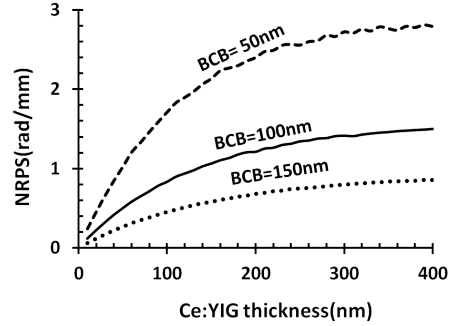


**Figure 2.11:** Variation of NRPS with Ce:YIG thickness for slab waveguide structure.

Ce:YIG layer is a critical factor which determines the guiding condition for the fundamental TM mode through the silicon waveguide, but this will be explained in the next chapter. The dependence of the NRPS on the Ce:YIG thickness for various BCB thicknesses is presented in Fig.2.11. It is clear that about 300 nm thickness of Ce:YIG layer is sufficient to achieve the maximum magneto-optical effect.

## 2.6 Conclusion

In this chapter we have discussed magneto-optics and nonreciprocal phenomena induced by a magnetic field. In the context of a waveguide type isolator, the NRPS has been extensively discussed for various waveguide configurations. First we have calculated the NRPS in a slab waveguide after which strip waveguides are considered in which light is confined in two dimensions. Both the models converge after a particular waveguide width. Furthermore the dependence of the Ce:YIG thickness on the NRPS is simulated for the slab waveguide case. From this simulation it is clear that a 300 nm thick Ce:YIG layer is sufficient to achieve maximum NRPS.

## References

- [1] E. Hecht. *Optics, 4/E*. Pearson Education, 2008.
- [2] A.K. Zvezdin and V.A. Kotov. *Modern Magneto-optics and Magneto-optical Materials*. Condensed Matter Physics. Taylor & Francis, 2010.

- [3] Francis A Jenkins and Harvey E White. *Fundamentals of optics*. New York: McGraw-Hill, 1957, 3rd ed., 1, 1957.
- [4] Robert C O'handley. *Modern magnetic materials: principles and applications*, volume 830622677. Wiley New York, 2000.
- [5] Jin Au Kong. *Electromagnetic wave theory*, volume 2. Wiley New York, 1990.
- [6] Shun Lien Chuang. *Physics of photonic devices*, volume 80. Wiley, 2012.
- [7] Wouter Van Parys. *Optimization of an Integrated Optical Isolator Based on a Semiconductor Amplifier with a Ferromagnetic Metal Contact*. PhD thesis, Universiteit Gent, 2009.
- [8] Yuya Shoji, Tetsuya Mizumoto, Hideki Yokoi, I-Wei Hsieh, and Richard M Osgood. *Magneto-optical isolator with silicon waveguides fabricated by direct bonding*. Applied Physics Letters, 92(7):071117–071117, 2008.
- [9] GJ Gabriel and ME Brodwin. *The solution of guided waves in inhomogeneous anisotropic media by perturbation and variational methods*. IEEE Transactions on Microwave Theory and Techniques, 13(3):364–370, 1965.
- [10] Sadahiko Yamamoto and Toshio Makimoto. *Circuit theory for a class of anisotropic and gyrotropic thin-film optical waveguides and design of nonreciprocal devices for integrated optics*. Journal of Applied Physics, 45(2):882–888, 1974.
- [11] AF Popkov, M Fehndrich, M Lohmeyer, and H Dotsch. *Nonreciprocal TE-mode phase shift by domain walls in magneto-optic rib waveguides*. Applied Physics Letters, 72(20):2508–2510, 1998.
- [12] Norbert Bahlmann, Manfred Lohmeyer, H Dotsch, and Peter Hertel. *Finite-element analysis of nonreciprocal phase shift for TE modes in magneto-optic rib waveguides with a compensation wall*. IEEE Journal of Quantum Electronics, 35(2):250–253, 1999.
- [13] Mathias Vanwolleghem. *An integrated InP-based Optical Waveguide Isolator Using Ferromagnetic CoFe Contacts*. PhD thesis, Universiteit Gent, 2005.
- [14] J Fujita, M Levy, RM Osgood Jr, L Wilkens, and H Dotsch. *Polarization-independent waveguide optical isolator based on nonreciprocal phase shift*. IEEE Photonics Technology Letters, 12(11):1510–1512, 2000.
- [15] Peter Bienstman. *Rigorous and efficient modelling of wavelength scale photonic components*. PhD thesis, Universiteit Gent, 2001.

- [16] <http://camfr.sourceforge.net/>.
- [17] Graham T Reed and Andrew P Knights. *Silicon photonics*. Wiley Online Library, 2008.
- [18] TD Visser, Bart Demeulenaere, Jan Haes, D Lenstra, Roel Baets, and H Blok. *Confinement and modal gain in waveguides*. *Journal of Lightwave Technology*, 14(5):885–887, 1996.
- [19] <http://www.photond.com>.

# 3

## Push-Pull Mach Zehnder interferometer optical isolator

**I**N this chapter we will elaborate on the Mach Zehnder interferometer (MZI) type isolator design. To start with the basic working principle of the MZI will be presented. Then a push-pull configuration will be discussed in the context of both the narrowband and the broadband isolator designs. Later on a first time demonstration of a MZI type optical isolator realized by adhesively bonding a ferrimagnetic garnet die on top of a silicon waveguide circuit is studied in great details. An isolation of 32 dB was achieved. Total insertion loss was also estimated for this device considering all the contributors towards total loss.

### **3.1 Mach Zehnder interferometer (MZI)**

This is one kind of interferometer which is ubiquitously used to determine the relative phase shift between two light beams from a coherent light source and named after the renowned physicists Ludwig Mach and Ludwig Zehnder. It is very similar to the Michelson interferometer only the optics used for splitting/-combining the light beams here is different. This simple technique is prevailing everywhere in the fields of optics and photonics as a basic building block for a variety of important applications such as wavelength division multiplexing

(WDM) [1–5], optical coherence tomography (OCT) [6–8], sensing [9–19] and many more. A schematic diagram of a simple waveguide based unbalanced MZI is presented in Figure 3.1. Two 3dB couplers are connected by two arms

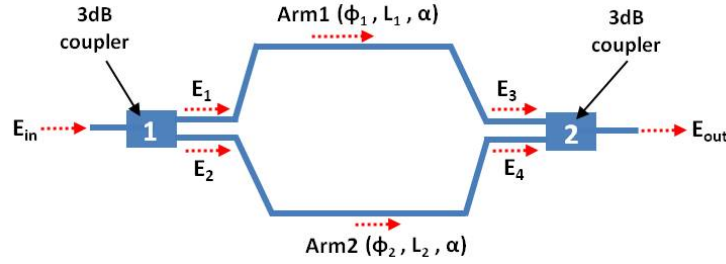


**Figure 3.1:** Schematic diagram of a Mach-Zehnder interferometer.

forming the MZI. Let us consider the length of arm1 and arm2 are  $L_1$  and  $L_2$  respectively. The optical path difference is then created as  $n_{eff} \cdot \Delta L$ , where  $\Delta L = L_1 - L_2$  and  $n_{eff}$  is the effective refractive index of the waveguide through which light is propagating in both the arms. Here the effective refractive index is taken as same for both the arms. Let us assume that a beam of light with electric field amplitudes  $E_{in}$  is passing through a splitter which splits the light equally ( $k = 0.5$ ) onto the both arms. The electric field just after the splitter are  $E_1 = \sqrt{k} \cdot E_{in}$  and  $E_2 = \sqrt{1-k} \cdot E_{in}$  in arm1 and arm2 respectively. If  $\phi_1$  and  $\phi_2$  are the phases experienced by the light whiling traveling through the arm 1 and arm 2 respectively then the corresponding electric fields just before the second 3 dB coupler can be written as,

$$E_3 = E_1 \exp(j\phi_1 - \alpha L_1) \quad (3.1)$$

$$E_4 = E_2 \exp(j\phi_2 - \alpha L_2) \quad (3.2)$$

where  $\alpha$  is the loss of the waveguide expressed in per unit length. Hence the field at the output of the second 3 dB coupler can be expressed as a sum of these two fields such that

$$E_{out} = \sqrt{k} E_3 + \sqrt{1-k} E_4 \quad (3.3)$$

Therefore the output intensity can be written as

$$I_{out} = |E_{out}|^2 \quad (3.4)$$

Now let us define the characteristic parameter of the MZI which is nothing but free spectral range (FSR). It is the spectral separation between two consecutive maxima or minima points and is related to the physical length difference between the arms of the MZI given by Eq.3.5.  $n_g$  is the group index of the light

traveling through a dispersive waveguide and related to the effective refractive index by the relation given in Eq.3.6.

$$FSR = \frac{\lambda^2}{n_g \Delta L} \quad (3.5)$$

$$n_g = n_{eff} - \lambda \frac{dn_{eff}}{d\lambda} \quad (3.6)$$

Now let us analyze the situation when the MZI arms experience a nonreciprocal phase shift ( $\theta_N/4$ ) on top of reciprocal phase that is opposite in both arms. Let us consider light propagating from left to right as forward direction and the opposite of that as the backward direction. Then the corresponding electric fields just before the second 3 dB coupler during forward propagation will take the forms like:

$$E_3^f = E_1 \exp(j\phi_1 + j\theta_N/4 - \alpha L_1), E_4^f = E_2 \exp(j\phi_2 - j\theta_N/4 - \alpha L_2) \quad (3.7)$$

Likewise the same entities just before the first 3dB coupler during the backward propagation will be:

$$E_1^b = E_3 \exp(j\phi_1 - j\theta_N/4 - \alpha L_1), E_2^b = E_4 \exp(j\phi_2 + j\theta_N/4 - \alpha L_2) \quad (3.8)$$

The sign of  $\theta_N$  in one arm is intentionally taken as opposite compared to the

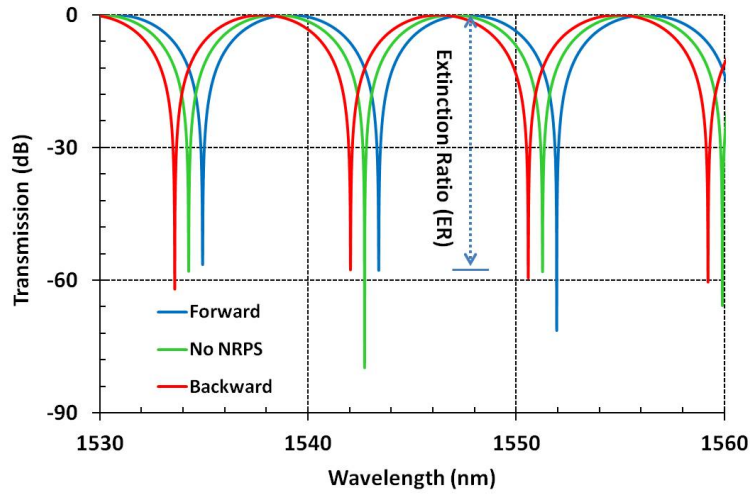


**Figure 3.2:** Illustration of transmission spectra of an unbalanced ( $\Delta L = 80 \mu\text{m}$ ) Mach Zehnder interferometer with different NRPS.

other arm. The reason behind such a choice will become clear on later part of

this chapter in the context of push-pull MZI type isolators. So we can immediately conclude from the Eq.3.7 and Eq.3.8 that the nonreciprocal phase shift (NRPS) obtained is equal to  $\theta_N$ . In this case NRPS is defined as difference in phase difference between both arms for forward and backward propagation of light. Analytically calculated transmission spectra of a MZI for different situations can be found in Fig.3.2 having FSR of 8nm ,  $\Delta L = 80 \mu\text{m}$  ,  $\theta_N = 1$  radian and  $\alpha = 0$  for loss less waveguides was assumed. From Fig.3.2 we can see that transmissions are different for the forward and backward propagations. So we can conclude that a nonreciprocal medium could be utilized to realize an optical isolator on a waveguide platform based on a MZI design.

## 3.2 Nonreciprocal MZI based optical isolator

### 3.2.1 Design schemes

From chapter 2 we have already learned that a nonreciprocal phase shifter can be created by bonding or depositing a magneto-optic (MO) material biased with the aid of an external magnetic field. To obtain the required NRPS the magnetic field ( $H$ ) and the light propagation ( $k$ ) should be in perpendicular orientation. Based on this fact two different types of design schemes can be realized as depicted in Fig.3.3. For the scheme shown in Fig.3.3(a) the MO garnet is covering both arms of the MZI symmetrically and an anti-parallel magnetic field is required to bias the magnetic material whereas in Fig.3.3(b) the garnet is bonded also symmetrically on top of the MZI arms but an unidirectional magnetic field is needed. The device based on the first scheme is demonstrated in [20] whereas this work is based on the second scheme which requires an unidirectional mag-

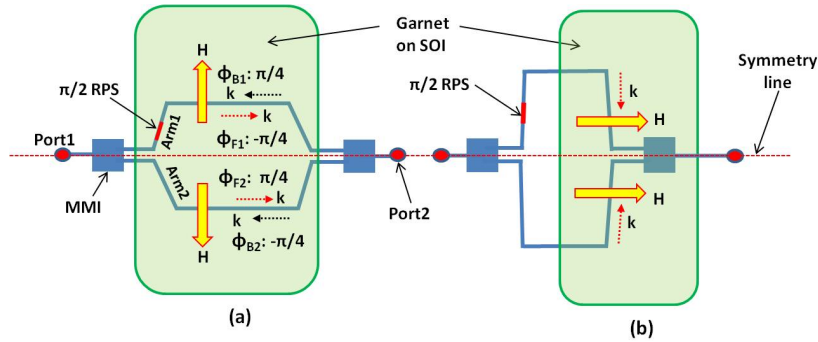


**Figure 3.3:** Schemes of isolator designs for (a) anti-parallel,(b) unidirectional magnetic field.  $H$  is the external magnetic field and  $k$  is the wave/light propagation vector. The arrows indicating the direction of the corresponding vectors. RPS is the reciprocal phase shifter

Path	Arm	RP	NRP	Total phase	Interference
1→2	1	$\pi/2$	$-\pi/4$	$\pi/4$	Constructive
1→2	2	0	$\pi/4$	$\pi/4$	
2→1	1	$\pi/2$	$\pi/4$	$3\pi/4$	Destructive
2→1	2	0	$-\pi/4$	$-\pi/4$	

**Table 3.1:** Total phases at the final ports.

netic field. Important to note that garnet is not totally transparent in telecom wavelengths hence the insertion loss in the structure due to the bonded garnet is relatively high compared to that of an air clad waveguide structure, so the bonded garnet parts on both arms of the MZI should be almost symmetric otherwise unequal loss will limit to attain a high extinction ratio (ER) of the MZI. For the case as shown in Fig.3.3(b) the garnet die should not cover the whole MZI otherwise the net NRPS will be zero for both arms.

The working principle of any of the aforementioned devices can be understood as follows considering the broadband operation. The nonreciprocal phase (NRP) experienced by the light in any arm of the garnet covered MZI under a transverse magnetic field is same in magnitude but with a opposite sign with respect to the other arm. Hence the nomenclature 'Push-Pull' is justified. Push-pull operation helps to shorten the overall device size and also importantly makes the device symmetric with respect to the line drawn through the middle of the MMIs as shown in Fig.3.3. For the sake of simplicity let us assume that the length of the arms of the MZI is designed in such a way that the NRP from any of the arms is  $\pm\pi/4$ , the exact sign depends on the orientation between  $\mathbf{H}$  and  $\mathbf{k}$ . The optical path difference between the arms is designed to obtain a  $\pi/2$  reciprocal phase shift as shown in Fig.3.3(a) between the arms. The NRP for the forward and backward light propagation from arm 1 are designated as  $\phi_{F1}$  and  $\phi_{B1}$  respectively. The same for the case of arm 2 are designated as  $\phi_{F2}$  and  $\phi_{B2}$  respectively. The total phase experiencing by light in any arm for any direction either forward (port 1 to port 2) or backward (port 2 to port 1) is tabulated in Table6.1.

So we can see that forward propagating light in the MZI arms meet with in-phase results in constructive interference at port 2 whereas backward propagating light meet out-of-phase and interferes destructively at port 1. The non-reciprocal phase shift (NRPS) between the forward and backward direction is equal to  $\pi$ . Typical transmission spectrums for a broadband isolators are shown in Fig.3.4 where the RPS is taken as  $\lambda/(4.n_{eff})$  instead of constant  $\pi/2$ .

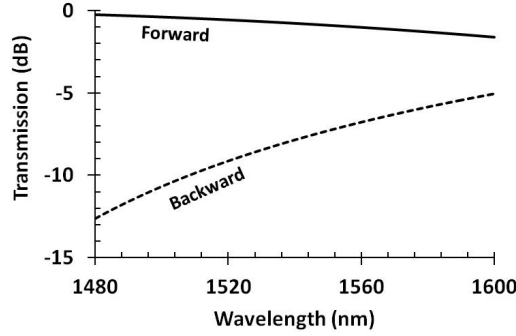


**Figure 3.4:** Illustration of transmission spectra of a broadband Mach Zehnder interferometer with  $NRPS = \pi$  considering lossless waveguides.

### 3.2.2 Analytical calculations of NRPS

To observe any small nonreciprocal effect an unbalanced MZI with a few nanometer of FSR is normally desired instead of a broadband one. To establish the analytical formulation of the NRPS for a MZI where the optical path difference between the MZI arms is  $\Delta L$  can be derive as below. Let us consider the length of arm 1 and arm 2 is  $L_1$  and  $L_2$  respectively.

The phase differences between the arms of the MZI for forward and backward light propagations are given by Eq.3.9 and Eq.3.10 respectively.

$$\theta_F = (\phi_{R1} - |\phi_{F1}|) - (\phi_{R2} + |\phi_{F2}|) \quad (3.9)$$

$$\theta_B = (\phi_{R1} + |\phi_{B1}|) - (\phi_{R2} - |\phi_{B2}|) \quad (3.10)$$

Where  $\phi_{R1}$  and  $\phi_{R2}$  are the reciprocal phase experienced by light in arm 1 and arm 2 respectively. The magnitude of the nonreciprocal phases on each arm are assumed the same. Now let us consider that constructive interference occurs at  $\lambda = \lambda_1$  at port 2 during forward propagation whereas the same happens at  $\lambda = \lambda_2$  during backward propagation at port 1. So,

$$\theta_F(\lambda_1) = \theta_B(\lambda_2) \quad (3.11)$$

$$-(|\phi_{F1}| + |\phi_{F2}| + |\phi_{B1}| + |\phi_{B2}|) = \phi_{R1}(\lambda_2) - \phi_{R2}(\lambda_2) - \phi_{R1}(\lambda_1) + \phi_{R2}(\lambda_1) \quad (3.12)$$

$$NRPS = 2\pi \cdot \Delta L \left( \frac{n_{eff}(\lambda_2)}{\lambda_2} - \frac{n_{eff}(\lambda_1)}{\lambda_1} \right) \quad (3.13)$$

assuming that the nonreciprocal phase shifts are wavelength independent. Negative sign is discarded because it has no significance in the context of phase shift. Let us consider  $\lambda_1 - \lambda_2 = \Delta\lambda$ . Hence,

$$n_{eff}(\lambda_1) = n_{eff}(\lambda_2) + \Delta\lambda \cdot \frac{dn_{eff}}{d\lambda} \quad (3.14)$$

So, from Eq.3.13 we can write

$$NRPS = \frac{2\pi \cdot \Delta L \cdot \Delta \lambda}{\lambda_1 \lambda_2} \left( n_{eff}(\lambda_2) - \lambda_2 \cdot \frac{dn_{eff}}{d\lambda} \right) \quad (3.15)$$

$$NRPS = \frac{2\pi \cdot \Delta L \cdot \Delta \lambda}{\lambda_1 \lambda_2} \cdot n_g(\lambda_2) \quad (3.16)$$

As  $\lambda_1 \approx \lambda_2$ , Eq.3.16 reduces to

$$NRPS = 2\pi \cdot \frac{\Delta \lambda}{FSR} \quad (3.17)$$

with FSR the free spectral range of the MZI. So we can conclude from the Eq.3.17 that to achieve full isolation or a  $\pi$  nonreciprocal phase shift a wavelength shift of half the FSR is required.

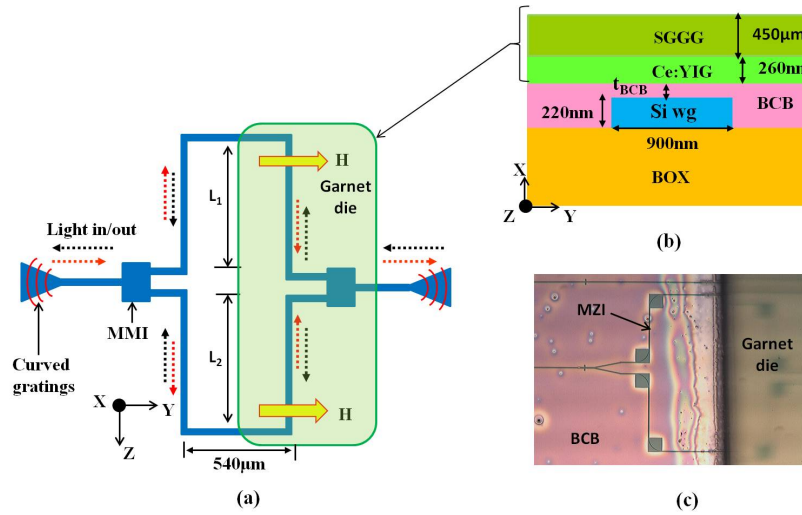


**Figure 3.5:** (a) Schematic top-view diagram of adhesively garnet bonded push-pull MZI for optical isolator, (b) schematic cross-section view of bonded waveguide stack and (c) optical micrograph of garnet bonded MZI.

### 3.3 Adhesively Bonded Garnet on SOI MZI

In this work a piece of garnet containing Cerium substituted Yttrium Iron Garnet (Ce:YIG) on Substituted (Ca, Mg or Zr) Gadolinium Gallium Garnet (SGGG) substrate is adhesively bonded on top of a MZI adopting the scheme shown in

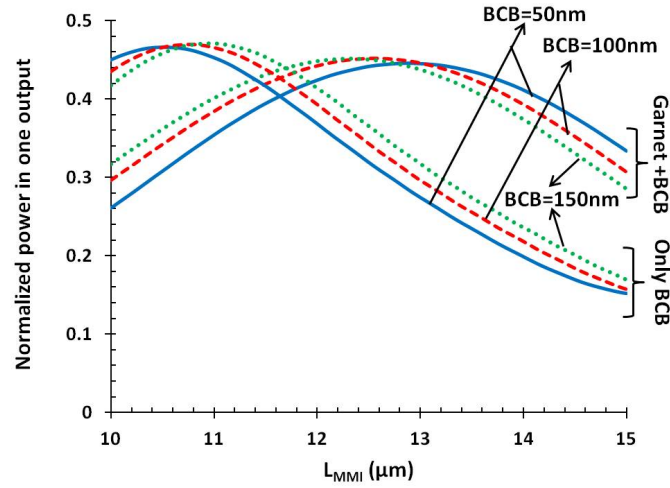


**Figure 3.6:** Efficiency of the designed MMIs as a function of  $L_{MMI}$  for  $W_{MMI} = 4.0\mu\text{m}$  and output waveguide offset of  $1.1\mu\text{m}$  at  $1550\text{ nm}$  wavelength.

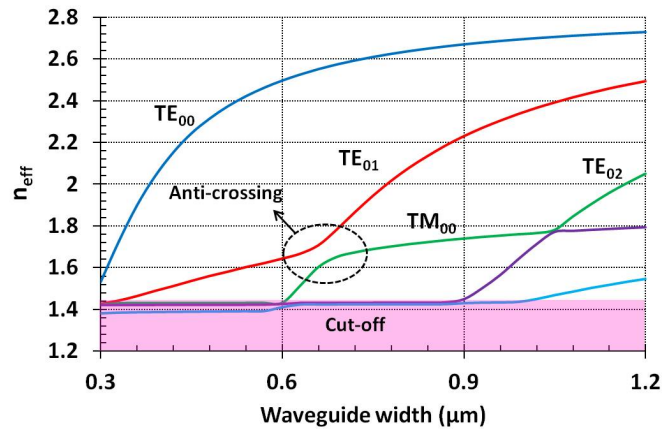


**Figure 3.7:** Variation of effective refractive index as a function of waveguide width for an air clad Si waveguide of thickness  $220\text{ nm}$  at  $1550\text{ nm}$  wavelength.

Fig.3.3(b). The fabrication procedure will be discussed shortly after design details. The details of the designed push-pull type MZI working for an unidirectional magnetic field is presented here. The schematic diagram of the garnet bonded MZI is depicted in Fig.3.5(a) together with a cross-section view of the

garnet bonded waveguide stack in Fig.3.5(b). A part of the garnet covered MZI after the bonding is shown in Fig.3.5(c). The thickness of the Ce:YIG layer on top of the 450  $\mu\text{m}$  thick SGGG layer is measured as 260 nm. The MZI consists of two  $1 \times 2$  multimode interference couplers (MMI), connected by two waveguides of unequal length. The MZI is partly covered by the Ce:YIG/SGGG die. Therefore, the design of the MMI covered by the nonreciprocal material is different from the one which is covered by BCB only. The length of the multimode section ( $L_{MMI}$ ) for the Ce:YIG covered MMI is 13.0  $\mu\text{m}$  whereas it is 11.0  $\mu\text{m}$  for the BCB covered MMI. The width of the multimode section ( $W_{MMI}$ ) and offset between output waveguides are designed as 4.0  $\mu\text{m}$  and 1.1  $\mu\text{m}$  respectively for both types of MMIs. The simulated efficiency of the respective MMIs is presented in Fig.3.6. A curved grating coupler is used to couple light between a single mode fiber and the quasi-TM fundamental mode of a 900 nm wide silicon waveguide [21]. The length difference between the MZI arms is 80  $\mu\text{m}$  which results in a FSR of 7.6 nm. This allows for a clear interpretation of the nonreciprocal phase shift. For a broadband device, equal arm lengths are required (more precisely a  $\pi/2$  reciprocal phase shifter is required in one of the arms). The bend radius was limited to 60  $\mu\text{m}$  to avoid radiation loss in the Ce:YIG covered part of the silicon waveguide. A unidirectional external magnetic field is applied transverse to the light propagation direction to achieve maximum isolation. The total waveguide length  $L = L_1 + L_2$  is measured as the effective length for the interaction of the fundamental TM mode with the Ce:YIG where the magnetic field is oriented perpendicular to the propagation direction. The distance between the BCB covered part and the garnet covered part of the MZI arm is kept about 540  $\mu\text{m}$  to ease the alignment of the garnet chip during the manual bonding procedure.

### 3.3.1 Waveguide design parameters and tolerance study

In this section the design of the waveguide to achieve optimal nonreciprocal phase shift for the transverse magnetic mode (TM) is studied. The important entity here is the effective refractive index ( $n_{eff}$ ) of the bonded waveguide stack. The variation of the effective index as a function of waveguide width for 220 nm thick air clad Si waveguide is shown in Fig.3.7. The same for a BCB plus Ce:YIG clad 220 nm thick Si waveguide is presented in Fig.3.8. To simulate the variation of  $n_{eff}$  as a function of waveguide width for different BCB interlayer thicknesses a waveguide stack similar to Fig.3.5(b) is used.

It is clear from the mode profile that the width for single mode TE (normally 450 nm) is not a suitable choice because in this regime the TM polarization can leak into the Ce:YIG slab. The region shaded in Fig.3.8 is a contemplative choice. The reason behind this choice is very obvious. The  $n_{eff}$  for the fundamental TM

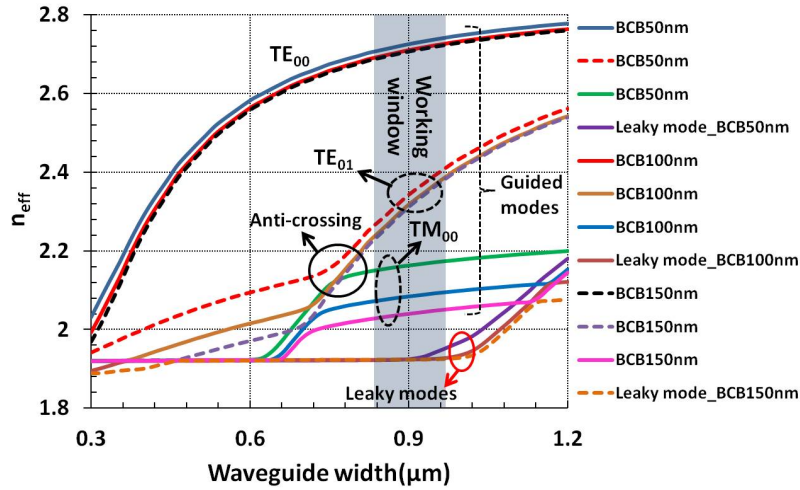


**Figure 3.8:** Variation of effective refractive index as a function of waveguide width for different BCB layer thickness at 1550 nm wavelength with 260 nm thick Ce:YIG layer.

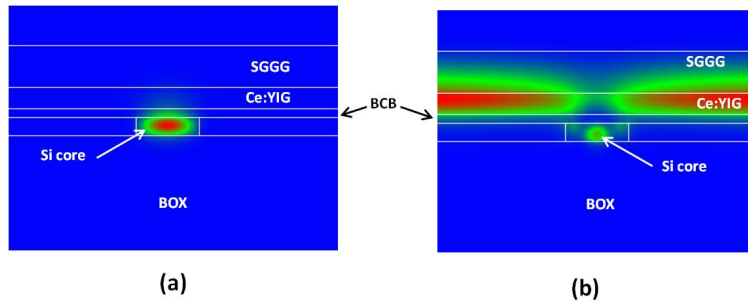


**Figure 3.9:** Intensity plot of (a) the fundamental guided TM in a BCB bonded garnet clad silicon waveguide of width 900 nm and thickness 220 nm and (b) leaky mode in the Ce:YIG layer. In this case a 260 nm thick Ce:YIG layer bonded by 100 nm BCB is assumed.

mode ( $TM_{00}$ ) for a particular BCB thickness is well above the  $n_{eff}$  for the TE slab mode guided in the Ce:YIG slab which is marked as leaky mode also. Therefore no leakage is to be expected. The intensity plots for the  $TM_{00}$  guided mode in the silicon waveguide and the TE slab mode in the Ce:YIG slab are shown in Fig.3.9.

One of the interesting phenomenon observed in the curves presented in

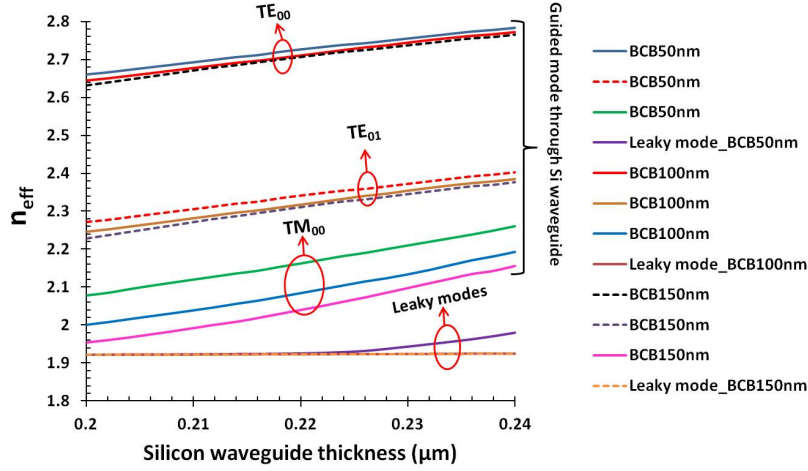


**Figure 3.10:** Variation of effective refractive index as a function of the silicon waveguide thickness for different BCB thicknesses at 1550 nm wavelength with 260 nm thick Ce:YIG layer and waveguide of width 900 nm.

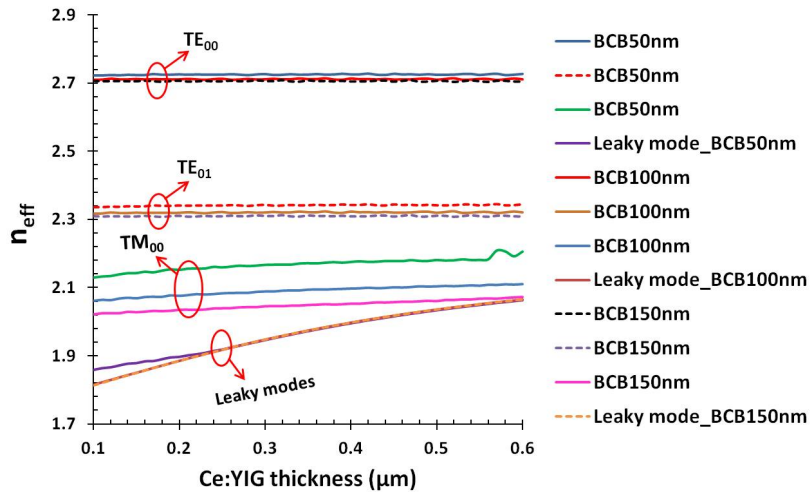


**Figure 3.11:** Variation of effective refractive index as a function of the Ce:YIG thickness for different BCB thicknesses at 1550 nm wavelength for a silicon waveguide of width 900 nm and thickness 220 nm.

Fig.3.8 is that the anti-crossing where the effective indices for the first order guided TE mode ( $TE_{01}$ ) and fundamental guided TM mode ( $TM_{00}$ ) are almost

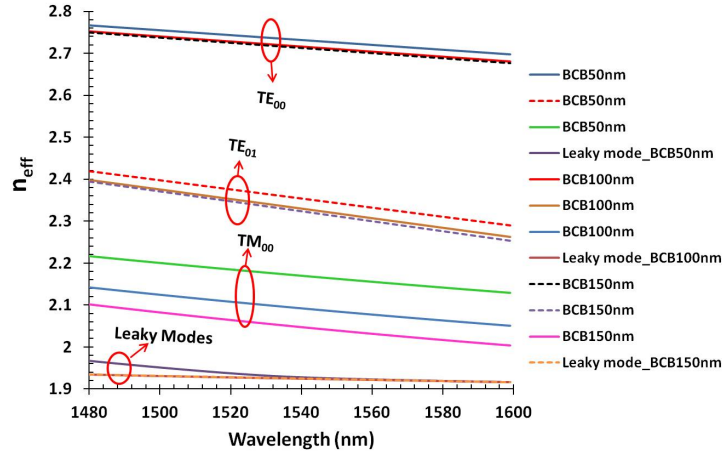


**Figure 3.12:** Spectral dependence of effective refractive index for various BCB thickness with waveguide of width 900 nm and thickness 220 nm, 260 nm thick Ce:YIG.

matched. As a consequence a power exchange between these modes can happen. Therefore in this application we should avoid working in this region. The waveguide stack required for this work shows the first anti-crossing point around a waveguide width of 700 nm according to Fig.3.8. So we have to select the working window sufficiently far away from the anti-crossing points for a reasonable BCB thickness range such as 50-150 nm. An increment of the BCB thickness results in lowering the effective refractive index, which implies that there exists a critical BCB thickness above which  $TM_{00}$  mode will not be guided anymore through the Si waveguide rather will it leak into the Ce:YIG layer.

In actual the fabrication process the thickness of the silicon waveguide could vary  $\pm 10$  nm, so a prior knowledge about the impact of this uncertainty on  $n_{eff}$  is required. The corresponding simulated graphs are presented in Fig.3.10 considering a waveguide of width 900 nm at 1550 nm wavelength and a 260 nm Ce:YIG thickness. Although the higher silicon thickness is better for strong confinement of the  $TM_{00}$  mode in the silicon core, the  $n_{eff}$  of the guided TM modes for different BCB thicknesses are well separated from the TE slab mode of the Ce:YIG slab within the given range of thickness variation.

As the refractive index of the Ce:YIG layer is very close to the  $n_{eff}$  of the  $TM_{00}$  mode, the thickness of the Ce:YIG layer also plays a crucial role. From Fig.3.11 we can see that  $n_{eff}$  for TE slab modes in the Ce:YIG slab increasing relatively faster than that of  $TM_{00}$  modes in the waveguide core, hence a situation arises where both of them are merging together. The BCB thickness is also responsi-

ble for such event. For thicker a Ce:YIG layer a thinner BCB layer is required. Nevertheless a 250-350 nm thick Ce:YIG layer is sufficient to achieve maximum NRPS as already shown in the chapter 2. The spectral dependence of  $n_{eff}$  is not a stringent one considering 900 nm wide and 220 nm thick silicon waveguide with 260 nm thick Ce:YIG layer on top of it bonded by BCB. From Fig.3.12 we can conclude that in the telecom window (S, C, L- bands) the  $TM_{00}$  mode is well guided through the silicon waveguide. It is noteworthy to mention that the transmission loss may vary due to the spectral dependence of absorption coefficient of Ce:YIG or change in confinement.

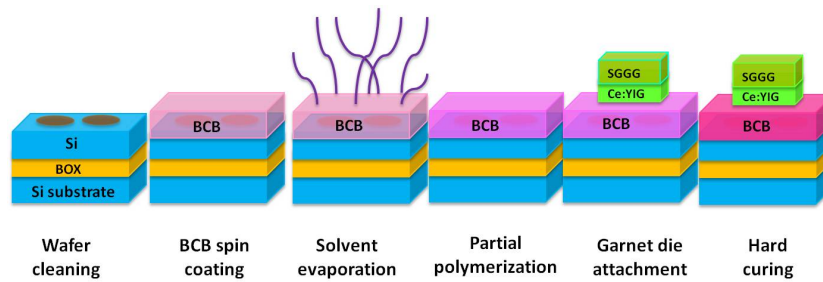


Figure 3.13: Bonding steps.

### 3.4 Fabrication Procedure

The SOI waveguide circuits were fabricated in a CMOS pilot line using 193 nm deep UV lithography via ePIXfab [22] following the procedure detailed by S. Selvaraja *et al.* [23, 24]. A 220 nm thick silicon waveguide layer on a  $2 \mu\text{m}$  buried oxide layer is used. The die-to-wafer bonding procedure is outlined in Fig.3.13. Prior to bonding, the SOI dies are cleaned by a Standard Clean 1 solution (SC-1) which is a mixture of deionized (DI) water,  $\text{NH}_4\text{OH}$ ,  $\text{H}_2\text{O}_2$  in 5:1:1 ratio at temperature of  $70^\circ\text{C}$ . Then adhesion promoter, AP3000 from Dow Chemicals, is spin coated on the SOI. Immediately afterwards mesitylene diluted BCB (1:3v/v) is spin coated at 5000 r.p.m for 50 seconds. Next, the SOI die is kept on a hot plate at  $150^\circ\text{C}$  for 3 minutes to evaporate the remaining mesitylene in the spin coated film. The evaporation time could vary depending on the BCB dilution. Residuals of mesitylene could result in blistering and consequently weak bonding.

The garnet dies were prepared at Tokyo Institute of Technology, Japan using a sputtering deposition technique. The composition of the sputtering target was  $\text{Ce}_1\text{Y}_2\text{Fe}_5\text{O}_{12}$ . The film was deposited on a SGGG substrate by RF sputtering at 50 W power in  $\text{Ar} + \text{O}_2$  ( $\text{Ar} : \text{O}_2 = 99:1$ ,  $\text{Ar} = 6.2 \text{ sccm}$ ) ambience with a substrate

temperature of 690°C. The deposition rate was around 2.2 nm/min. The garnet dies were cleaved in perfect 4 mm × 4 mm squares with a photoresist coated on the Ce:YIG side. In parallel with the SOI cleaning the garnet die is cleaned using acetone and isopropylalcohol (IPA). An ultrasonic cleaning procedure can be followed also for perfect cleaning.

The garnet die of size 4 mm × 4 mm is aligned on top of the MZI. Immediately after the garnet die attached the BCB is still semi-fluidic in nature as the temperature of the hot plat is kept at 150°C, so a slight maneuvering of the garnet die is also feasible to make sure that it covers only half of the MZI according to Fig.3.5(a). After the bonding the temperature of the hot plate gradually brought down to room temperature to achieve a good and sufficiently strong adhesion. But to obtain relatively better bonding the bonded SOI should undergo a final curing step where the sample is cured for about 3 hours following a standard BCB curing recipe. An extensive detailed study regarding BCB bonding technique can be found in [25–29]. In the first set of bonding experiments the garnet dies used were symmetrical in shape on both the Ce:YIG and SGGG sides which brings a extra difficulty to identify the appropriate side meant for bonding with SOI, so starting from cleaning to attachment precautions must be taken in all steps to make sure that the desired side is bonded. However in the second lot garnet chips were prepared as bevel shaped which eliminates this issue.

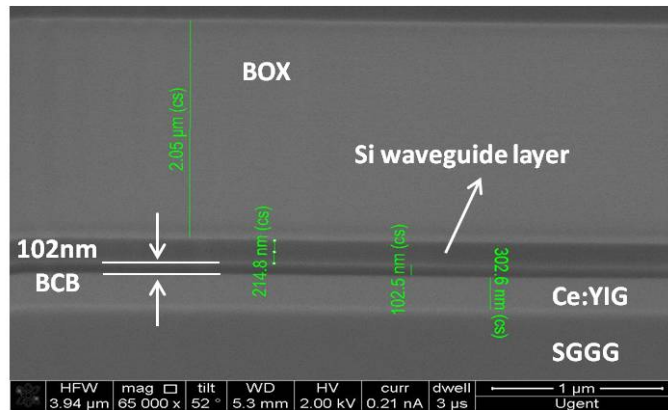


**Figure 3.14:** FIB cross-section of the inverted garnet bonded waveguide stack.

Focused ion beam (FIB) cross-sectioning of the bonded stack to know the actual BCB thickness after the bonding was performed. It was also a challenging task to do without removing the garnet stack from the SOI. Moreover detachment of garnet die could result a faulty BCB thickness measurement because some BCB could still be stuck to the garnet itself. To perform that cross-sectioning the bonded SOI was glued on top of a grinder chuck and then me-

chanically polished to achieve a sufficiently thin SOI (garnet die remain unaffected). The grinding was not parallel to the horizontal plane, rather it was a wedge shaped, so there was an interface between the garnet and the SOI where the thickness of the SOI has been just a few microns. Then the FIB milling was done at that point. The corresponding image is shown in Fig.3.14.

## 3.5 Measurement Details

### 3.5.1 Isolation measurement

In the experiment small Neodymium-alloy (Nd-Fe-B) permanent magnets are used to provide the required transverse magnetic field. The dimensions of a single magnet are  $3\text{ mm} \times 1\text{ mm} \times 1\text{ mm}$ . A stack of three magnets is used to make sure that the magnetic field is almost parallel to the Ce:YIG plane. These three magnets were attached together by magnetic attraction but a strong physical attachment was made by a gluing a tape on top of the three magnets which holds the stack stationary all the times during the measurements. The layout of the experimental setup and the magnet stack is shown in Fig.3.15. Single mode fiber (SMF) is used to carry light from a tunable laser source to the SOI chip and from the SOI chip to a power-meter. The magnetic field is estimated to be strong enough to saturate the Ce:YIG layer. TM light is injected and collected by curved TM grating couplers [21]. Transmission spectra were recorded both for the forward and backward propagation direction to characterize the MZI as an optical isolator. The input and output fibers were interchanged to realize for-

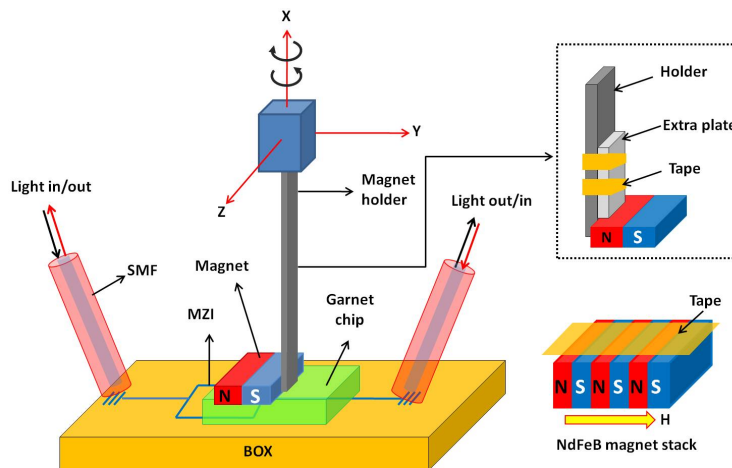


**Figure 3.15:** Artistic impression of the measurement set-up and the magnet stack.

ward and backward light propagations while the magnetic field is kept at a fixed direction. An optical switch could be used here to swap the fibers instead of manual changing of fibers. A holder comprising of three micrometer screws capable of 3D movements was designed to maneuver the magnet stack on top of the garnet chip. The utility of this facility will be understood shortly. The material for the holder was chosen as ferromagnetic so that the magnet stack could stick to it. Experimentally an optical isolation of 25 dB is achieved from the

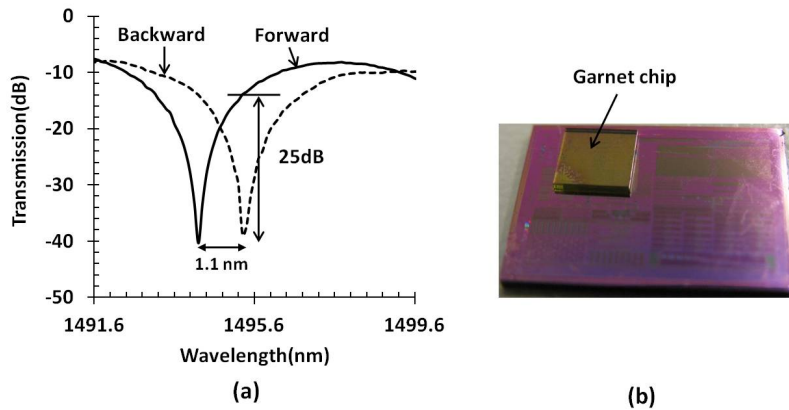


**Figure 3.16:** Sample-I: (a) Normalized MZI transmission spectra for the forward and backward propagation and (b) Picture of the garnet bonded SOI.

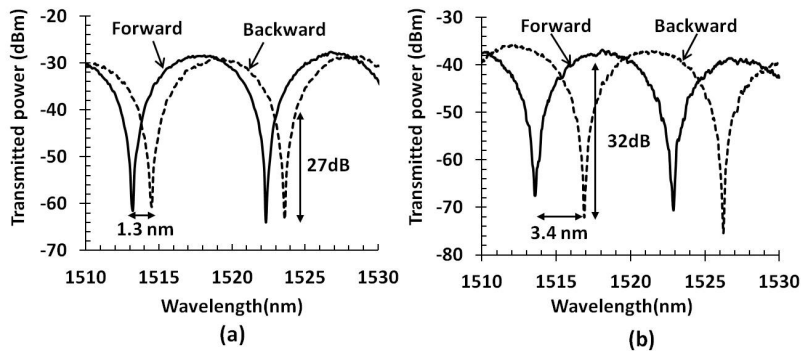


**Figure 3.17:** Sample-II: MZI transmission spectra for the forward and backward propagation (a)  $L = 400 \mu m$  (b)  $L = 920 \mu m$  (not normalized).

sample-I for the first time as depicted on Fig.3.16(a). A spectral shift of 1.1 nm is measured between the forward and backward propagation under the influence

of an external magnetic field. This spectral shift corresponds to an accumulated nonreciprocal phase shift  $\text{NRPS} \cdot L$  of  $52^\circ$ . With  $L = 920 \mu\text{m}$  (for sample-I), this corresponds to a nonreciprocal phase shift between the forward and backward direction of  $0.987 \text{ rad/mm}$  which is consistent with a BCB thickness of  $100 \text{ nm}$  as is clear from Fig.2.6 in chapter 2.

Relatively higher spectral shift and better isolation is achieved from another sample named as sample-II. In this case two MZIs with garnet covered waveguide length different from the sample-I give a NRPS of  $2.4 \text{ rad/mm}$  which means a BCB thickness of  $50\text{-}60 \text{ nm}$  was achieved in this case.

### 3.5.2 Hysteresis analysis

The influence of the applied magnetic field (H) orientation with respect to the propagation direction (k) was also assessed. The result is presented in Fig.3.18 for the sample-I. In the experimental setup the magnet is rotated from  $0^\circ$  to  $360^\circ$  about the x-axis (see Fig.3.15). The rotation of the magnet was carried out away from the Ce:YIG (i.e. by lifting the magnet). For each magnet orientation forward and backward transmission was recorded. The nonreciprocal wavelength shift is taken to be negative when the transmission spectrum for forward propagation is shifted towards longer wavelengths compared to the backward propagation. The wavelength shifts (or NRPS) both for  $0^\circ$  and  $180^\circ$  orientations are very small as compared to  $90^\circ$  and  $270^\circ$  orientations, which is a signature of the Voigt effect.

The variation of the nonreciprocal wavelength shift with respect to  $(h^2 + l^2)^{-3/2}$  is presented in Fig.3.19(a) for the sample-I, where  $h$  is the distance between the garnet die and the magnet and  $2l$  ( $3 \text{ mm}$ ) is the pole to pole distance of the magnet stack. The reason behind choosing  $(h^2 + l^2)^{-3/2}$  as a parameter is that the magnetic field at broadside-on position (it is the position of a point that lies at the center line of a magnet and perpendicular to the magnetic axis) of a bar magnet varies as  $(h^2 + l^2)^{-3/2}$ . The sequence of the measurements is illustrated in the figure. In part 1 of the curve the magnet is oriented perpendicular to the Ce:YIG covered Mach-Zehnder arms (say N-S orientation) and the forward and backward transmission is recorded for each increment of the distance between the magnet and the Ce:YIG. At the remanent point the magnet orientation was rotated  $180^\circ$  to S-N for part 2 of the curve, where the magnet stack approaches the garnet die. The nonreciprocal wavelength shift at the remanent condition is about  $0.5 \text{ nm}$  in this particular device. In part 3 of the curve, the distance between the magnet with S-N orientation and the Ce:YIG die is increased again. Finally, in part 4 of the curve the magnet again switches to N-S and the nonreciprocal wavelength shifts were recorded for each decrement of the distance. The parameter  $(h^2 + l^2)^{-3/2}$  is taken to be positive & negative for

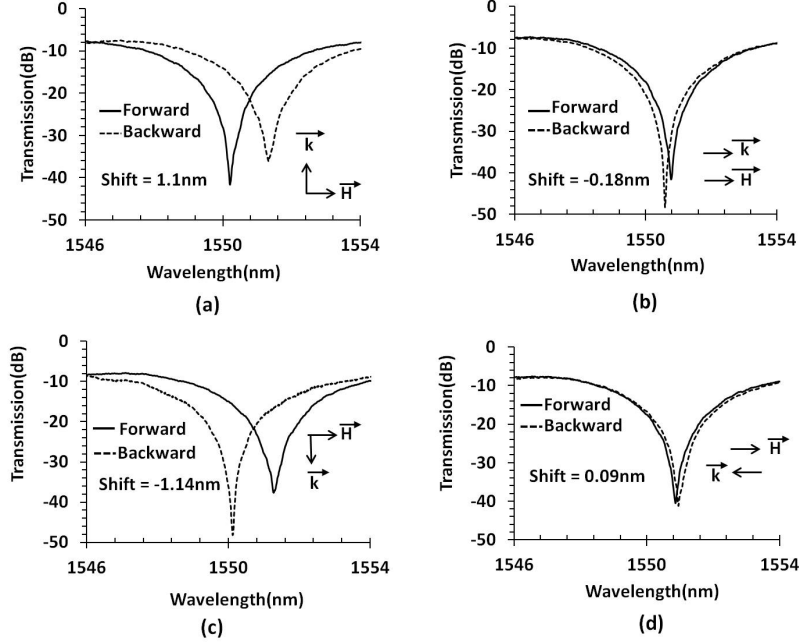


**Figure 3.18:** Normalized transmission spectra of the MZI (sample-I) for different angular orientations of the magnetic field with respect to the light propagation direction: (a)  $90^\circ$ , (b)  $0^\circ$ , (c)  $270^\circ$  and (d)  $180^\circ$ .

N-S & S-N orientations respectively. The magnetization of the Ce:YIG film of thickness 260 nm is also measured by alternating gradient force magnetometer (AGFM) at IMEC using a  $4 \text{ mm} \times 4 \text{ mm}$  garnet die. The magnetization curve of Ce:YIG film is shown in Fig.3.19(b) which is obtained after subtracting the paramagnetic contribution from the SGGG substrate from the overall magnetization curve as measured. Clearly there is a good qualitative agreement between these two curves.

### 3.6 Loss analysis

As can be seen on the transmission spectra, the insertion loss of the Mach-Zehnder structure is 8-9dB at the constructive interference point. Since the obtained nonreciprocal phase shift is less than 180 degrees, the insertion loss at the maximum optical isolation point is around 14dB. This implies that for a high isolation, broadband MZI isolator, a 3.46 times (52 degrees non-reciprocal phase shift versus the requires 180 degree phase shift) longer Ce:YIG/SOI non-reciprocal waveguide section is required.

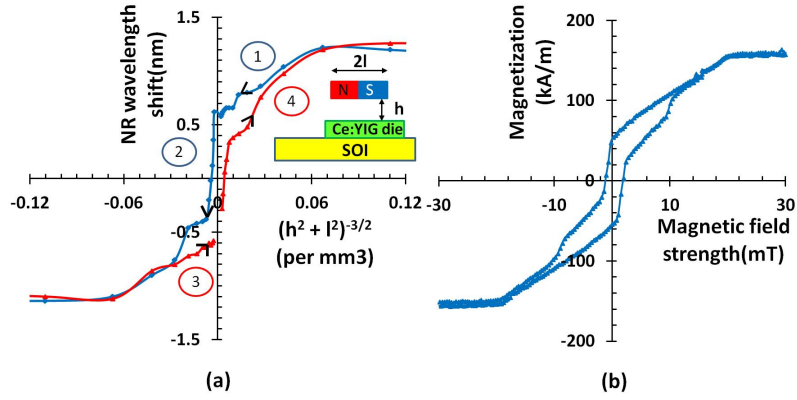


**Figure 3.19:** (a) Nonreciprocal wavelength shift as a function of the  $(h^2 + l^2)^{-3/2}$ , where  $h$  is the distance between the magnet and the Ce:YIG layer and  $2l$  is the distance between the two poles of the magnet stack. Negative values for  $(h^2 + l^2)^{-3/2}$  indicate that the magnet was rotated 180°, (b) magnetization curve of the Ce:YIG layer after subtracting contribution from paramagnetic SGGG substrate.

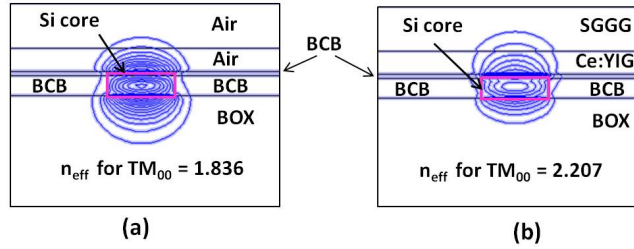


**Figure 3.20:** Contour plots of the  $E_x$  field of the  $TM_{00}$  mode for 900 nm wide and 220 nm silicon waveguides with (a) 50 nm BCB as top cladding and (b) 50 nm BCB plus garnet stack as top cladding.

The relatively high insertion losses of the device are due to a combination of mode mismatch losses at the interface between the plain SOI and the SOI covered with the diced Ce:YIG die (see Fig.3.20) and propagation losses in the Ce:YIG/SOI waveguide structure. The propagation loss of the Ce:YIG/SOI waveguide structure was assessed experimentally by comparing transmission spectra of a Ce:YIG covered SOI waveguide (using a 100 nm BCB bonding layer) and a plain SOI waveguide. The schematic for measurement and the corresponding measurement result is shown in Fig.3.21. The excess loss of the SOI waveguide structure covered by a 2 mm long garnet die is 4 dB compared to plain SOI. Taking into account the theoretical transition losses from Fig. 3.22(a)(2 times 0.8

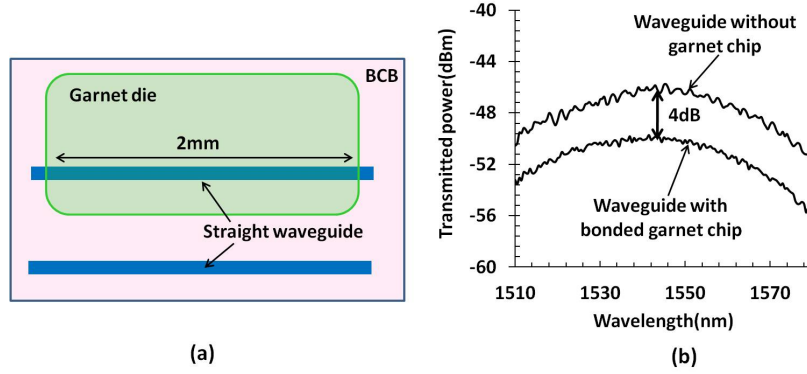


**Figure 3.21:** (a) Schematic diagram for measuring transmission loss and (b) Measured optical transmission for only BCB covered and BCB plus garnet covered straight TM waveguide.

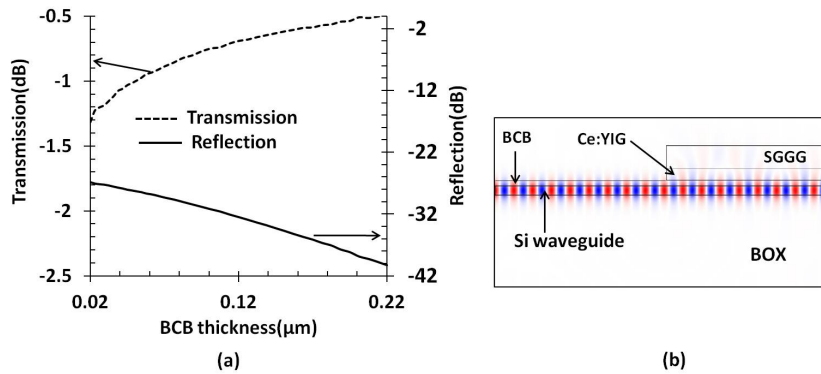


**Figure 3.22:** (a) Simulated insertion loss and reflection at the interface between a plain SOI waveguide and a Ce:YIG on SOI waveguide as a function of BCB bonding layer thickness and (b) field plot of light propagating from a plain BCB covered silicon waveguide to a BCB plus garnet covered silicon waveguide.

dB) this results in a Ce:YIG/SOI waveguide propagation loss of 12 dB/cm in excess of the 2.5 dB/cm propagation loss of a standard SOI waveguide. Fig.3.22(b) shows that the reflection is almost zero from a interface between plain BCB covered SOI and BCB plus garnet covered SOI considering 100 nm of BCB thickness. The cause of this large excess waveguide loss could not be unambiguously identified, but can be attributed to scattering and propagation losses in the Ce:YIG combined with the larger sensitivity of the Ce:YIG/SOI quasi-TM waveguide mode to Ce:YIG surface roughness, due to the slot waveguide field enhance-

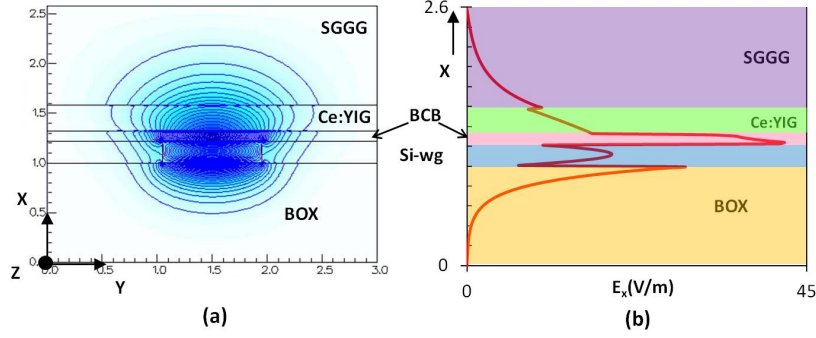


**Figure 3.23:** (a) Contour plot of the  $E_x$  field of the quasi-TM polarized mode and (b) field enhancement in the BCB bonding layer due to a vertical slot waveguide effect.

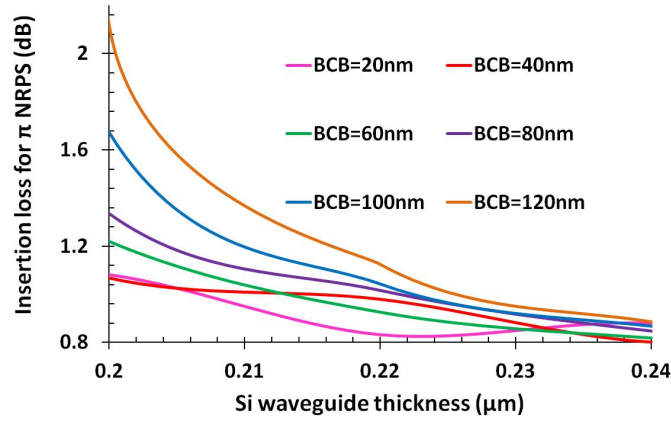


**Figure 3.24:** Estimation of insertion loss from a  $\pi$  nonreciprocal phase shifter for various BCB thickness at 1550 nm wavelength. In this simulation width of 220 nm thick silicon waveguide is 900 nm with a 260 nm thick Ce:YIG layer bonded by BCB. Material loss of Ce:YIG is taken as 60 dB/cm [30].

ment effect in the bonding layer as shown in Fig.3.23. Given the 4 mm $\times$ 4 mm Ce:YIG/SGGG die size in the experimental realization, this results in approximately 4.5mm of Si wire waveguide covered with Ce:YIG. Taking these propagation losses into account, together with the interface losses, this amounts to a total insertion loss of  $2 \times 0.8 \text{ dB} + 14.5 \text{ dB/cm} \times 0.45 \text{ cm}$  or 8.1 dB, which is close to the measured insertion loss. It also means that if the Ce:YIG/SGGG die size was reduced, such as to only cover the arms of the Mach-Zehnder interferom-

eter, while the Ce:YIG/SOI waveguide length inside the MZI interferometer was increased by a factor of 3.46 (to obtain 180 degree nonreciprocal phase shift), the insertion loss could be reduced to  $2 \times 0.8 \text{ dB} + 14.5 \text{ dB/cm} \times 3.46 \times 0.46 \text{ mm}$  or 3.9 dB. Moreover the garnet die used in this demonstration was as-deposited having a material loss of 60 dB/cm as reported in [30]. The material loss can be reduced upto 30 dB/cm by annealing the as-deposited garnet. The estimation of insertion loss from a  $\pi$  nonreciprocal phase shifter using an annealed garnet is shown in Fig.3.24. It is clear from Fig.3.24 that the insertion loss from the  $\pi$  nonreciprocal phase shifter is about 1 dB for 100 nm thick BCB layer.

### 3.7 Conclusion

In this chapter we have demonstrated an optical isolator integrated on the Silicon-on-insulator platform by adhesively bonding a Ce:YIG/SGGG die to a silicon waveguide circuit. The nonreciprocal phase shift (NRPS) or nonreciprocal wavelength shift has been studied both for transverse and longitudinal magnetic fields with respect to light propagation direction. The hysteresis behavior of the Ce:YIG film is also studied. While optical isolation and insertion loss of the device still can be optimized this approach opens a promising path towards the heterogeneous integration of an optical isolator with semiconductor lasers on the SOI platform.

### References

- [1] N. Takato, T. Kominato, A. Sugita, K. Jinguji, H. Toba, and M. Kawachi. *Silica-based integrated optic Mach-Zehnder multi/demultiplexer family with channel spacing of 0.01-250 nm*. IEEE Journal on Selected Areas in Communications, 8(6):1120–1127, Aug., 1990.
- [2] R. McDougall, G. Maxwell, R. Harmon, A. Poustie, L. Rivers, I. Lealman, and P. Townley. *40Gb/s Hybrid Integrated All-optical SOA-MZI Regenerator Incorporating Separately Optimised SOAs, On-chip Time Delays and WDM Combiners*. In ECOC 2006. European Conference on Optical Communications, pages 1–2, Sept., 2006.
- [3] K. Nara, H. Urabe, J. Hasegawa, N. Matsubara, and H. Kawashima. *MZI based 8-channel wideband WDM filter array with low loss ripple and high isolation using silica-based PLC [planar lightwave circuits]*. In Optical Fiber Communication Conference. Technical Digest. OFC/NFOEC, volume 4, pages 3 pp. Vol. 4–, March, 2005.

- [4] Sotirios Papaioannou, Dimitrios Kalavrouziotis, Konstantinos Vyrsokinos, Jean-Claude Weeber, Karim Hassan, Laurent Markey, Alain Dereux, Ashwani Kumar, Sergey I. Bozhevolnyi, Matthias Baus, Tolga Tekin, Dimitrios Apostolopoulos, Hercules Avramopoulos, and Nikos Pleros. *Active plasmonics in WDM traffic switching applications*. Scientific Reports, 2:–, 2012.
- [5] H.Y. Wong, W. K. Tan, A.C. Bryce, J.H. Marsh, J.M. Arnold, and M. Sorel. *Integrated asymmetric Mach-Zehnder interferometer WDM (de)multiplexer using quantum well intermixing*. In International Conference on Indium Phosphide and Related Materials, pages 28–30, May, 2005.
- [6] Christoph Hauger, Marco Wörz, and Thomas Hellmuth. *Interferometer for Optical Coherence Tomography*. Applied Optics, 42(19):3896–3902, Jul 2003.
- [7] C Flueraru, H Kumazaki, S Sherif, S Chang, and Y Mao. *Quadrature Mach-Zehnder interferometer with application in optical coherence tomography*. Journal of Optics A Pure and Applied Optics, 9(4):L5–L8, 2007.
- [8] Youxin Mao, Sherif Sherif, Costel Flueraru, and Shoude Chang. *3x3 Mach-Zehnder interferometer with unbalanced differential detection for full-range swept-source optical coherence tomography*. Applied Optics, 47(12):2004–2010, 2008.
- [9] Franz Brosinger, Herbert Freimuth, Manfred Lacher, Wolfgang Ehrfeld, Erk Gedig, Andreas Katerkamp, Friedrich Spener, and Karl Cammann. *A label-free affinity sensor with compensation of unspecific protein interaction by a highly sensitive integrated optical Mach-Zehnder interferometer on silicon*. Sensors and Actuators B: Chemical, 44(1):350–355, 1997.
- [10] Shih-Hsin Hsu and Yang-Tung Huang. *A Novel Mach-Zehnder Interferometer Based on Dual-ARROW Structures for Sensing Applications*. J. Lightwave Technol., 23(12):4200, Dec 2005.
- [11] F J Blanco, M Agirregabiria, J Berganzo, K Mayora, J Elizalde, A Calle, C Dominguez, and L M Lechuga. *Microfluidic-optical integrated CMOS compatible devices for label-free biochemical sensing*. Journal of Micromechanics and Microengineering, 16(5):1006, 2006.
- [12] Francisco Prieto, B Sepulveda, A Calle, Andreu Llobera, Carlos Domínguez, Antonio Abad, A Montoya, and Laura M Lechuga. *An integrated optical interferometric nanodevice based on silicon technology for biosensor applications*. Nanotechnology, 14(8):907, 2003.

- [13] Andrea Crespi, Yu Gu, Bongkot Ngamsom, Hugo JWM Hoekstra, Chaitanya Dongre, Markus Pollnau, Roberta Ramponi, Hans H van den Vlekkert, Paul Watts, Giulio Cerullo, et al. *Three-dimensional Mach-Zehnder interferometer in a microfluidic chip for spatially-resolved label-free detection*. *Lab on a Chip*, 10(9):1167–1173, 2010.
- [14] Adam L Washburn and Ryan C Bailey. *Photonics-on-a-chip: recent advances in integrated waveguides as enabling detection elements for real-world, lab-on-a-chip biosensing applications*. *Analyst*, 136(2):227–236, 2010.
- [15] Genni Testa, Yujian Huang, Pasqualina M. Sarro, Luigi Zeni, and Romeo Bernini. *High-visibility optofluidic Mach-Zehnder interferometer*. *Opt. Lett.*, 35(10):1584–1586, May 2010.
- [16] B Sepúlveda, J Sánchez del Río, M Moreno, FJ Blanco, K Mayora, Carlos Domínguez, and Laura M Lechuga. *Optical biosensor microsystems based on the integration of highly sensitive Mach-Zehnder interferometer devices*. *Journal of optics A: pure and applied optics*, 8(7):S561, 2006.
- [17] B Sepúlveda, G Armelles, and Laura M Lechuga. *Magneto-optical phase modulation in integrated Mach-Zehnder interferometric sensors*. *Sensors and Actuators A: Physical*, 134(2):339–347, 2007.
- [18] A. Densmore, D.-X. Xu, P. Waldron, S. Janz, P. Cheben, J. Lapointe, A. Delage, B. Lamontagne, J.H. Schmid, and E. Post. *A Silicon-on-Insulator Photonic Wire Based Evanescent Field Sensor*. *IEEE Photonics Technology Letters*, 18(23):2520–2522, Dec.1, 2006.
- [19] K. Benaissa and A. Nathan. *IC compatible optomechanical pressure sensors using Mach-Zehnder interferometry*. *IEEE Transactions on Electron Devices*, 43(9):1571–1582, Sep., 1996.
- [20] Yuya Shoji, Tetsuya Mizumoto, Hideki Yokoi, I-Wei Hsieh, and Richard M. Osgood. *Magneto-optical isolator with silicon waveguides fabricated by direct bonding*. *Applied Physics Letters*, 92(7):071117, 2008.
- [21] Diedrik Vermeulen, Karel Van Acoleyen, Samir Ghosh, Wout De Cort, Nebiyu Adello Yebo, Elewout Hallynck, Katrien De Vos, Peter Debackere, Pieter Dumon, Wim Bogaerts, et al. *Efficient tapering to the fundamental quasi-TM mode in asymmetrical waveguides*. *European Conference on Integrated Optics (ECIO)*, United Kindom, 2010.
- [22] [www.epixfab.eu](http://www.epixfab.eu).

- [23] S.K. Selvaraja, P. Jaenen, W. Bogaerts, D. Van Thourhout, P. Dumon, and R. Baets. *Fabrication of Photonic Wire and Crystal Circuits in Silicon-on-Insulator Using 193-nm Optical Lithography*. *Journal of Lightwave Technology*, 27(18):4076–4083, Sept.15,2009.
- [24] Shankar Kumar Selvaraja. *Wafer-Scale Fabrication Technology for Silicon Photonic Integrated Circuits*. PhD thesis, Universiteit Gent, 2011.
- [25] Gunther Roelkens. *Heterogeneous III-V/Silicon Photonics: Bonding Technology and Integrated Devices*. PhD thesis, Universiteit Gent, 2007.
- [26] Stevan Stankovic. *Stevan Stankovic, Hybride III-V/Si-DFB-lasers gebaseerd op polymeerbondingstechnologie, Hybrid III-V/Si DFB Lasers Based on Polymer Bonding Technology*. PhD thesis, Universiteit Gent, 2013.
- [27] G. Roelkens, D. Van Thourhout, and R. Baets. *Ultra-thin benzocyclobutene bonding of III-V dies onto SOI substrate*. *Electronics Letters*, 41(9):561–562, April,2005.
- [28] J. Brouckaert, G. Roelkens, D. Van Thourhout, and R. Baets. *Thin-Film III-V Photodetectors Integrated on Silicon-on-Insulator Photonic ICs*. *Journal of Lightwave Technology*, 25(4):1053–1060, April,2007.
- [29] S. Keyvaninia, M. Muneeb, S. Stanković, P. J. Van Veldhoven, D. Van Thourhout, and G. Roelkens. *Ultra-thin DVS-BCB adhesive bonding of III-V wafers, dies and multiple dies to a patterned silicon-on-insulator substrate*. *Opt. Mater. Express*, 3(1):35–46, Jan 2013.
- [30] Toshihiro Shintaku and Takehiko Uno. *Preparation of Ce-Substituted Yttrium Iron Garnet Films for Magneto-Optic Waveguide Devices*. *Japanese Journal of Applied Physics*, 35(Part 1, No. 9A):4689–4691, 1996.



# 4

## Asymmetric Arm Width Mach-Zehnder Interferometer Isolator

**I**N the previous chapter a push-pull MZI type optical isolator is discussed. In this chapter also a MZI type isolator design will be elaborated in detail. However the MZI in this case is different from the previous one. The design is based on the different NRPS experienced by both arms of the interferometer, which have a different waveguide width. Using the same adhesive bonding approach as discussed in the previous chapter we demonstrate an optical isolator integrated on a SOI waveguide platform. Simulation of NRPS versus silicon waveguide width is shown here for several different BCB bonding layer thicknesses for various silicon waveguide thicknesses and for a particular Ce:YIG/SGGG stack. A scanning electron microscopy image of the bonded device is shown to confirm the BCB thickness as well as the silicon waveguide thickness. Then an in-depth comparative study between the designed and the fabricated device is presented. Variation of NRPS as a function of MZI arm lengths in the presence of an external magnetic field is measured. 11 dB of isolation is experimentally obtained for a device having a footprint of  $1.5 \text{ mm} \times 4 \text{ }\mu\text{m}$ . Towards the end a theoretical fitting with measured data is presented to retrieve some important parameters of the design. Finally a conclusion is drawn by stat-

ing the possible improvements of the design to achieve better performance with respect to isolation as well as insertion loss.

## 4.1 Isolator design

The conventional MZI-based isolators described in [1–4] are constructed by connecting two multimode interference (MMI) couplers by two silicon waveguides of identical width and work on the basis of the opposite NRPS experienced by TM light propagating through the garnet covered waveguides (known as push-pull operation). Our proposed device also consists of two MMIs, which are however connected by two silicon wire waveguides of different width. Since both waveguides have a different width, they experience a different NRPS in a unidirectional magnetic field oriented identically in both waveguides, and hence a net non-reciprocal phase shift between both arms can be achieved. The device layout is shown in Fig.4.1. A similar approach using different cladding materials to induce a net non-reciprocal phase shift was presented in [5]. As can be seen, compact isolator structures can be realized this way. A ferrimagnetic 260 nm thick Ce:YIG layer on a 450  $\mu\text{m}$  thick SGGG substrate is bonded on top of the MZI as shown in Fig.4.2.

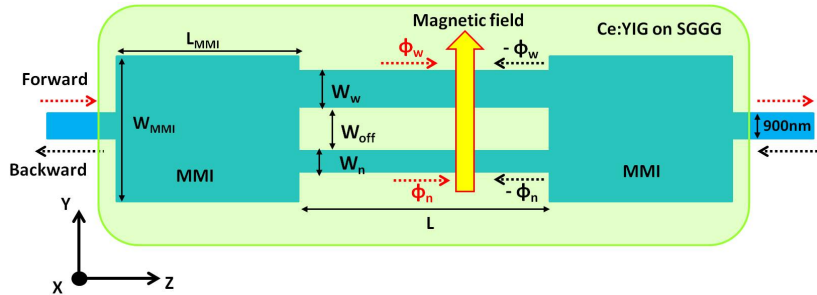


**Figure 4.1:** Layout of the proposed isolator using a Mach-Zehnder interferometer design.

## 4.2 Analytical calculations

The proposed device works on the basis of a differential nonreciprocal phase shift (DNRPS) when a magneto-optic garnet is bonded on top of the MZI as depicted on Fig.4.1 with the aid of an external magnetic field. In this section we establish the analytical formulation to calculate the DNRPS from the measured nonreciprocal spectral shift.



$$n_{eff}(\lambda_1, W_n) = n_{eff}(\lambda_2, W_n) + \Delta\lambda \cdot \frac{dn_{eff}(W_n)}{d\lambda} \quad (4.7)$$

in which  $\lambda_1 - \lambda_2 = \Delta\lambda$  is the nonreciprocal spectral shift between forward and backward light propagation. Substituting Eq.4.6 and Eq.4.7 into the Eq.4.5 we can write

$$\begin{aligned} DNRPS &= \frac{2\pi \cdot L \cdot \Delta\lambda}{\lambda_1 \cdot \lambda_2} \left[ \left( n_{eff}(\lambda_2, W_w) - \lambda_2 \cdot \frac{dn_{eff}(W_w)}{d\lambda} \right) \right. \\ &\quad \left. - \left( n_{eff}(\lambda_2, W_n) - \lambda_2 \cdot \frac{dn_{eff}(W_n)}{d\lambda} \right) \right] \\ &= \frac{2\pi \cdot L \cdot \Delta\lambda}{\lambda_1 \cdot \lambda_2} \left[ n_g(W_w, \lambda_2) - n_g(W_n, \lambda_2) \right] \\ &= 2\pi \cdot L \cdot \Delta n_g(\lambda_2) \frac{\Delta\lambda}{\lambda_1 \cdot \lambda_2} \\ &= 2\pi \cdot \frac{\Delta\lambda}{FSR} \end{aligned} \quad (4.8)$$

where the free spectral range (FSR) of this type of MZI is given by  $FSR = \frac{\lambda^2}{L \cdot \Delta n_g}$ . It is noteworthy to mention that  $n_g$  is the group index of the corresponding waveguide which depends on the wavelength of the propagating light and the width of the corresponding waveguide. Since  $\Delta\lambda$  is very small we can write  $\lambda_1 = \lambda_2 = \lambda$  and hence  $\lambda_1 \cdot \lambda_2 \approx \lambda^2$ . Therefore the DNRPS per unit length can be written as:

$$\Delta NRPS = DNRPS/L = 2\pi \cdot \frac{\Delta\lambda}{FSR \times L} \quad (4.9)$$

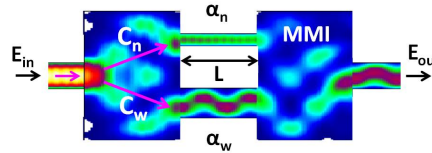


**Figure 4.3:** Illustration of simulated intensity profile of the designed MZI.

Now let us deduce the analytical formula for the extinction ratio (ER) of the MZI. Let us assume that the fundamental optical mode with amplitude  $E_{in}$  is injected at the input waveguide of one of the MMIs and  $E_{out}$  is the amplitude of the fundamental optical mode at the output of the system as shown in Fig.4.3.  $C_w^2$  and  $C_n^2$  are the power splitting coefficients to the wider and narrower arm respectively. The electric fields immediately after the multimode section of one of the MMIs can be written as  $C_w \cdot E_{in}$  and  $C_n \cdot E_{in}$  respectively. After traversing a length  $L$  the corresponding fields are experiencing an extra exponential term related to the loss of the respective waveguides, besides a phase term. Hence

the electric fields besides a phase term just before the second MMI are given as  $C_w.E_{in}exp(-\frac{\alpha_w}{2}.L)$  and  $C_n.E_{in}exp(-\frac{\alpha_n}{2}.L)$  respectively, where  $\alpha_w$  and  $\alpha_n$  are defined as the propagation losses of the corresponding waveguides per unit length. So the output electric fields at the constructive and the destructive interference points can be expressed as

$$E_{out,C} = C_w^2.E_{in}.exp(-\frac{\alpha_w}{2}.L) + C_n^2.E_{in}.exp(-\frac{\alpha_n}{2}.L) \quad (4.10)$$

$$E_{out,D} = C_w^2.E_{in}.exp(-\frac{\alpha_w}{2}.L) - C_n^2.E_{in}.exp(-\frac{\alpha_n}{2}.L) \quad (4.11)$$

The ER can be defined as

$$\begin{aligned} ER &= 10 \log \frac{T_{out,C}}{T_{out,D}} \\ &= 20 \log \left| \frac{E_{out,C}}{E_{out,D}} \right| \\ &= 20 \log \left| \frac{1 + R.exp(-\frac{\Delta\alpha}{2}.L)}{1 - R.exp(-\frac{\Delta\alpha}{2}.L)} \right| \end{aligned} \quad (4.12)$$

Where  $T_{out,C} = |E_{out,C}|^2$ ,  $T_{out,D} = |E_{out,D}|^2$ ,  $R = (\frac{C_n}{C_w})^2$  and  $\Delta\alpha = \alpha_n - \alpha_w$ .

### 4.3 Nonreciprocal phase shifter design

The theoretical calculation of the nonreciprocal phase shift (NRPS) for a slab waveguide and strip waveguide of rectangular geometry has already been discussed in Chapter 2. In this section NRPS is recalculated for trapezoidal type waveguide cross-sections rather than rectangular using the same perturbation formula as mentioned in Chapter 2. The waveguide geometry is depicted in Fig.4.4(a) as used for all the cases. In the actual fabrication the waveguide side walls turned out to be slanted making an angle of  $79^\circ$  with the horizontal plane (see Fig.4.4(a)). More information regarding the nanophotonic waveguide fabrication and parameter variations can be found here [6, 7]. So the top and bottom widths of the respective waveguides differ by approximately 80 nm for 210-230 nm silicon thickness. The top width of the waveguide is termed  $W_t$ . The bottom width of the waveguide is  $W_b = (W_t + 2 \times 40)$  nm. A finite difference method (FDM) existing in Fimmwave software [8] is adopted for all the simulations at 1500 nm wavelength. The variation of the NRPS with wavelength can be ignored. The resolution  $n_x$  along the waveguide thickness is 4 nm whereas  $n_y$  along the waveguide width is 10 nm. The BCB on top of the waveguide is assumed as the variable parameter called  $t_{BCB}$ . The dependence of the NRPS on waveguide width is shown in Fig.4.4(b) and Fig.4.5(a-b) for silicon thicknesses 210 nm, 220 nm and 230 nm respectively for various BCB thicknesses at 1500

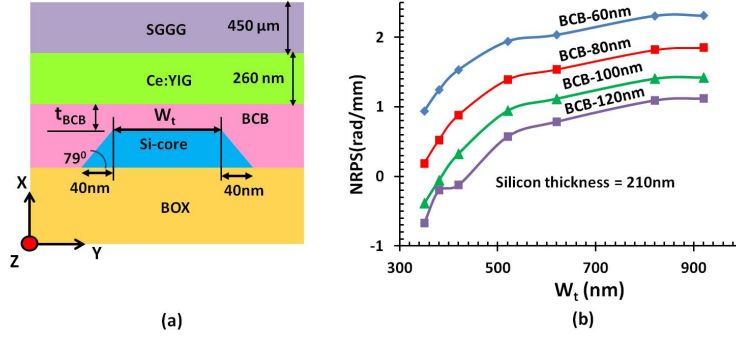


**Figure 4.4:** (a) Cross-section view of the garnet bonded trapezoidal silicon waveguide (b) NRPS vs.  $W_t$  for 210 nm thick silicon at 1500 nm wavelength.

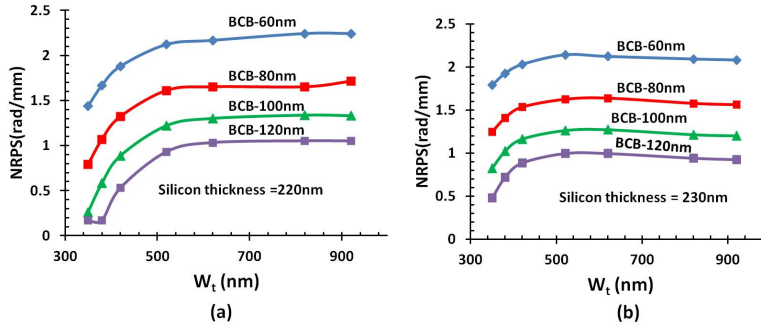


**Figure 4.5:** NRPS vs.  $W_t$  for (a) 220 nm (b) 230 nm thick silicon waveguide at 1500 nm wavelength.

nm wavelength. Clearly we can see that the value of NRPS increases for an increment of the waveguide width upto a certain width for any BCB thickness and then saturates. Therefore a substantial differential NRPS ( $\Delta$ NRPS) can be achieved if the arms of the MZI are designed accordingly. One interesting aspect of this kind of MZI design is that the NRPS starts to attain negative values in the narrower arm below some critical width for a given BCB thickness. The reason behind such behavior can be attributed to the alternation of sign of one of the important electric field components responsible for the NRPS.

One important issue should be mentioned, namely that the narrowing waveguide width renders the TM mode more vulnerable to leakage into the Ce:YIG slab as we have already shown in the previous chapter in the context of the nonreciprocal phase shifter design.  $\Delta$ NRPS between waveguides of top widths ( $W_t$ ) 350 nm and 850 nm for various BCB thicknesses is presented in

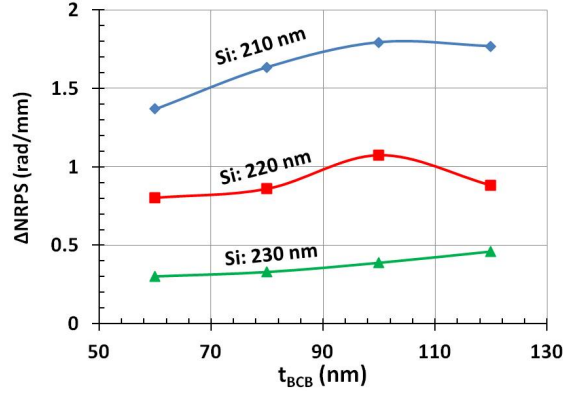


**Figure 4.6:**  $\Delta$ NRPS between waveguides of width ( $W_t = 350$  nm,  $W_b = 430$  nm) and ( $W_t = 850$  nm,  $W_b = 930$  nm) as a function of  $t_{BCB}$  for various silicon thicknesses at 1500 nm.

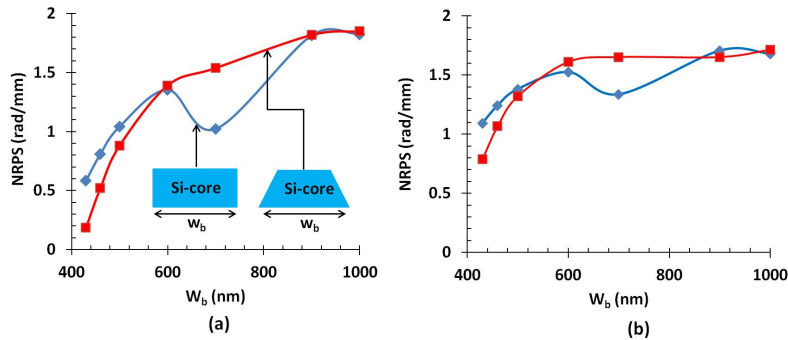


**Figure 4.7:** Influence of waveguide cross-section on NRPS as function of  $W_b$  for (a) 210 nm (b) 220 nm thick silicon waveguide at 1500 nm wavelength with 80 nm thick BCB between Si waveguide and 260 nm thick Ce:YIG layer. In this case  $W_t$  is varied as  $W_t = (W_b - 2 \times 40)$  nm.

Fig.4.6. Lowering the silicon thickness results in an increment in  $\Delta$ NRPS for a particular BCB thickness. The influence of waveguide geometry on NRPS is depicted in Fig.4.7. In this case two waveguide cross-sections are considered one as rectangle and the other one as trapezoid. The dip in NRPS for the case of rectangular waveguide around 700 nm waveguide width is because of hybrid nature of TM mode.

## 4.4 MMI design details

The important component of the device is the multimode interference (MMI) coupler connected to two output arms of different width. The MMIs are designed for having a bonded garnet layer on top of the waveguides. This relaxes the critical alignment requirements on the positioning of the Ce:YIG/SGGG dies, since the complete interferometer can be covered with the garnet. This design is chosen over an MMI design with identical output widths and a taper section in one arm due to the fact that during the tapering between a 1000 nm and 500 nm wide waveguide, a TE/TM mode anti-crossing, due to the vertical asymmetry in the layer stack, results in substantial power loss [9]. The length and width of the multimode section of the MMI are designated as  $L_{MMI}$  and  $W_{MMI}$  respectively in a  $t_{Si}$  thick silicon waveguide geometry. The power splitting ratio

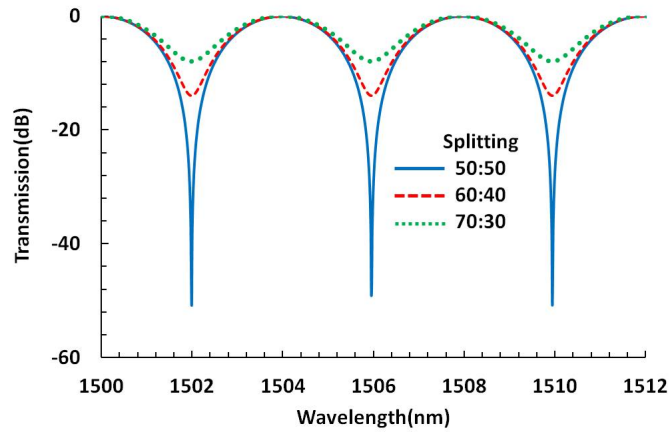


**Figure 4.8:** Analytical calculation of transmission of the MZI with dissimilar arm widths for three different splitting ratios considering lossless waveguides.

of this MMI has a big impact on the extinction ratio (ER) of the MZI and hence on the isolation as well. An analytical calculation is presented in Fig.4.8 to show the impact of power splitting ratio on the ER. From Fig.4.8 it is straight forward to understand the fact that perfect 3 dB couplers will provide highest ER. Hence a rigorous study of all the parameters related to the MMI are required.

To study the performance of the MMI as a function of different parameters the width of a wider and narrower output waveguide of the MMI are considered as  $W_w$  and  $W_n$  respectively with an offset of  $W_{off}$  between the outputs. The width of the input waveguide is 900 nm. The splitting efficiency of the MMI as a function of  $L_{MMI}$  for different BCB thicknesses is simulated. The corresponding

results are presented in Fig.4.9 for a 220 nm thick silicon waveguide layer at 1500 nm wavelength with a garnet stack on top of the waveguide.  $L_{MMI} = 12.5 \mu\text{m}$  is the suitable choice for a BCB thickness between 50 nm and 150 nm. Now the

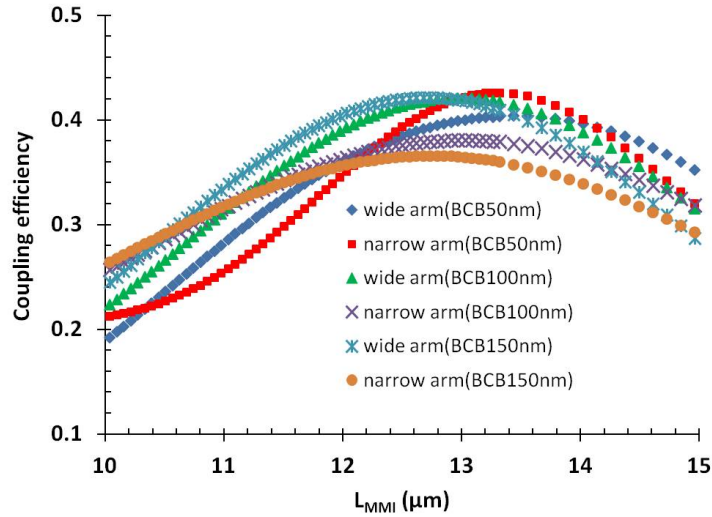


**Figure 4.9:** Normalized MMI power coupling/splitting efficiency vs.  $L_{MMI}$  for various BCB thicknesses at 1500 nm wavelength. Power coupling/splitting efficiency of a MMI arm is defined as the power on that arm divided by total power. In this case total power is equal to unity.

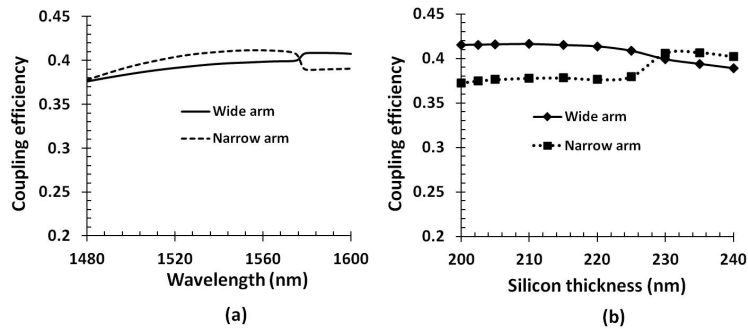


**Figure 4.10:** (a) Spectral dependence of normalized splitting efficiency of the MMI for 50 nm BCB and  $t_{Si} = 220 \text{ nm}$  (b) MMI splitting efficiency vs.  $t_{Si}$  for 100 nm BCB.  $L_{MMI} = 12.5 \mu\text{m}$  for both the cases.

spectral dependence of the designed MMI is examined for a given width and

length of the MMI section with fixed top cladding layers. Fig.4.10(a) shows that the designed MMI works as a broadband device. For all the simulations  $W_{MMI} = 4.0 \mu\text{m}$ , thickness of Ce:YIG = 260 nm,  $W_w = 1000 \text{ nm}$ ,  $W_n = 500 \text{ nm}$ ,  $W_{off} = 1.25 \mu\text{m}$ . The waveguide thickness is also a less influencing parameter on the performance of the designed MMI as depicted in Fig.4.10(b).

## 4.5 Fabrication and Measurements

The details about the SOI photonic integrated circuit fabrication and the bonding procedure are already described in Chapter 3, which are the same in this case. Four MZIs of varying lengths are covered by the same garnet die (size  $2 \text{ mm} \times 2 \text{ mm}$ ) to obtain the optimally performing device with high isolation and low insertion loss. The schematic diagram of the bonded MZIs is shown in Fig.4.11. The length ( $L$ ) of the MZIs is 1.4875 mm, 0.9875 mm, 0.4875 mm

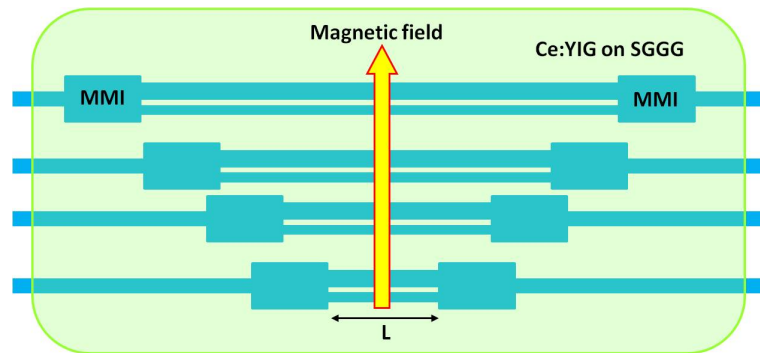


**Figure 4.11:** Schematic diagram of MZIs of varying lengths bonded by same garnet chip operating at unidirectional transverse magnetic field.

and 0.1875 mm whereas the width of each individual MZI is only  $4 \mu\text{m}$  (i.e the width of the multimode section of the MMI). The set-up and magnet used for the measurements are the same as described in previous chapter. TM light is injected and collected by curved TM grating couplers [9] designed at both ends of the MZIs. The grating-to-grating distance is designed to be about 4 mm, which is sufficient for the alignment of a small bar magnet stack in between the single mode input and output fibers. Optical transmission for both the forward and backward directions in the presence of a magnetic field was measured and recorded. The magnetic field orientation was transverse with respect to the light propagation direction for all the cases.

The measured transmission spectra for different MZIs are presented in Fig.4.12. The measured FSR of these devices are 2.3 nm, 3.4 nm, 6.8 nm and

18.4 nm respectively. The spectral shift between the forward and backward propagation direction is increasing with  $L$  but the  $\Delta NRPS$  (per unit length) should be almost the same for all the devices. Therefore  $\Delta NRPS$  could be extracted from the measurements using the formula given in Eq.4.9. The slope

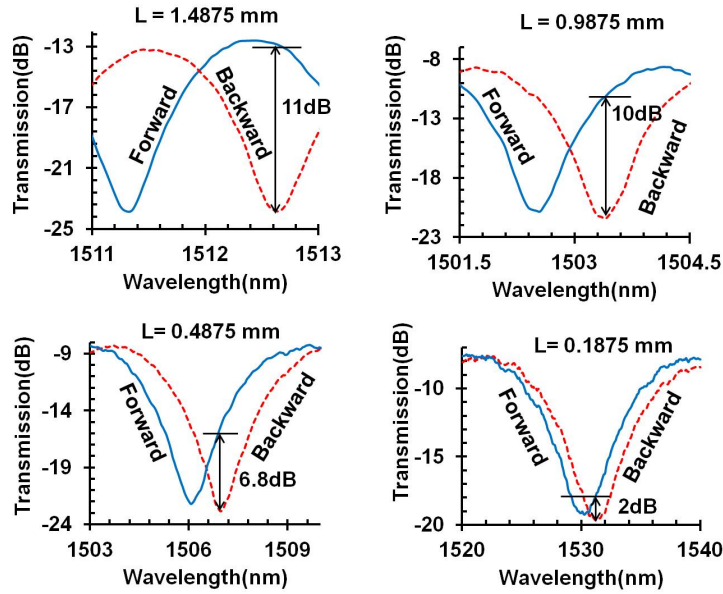


**Figure 4.12:** Measured transmission spectra for different MZI under the external magnetic field.

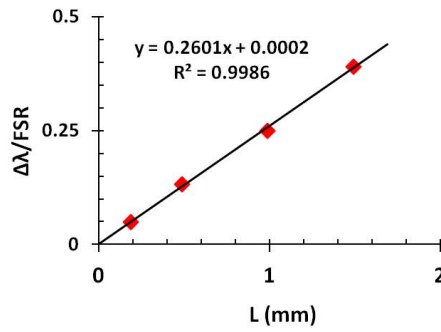


**Figure 4.13:** Plot of  $\Delta\lambda/FSR$  vs.  $L$ .

of the straight line is  $\frac{\Delta NRPS}{2\pi} = 0.2601$ . So the  $\Delta NRPS$  obtained is equal to 1.633 rad/mm. This implies that the thickness of the fabricated waveguide was not

220 nm rather it turned out as 210 nm according to Fig.4.6. Secondly  $W_t$  of the narrower and the wider waveguides are approximately 350 nm and 850 nm respectively. The thickness of the BCB and the silicon core are measured as 80 nm and 210 nm respectively as shown in Fig.4.14. The FIB cross-sectioning was performed in the vicinity of the interface between plain SOI and garnet bonded SOI. Due to severe charging issues the image captured by the scanning electron microscope (SEM) is not very clear.

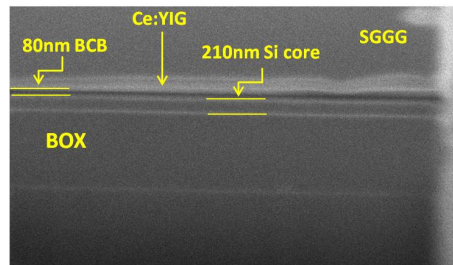


**Figure 4.14:** SEM cross-section view of the garnet stack bonded on the SOI.

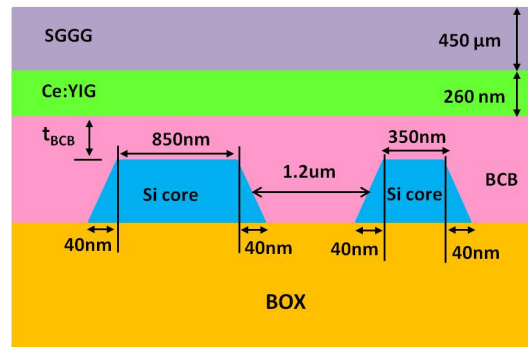


**Figure 4.15:** Schematic cross-section of fabricated MZI arms with the garnet bonded on top of it.

## 4.6 Analysis of as-fabricated device

From the experimental results and FIB cross-section it is clear that the fabricated MMI is different from the designed one. So here we need a detailed investigation of the as-fabricated MMI/MZI. The fabricated waveguide geometry at the MMI output after the bonding is shown in Fig.4.15. The top widths for the wider and narrower waveguides are 850 nm and 350 nm respectively whereas

the corresponding bottom widths are 930 nm and 430 nm. The distance between the output waveguides is  $1.2 \mu\text{m}$  measured at the middle of the silicon waveguide thickness. The multimode section of the MMI is also trapezoidal in shape with top width  $3.85 \mu\text{m}$  and bottom width  $3.93 \mu\text{m}$ . Normalized power splitting efficiency of the fabricated MMI to the wider and narrower arms as function of BCB thickness ( $t_{BCB}$ ) is shown in Fig.4.16(a) considering 210 nm silicon thickness. The wavelength dependence of the coupling efficiency is also estimated as shown in Fig.4.16(b) for the same waveguide geometries.

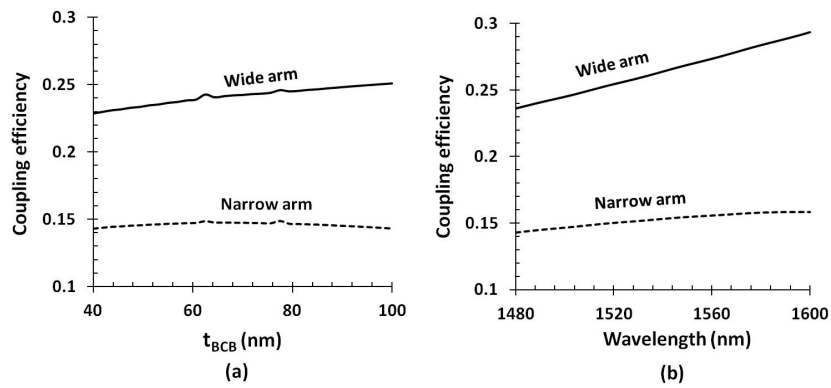


**Figure 4.16:** Coupling efficiency of the MMI to the wider and narrower arm as function of (a) BCB thickness at 1500 nm wavelength (b) Wavelength for 80 nm BCB thickness.

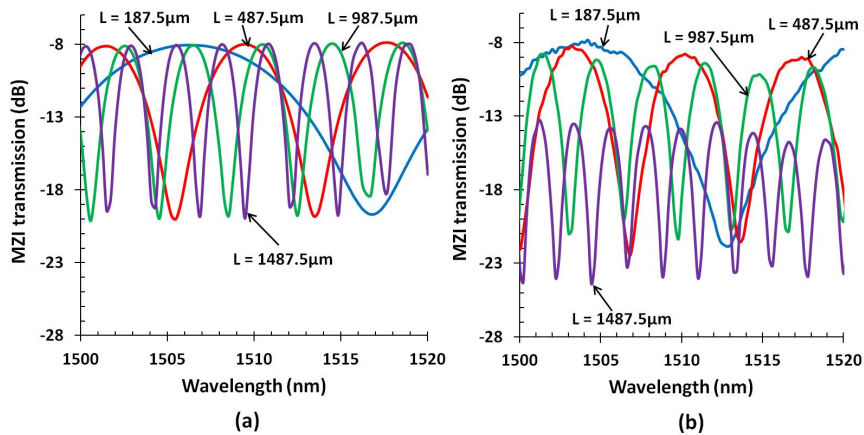


**Figure 4.17:** Spectra of the MZIs (a) Simulated (b) Measured.

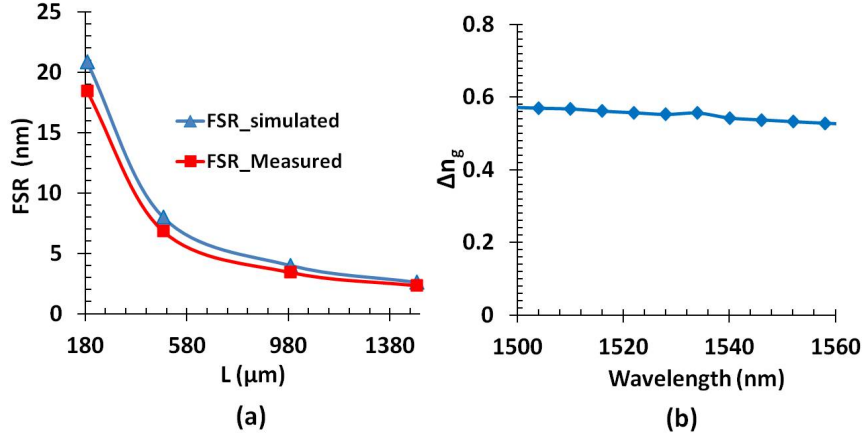


**Figure 4.18:** (a) Comparison between the measured and simulated FSR (b) Spectral dependence of  $\Delta n_g$  for the 210 nm thick silicon waveguide with 80 nm of BCB.

Transmission spectra of the fabricated MZIs are simulated considering the waveguide dimensions as mentioned earlier for a 210 nm thick silicon waveguide layer with 80 nm BCB between the waveguide and garnet stack. Good agreement between the simulated and measured transmission graphs can be observed from Fig.4.17. However there is a small mismatch between measured FSR and simulated FSR which could be due to a small variation of any of the parameters like waveguide dimensions or BCB thickness etc. The FSR of this type of MZI is inversely proportional to the differential group index ( $\Delta n_g$ ) between the wider and narrower arm. This small discrepancy is presented in Fig.4.18(a). The variation of  $\Delta n_g$  as a function of wavelength for 80 nm BCB is shown in Fig.4.18(b) considering the waveguide dimensions as mentioned above.

The transmission loss for the MZI having length  $L = 187.5\mu\text{m}$  is almost identical in simulation and measurement. However when L increases the product of  $\Delta\alpha$  and L also increases which results in an overall increment in loss and decrease in ER according to Eq.4.12. It is important to mention that the maximum transmission level is determined by distributed losses from different parts of the MZI. An illustrative analytical calculation of the MZI transmission is shown in Fig.4.19(a) in which collective propagation losses of the wider and narrower arm are presumed as 15 dB/cm and 25 dB/cm respectively.

Now let us estimate the value of  $\Delta\alpha$  and R (see Eq.4.12) from the measured MZI transmission spectra having four different length L. A 'sum square error' method is adopted for the prediction of the required quantities using Eq.4.12. The measured (between 1494 - 1510 wavelength) and the fitted ER of the MZIs

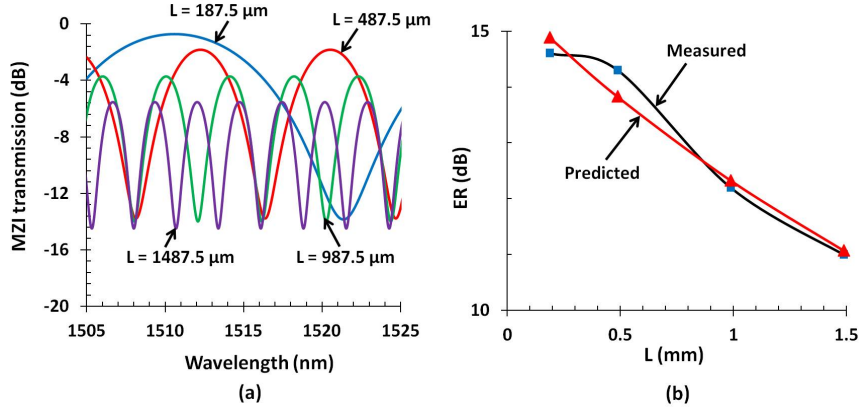


**Figure 4.19:** (a) Analytically calculated MZI spectrums considering  $\alpha_w = 3.45/\text{cm}$  (equivalently 15 dB/cm),  $\alpha_n = 5.76/\text{cm}$  (equivalently 25 dB/cm) (b) Fitting of measured extinction ratios (ER) for different MZIs between 1494-1510 nm wavelength.

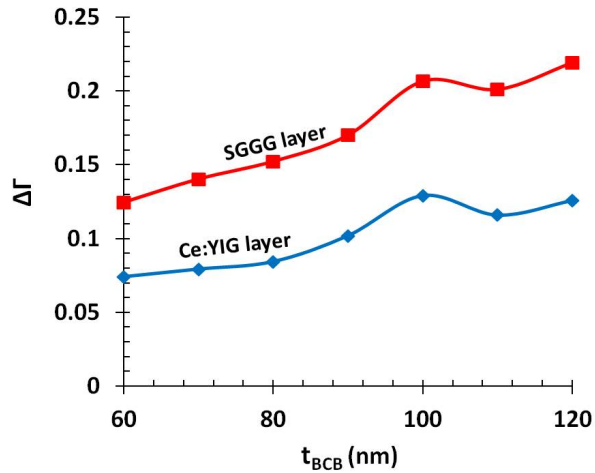


**Figure 4.20:** (a) Simulated  $\Delta\Gamma$  as a function of  $t_{BCB}$  at 1500 nm wavelength for the fabricated waveguide stack.

are presented in Fig.4.19(b). The value of  $R$  and  $\Delta\alpha$  as obtained from this fitting are 0.71 and 0.32/mm (or equivalently 1.4 dB/mm) respectively. A substantial deviation of theoretically calculated  $R$  is found after comparing with the simulated value as shown in Fig.4.16(a), which dictates a value for  $R$  of about 0.6 for 80 nm BCB at 1500 nm operating wavelength. The insertion loss due to the bonded garnet on any waveguide is directly proportional to the confinement

of the optical mode in the garnet layer. Therefore it is straight forward to express  $\Delta\alpha = \Delta\Gamma \times \text{material loss}$ . Where  $\Delta\Gamma$  is defined as the differential confinement factor of the TM mode between both arms of the MZI. In Fig.4.20  $\Delta\Gamma$  is shown for the Ce:YIG and SGGG layer as a function of the BCB thickness at 1500 nm wavelength. The material loss is measured as 60 dB/cm for the unannealed Ce:YIG as reported here [10]. So taking  $\Delta\Gamma = 0.08$  (at 80 nm BCB thickness) results in a value of  $\Delta\alpha$  of 0.48 dB/mm whereas the value obtained from fitting is 1.4 dB/mm. The difference between the theoretical and measured values can be partially explained by extra differential loss due to the confinement in the SGGG layer, which is assumed to be transparent in this analysis.

## 4.7 Conclusion

A very compact optical isolator on the SOI waveguide platform is realized by adhesive BCB bonding. A comprehensive study of the designed and the as-fabricated devices is presented. A fairly good agreement is found between the measured and the simulated results. The achieved maximum isolation is 11 dB at 1512.6 nm for an interferometer with 1.49 mm arm length. The extinction ratio of the MZI stringently depends on the power coupling ratio between the MZI arms. Therefore a modified design of the MMI where the waveguides are placed at the end of multimode section of the MMI in such a manner that the power coupling into these arms are identical will enhance the isolation by improving the extinction ratio. The differential nonreciprocal phase shift strongly varies with silicon waveguide thickness. The overall loss of the device can be reduced by using a low loss garnet material which can be achieved by annealing the garnet. So we have shown that not only the device performance can be improved in terms of insertion loss and isolation ratio, this device concept also allows for a dense integration of optical isolators on the SOI platform.

## References

- [1] J. Fujita, M. Levy, R. M. Osgood, L. Wilkens, and H. Doltsch. *Waveguide optical isolator based on Mach-Zehnder interferometer*. Applied Physics Letters, 76(16):2158, 2000.
- [2] Yuya Shoji, Tetsuya Mizumoto, Hideki Yokoi, I-Wei Hsieh, and Richard M. Osgood. *Magneto-optical isolator with silicon waveguides fabricated by direct bonding*. Applied Physics Letters, 92(7):071117, 2008.

- 
- [3] Yuya Shoji, Masatoshi Ito, Yuya Shirato, and Tetsuya Mizumoto. *MZI optical isolator with Si-wire waveguides by surface-activated direct bonding*. Optics express, 20(16):18440–8, July 2012.
- [4] S. Ghosh, S. Keyvavinia, W. Van Roy, T. Mizumoto, G. Roelkens, and R. Baets. *Ce:YIG/Silicon-on-Insulator waveguide optical isolator realized by adhesive bonding*. Optics Express, 20(2):1839–48, January 2012.
- [5] Yoshihiro Yazaki, Yuya Shoji, and Tetsuya Mizumoto. *Demonstration of Interferometric Waveguide Optical Isolator with a Unidirectional Magnetic Field*. Japanese Journal of Applied Physics, 46(8B):5460–5464, 2007.
- [6] Pieter Dumon. *Ultra-Compact Integrated Optical Filters in Silicon-on-insulator by Means of Wafer-Scale Technology*. PhD thesis, Universiteit Gent, 2007.
- [7] Graham T Reed and Andrew P Knights. *Silicon photonics*. Wiley Online Library, 2008.
- [8] <http://www.photond.com>.
- [9] Diedrik Vermeulen, Karel Van Acoleyen, Samir Ghosh, Wout De Cort, Nebiyu Adello Yebo, Elewout Hallynck, Katrien De Vos, Peter Debackere, Pieter Dumon, Wim Bogaerts, et al. *Efficient tapering to the fundamental quasi-TM mode in asymmetrical waveguides*. European Conference on Integrated Optics (ECIO), United Kindom, 2010.
- [10] Toshihiro Shintaku and Takehiko Uno. *Preparation of Ce-Substituted Yttrium Iron Garnet Films for Magneto-Optic Waveguide Devices*. Japanese Journal of Applied Physics, 35(Part 1, No. 9A):4689–4691, 1996.



# 5

## Isolator For Transverse Electric Polarized Light

**I**N last two chapters we have demonstrated optical isolators working for TM polarized light. Now most of the semiconductor lasers emit TE polarized light. To protect these lasers from back-reflections, an optical isolator operating in TE mode is required instead of the regular TM polarization operation mode. This chapter deals with this issue. In this chapter a SOI-based MZI type isolator for TE polarized light is discussed. The main physical principle behind optical isolation for these isolators remained same as TM mode isolators which is nothing but the NRPS experienced by the TM mode inside a magneto-optic cladding SOI waveguide under a transverse external magnetic field. Polarization rotators are implemented in the MZI arms to achieve the required functionality. To start with the basics principle behind this type of isolator is presented and there-after the details of the actual device design and fabrication are discussed. This is followed by a comparative study between as ideal design and as-fabricated devices. Finally measurement results and the corresponding analysis is presented. An isolation of 32dB is obtained experimentally from one of the devices.

## 5.1 Introduction

An elaborate discussion regarding the importance of an optical isolator in an optical communication system was already presented in Chapter 2. An active nonreciprocal loss (NRL) type isolator for TE mode was already reported several years back [1], in which a Fe layer was deposited on one of the sidewalls of the active waveguide and a vertical magnetic field was applied to bias the Fe layer to induce the magneto-optic effect. Of-late garnet materials like Yttrium Iron Garnet (YIG), Cerium substituted YIG (Ce:YIG) or Bismuth substituted YIG (BIG) are widely used as magneto-optic materials for their high Faraday rotation and low-loss in the telecom wavelength window. The present state-of-the-art technology can be used for direct sputtering or pulsed laser deposition of such garnet materials on top of a waveguide to achieve magneto-optical effects. But still that approach yields mediocre results due to various issues related to the material properties, optical loss etc. The other known approaches are direct molecular bonding and BCB bonding as already discussed in chapter 2. The demonstrated BCB bonding based integrated isolators in [2, 3] work only for transverse magnetic (TM) polarized light. The BCB bonding approach can also be implemented to isolate the TE mode by rotating it to the TM mode. In this work the TE mode in the waveguide is converted to TM using a polarization rotator.

## 5.2 Designs and operation principle

The proposed TE-mode isolator is realized by an interferometric configuration which works on the principle of the nonreciprocal phase shift (NRPS) experienced by the TM mode propagating through a waveguide under a transverse magnetic field. A detailed theoretical formulation regarding NRPS was already presented in Chapter 2. Different types of MZIs were designed with varying magneto-optical interaction length to achieve an optimal performance with respect to the total acquired NRPS and insertion loss. The schematic diagrams of some of the representative devices are shown in Fig.5.1, Fig.5.2 and Fig.5.3 respectively. Any of the proposed MZI-type isolators comprises several components such as a polarization rotator, a 380 nm thick silicon waveguide covered with Ce:YIG used as a nonreciprocal phase shifter, spot size converters between 220 nm thick silicon and 380 nm thick silicon waveguides, multimode interference (MMI) couplers and fiber-to-chip grating couplers for TE polarization [4]. The sections of the MZI consisting of two polarization rotators, two spot-size converters and one nonreciprocal phase-shifter is termed as an advanced passive (ADP) waveguide for the sake of simplicity as indicated on Fig.5.1, Fig.5.2 and on Fig.5.3. The nomenclature stems from the name of the MPW run for this type of thick Si waveguide used by ePIXfab. An enlarged view of an ADP

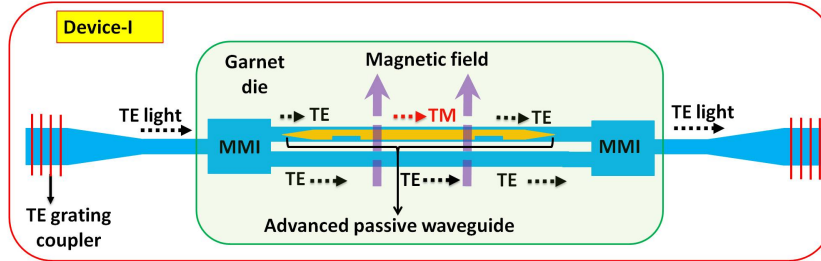


**Figure 5.1:** TE mode isolator: advanced passive waveguide/nonreciprocal phase shifter in one arm while the other arm is designed purely for TE mode.

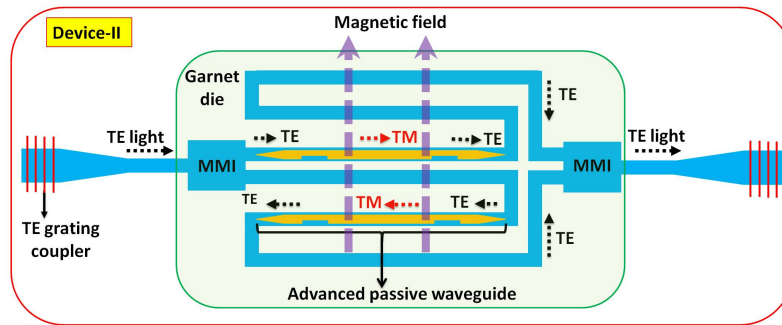


**Figure 5.2:** Push-pull type TE mode isolator: with one section of advanced passive waveguide on each arm of the MZI.

waveguide section is depicted in Fig.5.4(a), which shows all the aforementioned sub-components.

The simulation details of each subcomponent will be discussed in the next section. The fundamental TE mode in the 220 nm thick silicon waveguide is gradually converted to the fundamental TE mode in the 380 nm thick silicon waveguide via a spot-size converter with an appropriate tip width  $t_w$  and length  $L_{taper}$ . The width of the nonreciprocal phase shifter rib waveguide is designed as 600 nm to reduce the insertion loss of the isolator and is connected to 280 nm wide waveguides at both ends by 30  $\mu\text{m}$  long linear tapers, although shorter taper length is also feasible. Some of the MZIs are designed with ADP sections as shown in Fig.5.4(b), in which the NRPS width is 280 nm, the same as the symmetric waveguide section of the polarization rotator. In this narrow waveguide section polarization rotators are implemented as will be discussed later. The total dimensions of device-I, device-II and device-III are 6 mm  $\times$  0.1 mm, 6 mm  $\times$  0.14 mm and 6 mm  $\times$  0.2 mm respectively whereas the total lengths of the nonreciprocal phase shifter ( $L_{NRPS}$ ) are roughly 2.8 mm, 2 $\times$ 2.8 mm (1 $\times$ 2.8

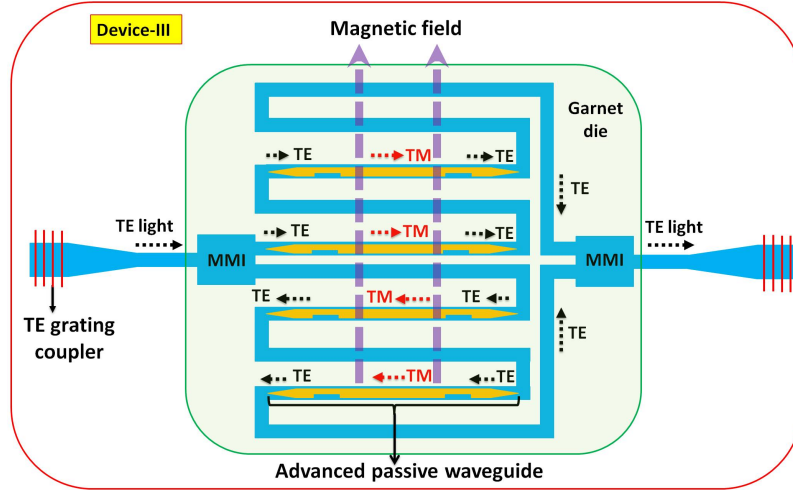


**Figure 5.3:** Push-pull type TE mode isolator: with two sections of advanced passive waveguide on each arm of the MZI.

mm in each arm) and  $4 \times 2.8$  mm ( $2 \times 2.8$  mm in each arm) respectively. The rib waveguide is realized by defining a narrower waveguide in the 160 nm thick top silicon overlay compared to the 220 nm thick bottom crystalline silicon. The width offset is designated as  $r_w$  on each side of the waveguide as indicated on Fig. 5.4. The waveguides are routed in a spiral manner to achieve a larger NRPS length and the push-pull operation particularly for device-II and device-III. To make the circuit compact bends are designed with a radius of curvature of  $10 \mu\text{m}$ . The necessary bends are designed in places where the waveguide is guiding only the fundamental TE ( $\text{TE}_{00}$ ) mode with a width of 600 nm and thickness of 220 nm ensuring no leaking of light into the Ce:YIG slab (it is noteworthy to mention that fundamental TM mode will not be guided in this waveguide stack having a BCB thickness higher than 160 nm).

The principle of operation of either devices as an isolator is as follows. TE polarized light is injected using a grating and then split using a 3 dB MMI coupler, taking two different routes through the MZI arms. Let us consider the propagation through any one of the arms of the MZI under the presence of a transverse magnetic field. TE polarized light at the input of an ADP section is rotated to TM polarization and experiences a nonreciprocal phase shift due to the presence of Ce:YIG on top of the silicon waveguide circuit and the transverse external magnetic field. After passing through the second polarization rotator in the same ADP section, the polarization is again rotated to TE and the waveguide can loop back without experiencing any nonreciprocal phase shift. This process keeps on repeating for the other ADP sections of the same arm. Fi-

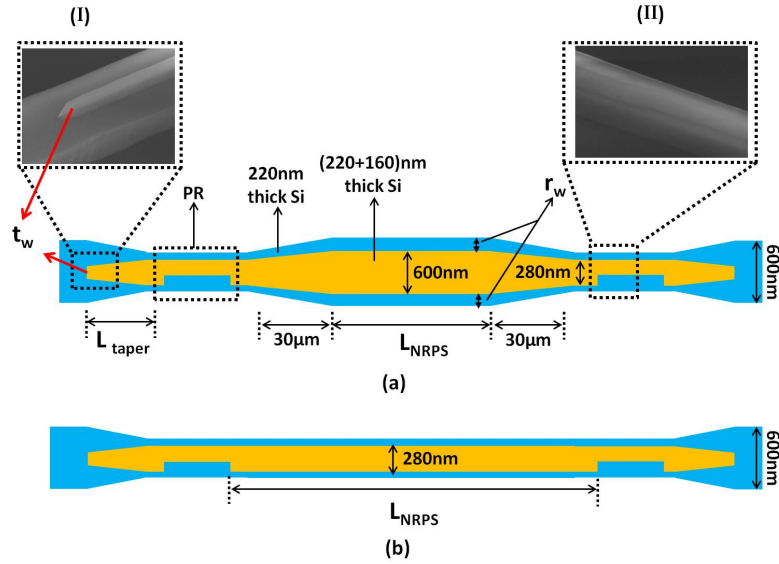


**Figure 5.4:** Enlarged sketch of an advanced passive (ADP) waveguide containing two spot-size converters, two polarization rotators and a nonreciprocal phase shifter. SEM pictures: inset (I) shows the taper tip of the spot-size converter; inset (II) shows the transition section between symmetrical and asymmetrical sections of polarization rotator (PR). (a) Type-I, where the nonreciprocal phase shifter is tapered to narrower symmetrical waveguide section of the PR (b) Type-II, widths of symmetrical section of the PR and the nonreciprocal phase shifter section are identical without any tapering. Spot-size converters and polarization rotators are defined by etching 160 nm thick poly-Si overlay situated on top of 220 nm thick c-Si.

nally, the TE polarized light from both the arms is combined at the second MMI and collected using the TE polarization grating coupler. The ADP sections are placed in both arms of the MZIs (for device-II and device-III) in such a way that the device works in a push-pull manner when an unidirectional magnetic field is applied transverse to the light propagation. In the case of device-I, only one arm of the interferometer provides NRPS while light through the other arm is totally unaffected by an external magnetic field as it is purely TE polarized.

### 5.2.1 Design of Nonreciprocal Phase shifter

We have learned from the previous section that this device works on the principle of the nonreciprocal phase shift (NRPS) resulting from the interaction

between the light propagating through the optical waveguide and an external magnetic field via a magneto-optic active material bonded on top of the waveguide. Therefore in this context an assumption of the NRPS is required to determine the device length for different waveguide parameter variations and different BCB layer thicknesses.

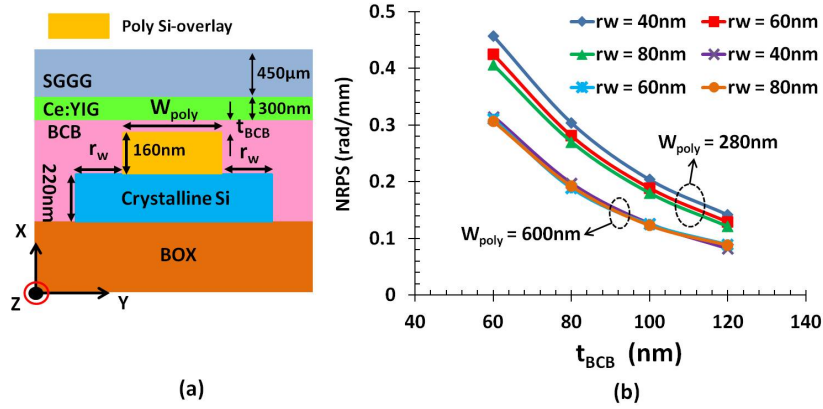


**Figure 5.5:** (a) Schematic cross-section of the garnet bonded waveguide at the nonreciprocal phase shifter of the ADP (b) Variation of NRPS per unit length as a function of BCB thickness ( $t_{BCB}$ ) at 1540 nm wavelength.

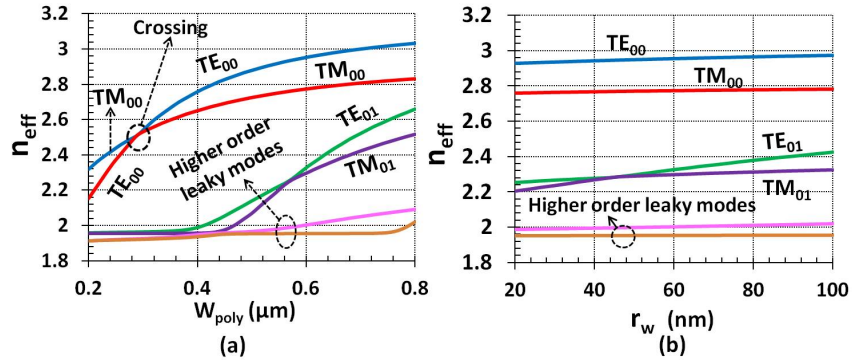


**Figure 5.6:** Variation of effective refractive index  $n_{eff}$  as a function of (a)  $W_{poly}$  for  $r_w = 60$  nm, 50 nm BCB at 1540 nm wavelength (b)  $r_w$  for  $W_{poly} = 0.6$  μm, 50 nm BCB at 1540 nm wavelength.

The corresponding waveguide cross-section used for this simulation is shown in Fig.5.5(a). The width of the poly-Si overlay is termed as  $W_{poly}$  which has constant values of either 600 nm or 280 nm and a thickness of 160 nm

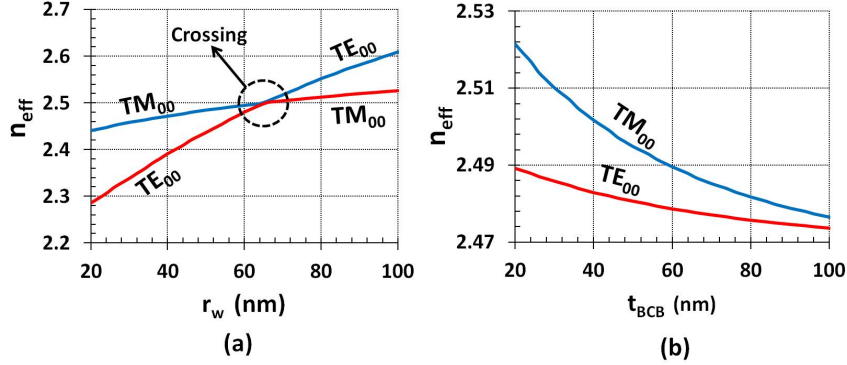


**Figure 5.7:** Variation of effective refractive index  $n_{eff}$  as a function of (a)  $r_w$  for  $W_{poly} = 0.28 \mu\text{m}$ , 50 nm BCB at 1540 nm wavelength (b)  $t_{BCB}$  for  $W_{poly} = 0.28 \mu\text{m}$ ,  $r_w = 60$  nm at 1540 nm wavelength.

whereas the width of the c-Si is  $W_{poly} + 2 \times r_w$  having 220 nm thickness. The thicknesses of the Ce:YIG and the SGGG layers are 300 nm and 450 nm respectively. The NRPS per unit length is calculated using the same approach as already presented in Chapter 3 in the context of a MZI with dissimilar arm widths. The corresponding result is plotted in Fig.5.5(b) for various BCB thicknesses. The NRPS achieved for this waveguide geometry is rather small compared to the 220 nm thick and 900 nm wide waveguide. Therefore, a longer device is required to obtain the same effect from this type of device. The decreased value of NRPS for wider  $W_{poly}$  as compared to the narrower  $W_{poly}$  is because of the increased interaction of the TM mode with the Ce:YIG for the latter case. The variation of  $r_w$  has more influence on the NRPS values for the same BCB thickness in the case of narrower  $W_{poly}$  as compared to the wider  $W_{poly}$ .

One important aspect for the waveguide-based devices is the modal effective refractive index ( $n_{eff}$ ) variation as a function of waveguide width. In this case  $W_{poly}$  is varied from 0.2  $\mu\text{m}$  to 0.8  $\mu\text{m}$  keeping  $r_w$  fixed at 60 nm. The corresponding effective index variation is presented in Fig.5.6(a) at 1540 nm wavelength for 50 nm BCB. We can see that the fundamental TE and TM modes are crossing around 280 nm. The waveguide of width 600 nm is a suitable choice as  $n_{eff}$  for all the guided modes are well separated from each other. If the  $r_w$  is changed within some nominal range all the modes are still well apart as shown in Fig.5.6(b). Some of the waveguides were also designed with  $W_{poly} = 280$  nm and the effective indices of fundamental TE and TM modes are depicted in Fig.5.7(a) where  $r_w$  is taken as a parameter (here other higher order modes are neglected as they are all radiation modes). When BCB thickness increases,  $n_{eff}$  for the  $TM_{00}$  mode decreases faster than the  $TE_{00}$  mode for a particular  $r_w$  as

depicted by Fig.5.7(b).

### 5.2.2 Design of polarization rotator

Silicon or III-V semiconductor materials offer excellent platforms for realizing microphotonic devices and also densely integrated photonic circuits. But the high-index-contrast silicon waveguide suffers from an inherent birefringence between TE and TM modes. One of the ways to deal with this polarization sensitivity issue is by adopting a polarization diversity scheme which can render devices insensitive to the polarization of light. To achieve this functionality polarization splitters or rotators need to be integrated monolithically with other photonic components. In general, a polarization rotator is a device which rotates the direction of the polarization axis of linearly polarized light. In the con-

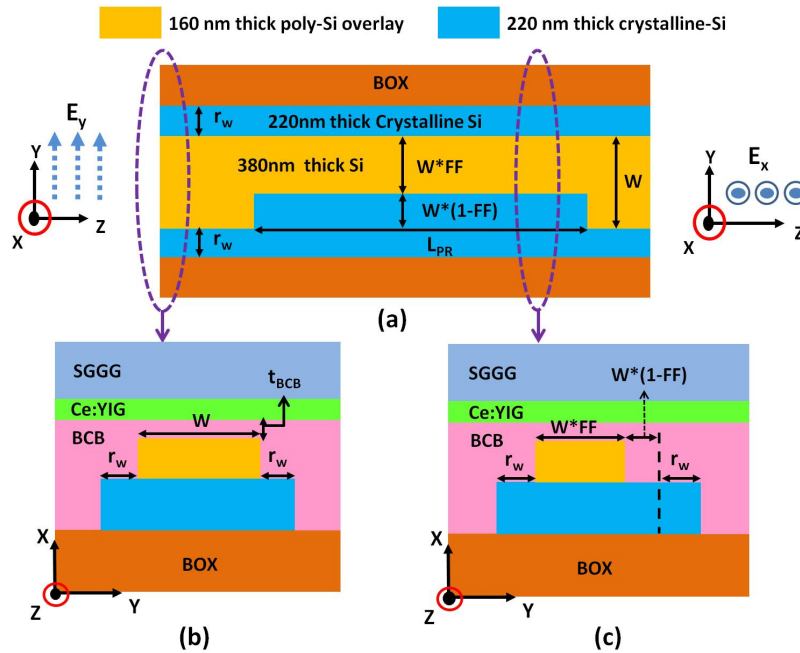


**Figure 5.8:** Schematic drawing of implemented polarization rotator(a) air clad top-view. Views of the garnet bonded waveguide stack at (b)symmetrical and (c) asymmetrical waveguide cross-section of the designed polarization rotator

text of integrated optics a polarization rotator transforms a TE mode to a TM mode and vice-versa. Numerous approaches have been reported for realizing an integrated polarization rotator. One approach is based on the mode evolution by twisted tapering of a 400 nm thick 200 nm wide silicon waveguide

to a 200nm thick 400nm wide silicon waveguide [5]. Due to the complex geometries of the waveguide structures, this approach is not straightforward to implement. Another method is the use of an asymmetrical directional coupler based splitter-rotator [6, 7]. In this approach, the TM and TE polarized light are separated and also rotated at the cost of longer device length and the need for a vertically asymmetrical structure. In the past, the use of an angled sidewall waveguide was demonstrated to break symmetry for polarization rotation but it also suffers from complicated fabrication steps [8, 9]. So less complex geometries and simple fabrication steps are highly desirable to obtain a polarization rotator.

The polarization rotator implemented in this work is based on the symmetry breaking by a silicon-overlay similar to the recently demonstrated work [10] except the top cladding in this case is BCB and the garnet stack (Ce:YIG on SGGG substrate). This type of polarization rotator is defined by symmetri-

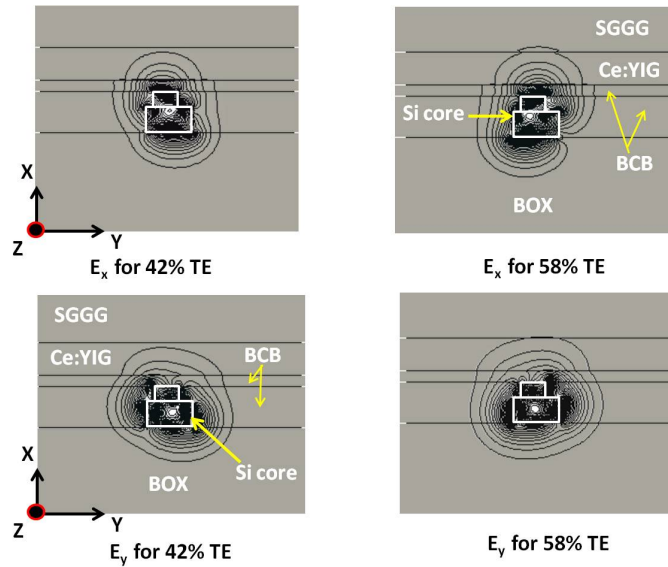


**Figure 5.9:** Contour plots of the electric fields ( $E_x, E_y$ ) for the hybrid modes at the asymmetrical waveguide cross-section of the polarization rotator.

cal and asymmetrical waveguide cross-sections. The working principle of such a polarization rotator can be understood as following. When a TE mode in the symmetrical section is launched into the asymmetrical section both TM and TE modes are excited. The asymmetrical section could be designed in such a manner that its eigen-axis rotated at  $45^\circ$  which excites both polarizations (TE and TM) equally. Now due to their difference in propagation constants these hybrid modes are phase shifted while traveling through the asymmetrical wave-

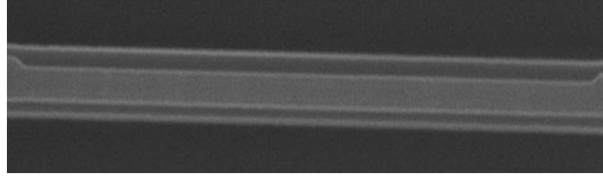


**Figure 5.10:** SEM image of the fabricated polarization rotator with air cladding.

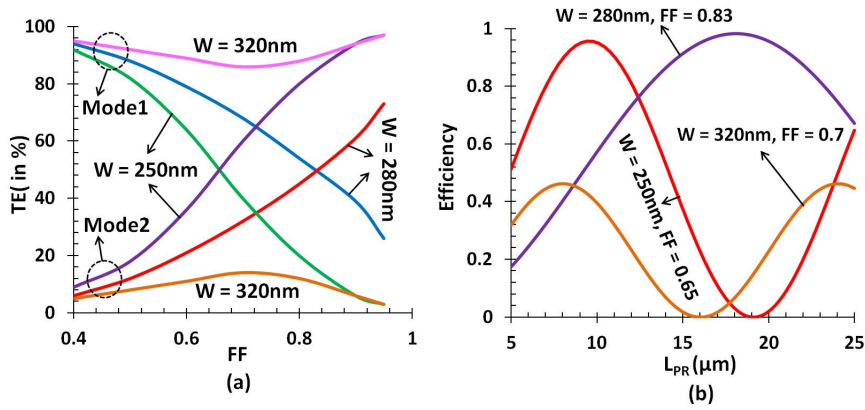


**Figure 5.11:** (a) Determination of cross-sections for the symmetrical and asymmetrical waveguides of the polarization rotator by varying the FF for 100 nm BCB,  $r_w = 60$  nm at 1540 nm wavelength (b) Normalized power transfer efficiency between TE and TM modes of the polarization rotator as a function of  $L_{PR}$  for 100 nm BCB thickness,  $r_w = 60$  nm at 1540 nm wavelength.

guide. The phase shift between them after traveling a length  $L_{PR}$  through the asymmetrical section can be written as  $\phi = \pi \frac{L_{PR}}{L_\pi}$ , in which  $L_\pi = \frac{\pi}{\beta_{TE} - \beta_{TM}}$  is the half-beat length.  $\beta_{TE}$  and  $\beta_{TM}$  are designated as the propagation constants for the TE and TM mode respectively. Finally at a distance which is equal to the half-beat length, the  $\pi$ -phase shifted modes are recombined to a TM mode in a symmetric output waveguide. In this way the TM mode is excited and the desired rotation is achieved. A detailed theoretical discussion on polarization rotator can be found in [11, 12]. A schematic top view and the cross-section of the symmetrical and asymmetrical waveguide structures of the designed polarization rotator (PR) are depicted in Fig.5.8.  $W$  is the width of the 160 nm thick silicon overlay on top of the 220 nm thick crystalline silicon layer that is  $(W+2 \times r_w)$  nm wide. In the asymmetrical section the Si-overlay width is reduced to  $W \times FF$ , where FF is the fill factor which determines the hybrid nature of the

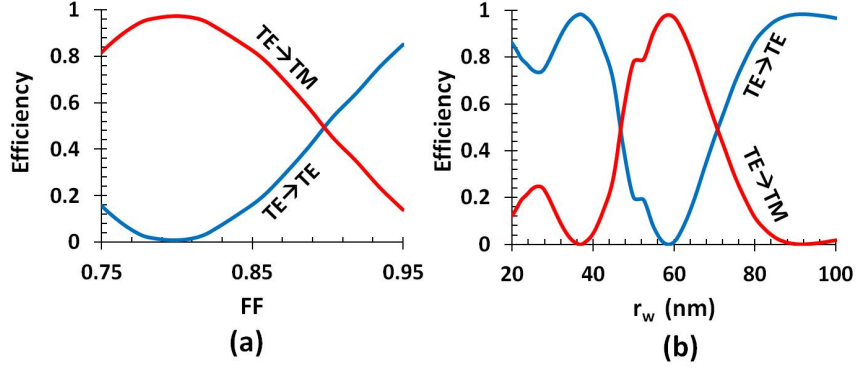


**Figure 5.12:** Normalized efficiency as a function of (a) FF at  $1.54 \mu\text{m}$  wavelength,  $L_{PR} = 15 \mu\text{m}$ ,  $r_w = 60 \text{ nm}$ ,  $100 \text{ nm}$  BCB thickness,  $W = 280 \text{ nm}$ ; (b)  $r_w$  for  $100 \text{ nm}$  BCB thickness,  $FF = 0.8$ ,  $L_{PR} = 15 \mu\text{m}$ ,  $W = 280 \text{ nm}$ , at  $1.54 \mu\text{m}$  wavelength.

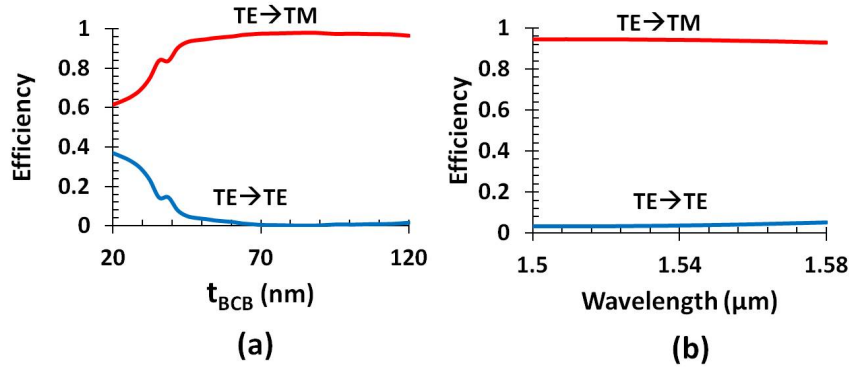


**Figure 5.13:** Normalized efficiency vs. (a) BCB thickness at  $1.54 \mu\text{m}$  wavelength,  $L_{PR} = 15 \mu\text{m}$ ,  $FF = 0.8$ ,  $W = 280 \text{ nm}$  (d) wavelength for  $L_{PR} = 15 \mu\text{m}$ , BCB thickness =  $50 \text{ nm}$ ,  $W = 280 \text{ nm}$ ,  $FF = 0.8$

optical modes in the asymmetrical waveguide section. To achieve the shortest length for 100% polarization rotation the asymmetric waveguide should support modes with an eigen-axis rotated at  $45^\circ$  with respect to the wafer surface. The contour plots of the electric fields (both  $E_x$  and  $E_y$ ) for such an asymmetric waveguide section are shown in Fig.5.9.  $r_w$  is varied here to obtain the best working device.  $L_{PR}$  is the length of the asymmetrical waveguide section which gives optimal polarization rotation. A SEM image of a PR from the top is shown in Fig.5.10.

The much needed polarization rotator is designed by adopting a simple ap-

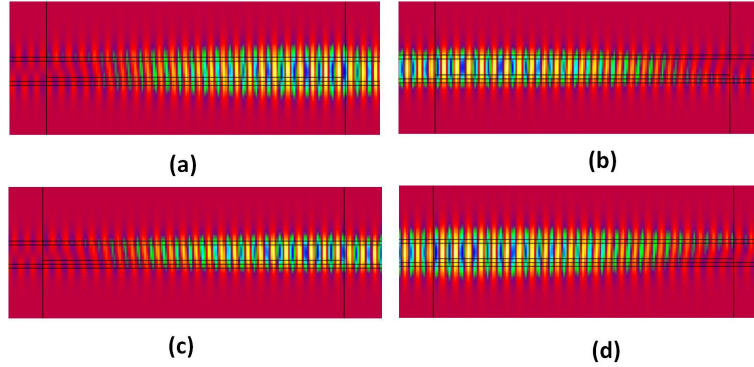


**Figure 5.14:** Simulated field views of a 97 % efficient polarization rotator for the various cases: (a)  $E_x$  for the  $TM_{00}$  as the input (b)  $E_y$  for the  $TM_{00}$  as the input (c)  $E_y$  for the  $TE_{00}$  as the input (d)  $E_x$  for the  $TE_{00}$  as the input. The input is on the L.H.S and the output is on the R.H.S for every figure.

proach. At first, three different waveguide widths ( $W$ ) are considered and subsequently the FF is also varied to obtain the 50% TE and 50% TM modes in that asymmetric cross-section as depicted in Fig.5.11(a).  $W = 280$  nm is chosen although narrower waveguides are also feasible however narrower dimensions are more prone to fabrication uncertainties. Then the required length for maximum polarization rotation is simulated considering those FF values where the TE fraction of mode 1 and mode 2 in the PR section are intersecting or tend to meet each other. The corresponding simulation is presented in Fig.5.11(b). The performance of the PR is tested when the FF is varied for  $W = 280$  nm as shown in Fig.5.12(a). From Fig.5.12(b) we can see that  $r_w$  has a critical impact on the efficiency of the polarization rotator compared to other parameters. In order to achieve a perfect working isolator, polarization rotators with three distinct  $r_w$  values such as 40 nm, 60 nm and 80 nm are implemented on the different MZIs which will be discussed in the measurement section. The impact of BCB thickness variations on the PR's performance is shown in Fig.5.13(a). The spectral dependence shown in Fig.5.13(b) reveals that the PR as designed is broadband in the telecom wavelength range. The simulated field conversions of different input polarization for a 97 % efficient PR are presented in Fig.5.14.

### 5.2.3 Design of MMI

The multi-mode interference (MMI) coupler required for this isolator is designed for the TE polarized light. Both the MMIs are covered by BCB plus garnet stack. The BCB thickness is inherently 160 nm thicker on top of the MMI as

compared to the ADP section because it is implemented in the 220 nm device layer instead of the 380 nm layer. The width ( $W_{MMI}$ ) and the length ( $L_{MMI}$ ) of the multi-mode section are designed as  $6.64 \mu\text{m}$  and  $2.8 \mu\text{m}$  respectively. The

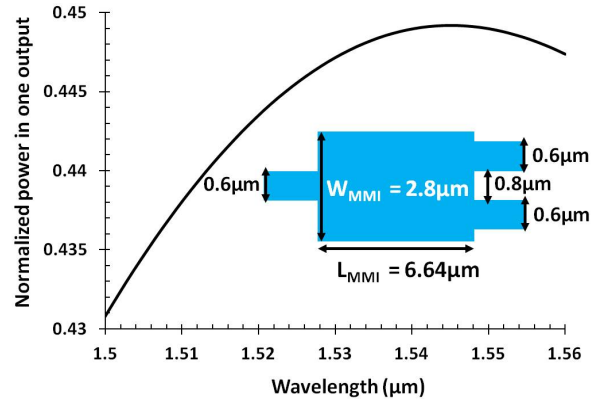


**Figure 5.15:** Spectral behaviour of the designed MMI with a top cladding consisting of (50 + 160) nm thick BCB together with the garnet stack.

input and output waveguides are 600 nm wide with a 800 nm gap between the output waveguides (center to center distance is  $1.4 \mu\text{m}$ ). The performance of the MMI is presented in Fig.5.15 over a broad wavelength range.

#### 5.2.4 Design of spot-size converter

To transform the fundamental TE mode from a 220 nm thick Si waveguide to a 380 nm thick Si waveguide and vice-versa a spot-size converter [13, 14] is necessary. A schematic of such a component is shown in Fig.5.16(a). The optical mode in the thicker rib waveguide of  $W_{poly} = 280 \text{ nm}$  with  $r_w$  is gradually converted to the mode in the thinner ridge waveguide by a taper of length  $L_{taper}$  with a tip of width  $t_w$ . Here  $L_{taper}$  and  $t_w$  are designed as  $40 \mu\text{m}$  and 100 nm respectively. Shorter taper length is however feasible. The designed spot-size converter is extremely robust with respect to BCB thickness or  $t_w$  variations. A side-view of the mode transition in the spot-size converter can be seen in Fig.5.16(b). The corresponding intensity profiles at different locations of the spot-size converter are shown in Fig.5.16(c).

### 5.3 Fabrication procedure

The SOI circuit is fabricated in a CMOS pilot line with 193 nm deep ultraviolet (DUV) lithography. The SOI wafer used consists of a 220 nm thick crystalline

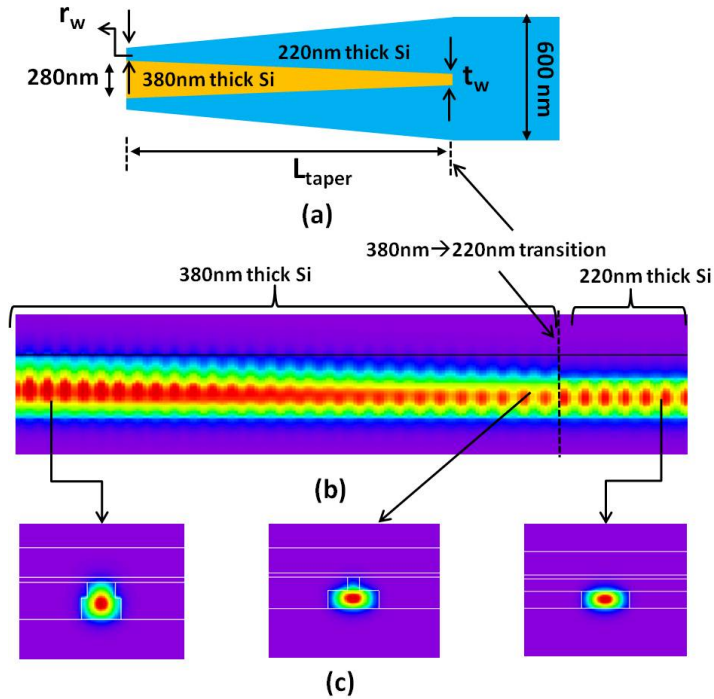


**Figure 5.16:** (a) Schematic of spot-size converter between 380 nm thick Si and 220 nm thick Si (b) Intensity profile of the spot-size converter when viewed from the side (c) Intensity at different cross-sections of the spot-size converter.

silicon layer on top of a 2  $\mu\text{m}$  thick buried oxide. In this work the 160 nm thick silicon overlay is polycrystalline silicon. This is achieved by sheet deposition of 160 nm thick amorphous silicon and selective removal by dry etching where required. In the exposed 220 nm waveguide layer, 70 nm deep etching allowed the realization of the grating couplers while a complete 220 nm deep etch defines the strip waveguides. In the final step the amorphous silicon is annealed to transform it to polycrystalline silicon. Fig.5.1 depicts that only the advanced passive waveguide sections of the MZI arms have a poly-Si overlay. In principle the poly-crystalline silicon can be substituted by crystalline silicon which results in lower loss, however this process was not available at the time of fabrication. After SOI wafer fabrication a 4 mm  $\times$  4 mm garnet die containing Ce:YIG on SGGG is bonded on top of the SOI using BCB. In this process, the SOI is cleaned by a standard SC-1 cleaning method (15 minutes in a solution of de-ionized water: $\text{H}_2\text{O}_2$ : $\text{NH}_4\text{OH}$  = 5:1:1 at 70°C), after which it is rinsed and dried

at 150°C. Mesitylene-diluted BCB (Mesitylene:BCB = 3:1) is spin coated onto the SOI at 3000 rotations per minute for 40 seconds. In this device, the trenches of the silicon waveguide were not filled by SiO<sub>2</sub> prior to bonding to achieve a planarized bonding surface, rather the trenches were filled by BCB after spin coating. Since the refractive index of BCB (1.54) is similar to that of SiO<sub>2</sub> (1.45) the performance of the polarization rotator is not affected. The BCB coated SOI is kept at 150°C for 10 minutes prior to bonding to evaporate the mesitylene so that only a thin layer of BCB remains on top of the SOI. Meanwhile the garnet die is also cleaned by acetone and iso-propylalcohol (IPA) and it is placed on top of the SOI waveguide circuit, after which it is cured.

#### 5.4 Analysis of fabricated polarization rotator

The actual fabricated polarization rotator is different from the designed one. In general any designed rectangular waveguide turned out to be trapezoidal after fabrication as discussed in the previous chapters. In practical fabrication the silicon overlay is not directly lying on c-Si layer but there is a thin layer of SiO<sub>2</sub> layer in between them which acts as etch stop layer for the polycrystalline silicon overlay. Moreover the BCB layer on top of waveguide is not planar due to the 380 nm deep trench on both sides of the waveguide. Noteworthy to mention that the refractive index of poly-Si is different from the c-Si which has also an impact on the efficiency of the polarization rotator. Hence in this section all these issues will be taken under consideration to study the tolerance of fabricated polarization rotator.

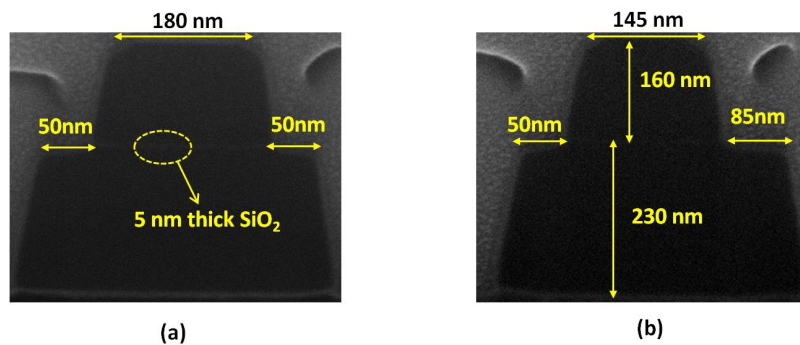


**Figure 5.17:** SEM image of the fabricated polarization rotator with air cladding (a) symmetric waveguide section (b) asymmetric waveguide section.

A focused ion beam cross-section at the polarization rotator showing the

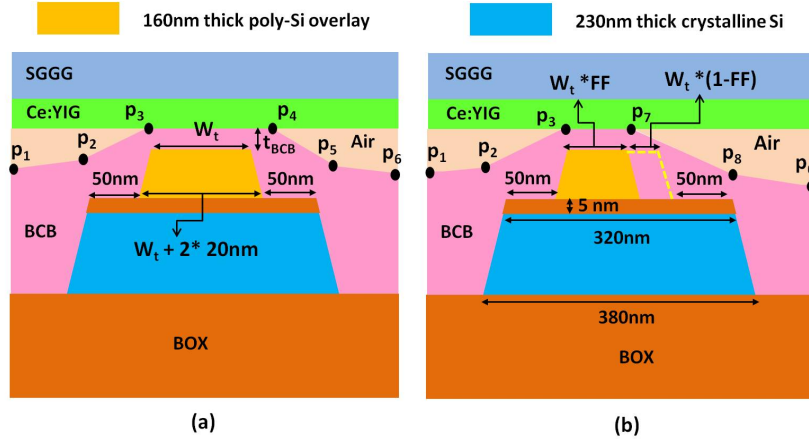


**Figure 5.18:** Schematic diagram of the waveguide cross-sections at the (a) symmetrical and (b) asymmetrical portions of the polarization rotator with garnet stack bonded by BCB. Note that the BCB is not flat on top of the waveguide trench. A wedge shape is assumed in which  $p_1$ ,  $p_2$ ,  $p_3$ ,  $p_4$ ,  $p_5$ ,  $p_6$ ,  $p_7$  and  $p_8$  are any arbitrary points considered to approximate the BCB shape.  $p_1$ ,  $p_2$  and  $p_3$  are identically situated for both the cross-sections whereas the co-ordinates of the points on the R.H.S are different for both the cases.

waveguide geometry after fabrication is shown in Fig.5.17. Fig.5.17(a) is the cross-section for the symmetric waveguide section and Fig.5.17(b) represents the asymmetric waveguide cross-section.  $r_w$  was designed as 60 nm, and turns out to be about 50 nm in this case. The thickness of the c-Si is 230 nm and the poly-Si overlay is 160 nm. A dim line of 5 nm thick  $\text{SiO}_2$  layer can be observed between c-Si and poly-Si. The widths of the poly-Si layer at the symmetric and asymmetric section are 180 nm and 145 nm respectively. However the corresponding widths were designed as 280 nm and 225 nm respectively leaving the  $\text{FF} = 0.8$ , as designed. The bottom width of the c-Si layer differs by approximately 60 nm from the top width where the same differs by 40 nm for the poly-Si layer according to SEM cross-sections.

Now let us discuss the performance of the fabricated polarization rotator with garnet bonded on top using an adhesive BCB layer. To simulate the structure  $L_{PR}$  is taken as  $15 \mu\text{m}$  and the refractive index for poly-Si as 3.6. The polarization rotation efficiency as a function of FF is shown in Fig.5.19(a) for two different BCB thicknesses considering all the dimensions as fabricated. BCB is assumed to be perfectly planarizing in the ideal scenario. However in the actual case the BCB surface on top of the Si waveguide is wedge shaped instead of planar. The spectral response of the fabricated polarization rotator is sim-

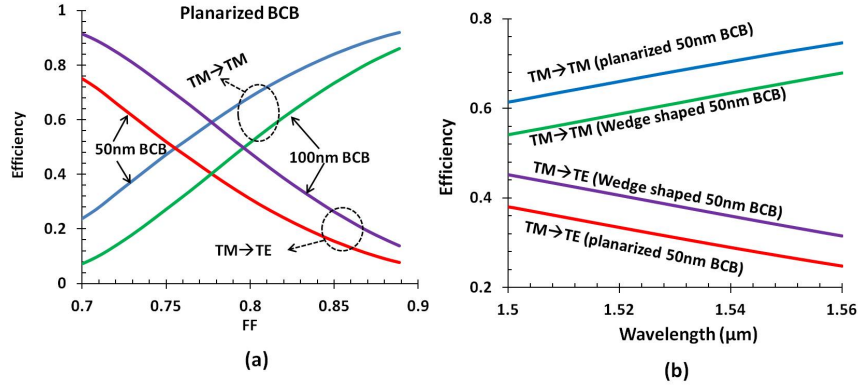


**Figure 5.19:** (a) Estimation of polarization rotation efficiency of the fabricated polarization rotator as a function of FF for  $W_t = 180$  nm with planarized BCB plus garnet stack and (b) Comparison of spectral responses of the fabricated polarization rotator with planarized BCB to the wedge shaped BCB on top of the waveguide for  $W_t = 180$  nm and  $FF = 0.8$ . Both the simulations are performed at 1540 nm wavelength.

ulated both for planar BCB and wedge shaped BCB as depicted in Fig.5.19(b). Therefore we can conclude that the nature of the spectral dependence of PR's efficiency remains invariant under the BCB shape although the absolute value of efficiency depends on the BCB shape.

## 5.5 Measurement results

TE polarized light from a tunable laser is injected and collected by grating couplers at the ends of the MZI. An external magnetic field transverse to the light propagation is applied with the aid of a miniature Nd-Fe-B magnet stack placed on top of the garnet die. Forward and backward transmission curves are obtained by switching optical input and output fibers during the measurements while keeping the magnetic field unaltered. The prototype devices discussed are designed to be optically narrow band to easily observe the isolation behavior, by introducing a path length difference between both arms of the interferometer. Two samples comprising various types of designs were tested. The samples were taken from different columns of the wafer and as a result they might be slightly different from each other. The device details are listed in the Table 5.1.

**Sample-I:** MZI-1 to MZI-6 are identical to the Device-I (see Fig.5.1). MZI-

Name	PR	ADP type	NRPS width ( $W_{poly}, r_w$ )	$L_{NRPS}$	MZI type
MZI-1	$r_w=40$ nm	I	600 nm, 40 nm	2.86 mm	NPP
MZI-2	$r_w=60$ nm	I	600 nm, 40 nm	2.86 mm	
MZI-3	$r_w=80$ nm	I	600 nm, 40 nm	2.86 mm	
MZI-4	$r_w=40$ nm	II	280 nm, 40 nm	2.82 mm	NPP
MZI-5	$r_w=60$ nm	II	280 nm, 60 nm	2.82 mm	
MZI-6	$r_w=80$ nm	II	280 nm, 80 nm	2.82 mm	
MZI-7	$r_w=40$ nm	I	600 nm, 40 nm	5.72 mm	PP
MZI-8	$r_w=60$ nm	I	600 nm, 40 nm	5.72 mm	
MZI-9	$r_w=80$ nm	I	600 nm, 40 nm	5.72 mm	
MZI-10	$r_w=40$ nm	II	280 nm, 40 nm	5.64 mm	PP
MZI-11	$r_w=60$ nm	II	280 nm, 60 nm	5.64 mm	
MZI-12	$r_w=80$ nm	II	280 nm, 80 nm	5.64 mm	
MZI-13	$r_w=40$ nm	I	600 nm, 40 nm	11.44 mm	PP
MZI-14	$r_w=60$ nm	I	600 nm, 40 nm	11.44 mm	
MZI-15	$r_w=80$ nm	I	600 nm, 40 nm	11.44 mm	

PP- Push-Pull, NPP- Non Push-Pull

**Table 5.1:** MZI details

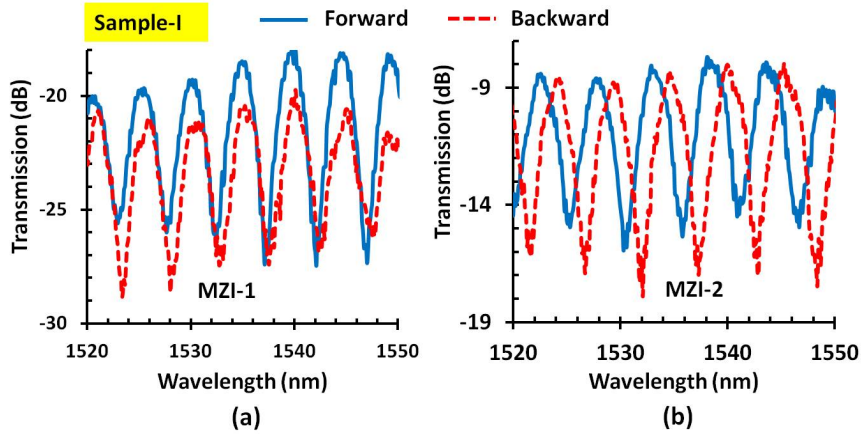


**Figure 5.20:** Normalized MZI transmission spectra for forward and backward propagation for (a) MZI-1 (b) MZI-2.

7 to MZI-12 resemble the Device-II (see Fig.5.2). MZI-13 to MZI-15 are similar to the Device-III (see Fig.5.3). All the MZIs contain two types of ADP sections, type-I is as shown in Fig.5.4(a) and type-II is shown in Fig.5.4(b). The geometry and length of the NRPS was also varied from one MZI to another. Comparing measurement results for the MZI-1 to MZI-3 for the sample-I we can remark that polarization rotator with  $r_w = 60$  nm as designed is the best one among the other

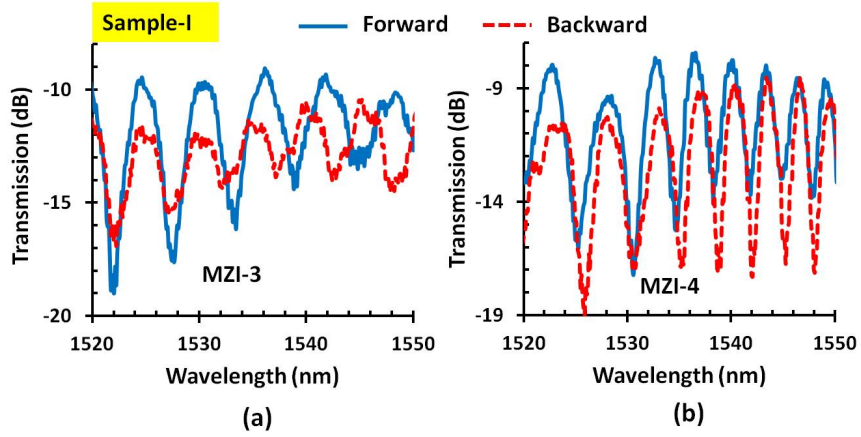


**Figure 5.21:** Normalized MZI transmission spectra for forward and backward propagation for (a) MZI-3 (b) MZI-4.

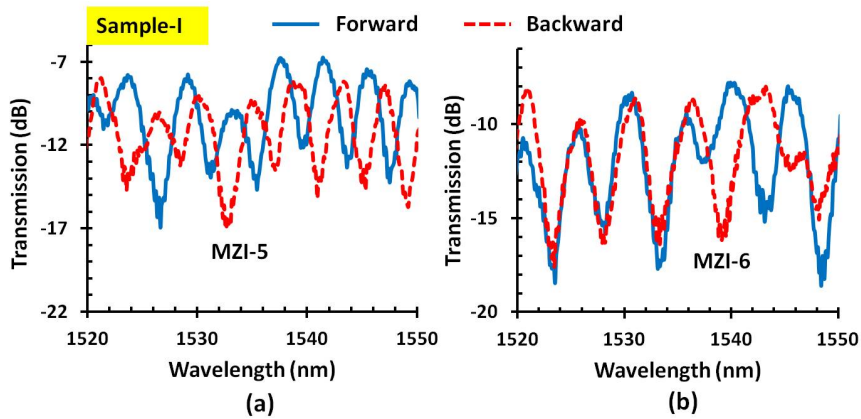


**Figure 5.22:** Normalized MZI transmission spectra for forward and backward propagation for (a) MZI-5 (b) MZI-6.

two. The maximum isolation achieved is about 5 dB at 1532 nm wavelength for MZI-2. Similarly the maximum spectral shift is observed for the MZI-5 (for which  $r_w$  in the polarization rotator is 60 nm) when we compare the obtained results from MZI-4 to MZI-6. The extinction ratios for all the MZIs from 1 to 6 are very low which limits the obtainable isolation. The reason may be the unequal losses in the two arms of the MZI as one arm is carrying purely TE polarized light while the other arm is guiding both TE and TM. The corresponding measured transmission spectra for MZIs 1 to 6 for forward and backward directions are

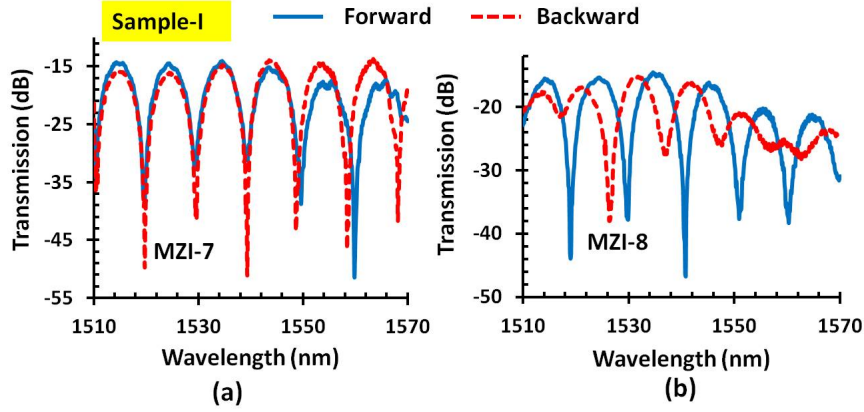


**Figure 5.23:** Normalized MZI transmission spectra for forward and backward propagation for (a) MZI-7 (b) MZI-8.

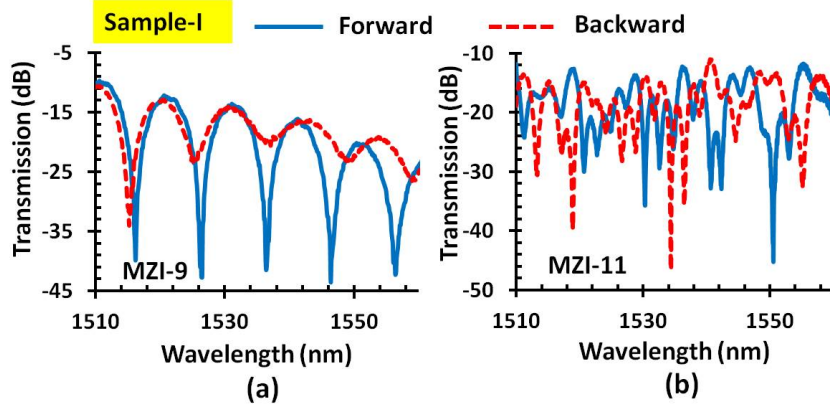


**Figure 5.24:** Normalized MZI transmission spectra for forward and backward propagation for (a) MZI-9 (b) MZI-11.

presented from Fig.5.20 to Fig.5.22 respectively.

MZI-7 to MZI-9 show excellent extinction ratios as both arms experiences identical loss. In this case MZI-8 showed a maximum spectral shift between forward and backward light propagation consequently a maximum isolation of about 30 dB is achieved at 1540 nm wavelength. The irregular transmission spectra for the MZI-11 and MZI-12 may be due to interference between the guided  $TE_{00}$  and  $TM_{00}$  modes as the effective indices for both the modes are almost identical according to Fig.5.7(a). MZI-14 demonstrated an isolation of 32 dB at a wavelength of 1540.5 nm. The measured transmission graphs for all

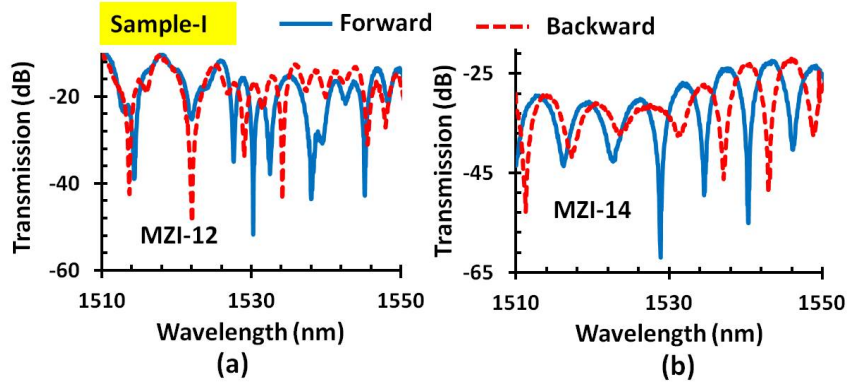


**Figure 5.25:** Normalized MZI transmission spectra for forward and backward propagation for (a) MZI-12 (b) MZI-14.

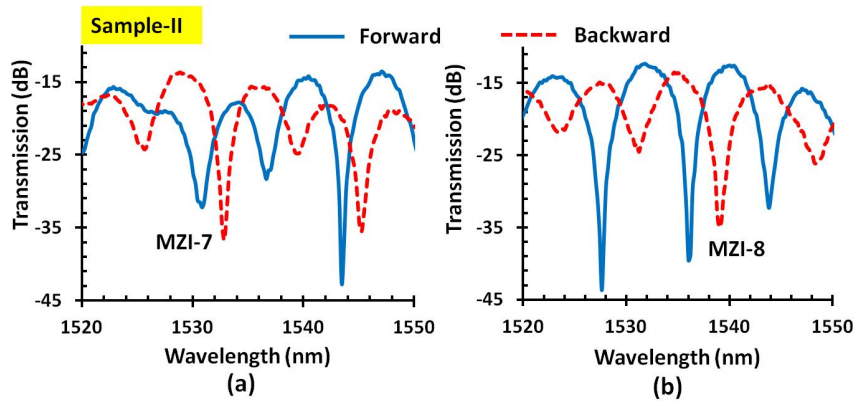


**Figure 5.26:** Normalized MZI transmission spectra for forward and backward propagation for (a) MZI-7 (b) MZI-8.

the MZIs from 7 to 14 (except 10 and 13) are shown in Fig.5.23 to Fig.5.25 in an ascending order.

**Sample-II:** Some MZIs from sample-II showed almost identical behavior as in sample-I. In this case MZI-9 and MZI-12 did not show any spectral shift due to the external magnetic field which means that the polarization rotators attached with these MZIs are not rotating TE polarization into TM and vice-versa. The isolation as measured from the MZI-8 and MZI-14 at 1540 nm wavelength is about 20 dB. The corresponding measurement results for the MZIs 7 to 14 are presented in Fig.5.26 to Fig.5.29 respectively. It is important to mention that the

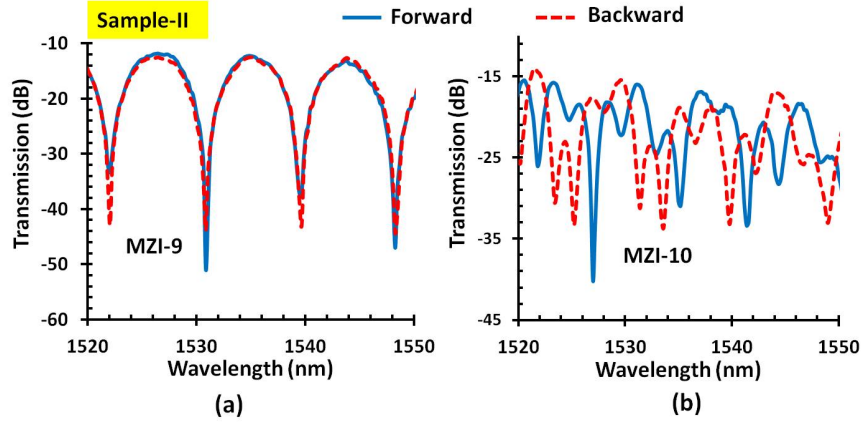


**Figure 5.27:** Normalized MZI transmission spectra for forward and backward propagation for (a) MZI-9 (b) MZI-10.

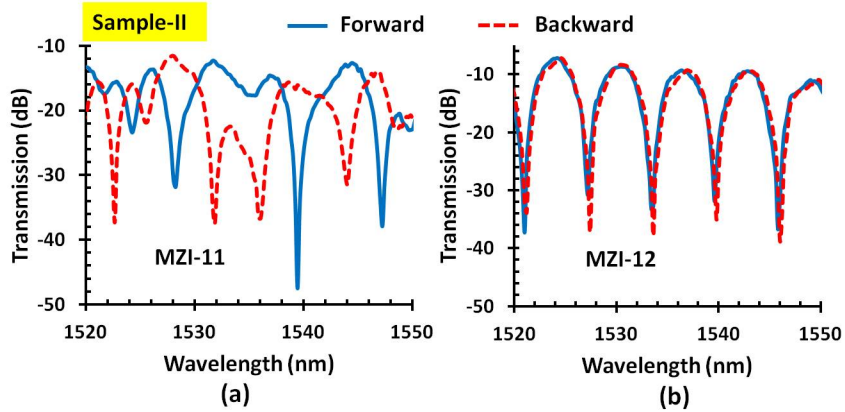


**Figure 5.28:** Normalized MZI transmission spectra for forward and backward propagation for (a) MZI-11 (b) MZI-12.

MZIs which responded to the external magnetic field (for both the samples) not only showed spectral shifts but also a nonreciprocal nature of extinction ratio for some wavelengths (for an example see MZI-8 or 14). The reason for this behavior is not clear yet.

When light propagation ( $k$ ) and magnetic field ( $H$ ) are oriented in the same direction a very small spectral shift is observed as shown in Fig.5.30(a) for MZI-8 which confirms the Voigt-configuration behavior. The insertion loss varied from device to device depending on  $L_{NRPS}$  mostly. In this case we will consider only MZI-8 and MZI-14. The exact breakdown of the insertion loss is difficult

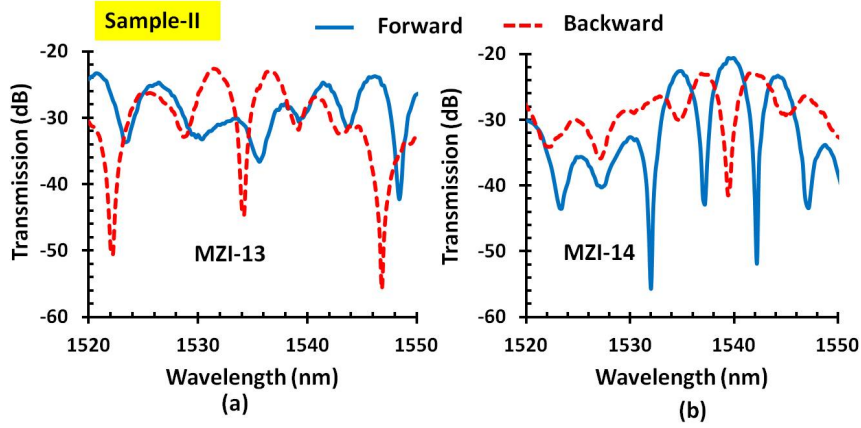


**Figure 5.29:** Normalized MZI transmission spectra for forward and backward propagation for (a) MZI-13 (b) MZI-14.

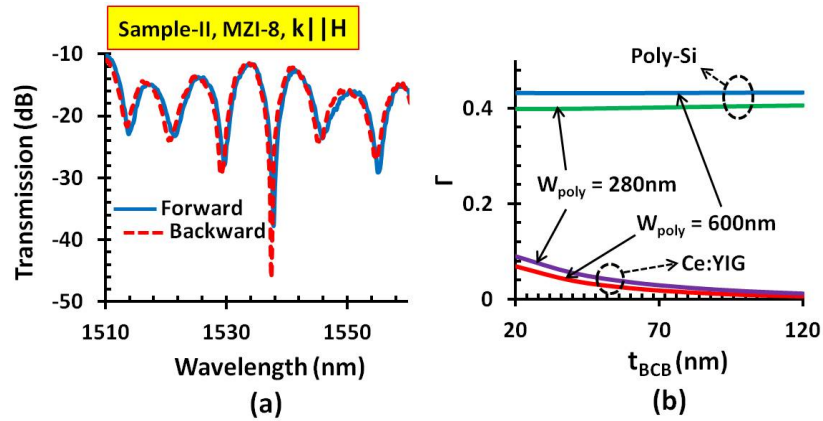


**Figure 5.30:** (a) Normalized MZI transmission spectra for forward and backward propagation of MZI-8 when the wave propagation vector ( $k$ ) and the external magnetic field ( $H$ ) are in parallel orientation (b) Simulation of the confinement factor ( $\Gamma$ ) of the TM mode into poly-Si overlay and Ce:YIG layer at 1540 nm wavelength.

to assess based on the fabricated devices but can for a large part be attributed to the scattering losses in the poly-Si (20 dB/cm) and in the Ce:YIG (30 dB/cm for annealed garnet). Therefore switching to c-Si overlay and improving the Ce:YIG deposition process is key to reducing the insertion loss of the device. To estimate the insertion losses both from the poly-Si layer and Ce:YIG layer, the confinement factor ( $\Gamma$ ) of the TM mode into these respective layers has to

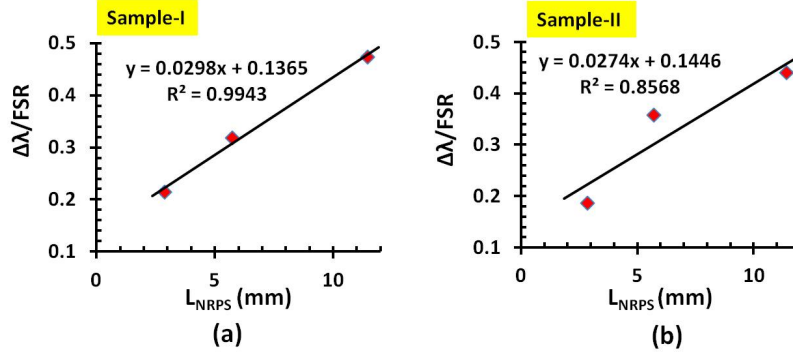


**Figure 5.31:** Plots of  $\Delta\lambda/FSR$  vs.  $L_{NRPS}$  considering MZI-2, 8 and 14 for (a) sample-I and (b) sample-II, where  $\Delta\lambda$  is the spectral shift between forward and backward light propagations as measured under the unidirectional transverse magnetic field.

be simulated. The simulation results are shown in Fig.5.30(b), assuming a rectangular waveguide geometry having 160 nm thick poly-Si on top of 230 nm c-Si together with a 5 nm thick  $SiO_2$  layer sandwiched between them. This accounts for 2 dB/cm loss due to the garnet and 8 dB/cm due to the poly-Si. The measured difference in the losses between MZI-8 and MZI-14 is approximately 7-8 dB. Hence one ADP waveguide section is responsible for 7-8 dB loss. This implies that the remaining insertion loss per polarization rotator amounts to 2.0 - 2.5 dB.

The NRPS is calculated from the relation  $\frac{\Delta\lambda}{FSR} = L_{NRPS} \cdot \frac{NRPS}{2\pi}$ , based on the measurements from MZI-2, 8 and 14 for both the samples. The NRPS from sample-I and sample-II are calculated as 0.19 rad/mm and 0.17 rad/mm respectively. Which implies that the BCB thickness between the Ce:YIG and silicon for sample-I was around 80 nm and slightly thicker for sample-II.

## 5.6 Conclusion

In this chapter a practical realization of a novel optical isolator for TE polarized light integrated on Silicon-on-insulator is discussed. Every component is discussed in great detail discussing both the ideal and real situation. A variety of devices were tested to get a good idea of the optimally performing device. Out of three designed polarization rotators one of them worked efficiently. A maximum isolation of 32 dB was obtained experimentally at 1540.5 nm wavelength for a nonreciprocal phase shifter length of 11.44 mm. The measured insertion of this device is about 23 dB. The insertion loss can be reduced by using a better

fabrication process and also by redesigning the polarization rotator. The MZI containing 600 nm wide NRPS section is the better choice over the MZI with 280 nm wide NRPS section. This type of isolator could be useful particularly for isolating semiconductor laser diodes integrated on silicon waveguide circuits as demonstrated recently [15]. To conclude this demonstration provides a path towards the direct heterogeneous integration of optical isolators and laser diodes on a silicon platform.

## References

- [1] Hiromasa Shimizu and Yoshiaki Nakano. *Fabrication and Characterization of an InGaAsp/InP Active Waveguide Optical Isolator With 14.7 dB/mm TE Mode Nonreciprocal Attenuation*. IEEE Journal of Lightwave Technology, 24(1):38–43, 2006.
- [2] S. Ghosh, S. Keyvavinia, W. Van Roy, T. Mizumoto, G. Roelkens, and R. Baets. *Ce:YIG/Silicon-on-Insulator waveguide optical isolator realized by adhesive bonding*. Optics Express, 20(2):1839–48, January 2012.
- [3] Samir Ghosh, Shahram Keyvaninia, Yuya Shoji, Wim Van Roy, Tetsuya Mizumoto, Gunther Roelkens, and Roel G Baets. *Compact Mach-Zehnder Interferometer Ce:YIG/SOI Optical Isolators*. IEEE Photonics Technology Letters, 24(18):1653–1656, 2012.
- [4] Dirk Taillaert, Peter Bienstman, and Roel Baets. *Compact efficient broadband grating coupler for silicon-on-insulator waveguides*. Optics Letters, 29(23):2749–51, December 2004.
- [5] Jing Zhang, Mingbin Yu, Guo-qiang Patrick Lo, Dim-lee Kwong, and A Abstract. *Silicon-Waveguide-Based Mode Evolution Polarization Rotator*. IEEE Journal of Selected Topics in Quantum Electronics, 16(1):53–60, 2010.
- [6] Daoxin Dai and John E Bowers. *Novel concept for ultracompact polarization splitter-rotator based on silicon nanowires*. Optics Express, 19(11):10940–9, May 2011.
- [7] Liu Liu, Yunhong Ding, Kresten Yvind, and Jørn M Hvam. *Silicon-on-insulator polarization splitting and rotating device for polarization diversity circuits*. Optics Express, 19(13):12646–51, June 2011.
- [8] Chris Brooks, Paul E. Jessop, Henghua Deng, David O. Yevick, and Garry Tarr. *Passive silicon-on-insulator polarization-rotating waveguides*. Optical Engineering, 45(4):044603–044603–5, 2006.

- 
- [9] Daryl M Beggs, Michele Midrio, and Thomas F Krauss. *Compact polarization rotators for integrated polarization diversity in InP-based waveguides*. Optics Letters, 32(15):2176–8, August 2007.
- [10] Diedrik Vermeulen, Student Member, Shankar Selvaraja, Peter Verheyen, Philippe Absil, Wim Bogaerts, Dries Van Thourhout, and Gunther Roelkens. *Silicon-on-Insulator Polarization Rotator Based on a Symmetry Breaking Silicon Overlay*. IEEE Photonics Technology Letters, 24(6):482–484, 2012.
- [11] C Alonso-Ramos, Robert Halir, Al Ortega-Moñux, Pavel Cheben, Laurent Vivien, Iñ Molina-Fernández, Delphine Marris-Morini, Si Janz, D-XXu, and Jens Schmid. *A general approach for integrated polarization rotators*. In SPIE Optics+ Optoelectronics, pages 878109–878109. for, 2013.
- [12] Jos JGM van der Tol, Manuela Felicetti, and Meint K Smit. *Increasing tolerance in passive integrated converters*. Journal of Lightwave Technology, 30(17):2884–2889, 2012.
- [13] Kurt De Mesel, Steven Verstuyft, Ingrid Moerman, Peter Van Daele, and Roel Baets. *Oxide-confined laser diodes with an integrated spot-size converter*. IEEE Journal of Selected Topics in Quantum Electronics, 8(6):1372–1380, 2002.
- [14] Seung Yeol Lee, Jae Su Yu, and Yong Tak Lee. *Fabrication of self-aligned ridge waveguide lasers with spot-size converter for quantum well intermixed superluminescent diodes*. Semiconductor Science and Technology, 23(2):025013, 2008.
- [15] Shahram Keyvaninia, Gunther Roelkens, Dries Van Thourhout, Christophe Jany, Marco Lamponi, Alban Le Liepvre, Francois Lelarge, Dalila Make, Guang-Hua Duan, Damien Bordel, and Jean-Marc Fedeli. *Demonstration of a heterogeneously integrated III-V/SOI single wavelength tunable laser*. Opt. Express, 21(3):3784–3792, Feb 2013.

# 6

## Optical Circulator on Silicon-on-Insulator(SOI)

**T**his chapter is devoted to the study of an integrated optical circulator based on MZI type design on the Silicon-on-Insulator (SOI) platform. To start with, a general overview of circulators is presented. Then the MZI-based broadband design is elaborated. Furthermore the idea of a broadband design is extended to realize a relatively narrowband device in the context of the BCB bonding approach. The MZI is built by two identical directional couplers. As a consequence the performance of the device is mostly dictated by the performance of these couplers. To achieve the best performing circulator different MZIs are designed by varying the coupling length of the directional coupler. Finally some measurement results are reported based on these devices.

### **6.1 Basics of an optical circulator**

The nomenclature itself suggests that a circulator is a three or multi-port device in which an electromagnetic (EM) wave circulates in a particular pre-defined direction. Ports are the points where waveguides or transmission lines (like a co-axial cable or a micro-strip line) are connected to the device. Symbolic views of a 3-port circulator operating in the clockwise (CW) and the counter clockwise

(CCW) directions are depicted in Fig. 6.1(a) and 6.1(b) respectively. If an EM signal is injected at port 1 the corresponding output power will appear at port 2 and not at port 3, and in the same manner the input at port 2 will appear at port 3, and not at port 1 for the case of CW operation. There are varieties of circulators available in the market for different frequency bands starting from very high frequency (VHF) to optical frequencies. Optical circulators are widely used in the fiber-optic communication systems. In all the wavelength regimes, the circulator works under the influence of an external magnetic field. Very low frequency circulators require very long device length, which makes it expensive, such that a non-magnetic approach is adopted for the low frequency operation [1].



**Figure 6.1:** Symbolic representation of a 3-port circulator operating in (a) CW (b) CCW directions.

## 6.2 Integrated circulator

In recent years, the SOI platform has become a promising technology platform for highly integrated photonic circuits by virtue of the high-index-contrast between the silicon waveguide core and silicon dioxide (SiO<sub>2</sub>) cladding. Although many bulk optical components have already been realized in an integrated format nonreciprocal devices like circulators are yet to be realized in an integrated format. These are essential components in an optical circuits as they can suppress any kind of unwanted reflection or can circulate the light in a particular direction. The applications of circulators in an optical communication system are numerous. Currently, commercially available circulators are built by assembling bulk optical components such as Faraday rotators, half-wave plates and polarization beam splitters.

The bulk scheme to realize a circulator can not be exploited in the case of a waveguide-based circulator because of phase mismatch between the TE and the TM modes of propagation [2]. To miniaturize an optical circulator a number of endeavors have already been reported with device lengths ranging from a few wavelengths [3–8] to hundreds of wavelengths [9–12]. Theoretically resonator

type designs have also been presented in which the clockwise and the counter clockwise modes of propagation experience a different phase velocity due to the influence of an external magnetic field [4, 13–15]. It is noteworthy to mention that the resonator-based devices inherently suffer from extremely narrowband operation although the device footprint is very small. The theoretical concept of a broadband planar optical circulator based on a 2D magneto-optical photonic crystal was reported in [16] by utilizing a one-way waveguide as described in [17–20]. Polarization rotation have also been implemented to build waveguide type optical circulators [10, 12]. Mach-Zehnder interferometer (MZI) type optical circulators were already investigated almost two decades ago [21]. Recently a direct molecular bonding method was used to demonstrate a 4-port optical circulator on a SOI platform [22, 23]. In this work, a different bonding approach namely BCB bonding is adopted to achieve the desired bonding between garnet-die and SOI. The merit of this approach over the direct molecular bonding approach was already discussed in Chapter 1. In the next section, the working principle of a broadband optical circulator is presented.

### 6.3 Principle of operation

MZI-based designs are widely used devices either for optical isolators or circulators due to its simple construction. To understand the operation principle of a MZI-based design as a circulator a broadband design is considered. The schematic diagram of the corresponding design is depicted in Fig.6.2. The de-

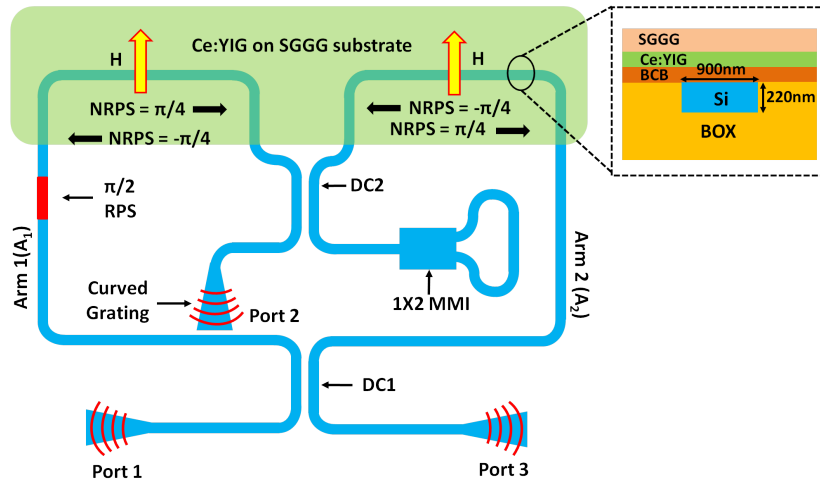


**Figure 6.2:** Schematic diagram of a 3-port broadband circulator

sign mainly consists of two directional couplers (DC1 and DC2) and a 1×2 MMI.

Light is injected and collected by curved grating couplers. The arms of the MZI is termed arm 1 ( $A_1$ ) and arm 2 ( $A_2$ ). One of the outputs of DC2 is connected to the MMI and the outputs of it are connected to form a loop which transforms the 4-port device into a 3-port device. Noteworthy to mention a 4-port device is easily realizable just by removing the MMI loop. For some particular cases 3-port circulators are desirable over a 4-port configuration. Some particular cases where 3-port circulators are used can be found in [24, 25]. A garnet-die containing ferrimagnetic Ce:YIG on SGGG substrate is symmetrically bonded on top of the MZI arms in such a way that the nonreciprocal phase shift (NRPS) provided by the garnet covered waveguides will be the same in magnitude but with a opposite sign when a unidirectional transverse magnetic field ( $H$ ) is applied. The length of the garnet covered part of the MZI arm which is transverse to the external magnetic field is assumed to be sufficient for a NRPS of  $|\pi/4|$ . Both the directional couplers are designed to be identical so that their coupling efficiency is same for any BCB layer thickness on top of it. The cross-section of the garnet bonded waveguide is shown in the inset of Fig.6.2. Arm 1 is slightly longer than Arm 2 to provide a reciprocal phase shift of  $\pi/2$  for light propagating either way.

Now we will analyze how the circuit behaves like a broadband 3-port circulator. Let us consider the light transmission between the ports 1 & 2 and 2 & 3. Light traveling through any arm of the MZI will experience different phase shifts at different parts of the circuit. All the aforementioned transmission are tabulated in Table 6.1 below: RP and NRP are the abbreviations used for recip-

Path	Arm	RP	NRP	$\phi$	Resultant interference
1→2	$A_1$	$\pi/2$	$\pi/4$	$3\pi/4$	Constructive
1→2	$A_2$	$\pi$	$-\pi/4$	$3\pi/4$	
2→1	$A_1$	$\pi/2$	$-\pi/4$	$\pi/4$	Destructive
2→1	$A_2$	$\pi$	$\pi/4$	$5\pi/4$	
2→3	$A_1$	$\pi$	$-\pi/4$	$3\pi/4$	Constructive
2→3	$A_2$	$\pi/2$	$\pi/4$	$3\pi/4$	
3→2	$A_1$	$\pi$	$\pi/4$	$5\pi/4$	Destructive
3→2	$A_2$	$\pi/2$	$-\pi/4$	$\pi/4$	

**Table 6.1:** Total phases at final ports without loop path

rocal phase and nonreciprocal phase respectively whereas  $\phi$  is the sum of them at the port where the output signal is collected finally. RP accounts for the contributions from all the reciprocal phase shifters in the circuit for any particular optical path not only from the  $\pi/2$  reciprocal phase shifter. The output signal at the cross-port of a directional is assumed to be  $\pi/2$  phase shifted as compared to the output signal at the bar-port. Transmission between ports 1 & 3 can be

explain by using Table 6.2, but in this case the analysis is more complicated because of the loop way (L) created by the  $1 \times 2$  MMI. Let us consider port 1 as input

Path	RP	NRP	$\phi$	Resultant interference
$1 \rightarrow A_1 \rightarrow L \rightarrow A_1 \rightarrow 3$	$5\pi/2$	0	$5\pi/2$	Destructive
$1 \rightarrow A_1 \rightarrow L \rightarrow A_2 \rightarrow 3$	$\pi$	$\pi/2$	$3\pi/2$	
$1 \rightarrow A_2 \rightarrow L \rightarrow A_1 \rightarrow 3$	$2\pi$	$-\pi/2$	$3\pi/2$	
$1 \rightarrow A_2 \rightarrow L \rightarrow A_2 \rightarrow 3$	$\pi/2$	0	$\pi/2$	
$3 \rightarrow A_1 \rightarrow L \rightarrow A_1 \rightarrow 1$	$5\pi/2$	0	$5\pi/2$	Constructive
$3 \rightarrow A_1 \rightarrow L \rightarrow A_2 \rightarrow 1$	$2\pi$	$\pi/2$	$5\pi/2$	
$3 \rightarrow A_2 \rightarrow L \rightarrow A_1 \rightarrow 1$	$\pi$	$-\pi/2$	$\pi/2$	
$3 \rightarrow A_2 \rightarrow L \rightarrow A_2 \rightarrow 1$	$\pi/2$	0	$\pi/2$	

**Table 6.2:** Total phases at final ports with loop path

and port 3 as output. Any input light at port 1 takes two routes via  $A_1$  and  $A_2$  after splitting at DC1. Input light in  $A_1$ , after the reflection from the  $1 \times 2$  MMI loop (L) is again divided by two parts at DC2 and follows two paths through  $A_1$  and  $A_2$ , finally meeting at port 3. This situation is depicted on the first two rows in Table 6.2 which shows that they are interfering out of phase and hence destructive interference occurs at port 3. An identical scenario occurs with input light in  $A_2$  which is shown by the 3rd and 4th row of Table 6.2 and results in destructive interference when they meet at port 3. Now for port 3 as input and port 1 as output similar phenomena will happen. The corresponding phases experienced by the light while traveling through the circuit is presented from the 5th to the 8th row of Table 6.2.

## 6.4 Narrowband device

In this work, the MZI is intentionally designed as perfectly balanced which means that there is no reciprocal phase shifter (RPS) in any of the MZI arms. The garnet-die is bonded in such a way that it could provide a reciprocal phase shift even for a perfectly balanced MZI. The group index of the BCB plus garnet clad waveguide substantially differs from only the BCB clad waveguide (for identical waveguide cross-sections) and hence a slightly tilted garnet die creates an effective optical path difference ( $\Delta L$ ) between arms of the MZI. The schematic of the bonded device is depicted in Fig.6.3. The free spectral range (FSR) of the MZI depends on the  $\Delta L$  provided by the garnet die. The FSR of the

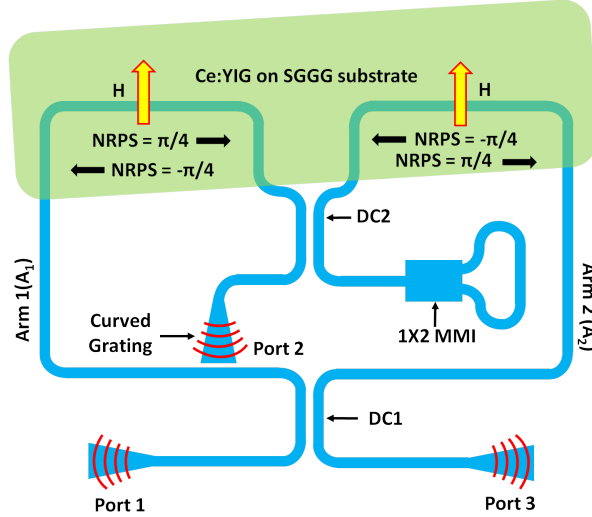


**Figure 6.3:** Schematic diagram of a 3-port narrow-band circulator.

fabricated MZI can be written as

$$FSR = \frac{\lambda_0^2}{\Delta n_g \cdot \Delta L} \quad (6.1)$$

where  $\lambda_0$  is the vacuum wavelength of light.  $\Delta n_g$  is the difference in group indices of the fundamental TM modes in the BCB plus garnet clad waveguide and in the waveguide only clad with BCB as shown in Fig. 6.4.

## 6.5 Design of directional coupler

The operation of the circulator mainly depends on the performance of the directional couplers (DC1 and DC2 in this case). In this work, both the directional couplers are identically designed and both of them are assumed to be covered by the same BCB thickness. The power splitting efficiency together with the phase difference between the output signal of the directional coupler as a function of various parameters is presented here in great detail. For all the cases a rectangular shaped waveguide cross-section is considered. The artistic impression of the directional coupler is presented in Fig.6.5. The trench of the silicon waveguide is filled with SiO<sub>2</sub>. The silicon waveguide throughout the circuit is 900 nm wide with a silicon device thickness  $t_{Si}$ . The gap between two identical waveguides at the coupling section is  $g$  and has a length  $L_c$ . Apart from that constant coupling length a contribution also comes from the curved waveguides. An equivalent straight length adding to  $L_c$  from that bent coupling sec-

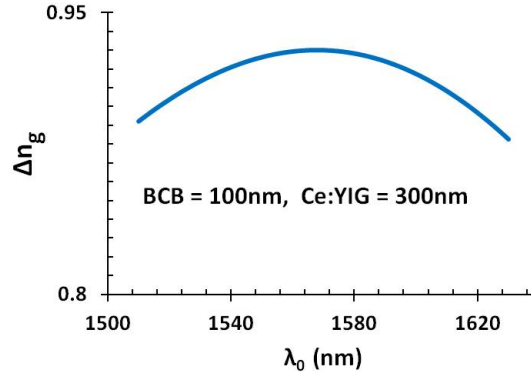


**Figure 6.4:** Variation of  $\Delta n_g$  as a function of the vacuum wavelength for waveguides of width 900 nm and height 220 nm with 100 nm BCB and 300 nm thick Ce:YIG layer.

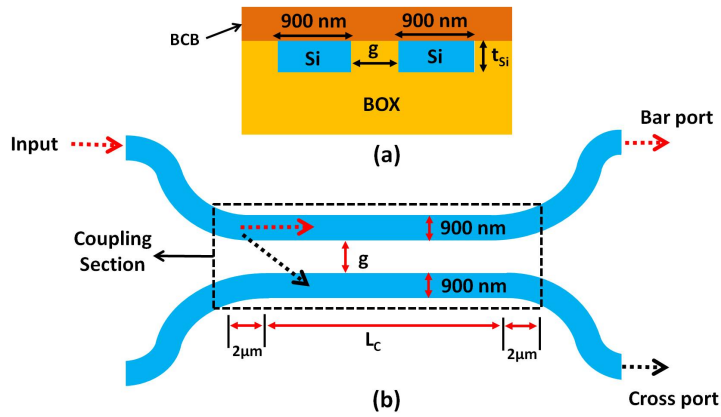


**Figure 6.5:** Artistic impression of directional coupler (a) Cross-section view of coupling section, (b) Top-view of directional coupler.

tion is taken as  $2\mu\text{m}$  on each side of the directional coupler. The output power at bar and cross port of the directional coupler as a function of the length of the coupling section ( $L_c$ ) is shown in Fig.6.6. The coupling section is defined as the straight-section with a constant gap ( $g$ ). From Fig.6.6, we can see that for a particular  $L_c$  the directional coupler performs as a perfect 3dB coupler/splitter. Noteworthy to mention that this splitting ratio is also wavelength dependent. It obviously means that the designed narrowband circulator will show variable extinction ratios depending on the working wavelength which will be verified later in the experimental results. In this context, the variation of the coupling

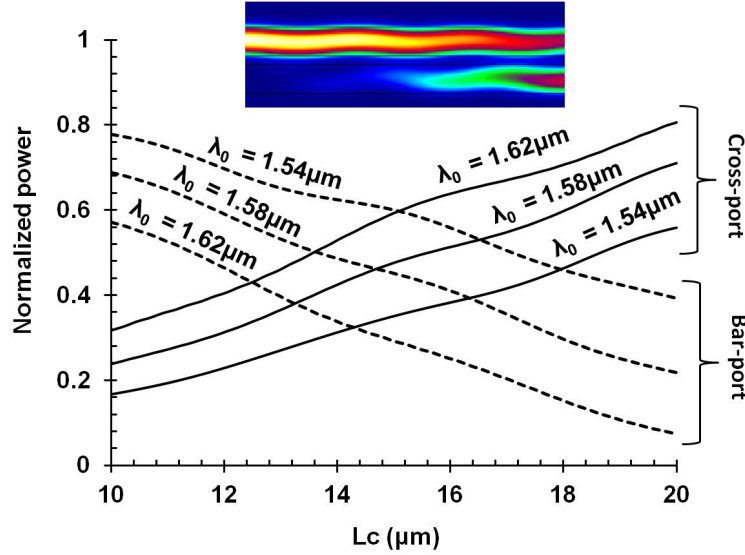


**Figure 6.6:** Coupling efficiency as a function of coupling length ( $L_c$ ) for a 250 nm gap ( $g$ ) between two identical rectangular shaped silicon waveguides of width 900 nm and thickness 220 nm with a trench filled with  $\text{SiO}_2$  and 100 nm thick BCB as top cladding.

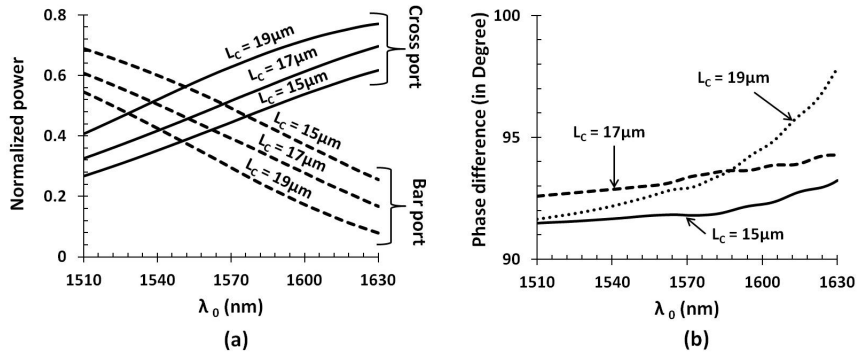


**Figure 6.7:** (a) Coupling efficiency as a function of wavelength ( $\lambda_0$ ) for different  $L_c$ , (b) Phase difference between the bar and the cross port as a function of wavelength ( $\lambda_0$ ). The width and height of the identical waveguides are 900 nm and 220 nm respectively with 100 nm BCB.

efficiency as a function of wavelength ( $\lambda_0$ ) for different values of  $L_c$  is depicted in Fig.6.7. The dependence of the coupling efficiency on the Si waveguide thickness ( $t_{Si}$ ) as well as on the BCB thickness is shown in Fig.6.8(a) and Fig.6.8(b)

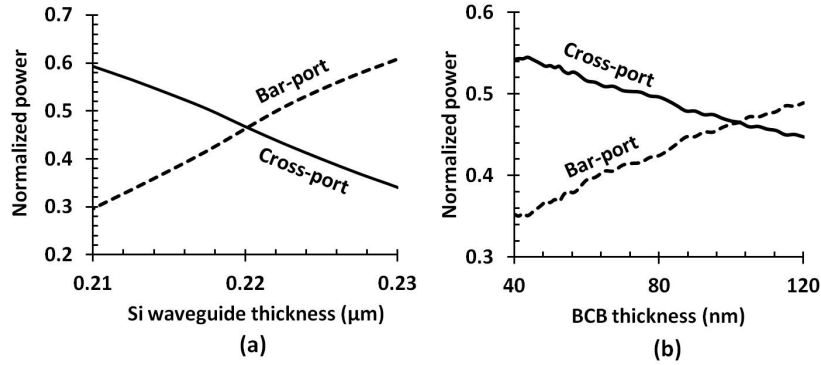


**Figure 6.8:** (a) Coupling efficiency as a function of silicon waveguide thickness for  $L_c = 15 \mu\text{m}$ , 100 nm thick BCB at 1577 nm wavelength (b) Phase difference between the bar and the cross port as a function of wavelength ( $\lambda_0$ ). The width and thickness of the identical waveguides are 900 nm and 220 nm respectively with 100 nm BCB.

respectively.

### 6.5.1 MMI as a replacement for directional coupler

We have already seen that the performance of the directional coupler is very sensitive to the silicon waveguide thickness as well as BCB thickness. Moreover the extinction ratio of the MZI based on directional couplers varies with the wavelength because the splitting ratios of the directional couplers designed are strongly dependent on the wavelength. Therefore, a suitable replacement for the directional coupler is stringently required to achieve an almost uniform extinction and hence an isolation throughout the operational wavelength window.

The schematic diagram of the MMI is shown in Fig.6.9(a) depicting all the designed parameters. The length of the multimode section ( $L_{MMI}$ ) is simulated for optimum performance. The optimal length is  $14.3 \mu\text{m}$  according to Fig.6.9(b) for 100 nm of BCB at 1550 nm wavelength. The spectral dependence of the power splitting efficiency as well as the relative phase difference between the output light at the bar and cross ports of this designed  $2 \times 2$  MMI are shown in Fig.6.10(a) and Fig.6.10(b) respectively. Two other important variables are the thicknesses of the silicon waveguide and the BCB. The behavior of the MMI with respect to these variables are depicted in Fig.6.11. From Fig.6.7(a) and Fig.6.10(a) it is clear that the power splitting efficiency of the  $2 \times 2$  MMI is less sensitive to the wavelength variation as compared to the directional coupler.

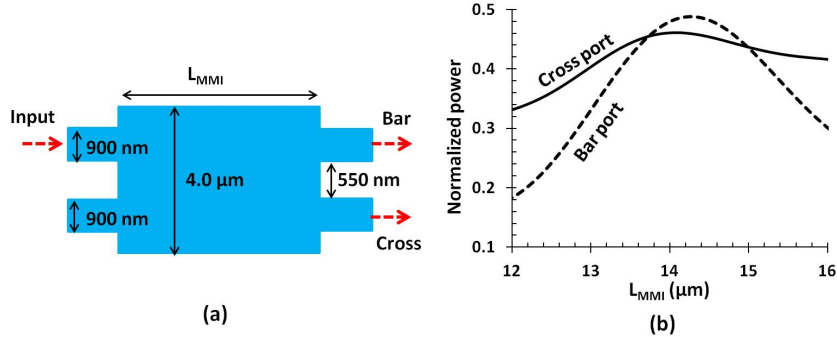


**Figure 6.9:** (a) Schematic diagram of a  $2 \times 2$  MMI (b) simulation of the length of the multimode section ( $L_{MMI}$ ) of the MMI for 100 nm BCB at 1550 nm wavelength.

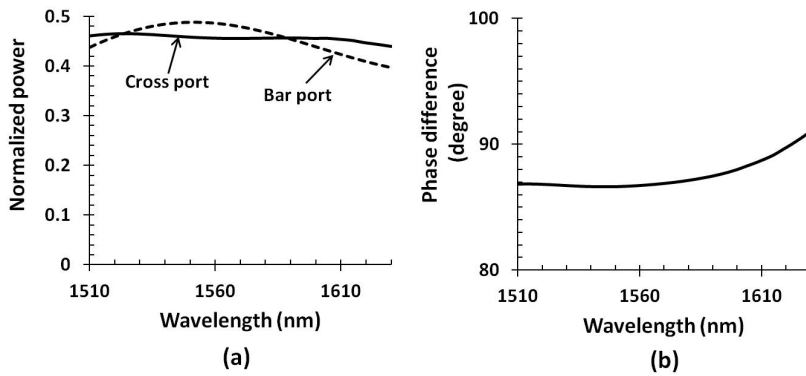


**Figure 6.10:** (a) Power splitting efficiencies of the MMI at the bar and cross ports of a  $2 \times 2$  MMI when the wavelength is varied (b) Phase difference between the bar and cross ports as a function of wavelength. The BCB thickness is 100 nm.

Comparing Fig.6.8 and Fig.6.11 we can see that power splitting efficiency of the  $2 \times 2$  MMI is remained almost constant as compared to directional coupler when Si waveguide thickness or BCB thickness are varied. Therefore we can conclude that a  $2 \times 2$  MMI is very robust as compared to a directional coupler.

## 6.6 Measurements

As only the TM mode can experience the NRPS in this configuration, TM curved grating couplers were used to inject and collect light from the respective ports

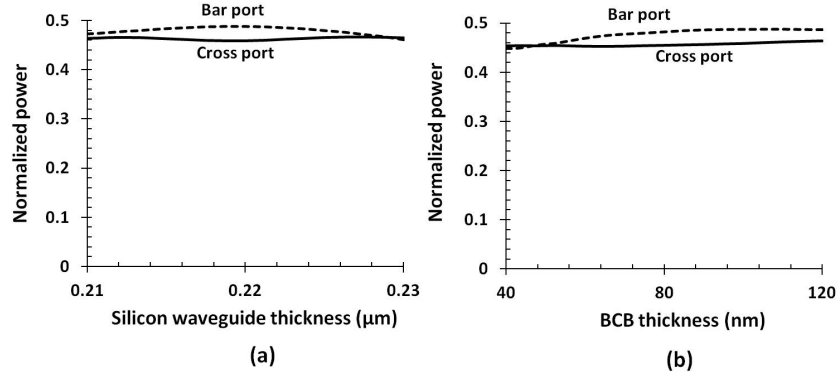


**Figure 6.11:** (a) Power splitting efficiencies to the bar and cross ports of a  $2 \times 2$  MMI as a function (a) silicon waveguide thickness and (b) BCB thickness.

[26]. A stack of three miniature Nd-B-Fe magnets are used to bias the ferrimagnetic Ce:YIG layer. Input and output fibers are swapped while the magnet orientation is kept fixed during the measurements. Several samples were bonded with varying orientation of the garnet-die on the MZI arms to obtain MZIs with varying FSR. In this section, we will elaborate on the measurement results from different samples. For the sake of simplicity, these samples are called sample-I, sample-II and sample-III. A set-up was designed in which three fibers could be aligned onto three ports of the MZI simultaneously with a fixed magnetic field.

For the case of sample-I, the MZI contains directional couplers of  $L_c = 19 \mu\text{m}$ . The power transmission results are shown in Fig.6.12(a) and Fig.6.12(b) for the counterclockwise (CCW) and the clockwise (CW) propagation through the circulator respectively. Power transmission between all the combination of ports at 1568 nm are shown in Table 6.3. The FSR of the MZI increases with the wavelength which could be due to the dependence of group index on wavelength. The average measured FSR between 1550-1570 nm wavelength is about 11 nm. This means that the difference in garnet covered lengths in both the arms is about  $240 \mu\text{m}$  as the mean group index of garnet and BCB clad waveguide differs from only from that of the BCB clad waveguide by 0.92 in the 1550-1570 nm wavelength range. The maximum isolation between two particular port is varying with wavelength. For instance a maximum of 18 dB isolation was measured at 1528 nm between ports 1 and 2 whereas for the case of ports 2 and 3 a maximum of 27 dB isolation was observed at 1604.4 nm.

For the case of sample-II, the MZI is built by directional couplers of  $L_c = 15 \mu\text{m}$ . Transmission results are depicted in Fig.6.13(a) and Fig.6.13(b) for the counterclockwise (CCW) and the clockwise (CW) propagation through the cir-

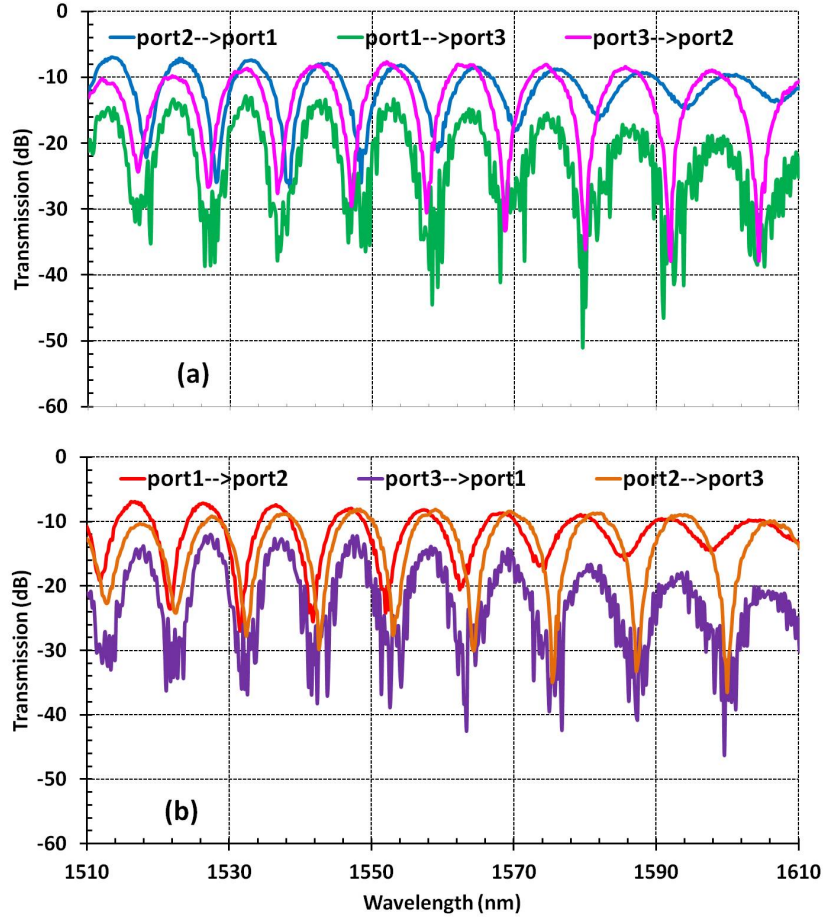


**Figure 6.12:** Sample-I: Measured optical transmission spectra at different ports of the circulator under a constant magnetic field (a) CCW (b) CW.

Ports	Transmission(dB)	Ports	Transmission(dB)
1→2	-9	2→1	-13
2→3	-10	3→2	-23
3→1	-17	1→3	-30

**Table 6.3:** Sample-I: Measured transmissions(T) at 1568 nm

culator respectively. The average FSR of 20 nm implies that the difference in garnet covered lengths in both arms is about 135  $\mu\text{m}$ . This is because the mean

group index of BCB plus garnet clad waveguide differs from only BCB clad waveguide by 0.92 in the 1540-1600 nm wavelength range. An isolation of 22dB is observed between ports 1 and 2 at 1562 nm.

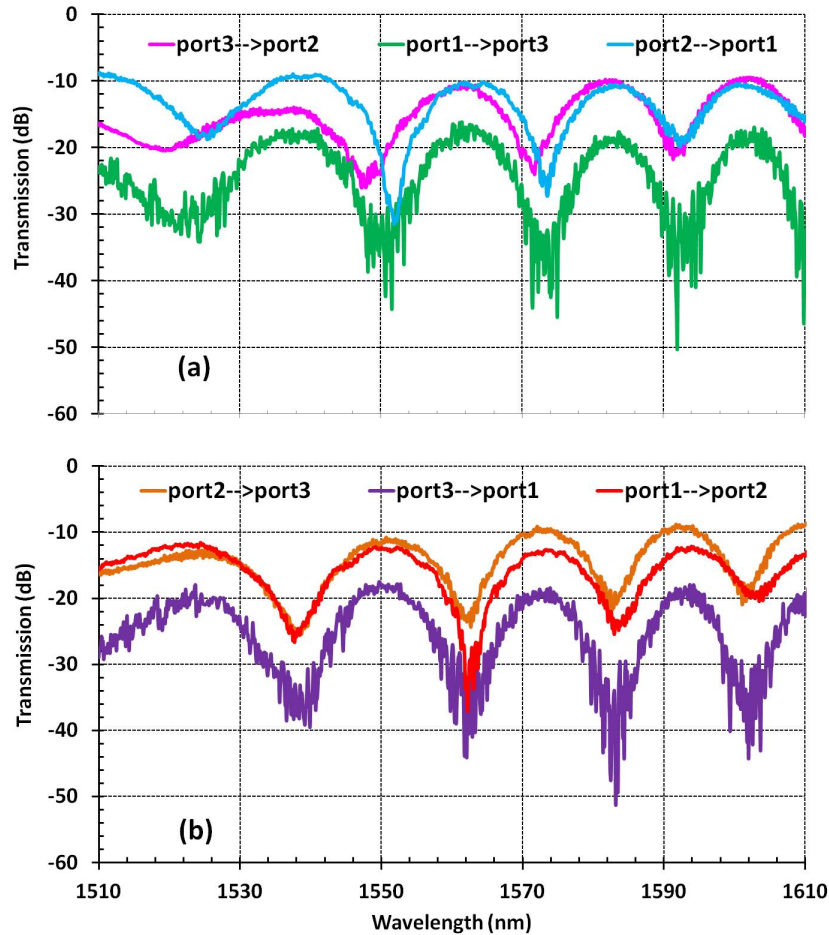


**Figure 6.13:** Sample-II: Measured optical transmission spectra at different ports of the circulator under a constant magnetic field (a) CCW (b) CW.

For the case of sample-III, the MZI contains directional couplers of  $L_c = 15 \mu\text{m}$ . The measured transmission spectra for the CCW and the CW direction are presented in Fig.6.14(a) and Fig.6.14(b) respectively. The characteristics of these two graphs are very different from the graphs for the other two samples (sample-I and sample-II). In particular the most interesting phenomena hap-

Ports	Transmission(dB)	Ports	Transmission(dB)
1→2	-13	2→1	-22
2→3	-9	3→2	-20
3→1	-19	1→3	-32

**Table 6.4:** Sample-II: Measured transmissions(T) at 1573 nm

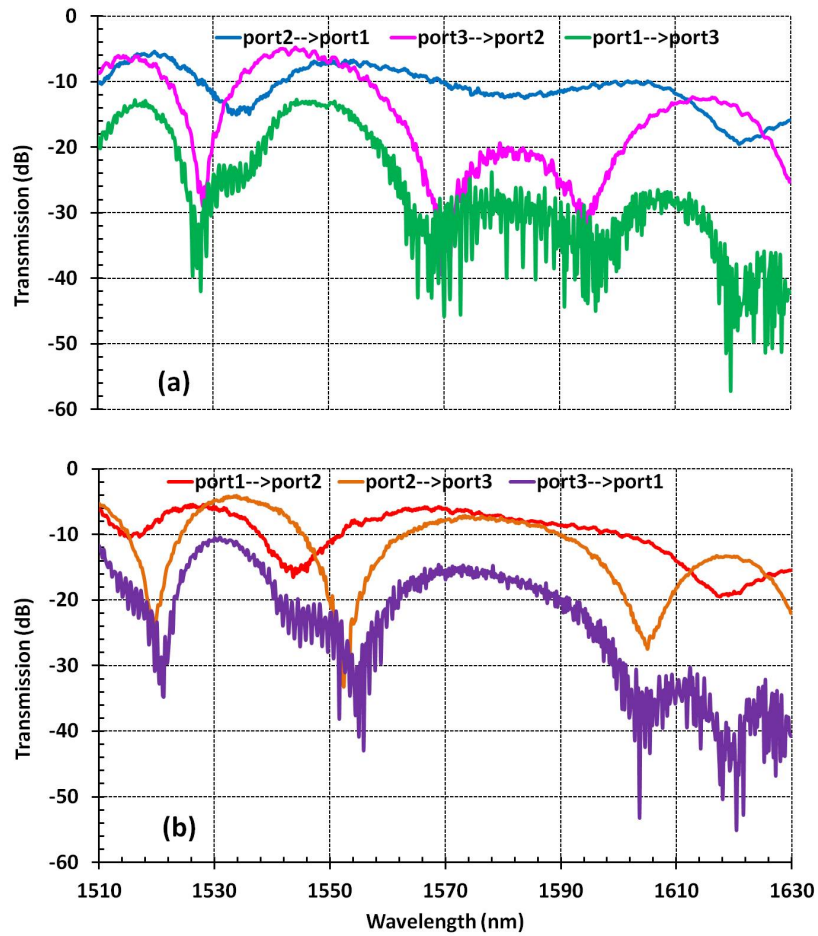


**Figure 6.14:** Sample-III: Measured optical transmission spectra at different ports of the circulator under a constant magnetic field (a) CCW (b) CW.

Ports	Transmission(dB)	Ports	Transmission(dB)
1→2	-7	2→1	-12
2→3	-8	3→2	-20
3→1	-17	1→3	-27

**Table 6.5:** Sample-III: Measured transmissions(T) at 1580 nm

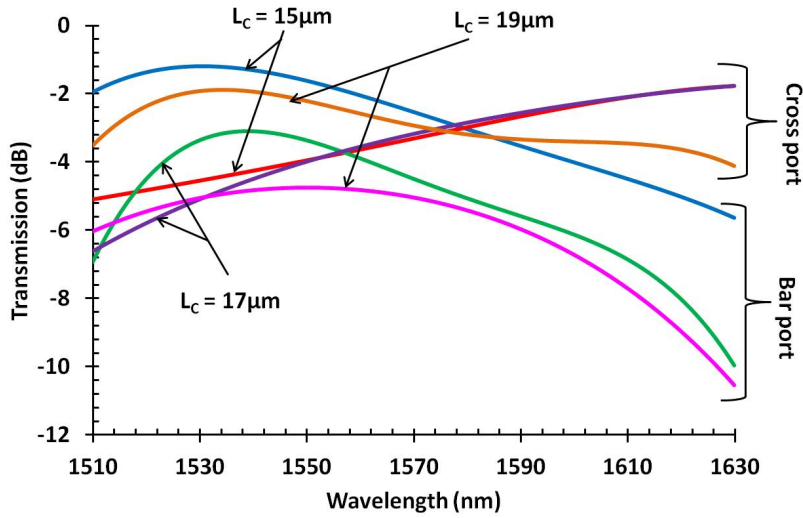


**Figure 6.15:** Sample-I: Measured optical transmission spectra at bar and cross ports of different reference directional couplers.

pens between 1550-1610 nm wavelength range. Relatively broadband operation is observed for the transmission between the corresponding ports. It is important to mention that all the six measurements were not obtained simultaneously because of the set-up constraints and for each set of measurements the magnet-stack needed to be moved while keeping the direction of the magnetic field unaltered. This may have resulted in a small offset of the wavelengths at which perfect constructive and destructive interference occurred. Perfectly balanced splitters would result in an even higher optical isolation. The power transmission levels between ports 1 and 3 are about 8-10 dB less compared to the other ports because of the double path length traversed by the light after reflecting back from the  $1 \times 2$  MMI including 0.5 dB loss due to the MMI. The total insertion loss for the transmission between ports 1 and 2 or ports 2 and 3 (for the sample I and II) is about 10 dB which is consistent with the value reported in [27, 28]. The performance of the reference directional couplers was also characterized

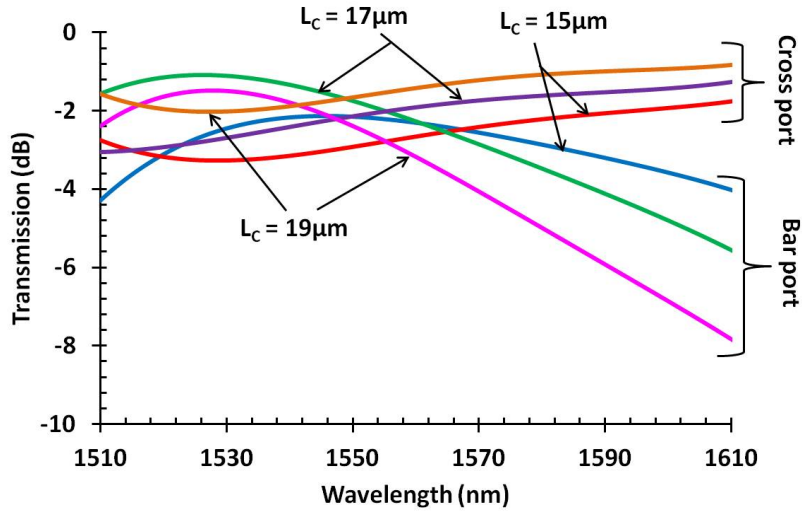


**Figure 6.16:** Sample-II: Measured optical transmission spectra at bar and cross ports of different reference directional couplers.

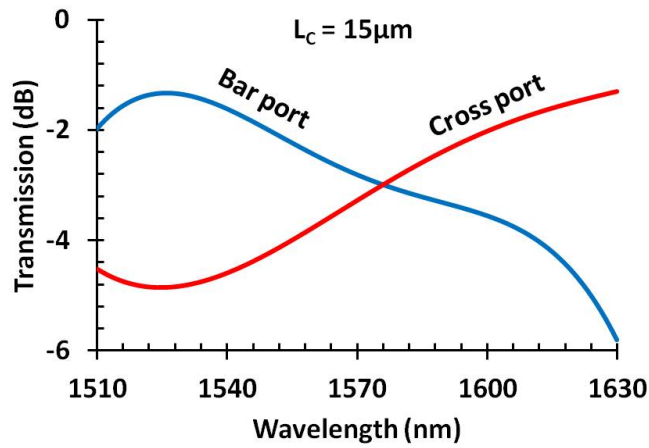


**Figure 6.17:** Sample-III: Measured optical transmission spectra at bar and cross ports of the reference directional coupler.

separately as shown in Fig.6.15, Fig.6.16 and Fig.6.17 for sample I, II and III respectively, which are assumed to have been covered by 100 nm BCB thickness. The trend shown in Fig.6.7 also corresponds to the measured values as shown in the aforementioned figures.

## 6.7 Conclusion

In conclusion, a 3-port circulator was demonstrated on the SOI platform using an adhesive BCB bonding technique. SOI-based MZI structures were designed. The main building block of the circular used in this work was the directional coupler. The performance or power splitting efficiency of the directional coupler was simulated and also measured experimentally. The power splitting efficiency of the directional coupler was very sensitive to the wavelength, Si waveguide thickness and BCB thickness which limit the obtainable isolation. Hence, to find an alternative for the directional coupler performance of a  $2 \times 2$  MMI was studied by simulating its power splitting efficiency as a function of wavelength, Si waveguide thickness and BCB thickness. It was clear from the simulations that a  $2 \times 2$  MMI is a better choice in the place of a directional coupler. Different types of circulars were designed and characterized using directional couplers of varying lengths. Not only that FSR of the MZI was also varied by changing orientation of garnet die during manual bonding. A maximum of 27 dB of optical isolation was measured at 1604.4 nm. While the performance and the insertion loss of the device can be improved, the demonstration provides scope for the integration of circulators with other photonic components to achieve a fully functional photonic integrated circuit.

## References

- [1] Charles Wenzel. *Low frequency circulator/isolator uses no ferrite or magnet*. RF Design, pages 39–43, 1991.
- [2] Tauhid R Zaman, Xiaoyun Guo, and Rajeev J Ram. *Semiconductor waveguide isolators*. Journal of Lightwave Technology, 26(2):291–301, 2008.
- [3] Zheng Wang and Shanhui Fan. *Magneto-optical defects in two-dimensional photonic crystals*. Applied Physics B, 81(2-3):369–375, 2005.
- [4] Zheng Wang and Shanhui Fan. *Optical circulators in two-dimensional magneto-optical photonic crystals*. Optics letters, 30(15):1989–1991, 2005.
- [5] Zheng Wang and Shanhui Fan. *Suppressing the effect of disorders using time-reversal symmetry breaking in magneto-optical photonic crystals: An illustration with a four-port circulator*. Photonics and Nanostructures-Fundamentals and Applications, 4(3):132–140, 2006.
- [6] Wojciech Śmigaj, Javier Romero-Vivas, Boris Gralak, Liubov Magdenko, Béatrice Dagens, and Mathias Vanwolleghem. *Magneto-optical circulator designed for operation in a uniform external magnetic field*. Optics letters, 35(4):568–570, 2010.

- [7] Kazuo Yayoi, Kazuma Tobinaga, Yusuke Kaneko, Alexander V Baryshev, and Mitsuteru Inoue. *Optical waveguide circulators based on two-dimensional magnetophotonic crystals: Numerical simulation for structure simplification and experimental verification*. Journal of Applied Physics, 109(7):07B750–07B750, 2011.
- [8] Haibin Zhu and Chun Jiang. *Optical isolation based on nonreciprocal micro-ring resonator*. Journal of Lightwave Technology, 29(11):1647–1651, 2011.
- [9] Manfred Lohmeyer, Mikhail Shamonin, and Peter Hertel. *Integrated optical circulator based on radiatively coupled magneto-optic waveguides*. Optical Engineering, 36(3):889–895, 1997.
- [10] N Sugimoto, T Shintaku, A Tate, H Terui, M Shimokozono, E Kubota, M Ishii, and Y Inoue. *Waveguide polarization-independent optical circulator*. IEEE Photonics Technology Letters, 11(3):355–357, 1999.
- [11] Junichiro Fujita, Reinald Gerhardt, and Louay A. Eldada. *Hybrid-integrated optical isolators and circulators*. pages 77–85, 2002.
- [12] Naoki Hanashima, Kenjiro Hata, Reio Mochida, Toru Oikawa, Tohru Kineri, Yoshinori Satoh, and Shinji Iwatsuka. *Hybrid optical circulator using garnet-quartz composite embedded in planar waveguides*. Photonics Technology Letters, IEEE, 16(10):2269–2271, 2004.
- [13] P Pintus, Ming-Chun Tien, and John E Bowers. *Design of Magneto-Optical Ring Isolator on SOI Based on the Finite-Element Method*. Photonics Technology Letters, IEEE, 23(22):1670–1672, 2011.
- [14] Naoya Kono, Kuniaki Kakihara, Kunimasa Saitoh, and Masanori Koshiba. *Nonreciprocal microresonators for the miniaturization of optical waveguide isolators*. Optics Express, 15(12):7737–7751, 2007.
- [15] Dirk Jalas, Alexander Petrov, Michael Krause, Jan Hampe, and Manfred Eich. *Resonance splitting in gyrotropic ring resonators*. Optics letters, 35(20):3438–3440, 2010.
- [16] Wenjun Qiu, Zheng Wang, and Marin Soljačić. *Broadband circulators based on directional coupling of one-way waveguides*. Opt. Express, 19(22):22248–22257, 2011.
- [17] FDM Haldane and S Raghu. *Possible realization of directional optical waveguides in photonic crystals with broken time-reversal symmetry*. Physical review letters, 100(1):013904, 2008.

- [18] Zheng Wang, Y. D. Chong, John D. Joannopoulos, and Marin Soljačić. *Reflection-Free One-Way Edge Modes in a Gyromagnetic Photonic Crystal*. Phys. Rev. Lett., 100:013905, Jan 2008.
- [19] Zongfu Yu, Georgios Veronis, Zheng Wang, and Shanhui Fan. *One-Way Electromagnetic Waveguide Formed at the Interface between a Plasmonic Metal under a Static Magnetic Field and a Photonic Crystal*. Phys. Rev. Lett., 100:023902, Jan 2008.
- [20] Zheng Wang, Yidong Chong, and Marin Soljačić & JD Joannopoulos. *Observation of unidirectional backscattering-immune topological electromagnetic states*. Nature, 461(7265):772–775, 2009.
- [21] T Mizumoto, H Chihara, N Tokui, and Y Naito. *Verification of waveguide-type optical circulator operation*. Electronics Letters, 26(3):199–200, 1990.
- [22] Kota Mitsuya, Yuya Shoji, and Tetsuya Mizumoto. *The First Demonstration of Silicon Waveguide Optical Circulator*. In National Fiber Optic Engineers Conference. Optical Society of America, 2013.
- [23] K. Mitsuya, Y. Shoji, and T. Mizumoto. *Demonstration of a Silicon Waveguide Optical Circulator*. IEEE Photonics Technology Letters, 25(8):721–723, 2013.
- [24] Hiroki Takesue and Toshihiko Sugie. *Wavelength channel data rewrite using saturated modulator for WDM networks with centralized*. Journal of lightwave technology, 21(11):2546, 2003.
- [25] Satoshi Narikawa, Hiroaki Sanjoh, Naoya Sakurai, and Kiyomi Kumozaki. *Gbit-class using data rewriter for WDM-PON*. IEICE transactions on communications, 91(2):399–408, 2008.
- [26] Diedrik Vermeulen, Karel Van Acoleyen, Samir Ghosh, Wout De Cort, Nebiyu Adello Yebo, Elewout Hallynck, Katrien De Vos, Peter Debackere, Pieter Dumon, Wim Bogaerts, et al. *Efficient tapering to the fundamental quasi-TM mode in asymmetrical waveguides*. European Conference on Integrated Optics (ECIO), United Kindom, 2010.
- [27] Samir Ghosh, Shahram Keyvaninia, W Van Roy, T Mizumoto, Günther Roelkens, and Roel Baets. *Ce: YIG/SOI optical isolator realized by BCB bonding*. In Group IV Photonics (GFP), 2011 8th IEEE International Conference on, pages 196–198. IEEE, 2011.
- [28] S. Ghosh, S. Keyvavinia, W. Van Roy, T. Mizumoto, G. Roelkens, and R. Baets. *Ce:YIG/Silicon-on-Insulator waveguide optical isolator realized by adhesive bonding*. Optics Express, 20(2):1839–48, January 2012.



# 7

## Nonreciprocal Nested Ring Mach-Zehnder Interferometer

**T**his chapter is devoted to the study of an optical isolator based on a resonator type device. In the first section, the basic idea will be presented and thereafter this idea will be implemented with different schemes to achieve optical isolation. The devices presented here are nested ring Mach-Zehnder interferometers (NRMZI). Two types of NRMZI are presented distinguished by the coupling section. A rigorous analytical calculation of such devices is presented. At the end of this chapter transmission measurements for such devices are presented. These new designs show a promising path for an optical isolator with a small footprint and narrowband operation.

### 7.1 Nested ring resonator MZI

Micro-ring resonators (MRR) are attractive building blocks in integrated optics due to their high wavelength selectivity which makes them interesting for various applications like filters, modulators and sensors [1–3]. A MRR is constructed by several waveguides in which at least one waveguide forms a close loop. The most simple configuration is the one which contains only one straight waveguide and a loop path for feedback as depicted in Fig.7.1(a), known as an all-

pass ring resonator. If these two waveguides are designed in such a manner that some input light is coupled into the loop then this optical feedback can interfere constructively or destructively with the input light depending on the phase relationship between them. Another ubiquitously used configuration is the add-drop ring resonator as shown in Fig.7.1(b). In both the figures  $t$  and  $k$  are denoted as self and cross coupling coefficients respectively. Therefore,  $t^2$  and  $k^2$  are respectively known as the power splitting ratios of the coupler, such that  $t^2 + k^2 = 1$ . A detailed comprehensive discussion on Silicon-on-insulator (SOI) based optical ring resonator has been studied extensively and can be found in various literature [4–7]. In the context of optical isolators, we will confine our discus-

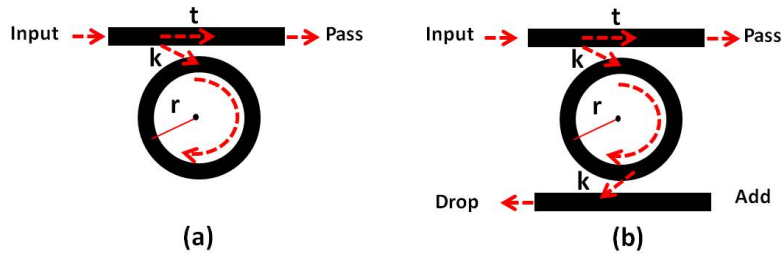


**Figure 7.1:** Micro-ring resonator configurations (a) all-pass (b) add-drop.

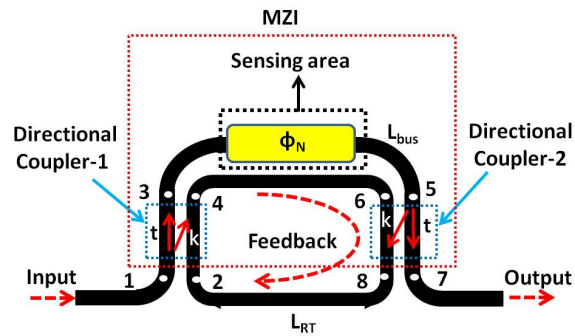


**Figure 7.2:** Schematic diagram of a nested ring MZI (NRMZI).

sions only to the NRMZI rather than an all pass configuration as shown here [8]. A NRMZI comprises of a MRR and a feedback loop as shown in Fig.7.2. If the coupling sections are designed optimally then this type of device could provide a high quality factor (Q-factor) and a high extinction ratio (ER). The main advantage of this kind of device over the simple all pass configuration is the fact that the resonance condition (under coupled, critically coupled, over coupled) of the ring depends on the relative phase relationship between the arms of MZI

formed by the bus and the ring waveguides (see Fig.7.2). A small index change by any external effect on the bus waveguide could lead to a drastic change in the resonance behavior of the circuit. Some notable demonstrations can be found here [9–11].

Now let us discuss the situation when a nonreciprocal phase shifter is integrated in the sensing region of the bus waveguide as shown in Fig.7.2. Let us assume that a signal of field amplitude  $E_1$  is launched at port 1 of the circuit. After the coupler-1 the signal is split between the bus waveguide and ring waveguide depending on the value of  $k$ . The amplitude of the nonreciprocal phase shift is taken as  $\phi_N$ , whereas the sign of it solely depends on the relative orientation between wave propagation and magnetic field. The couplers are assumed to be identical with coupling length  $L_c$ . The straight race-track length of the ring is  $L_{RT}$  with  $r$  the radius of curvature of the bend section. The perimeter of the ring is therefore  $L_{ring} = 2 \times L_c + 2\pi r + 2 \times L_{RT}$ . The length of the bus waveguide is  $L_{bus}$ .

The electric field amplitudes at the different port ( the subscripts attached with the electric fields are corresponding to the respective ports as indicated by white dots on the circuit ) of the circuit can be written as below

$$E_3 = \sqrt{(1-k^2)}.E_1 - jk.E_2 \quad (7.1)$$

$$E_4 = -jk.E_1 + \sqrt{(1-k^2)}.E_2 \quad (7.2)$$

$$E_5 = \exp(-\alpha_{bus}.L_{bus}).\exp(-j\phi_{bus}).E_3 \quad (7.3)$$

$$E_6 = \exp(-\alpha_{ring}.\frac{L_{ring}}{2}).\exp(-j\phi_{ring}).E_4 \quad (7.4)$$

$$E_7 = \sqrt{(1-k^2)}.E_5 - jk.E_6 \quad (7.5)$$

$$E_8 = -jk.E_5 + \sqrt{(1-k^2)}.E_6 \quad (7.6)$$

$$E_2 = \exp(-\alpha_{ring}.\frac{L_{ring}}{2}).\exp(-j\phi_{ring}).E_8 \quad (7.7)$$

where  $\phi_{bus}$  and  $\phi_{ring}$  are referred to as the phases experienced by light while passing through bus (between ports 3 & 5) and ring waveguide ( between ports 4 & 6 or 2 & 8) respectively. The propagation loss of the bus and the ring waveguides are  $2\alpha_{bus}$  and  $2\alpha_{ring}$  respectively expressed in per length unit.

$E_7$  is the output of the whole circuit which can be written in terms of  $E_2$  by substituting other fields like

$$E_7 = [A(1-k^2) + Bk^2]E_1 - j[Ak\sqrt{1-k^2} + Bk\sqrt{1-k^2}]E_2 \quad (7.8)$$

where  $A = \exp(-\alpha_{bus}.L_{bus}).\exp(-j\phi_{bus})$  and  $B = \exp(-\alpha_{ring}.\frac{L_{ring}}{2}).\exp(-j\phi_{ring})$ . Likewise,  $E_2$  can be written in terms of  $E_1$  as

$$E_2 = -jE_1.\frac{B(Ak\sqrt{1-k^2} + Bk\sqrt{1-k^2})}{1 + ABk^2 - B^2(1-k^2)} \quad (7.9)$$

By substituting Eq.7.9 into Eq.7.8 we get

$$\frac{E_7}{E_1} = A(1 - k^2) + Bk^2 - \frac{B(A + B)(Ak\sqrt{1 - k^2} + Bk\sqrt{1 - k^2})}{1 + ABk^2 - B^2(1 - k^2)} \quad (7.10)$$

In the context of an optical isolator we will put emphasize on the case where the value of  $\phi_{bus}$  is influenced by the nonreciprocal phase shift (NRPS). The values of  $\phi_{bus}$  for forward and backward light propagation will take the form

$$\phi_{bus}^+ = \frac{2\pi n_{bus}}{\lambda} \cdot L_{bus} + \phi_N \quad (7.11)$$

$$\phi_{bus}^- = \frac{2\pi n_{bus}}{\lambda} \cdot L_{bus} - \phi_N \quad (7.12)$$

where  $n_{bus}$  is the effective refractive index of the bus waveguide at the wavelength  $\lambda$ . The NRPS between the forward and the backward light propagation can be expressed as  $NRPS = 2\phi_N$ .

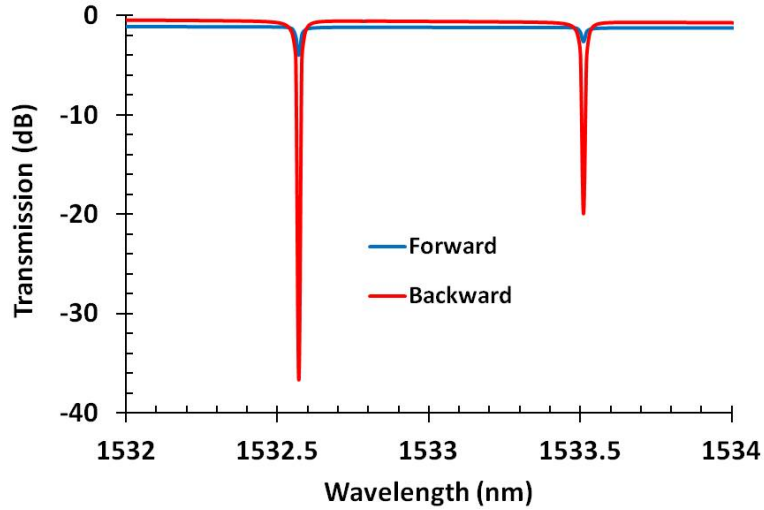


**Figure 7.3:** Analytically calculated transmission spectra for forward and backward light propagation for  $NRPS = 1$  rad and  $k = 0.2$ .

Analytically calculated transmission spectra for the forward and the backward light propagation for 1.0 rad of NRPS is presented in Fig.7.3 considering 4% cross-coupling ( $k$ ). The resonance condition of the NRMZI strongly depends on the NRPS in the bus waveguide. From Fig.7.4 we can directly see the change in extinction ratio with the change of NRPS in the bus waveguide. For all the analytical calculations the following assumptions were made:  $L_{bus} = 377 \mu\text{m}$ ,  $L_{ring} = 714 \mu\text{m}$ ,  $\alpha_{bus} = 1.15 \text{ cm}^{-1}$  and  $\alpha_{ring} = 3.46 \text{ cm}^{-1}$ .

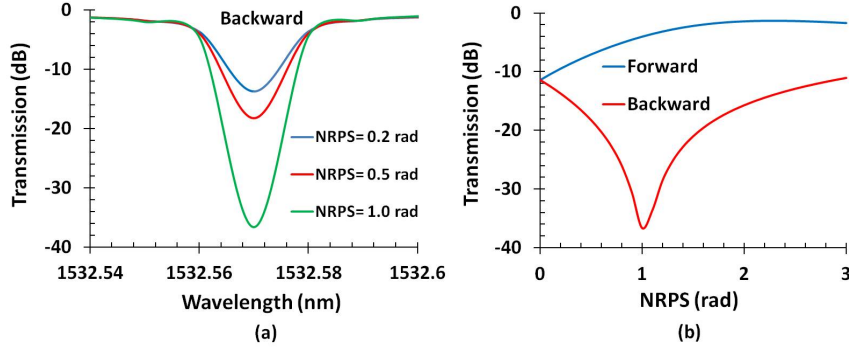


**Figure 7.4:** (a) Dependence of extinction ratio of the NRMZI on NRPS for  $k = 0.2$  (b) transmission as a function of NRPS at 1532.57 nm wavelength for  $k = 0.2$ .

## 7.2 Isolator design concepts

### 7.2.1 Asymmetric directional coupler

The device presented here works on the basis of the NRPS experienced by the TM polarized light under the influence of an external magnetic field. It is clear from the previous section that the relative phase between the bus and the ring waveguide of the NRMZI is important to achieve optical isolation. When the light is traveling in the same direction on the bus and the ring arm (assumed to have identical waveguide cross-section) of the NRMZI, no effective nonreciprocal effect is possible when the applied magnetic field is unidirectional as depicted in Fig.7.5. To circumvent this problem and adopt the BCB bonding approach, the coupling sections of the NRMZI are designed as asymmetrical. The asymmetrical directional coupler is comprised of two waveguides of dissimilar widths. The couplers are designed in such a manner that the fundamental TE mode ( $TE_{00}$ ) in the narrower waveguide is phase matched with the fundamental TM mode ( $TM_{00}$ ) of the wider waveguide. The widths of the bus and the ring waveguides are chosen according to effective index plots as shown in Fig.7.6. The width of the narrower waveguide is 336 nm whereas the width of the wider one is 900 nm. From Fig.7.6 we can see that for 50 nm of BCB thickness variation the phase matching condition between  $TE_{00}$  of the narrower waveguide and  $TM_{00}$  of the wider waveguide holds. It is noteworthy to mention that the wider waveguide is guiding three modes whereas the narrower one is monomode and guides only the  $TE_{00}$  mode. Power coupling between the  $TE_{00}$  mode of the ring waveguide and  $TE_{00}$ ,  $TE_{01}$  of the bus waveguide is however negligibly small. The length of the coupling section ( $L_c$ ) is simulated for a constant gap ( $g$ ) of 230 nm

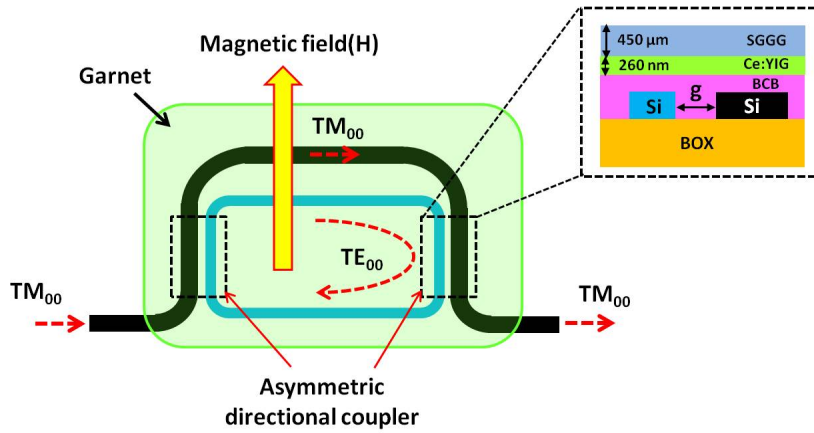


**Figure 7.5:** Schematic diagram of a nested ring MZI with asymmetric directional couplers. Waveguide cross-section at coupling section (inset).

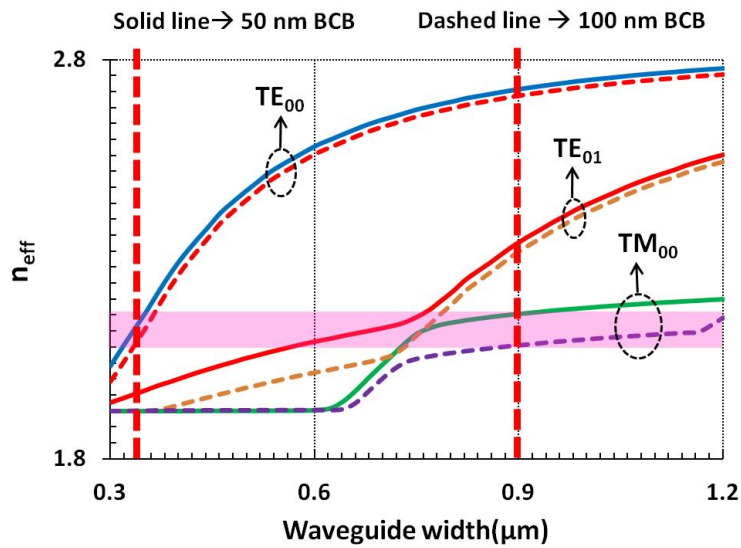


**Figure 7.6:** Effective index variation as a function of waveguide width for 260 nm thick Ce:YIG layer at 1550 nm wavelength.

as presented in Fig.7.7(a) at 1550 nm wavelength. The spectral dependence of such a directional coupler is also simulated for various  $L_c$  for 100 nm BCB as depicted in Fig.7.7(b). The width of the ring waveguide is a very crucial and determining factor for the efficiency of this kind of directional coupler. We can see from Fig.7.8 that the window of efficient power coupling between the  $TE_{00}$

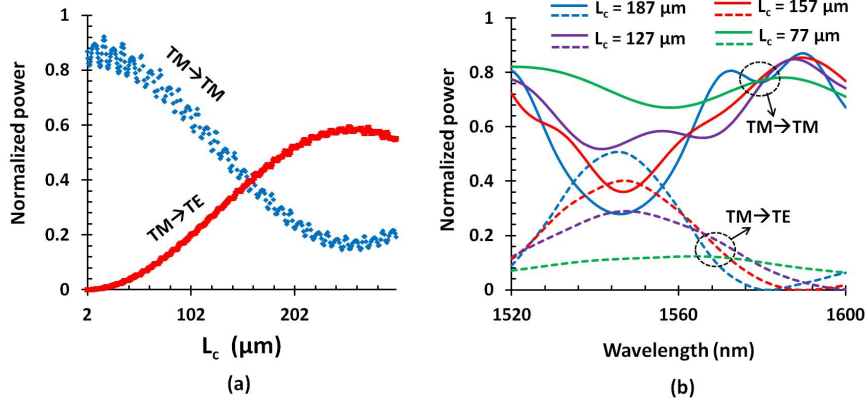


**Figure 7.7:** Efficiency of the asymmetric directional coupler (a) as a function of coupling length ( $L_c$ ) at 1550 nm wavelength (b) when wavelength tuned for various  $L_c$ . Width of the bus and ring waveguide are 900 nm and 336 nm respectively for  $g = 230$  nm and 100 nm of BCB.

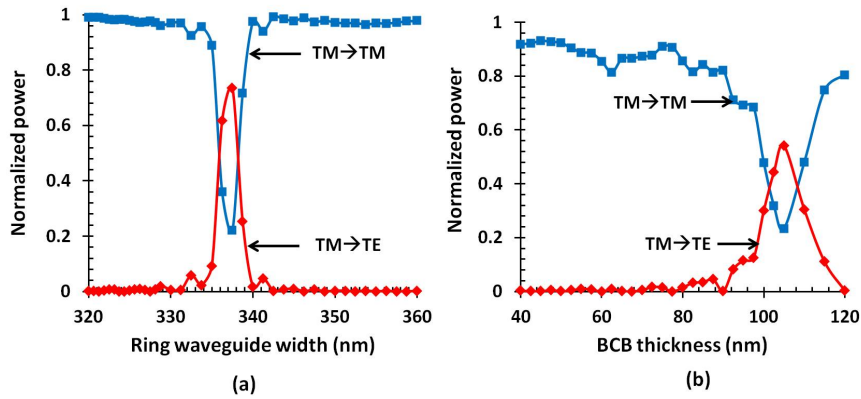


**Figure 7.8:** Efficiency of the asymmetric directional coupler as a function of (a) ring waveguide width for 900 nm wide bus waveguide and 100 nm BCB at 1560 nm wavelength (b) BCB thickness for 336 nm wide ring waveguide and 900 nm wide bus waveguide at 1560 nm wavelength.

mode of the ring waveguide and the  $\text{TM}_{00}$  mode of the bus waveguide is very narrow with respect to the ring waveguide width and also the BCB thickness.

### 7.2.2 Symmetric directional coupler

We have seen from the previous section how a NRMZI could be utilized as an optical isolator. From the fabrication point of view the narrow waveguide dimension is not optimal and susceptible to fabrication variations. So the performance of the asymmetrical directional coupler is less predictable. To resolve this issue while using the same bonding approach a simple trick could be adopted. The directional couplers are designed symmetrically for TM modes and then a thin layer of silicon nitride ( $\text{Si}_3\text{N}_4$ ) could be deposited selectively on top of the bus waveguide while the ring waveguide is not covered with nitride. The benefit of this approach is manifold. Firstly the performance of the directional coupler as designed is predictable due to the symmetric waveguide dimensions and less fabrication imperfections. Secondly, the BCB thickness on top of the bus waveguide is smaller than that on the ring waveguide and hence a net NRPS is obtained from the MZI. The net nonreciprocal effect from the race-track ring will be zero which is obvious from Fig.7.9. To maintain a constant BCB thickness difference between the bus and the ring waveguide while garnet is stably bonded on top of the structure, some auxiliary nitride is also deposited at nearby sites as depicted in Fig.7.9.

The waveguides are 900 nm wide and 220 nm thick through the circuit. The gap between the identical waveguides of the directional coupler is  $g$ . Now we will study the dependence of the NRPS on the nitride thickness as well as the BCB thickness. However, it is important to mention that direct deposition of garnet only on top of the bus waveguide by sputtering or by means of any other method could potentially solve all the issues. This is elaborated in Chapter 8. Fig.7.10 shows the variation of the differential NRPS ( $\Delta\text{NRPS}$ ) between the bus and the ring waveguide as a function of nitride thickness for various BCB thicknesses. The refractive index of  $\text{Si}_3\text{N}_4$  is taken as 2. The BCB thickness on top of the ring waveguide is always higher by an amount determined by the  $\text{Si}_3\text{N}_4$  thickness on top of the bus waveguide. It is clear from the Fig.7.10 that thinner BCB is desirable to obtain higher nonreciprocal effect for any fixed  $\text{Si}_3\text{N}_4$  thickness.

## 7.3 Device fabrication and measurements

The SOI waveguide circuits were fabricated in a CMOS pilot line using 193 nm DUV-lithography as already described in chapter 3. The bonding of the garnet die was also performed using the process described in chapter 3. NRMZIs of varying  $L_c$  were designed for both types of directional couplers. Magneto-optical measurements of the garnet bonded NRMZIs with asymmetric directional couplers were performed with the help of an external magnetic field pro-

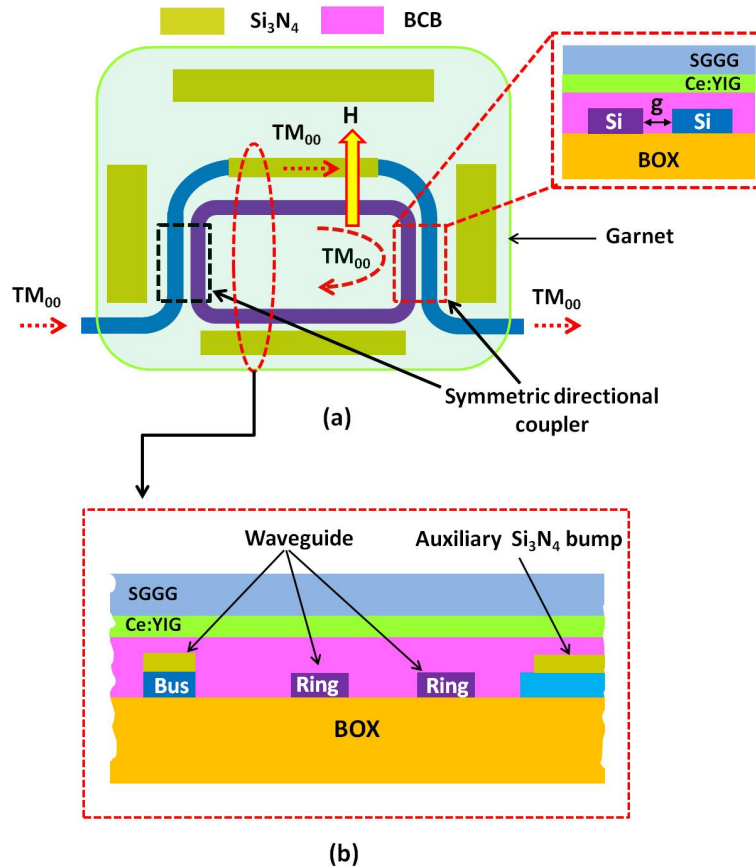


**Figure 7.9:** (a) Schematic diagram of a nested ring MZI with symmetric directional couplers. Waveguide cross-sections at MZI section shown in inset (b) Artistic impression of the bonded stack.

vided by a tiny Nd-B-Fe magnet stack. Due to lack of time any experimental demonstration of NRMZIs with symmetric directional couplers was not done. TM polarized light was injected and collected by the curved TM grating couplers put at both the ends of the NRMZI. The measured transmitted power spectra for the forward and the backward light propagation with a unidirectional magnetic field applied transverse to the light propagation corresponding to  $L_c = 187\mu\text{m}$  and  $L_c = 157\mu\text{m}$  are depicted in Fig.7.11(a) and Fig.7.11(b) respectively. It is important to clarify that the nomenclature ‘forward’ or ‘backward’ are arbitrarily chosen and depend on the relative orientation between the external magnetic field ( $H$ ) and the light propagation direction. While high optical isolation can be achieved none of the spectra are like the spectra shown in Fig.7.3. One of the

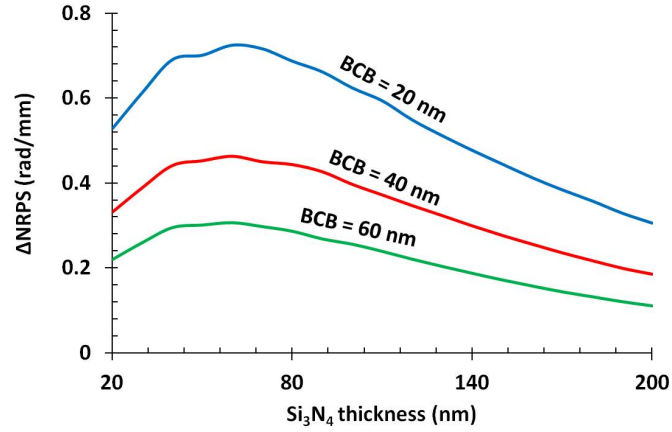


**Figure 7.10:** Differential NRPS ( $\Delta NRPS$ ) as a function of  $Si_3N_4$  thickness for various BCB thicknesses at 1550 nm wavelength.

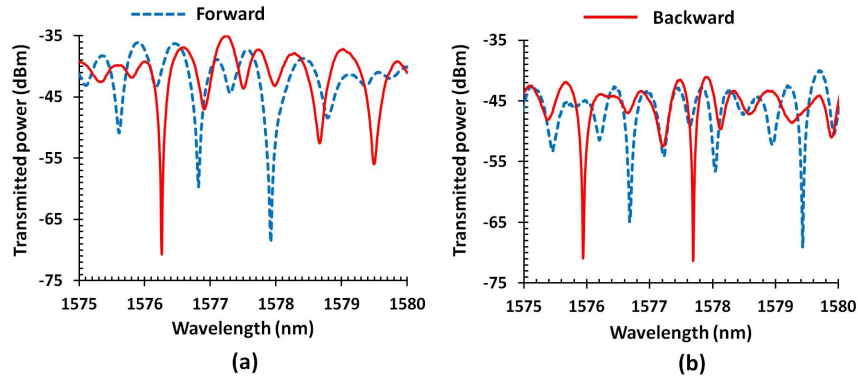


**Figure 7.11:** Measured transmitted power spectra for the forward and backward directions through NRMZI containing asymmetrical directional couplers corresponding to (a)  $L_c = 187 \mu m$  (b)  $L_c = 157 \mu m$ .

possible reasons for such a substantial deviation could be due to the fabrication inaccuracy of the asymmetric directional coupler.

A scanning electron microscopic (SEM) image for such a directional coupler is depicted in Fig.7.12(a). The actual fabricated waveguide dimensions at the asymmetric directional coupling section are revealed by focused ion beam (FIB) cross-section as shown in Fig.7.12(b). Clearly the top of the waveguide is 100 nm narrower than the bottom.

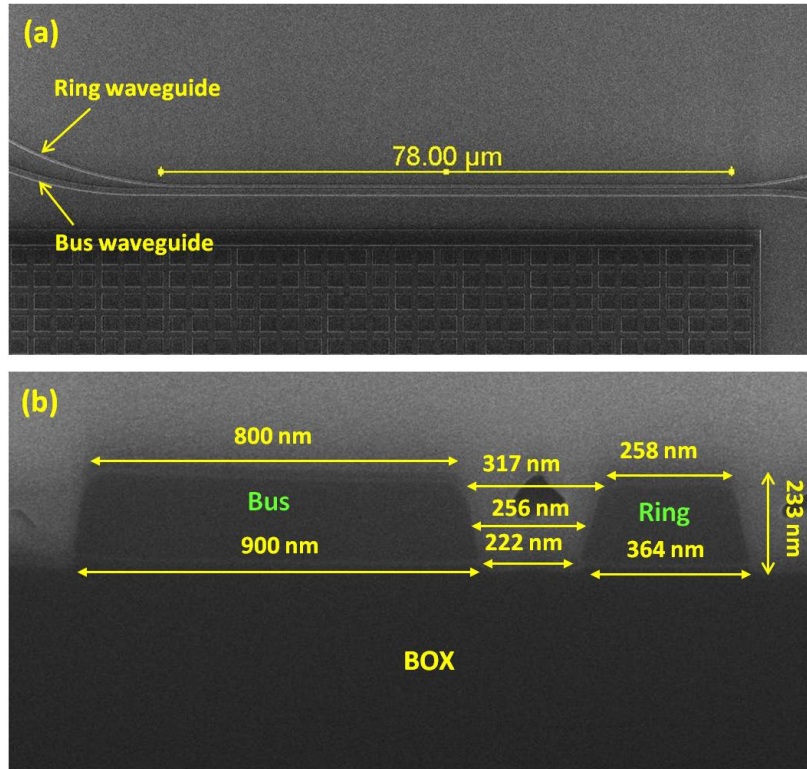


**Figure 7.12:** SEM image of the asymmetric directional coupler (a) top-view (b) cross-sectional view.

## 7.4 Conclusion

We have demonstrated a novel concept based on the NRMZI designs to achieve optical isolation. The performance of the NRMZI is very sensitive to fabrication errors for the case of an asymmetric directional coupler. Robustness in the design is a primary requirement for such kind of device to obtain optimal performance. An NRMZI with symmetrical directional couplers is more tolerant. Key factor to achieve high isolation in this case is a thin BCB layer on top of the  $\text{Si}_3\text{N}_4$  deposited bus waveguide. The refractive index of the deposited  $\text{Si}_3\text{N}_4$  layer also plays an important role to determine the length of the bus waveguide required to provide a perceptible NRPS.

## References

- [1] Brent E Little, Sai T Chu, Hermann A Haus, J Foresi, and J-P Laine. *Microring resonator channel dropping filters*. Journal of Lightwave Technology, 15(6):998–1005, 1997.
- [2] Graham T Reed, G Mashanovich, FY Gardes, and DJ Thomson. *Silicon optical modulators*. Nature Photonics, 4(8):518–526, 2010.
- [3] Chung-Yen Chao and L Jay Guo. *Design and optimization of microring resonators in biochemical sensing applications*. Journal of Lightwave Technology, 24(3):1395, 2006.
- [4] Katrien De Vos. *Label-Free Silicon Photonics Biosensor Platform with Microring Resonators*. PhD thesis, Universiteit Gent, 2010.
- [5] Tom Claes. *Advanced Silicon Photonic Ring Resonator Label-free Biosensors*. PhD thesis, Universiteit Gent, 2012.
- [6] J. Heebner, R. Grover, and T.A. Ibrahim. *Optical Microresonators: Theory, Fabrication, and Applications*. Optical Sciences, 138. Springer, 2008.
- [7] Otto Schwelb. *Transmission, group delay, and dispersion in single-ring optical resonators and add/drop filters—a tutorial overview*. Journal of Lightwave Technology, 22(5):1380, 2004.
- [8] Ming-Chun Tien, Tetsuya Mizumoto, Paolo Pintus, Herbert Kromer, and John E. Bowers. *Silicon ring isolators with bonded nonreciprocal magneto-optic garnets*. Opt. Express, 19(12):11740–11745, Jun 2011.
- [9] Daoxin Dai and Sailing He. *Highly sensitive sensor based on an ultra-high-Q Mach-Zehnder interferometer-coupled microring*. JOSA B, 26(3):511–516, 2009.
- [10] Huaxiang Yi, David S. Citrin, and Zhiping Zhou. *Coupling-induced high-sensitivity silicon microring intensity-based sensor*. J. Opt. Soc. Am. B, 28(7):1611–1615, Jul 2011.
- [11] Xiao-Yang Zhang, Tong Zhang, Xiao-Jun Xue, Jin-Ling Zhang, Jun Hong, Peng-Qin Wu, and Qiu-Yue Chen. *Tunable Optical Ring Resonator Integrated With Asymmetric Mach-Zehnder Interferometer*. Journal of Lightwave Technology, 28(17):2512–2520, 2010.

# 8

## Sputtering Deposition Approach of Garnet for Integrated Nonreciprocal Optical devices on SOI

**I**N this chapter, we will discuss a different approach to integrate magneto-optic garnet material on top of SOI waveguide circuits. In the previous chapters adhesive bonding approach is presented. First, a literature survey based on different types of deposition techniques is presented and then more discussions are devoted to our work based on a magnetron sputtering technique. Later on some results are presented regarding material properties of sputtered grown garnet. Push-pull MZI type isolator designs are used for the optical and the magneto-optical characterizations. Optical loss of TM polarized light due to sputtered garnet on SOI waveguide is measured as 6.6 dB/mm around 1550 nm wavelength. Unfortunately no NRPS is detected when an external magnetic field is applied transverse to the light propagation.

### 8.1 Introduction

Yttrium iron garnet (YIG) and Bismuth (Bi) or Cerium (Ce) substituted YIG have been widely used to realize nonreciprocal devices like optical isolators, circula-

tors and magnetic field sensors due to their strong magneto-optical properties in combination with low optical loss in the telecom wavelength window. In the previous chapters, for all the devices, an adhesive BCB bonding approach was used to integrate a magneto-optic garnet die (Ce:YIG on SGGG substrate) on SOI circuits. Bonding approaches based either on molecular or adhesive bonding suffer from various issues. For example, the bonding approach puts limitations on the size of the garnet die that can be handled by machine or hand. As a result it inherently demands larger device dimensions although the effective interaction length required to obtain sufficient magneto-optic effect still is quite small. Sometimes device designs meant for a bonding approach require a critical alignment of the garnet die on top of the waveguide circuit [1, 2]. Therefore, the main advantages of the deposition approach over the bonding approach are the reduced effective device footprint and the possibility of selective patterning of the YIG on top of a waveguide circuit, which are desirable aspects for mass scale production. Plenty of efforts have already been described on the deposition of YIG or Bi or Ce-substituted YIG on various substrate [3–15].

Several techniques are available for such a thin film deposition like chemical vapor deposition (CVD), epitaxy, physical vapor deposition (PVD) etc. For the CVD, process the substrate is kept inside a chamber where various gases are supplied. Then a chemical reaction between two source gases leads to a solid product which is eventually deposited on the substrate. This type of process could create several hazardous byproducts although it is an ideal process to obtain a high quality thin film with less defects. Epitaxy is very similar to the CVD process however it is an ideal technique if the deposited film needs to acquire the same crystallographic orientation as the substrate material. The substrate behaves like a seed layer for the deposition. PVD is commonly used for metal deposition. In this case the film is directly transferred onto the substrate either by evaporation or sputtering. Although this is a cheaper deposition technique as compared to CVD, the film quality is not as good as for the case of CVD.

In the context of the current work, only the magnetron sputtering deposition technique is discussed in some detail. A typical magnetron sputtering system is shown in Fig.8.1. Sputtering is a type of PVD method. It is a very simple method to understand. The material which is supposed to be deposited on a silicon substrate or any other substrate is used as a target. The target in this particular case are magneto-optic garnet materials such as YIG or Ce:YIG. An inert gas like Argon (Ar) is supplied into the chamber at low pressure. When a high radio frequency (RF) power is applied between the electrodes a gas plasma is generated. Positively charged Ar ions are influenced by the combined effect of the electric and magnetic fields and are compelled to come a close vicinity to the target surface. The Ar ions bombard the target and eventually some target atoms break off from the target. As the ejected free particles from the target are

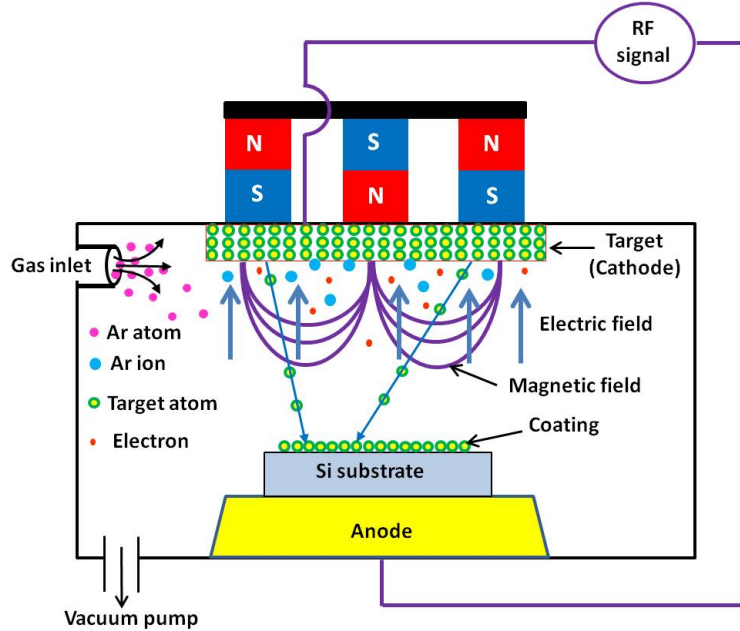


Figure 8.1: RF magnetron sputtering system.

electrically neutral they are unaffected by either electric or magnetic fields and are deposited onto the substrate. The free electrons generated after the ionization process of the Ar atoms follow a helical path around the magnetic field line and as a result more collisions occur with the neutral gas atoms. These extra Ar ions help to enhance the deposition rate.

## 8.2 Garnet deposition by magnetron sputtering

### 8.2.1 Process flow

To obtain garnet selectively on different parts of the SOI circuit, the following steps need to be performed before and after deposition. At first, the SOI chip is cleaned sequentially by acetone, IPA and DI water then a negative photoresist AZ5214 is spin coated at 4000 rpm for 30 seconds. The thickness of the photoresist is around  $1.5 \mu\text{m}$ . The photoresist coated SOI is baked at  $110^\circ\text{C}$  on a hot-plate for 1 minute. Then this baked SOI chip is illuminated by UV-radiation in a standard Carl Zeiss MA-6 mask aligner. A chrome contact mask is used to define the area where garnet is required. The UV exposure time can vary depending on the photoresist thickness. Then this UV illuminated SOI is baked

again on a hot-plate at 120°C for 2 minutes. Afterwards a flood exposure is carried out. Then the SOI is rinsed in a developer solution (AZ400K : DI water = 5 : 1) for about 20 seconds. Now the windows for garnet deposition are realized. A garnet layer is deposited by sputtering everywhere on top of the chip. A lift-off process by using acetone is then performed to remove the unwanted garnet. The time required for the lift-off mostly depends on the thickness of the garnet layer. Finally this as-deposited SOI chip undergoes a rapid thermal annealing (RTA) process to crystallize the garnet to a great extent. The process steps are depicted in Fig.8.2.

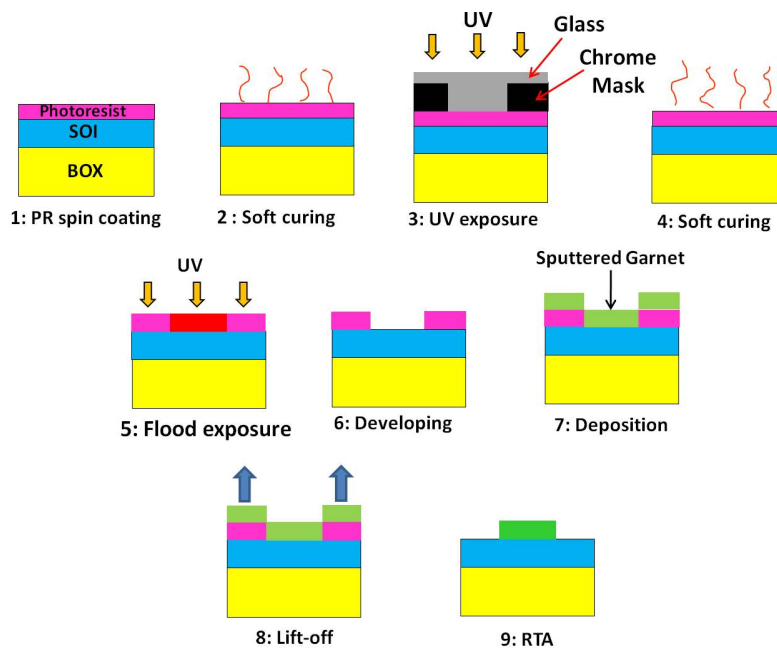


**Figure 8.2:** Process steps for selective garnet deposition by sputtering.

### 8.2.2 YIG deposition

In this work, various issues were studied to achieve a good YIG quality on SOI. The deposition of YIG was performed at imec, Leuven. Magnetron sputtering was carried out for 30 minutes with 16 sccm (cubic centimeter per minute at STP) of Ar and 4 sccm of O<sub>2</sub> keeping the target bias power at 200 W. The properties of these deposited garnets mainly depend on the crystallinity after deposition as well as their composition. The crystallinity of the deposited material is determined by the crystallinity of the substrate. For this reason lattice param-

ters of both of them should be nearly equal. The crystallinity of the as-deposited materials are generally not optimal to provide the expected magneto-optical effect. So a thermal treatment is commonly used to enhance the crystallinity. The role of thermal annealing to change the crystallographic orientation as well as the in-plane magnetization of the as-deposited YIG film on a Si substrate can be seen in Fig.8.3(a) and Fig.8.3(b) respectively. Clearly an improvement is seen on as-deposited film after the thermal annealing. In this case the annealing was performed at 800°C for 2 minutes in an O<sub>2</sub> ambient. It is important to mention that there is a huge mismatch both in the lattice parameters and the thermal expansion coefficients between Si and YIG. The lattice parameters for Si and YIG are 5.43 Å and 12.54 Å respectively. The thermal expansion coefficients for Si and YIG are  $2.3 \times 10^{-6} K^{-1}$  and  $9.2 \times 10^{-6} K^{-1}$  respectively. So the annealing of the as-deposited garnet film resulted in cracking due to the huge stress at the interface between the garnet and the non-garnet layers. The surface mor-

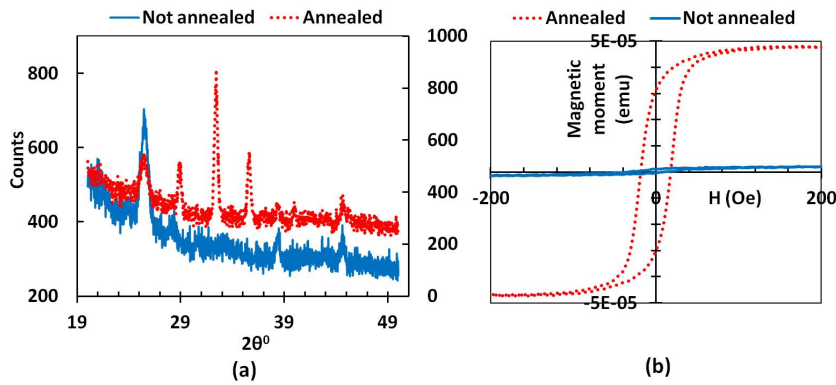


**Figure 8.3:** (a) X-ray diffraction (XRD) patterns of the as-deposited/not-annealed and annealed films (b) Hysteresis curves of the as-deposited and the annealed films detected by an alternating gradient force magnetometer (AGFM).

phology after the rapid thermal annealing (RTA) is shown in Fig.8.4. The grain boundaries between adjacent grains are clearly observed.

### 8.2.3 Ce:YIG deposition

YIG grown on a MgO substrate by sputtering followed by RTA has a Faraday rotation coefficient of about 1200-2200 deg/cm at 633 nm wavelength [13]. It is noteworthy to mention that the Faraday rotation is even smaller for the telecom wavelengths window. However, substitution of a small amount of Y by Ce or Bi in the YIG enhances the Faraday rotation by an order of magnitude. The

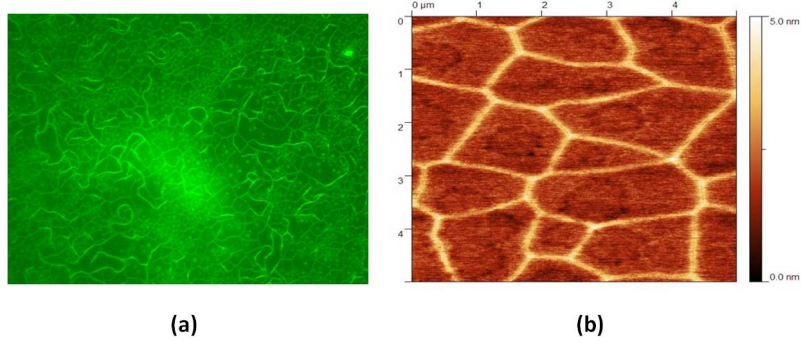


**Figure 8.4:** (a) Dark-field microscopic image (b) Atomic force microscopic (AFM) image of the annealed YIG on Si substrate.

main reason for such an enhancement can be related to a charge transfer between  $\text{Ce}^{3+}$  and  $\text{Fe}^{3+}$  as proposed by Gomi *et al* [16]. The main issue during the sputtering deposition of such a substituted target is the occurrence of various secondary non-garnet phases. So a well controlled way of deposition together with an optimized RTA recipe is required to obtain a good garnet film.

Recently, a new approach was developed based on pulsed laser deposition (PLD) in which first an ultra-thin layer of YIG is deposited on the Si substrate followed by a RTA and then a relatively thick layer of Ce:YIG is deposited on top it [10, 17]. The initial thin layer serves as a seed layer for the second thick layer. For the 100 nm thick Ce:YIG layer deposited on 10 nm thick YIG no cracking was found. The saturation Faraday rotation is reported to be 830 deg/cm with a transmission loss of nearly 40 dB/cm at 1550 nm wavelength.

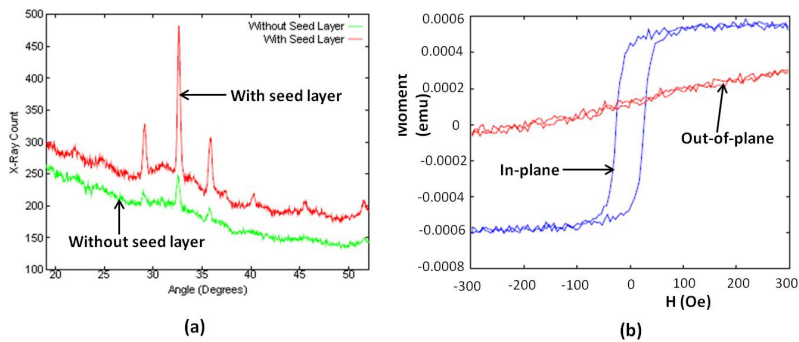


**Figure 8.5:** (a) XRD patterns for Ce:YIG with and without seed layer (b) in-plane and out-of-plane Magnetization of the Ce:YIG film measured by VSM.

In the current work, we have achieved good quality Ce:YIG by following the aforementioned two step deposition method in collaboration with the University of Minnesota (UMN). The proposed deposition technique uses magnetron sputtering instead of PLD although it is believed that it will not bring much change in film quality. The maximum Faraday rotation coefficient ( $\theta_F$ ) as measured by UMN was 1500 deg/cm which is almost 1/3 of single crystalline Ce:YIG grown on SGGG substrate. The change in crystallinity after depositing Ce:YIG on top of a YIG seed layer is clearly observed from the XRD analysis as shown in Fig.8.5(a). The in-plane magnetization is also very strong as compared to out-of-plane magnetization as revealed by vibrating sample magnetometer (VSM) measurements depicted in Fig.8.5(b), which is highly desirable for photonic integrated circuits.

### 8.3 Isolator design

A variety of designs can be implemented, to be used as optical isolator or circulator using deposited garnet. For experimental purposes several MZIs of varying lengths were designed. To accommodate many devices in a small space the arms of the MZI are meandering as shown in Fig.8.6(a). Another advantage is that a unidirectional magnetic field will be sufficient to achieve push-pull operation from this design. The required length of the nonreciprocal phase shifter can be calculated from Fig.8.7 in which the nonreciprocal phase shift is calculated for various Ce:YIG thicknesses considering a Faraday rotation coefficient of 1500 deg/cm. The actual garnet deposited MZI is shown in Fig.8.6(b). The

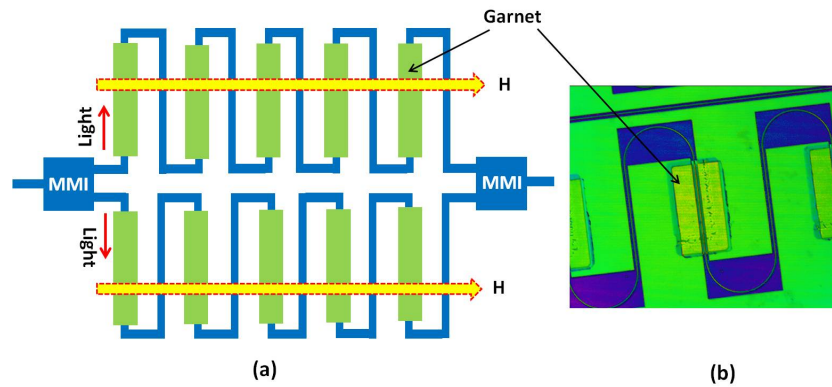


**Figure 8.6:** (a) MZI based isolator design (b) Garnet deposited on MZI arm.

process flow to obtain selectively deposited garnet on MZI arms is already explained in Fig.8.2.

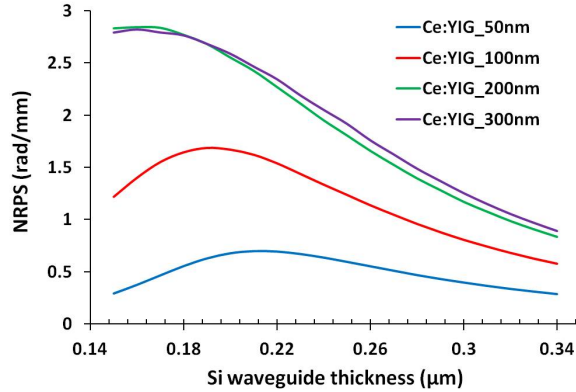


**Figure 8.7:** Simulation of nonreciprocal phase shift (NRPS) when the Faraday rotation coefficient is 1500 deg/cm.

## 8.4 Loss measurements

The conventional way to characterize optical propagation loss is by a standard cut-back method in which spirals of varying length are used. In this case, optical transmission spectra obtained from such long garnet deposited spirals are not suitable to extract loss information. Hence MZIs of varying length are used instead. As only transverse magnetic (TM) polarized light can provide nonreciprocal phase shift in this configuration, TM light is injected and collected by curved TM grating couplers. The garnet covered lengths ( $L$ ) of four different MZIs are 0.85 mm, 1.2 mm, 1.8 mm and 2.8 mm respectively. The corresponding transmission spectra are shown in Fig.8.8(a). To extract the propagation loss the constructive interference points are considered. In this case the 1545-1555 nm wavelength window is considered. The slope of the straight line drawn for constructive transmission point as function of  $L$  gives the loss per unit length as shown in Fig.8.8(b). The obtained propagation loss for the TM polarized light is approximately 6.6 dB/mm in that spectral range. The loss depends on various parameters like ratio of gases during deposition, purity of garnet phase, RTA recipe and also on the thickness of the garnet layer. Magneto-optical measurements are also performed using small Nd-Fe-B magnet stack. However no NRPS was observed from these samples. The reason behind this may be attributed to the shape anisotropy of garnet film on SOI waveguide or poor material quality. It is important to mention that the SOI waveguides were not planarized and as a result garnet widths on top of the waveguides were only 900 nm wide (almost same as the waveguide width). So the aspect ratio between length and width of the garnet film was huge. This may lead to high demagnetization factor means

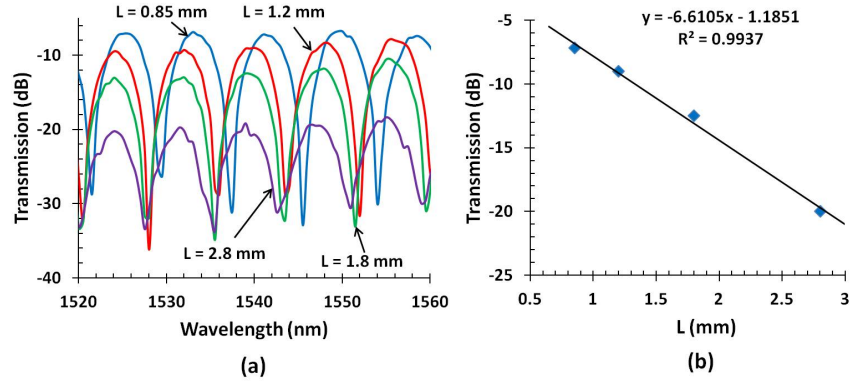


**Figure 8.8:** (a) Measured transmission spectra for the MZIs of varying lengths (b) plot of MZI transmission at constructive interference points vs. length of the garnet covered MZI arm lengths (L).

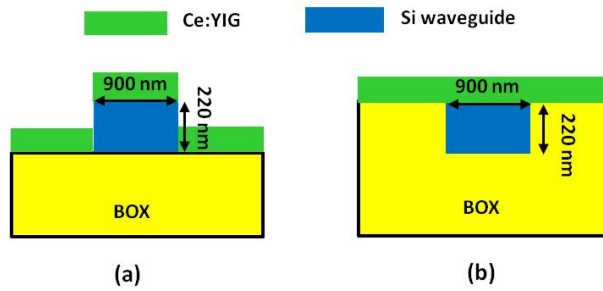


**Figure 8.9:** Waveguide cross-sections (a) Ce:YIG on non-planarized SOI waveguide (b) Ce:YIG on top of planarized SOI waveguide.

a substantially higher magnetic field would require to saturate the garnet film along width as compared to the length. Garnet on both non-planarized and planarized SOI surfaces are depicted in Fig.8.9.

## 8.5 Conclusion

In this chapter we have briefly studied one of the elegant approaches for the incorporation of magneto-optical garnet materials on top of SOI circuits. Substitution of the Y by the rare earth elements like Ce is demonstrated to achieve strong magneto-optical effects. The optical propagation loss is measured as 6.6 dB/mm for the TM mode. Although the obtained optical propagation loss is very high it could be reduced to an affordable number by optimizing deposition

parameters and garnet thickness. Shape anisotropy and poor material quality are supposed to be responsible for no magneto-optical effect or NRPS. Therefore further extensive research is required to improve the material quality as well as the demagnetization effect due to shape anisotropy of the garnet film.

## References

- [1] S. Ghosh, S. Keyvavinia, W. Van Roy, T. Mizumoto, G. Roelkens, and R. Baets. *Ce:YIG/Silicon-on-Insulator waveguide optical isolator realized by adhesive bonding*. Optics Express, 20(2):1839–48, January 2012.
- [2] Yuya Shoji, Tetsuya Mizumoto, Hideki Yokoi, I-Wei Hsieh, and Richard M. Osgood. *Magneto-optical isolator with silicon waveguides fabricated by direct bonding*. Applied Physics Letters, 92(7):071117, 2008.
- [3] Bethanie Stadler, Kenneth Vaccaro, Pearl Yip, Joseph Lorenzo, Yi-Qun Li, and Monher Cherif. *Integration of magneto-optical garnet films by metal-organic chemical vapor deposition*. IEEE Transactions on Magnetics, 38(3):1564–1567, 2002.
- [4] Sadao Higuchi, Yasunori Furukawa, Shunji Takekawa, Osamu Kamada, Kenji Kitamura, and Kiyotaka Uyeda. *Magneto-optical properties of cerium-substituted yttrium iron garnet single crystals for magnetic-field sensor*. Sensors and Actuators A: Physical, 105(3):293–296, 2003.
- [5] Shinji Mino, Akiyuki Tate, Takehiko Uno, Toshihiro Shintaku, and Atsushi Shibukawa. *Structure and lattice deformation of Ce-substituted yttrium iron garnet film prepared by RF sputtering*. Japanese journal of applied physics, 32(7):3154–3159, 1993.
- [6] M Gomi, K Satoh, H Furuyama, and M Abe. *Sputter deposition of Ce-substituted iron garnet films with giant magneto-optical effect*. IEEE Translation Journal on Magnetics in Japan, 5(4):294–299, 1990.
- [7] Manabu Gomi, Kensuke Satoh, and Masanori Abe. *Giant Faraday rotation of Ce-substituted YIG films epitaxially grown by RF sputtering*. Jpn. J. Appl. Phys, 27(8):L1536, 1988.
- [8] Taichi Goto, Mehmet C Onbaşlı, and CA Ross. *Magneto-optical properties of cerium substituted yttrium iron garnet films with reduced thermal budget for monolithic photonic integrated circuits*. Optics express, 20(27):28507–28517, 2012.

- [9] M. Chandra Sekhar, Mahi R. Singh, Shantanu Basu, and Sai Pinnepalli. *Giant Faraday rotation in  $\text{Bi}_x\text{Ce}_3\text{-xFe}_5\text{O}_{12}$  epitaxial garnet films*. Opt. Express, 20(9):9624–9639, Apr 2012.
- [10] Lei Bi, Juejun Hu, Gerald F Dionne, Lionel Kimerling, and CA Ross. *Monolithic integration of chalcogenide glass/iron garnet waveguides and resonators for on-chip nonreciprocal photonic devices*. In Proc. SPIE, volume 7941, page 794105, 2011.
- [11] NB Ibrahim, C Edwards, and SB Palmer. *Pulsed laser ablation deposition of yttrium iron garnet and cerium-substituted YIG films*. Journal of magnetism and magnetic materials, 220(2):183–194, 2000.
- [12] S Kahl and Alexander M Grishin. *Pulsed laser deposition of  $\text{YFeO}$  and  $\text{BiFeO}$  films on garnet substrates*. Journal of applied physics, 93:6945, 2003.
- [13] Sang-Yeob Sung, Xiaoyuan Qi, and Bethanie JH Stadler. *Integrating yttrium iron garnet onto nongarnet substrates with faster deposition rates and high reliability*. Applied Physics Letters, 87(12):121111–121111, 2005.
- [14] BM Holmes and DC Hutchings. *Demonstration of quasi-phase-matched nonreciprocal polarization rotation in III-V semiconductor waveguides incorporating magneto-optic upper claddings*. Applied physics letters, 88(6):061116–061116, 2006.
- [15] Toufik Boudiar, Beatrice Payet-Gervy, M-F Blanc-Mignon, J-J Rousseau, Martine Le Berre, and H Joisten. *Magneto-optical properties of yttrium iron garnet (YIG) thin films elaborated by radio frequency sputtering*. Journal of magnetism and magnetic materials, 284:77–85, 2004.
- [16] Manabu Gomi, H Furuyama, and M Abe. *Strong magneto-optical enhancement in highly Ce-substituted iron garnet films prepared by sputtering*. Journal of applied physics, 70(11):7065–7067, 1991.
- [17] Lei Bi, Juejun Hu, Peng Jiang, Dong Hun Kim, Gerald F Dionne, Lionel C Kimerling, and CA Ross. *On-chip optical isolation in monolithically integrated non-reciprocal optical resonators*. Nature Photonics, 5(12):758–762, 2011.



# 9

## Conclusions and Outlook

### 9.1 Conclusions

The context of this work was to demonstrate nonreciprocal optical devices like isolators and circulators on the Silicon-on-insulator (SOI) platform by incorporating a magneto-optic garnet material. Although nonreciprocal devices such as isolators and circulators have already been demonstrated using molecular bonding approach, this work takes two different routes to integrate magneto-optical materials on a planar waveguide circuit: adhesive BCB bonding and sputtering deposition. The garnet materials used for the bonding work was supplied by the Tokyo Institute of Technology, Japan. The sputtering work is still going on in collaboration with the University of Minnesota, USA.

A variety of device designs were considered. The physical phenomenon behind all the devices is the nonreciprocal phase shift (NRPS) experienced by transverse magnetic (TM) polarized light induced by an external magnetic field. To start the work first necessary step was to prove that there is a magneto-optical interaction between the garnet and SOI waveguide to achieve the NRPS. Therefore a Mach-Zehnder interferometer (MZI) type SOI waveguide circuit was designed to which the garnet die was bonded by means of BCB. The device works in a push-pull manner under an external magnetic applied transverse to the light propagation direction. This device showed an isolation of 25 dB. The effective garnet covered length of the MZI arms was around 0.92 mm. This was

the first demonstration of on-chip optical isolation using an adhesive bonding technique. A comparison between the experimental result and simulation reveals that the BCB thickness was about 100 nm on top of the SOI waveguide. Although this device was designed for proof-of-principle purposes the main issue with it is the insertion loss which depends on the effective garnet covered SOI waveguide length. This problem can be mitigated by lowering the effective garnet covered waveguide length which is possible when the BCB layer is thinner than 100 nm. In some other devices the BCB thickness was 50 nm as estimated by simulation.

The push-pull type MZI design requires an alignment of the garnet die on top of the MZI which makes the device footprint larger as well as the bonding process more difficult. To circumvent this issue a compact design is proposed working for TM polarized light. This design is based on a MZI in which the arms are equally long but have dissimilar widths. A differential NRPS (DNRPS) is achieved from the garnet bonded MZI when an unidirectional magnetic field is applied transverse to the light propagation. The main advantage in this design is that the garnet die covers the whole MZI which makes bonding much easier. The width of the MZI arms is 1000 nm and 500 nm. Two multimode interference (MMI) couplers with output arms width of 1000 nm and 500 nm are connected to form the required MZI. The dependence of NRPS on waveguide width is simulated for various BCB thicknesses. An isolation of 11 dB is measured for a MZI with 1.49 mm arm length. The isolation is determined by the extinction ratio of the MZI which is related to the MMI splitting ratio and the differential loss in both waveguide arm. So by redesigning the MMI a better isolation is possible.

Another device is proposed based on resonance phenomena which could potentially lower the device size even further. A nested ring MZI (NRMZI) is considered for this purpose in which the coupling sections are designed with asymmetrical directional couplers. Asymmetrical directional coupler consists of two rectangular waveguides of dissimilar widths. The narrower waveguide forms the ring loop while the wider waveguide constructs a MZI. The TM mode in the wider waveguide is phase matched with the TE mode in the narrower waveguide. The TM mode in the bus waveguide (one of the MZI arms) experiences a NRPS for an unidirectional magnetic applied transverse to the light propagation. The main advantage of this device is that if the device is designed properly then a small NRPS could change the resonance condition in such a way that for the forward propagation, the NRMZI is under coupled whereas in the reverse propagation it is critically coupled. Some measurement results are presented with exceptionally high isolation. The main drawbacks of such a device are that the operational bandwidth is extremely narrow and that the performance of the asymmetrical directional coupler is very sensitive to the fabrication tolerance.

Most semiconductor laser diodes emit transverse electric (TE) polarized

light. So an isolator working for TE polarization is desirable. Therefore the next task is to design an optical isolator working for TE. In this case polarization rotators were designed to rotate the polarization of light allowing the TM mode to experience NRPS after which the polarization is rotated back to TE. Therefore the overall effect is observed for the TE light. The polarization rotators and the nonreciprocal phase shifters are fabricated in 380 nm thick silicon waveguides. The 380 nm thick silicon waveguide is created by depositing a 160 nm polycrystalline silicon overlay on top of the 220 nm thick crystalline silicon. Although an isolation of 32 dB is achieved from one of the devices, the insertion loss is as high as 22 dB. The main reason behind such a high loss could be attributed to the scattering loss due to the poly-Si overlay and the garnet.

An optical circulator is also a device which is not yet realized on an integrated platform. So the next goal was to explore optical circulators on the SOI platform. A three port MZI-based design is fabricated. The operation principle is the same as the push-pull type TM mode isolator. Two identical direction couplers are connected by 900 nm wide and 220 nm thick silicon waveguides to define the MZI. An optical circulator is demonstrated with a maximum isolation of 22 dB. The isolation is controlled by the efficiency of the direction coupler. The efficiency of the directional coupler is very sensitive to wavelength. Simulation shows that  $2 \times 2$  MMI provide a less wavelength sensitive optical circulator. The insertion loss is also similar to push-pull type MZIs and can be improved by decreasing the garnet covered waveguide length.

## 9.2 Outlook

The concept of nonreciprocal phase shifter based optical isolators and circulators is demonstrated on the SOI platform using an adhesive bonding approach. In this work different types of designs are explored. The devices presented here were designed for proof-of-principle demonstrations. Although this work shows a promising path towards heterogeneous integration of an optical isolator or circulator with a semiconductor laser diode or other optical components, some challenges are still present. In the next few paragraphs we will discuss the scopes for future improvements for both the bonding and sputtering approaches.

High optical isolation with a negligible insertion loss is the desirable combination for an optical isolator or circulator. Although remarkable isolations are achieved from some of the garnet bonded devices, insertion loss is not low enough to be implemented in an optical communication system. The total insertion loss of the device is the sum of contributions from different sources. But a large part comes from the material absorption/scattering of the magneto-optical garnet material itself. There are several possible ways to reduce this con-

tribution:

- By reducing the length of garnet covered SOI waveguide
- By improving the quality of garnet material

In some devices we have seen that garnet bonded SOI waveguide length to generate the required nonreciprocal phase shift is sufficiently small compared to the actual bonded garnet die size. So smaller garnet dies should be used. Material absorption can be minimized by annealing the garnet die before bonding.

The magneto-optical properties of the sputtered garnet on SOI is almost 1/3 of the garnet used for bonding work. The obvious advantages of this approach are the freedom in design and mass production possibility. But the main challenge here is the high insertion loss. Therefore further intensive research is required to optimize the material loss in combination while maintaining strong magneto-optical properties.

It is important to mention that external magnets are required to bias the garnet material. Although small magnets (like Nd-B-Fe) can be used, it would be better if this magnet is replaced by a thin film permanent magnet. So this is also a scope for further improvement.

Another improvement on bonded devices could be done by removing or thinning down the SGGG layer. This can be achieved by means of a chemical etchant or by chemical mechanical polishing (CMP). Thinner substrate may be useful for the case of a dense integrated circuit in which a half millimeter thick garnet substrate could bring difficulties for other devices. Moreover lesser magnetic field may require to saturate the Ce:YIG layer.

Lastly broadband operation is also an important aspect for the optical isolator or circulator. The designs of MZI-based isolators or circulators presented in this thesis can be extended towards broadband operation if needed. To achieve this a controlled way of bonding technique need to be followed in which the bonding thickness can be pre-defined. So in this case also some further research is necessary to optimize the bonding method which will dictate the device performance.



